Ice - Ocean - Atmosphere Interactions in the Southern Ocean and Implications for Phytoplankton Phenology

Mark Hague

A dissertation submitted to the University of Cape Town in accordance with the requirements for award of the degree of Doctor of Philosophy in the Faculty of Science

Department of Oceanography

October 2020

Word Count:

47 793

Abstract

The annual advance and retreat of sea ice in the Southern Ocean is recognised as one of the largest seasonal events on Earth. Such considerable physical changes have profound effects on the vertical structure of the water column, and hence controls the availability of both light and nutrients to phytoplankton. This means that in the region seasonally covered by sea ice (the SSIZ), the timing of the growth and decline (phenology) of phytoplankton is determined to a large degree by the dynamic interactions between ice, ocean and atmosphere. However, this region is simultaneously one of the most poorly observed in the global ocean, and one of the most complex. This has led to significant gaps in our understanding of how sea ice modulates the exchanges of heat and momentum between atmosphere and ocean, as well as the implications this has for phytoplankton phenology in the SSIZ.

This study seeks to address these gaps by combining both model and observationally-based methods. The lack of observational data is directly tackled through an analysis of BGC-Argo float data sampling under ice. Such data reveal high growth rates in the presence of near full ice cover and deep mixed layers, conditions previously thought to prevent growth. These results suggest a revision of our current understanding of the drivers of under ice phytoplankton phenology, which should take into account the unique character of Antarctic sea ice and its effect on the under ice light environment. In addition, results obtained from several numerical process studies indicates that phytoplankton may have a higher affinity for low light conditions than previously thought.

From a modelling perspective, an analysis and intercomparison of 11 Earth System Models (ESMs) and their representation of vertical mixing and phenology is presented. This revealed that misrepresentations in phenology where driven by model biases in sea ice cover and vertical mixing. That is, only models with either too much or too little ice cover were able to simulate phenology close to observations. Furthermore, a strong correlation between the location of the ice edge and the extent of vertical mixing suggested that ESMs overly dampen ocean-atmosphere fluxes as mediated by sea ice. This led to the development of a regional ocean-sea ice model of the Atlantic sector of the Southern Ocean, from which experiments enhancing both heat and momentum fluxes could be conducted. It was found that the model responded more uniformly to enhanced heat flux, generally deepening the mixed layer closer to observations in winter. On the other hand, the effects of enhanced momentum flux (implemented by increased air-ice drag) where more complex and spatially heterogeneous, with contrasting responses depending on the initial vertical density structure of the water column. Overall, the argument is made that the unique features of Antarctic sea ice should be included in models if we are to improve the representation of the SSIZ mixed layer, and hence phenology.

Author's Declaration

I declare that the work in this dissertation was carried out in accordance with the requirements of the University's Regulations and Code of Practice for Research Degree Programmes and that it has not been submitted for any other academic award. Except where indicated by specific reference in the text, the work is the candidate's own work. Work done in collaboration with, or with the assistance of, others, is indicated as such. Any views expressed in the dissertation are those of the author.

Mark Hague
16 October 2020

Acknowledgements

This PhD was funded by several National Research Foundation projects, including SANAP, NRF 112632 and NRF 118745. Funding for courses I attended at the University of Bergen, Norway was provided the Nansen-Tutu SCAMPI project. I would like to thank all the above projects and agencies for providing me with this invaluable opportunity. The research presented in Chapter 4 was made possible using facilities provided by the University of Cape Town's ICTS High Performance Computing team: hpc.uct.ac.za.

I would like to especially thank Dr. Marcello Vichi for his guidance, support and encouragement throughout my postgraduate career, as well as for giving me the freedom to pursue my own ideas and make my own mistakes. My sincere thanks also for providing so many opportunities over the years, from attending internation conferences and courses to visits at other research institutions. Thank you for sharing your passion for science during our countless hours of discussion, from which I have learned a great deal.

A special thanks to Dr. Robinson Hordoir for his many hours of help in setting up and debugging my regional NEMO model, both in person and remotely (and for even replying to emails while on holiday), as well as for hosting me at SMHI and keeping me entertained in Norrköping. Similarly, I would like to thank Dr. Julie Deshayes for her help in setting up the model and for hosting me at L'OCEAN. My thanks also to Andrew Lewis for his technical support and understanding in running the model on the UCT HPC.

I would also like to extend my thanks to all those at the UCT Oceanography department who made it a stimulating and inviting place to work. In particular, my thanks go to Sharon Bosma for all her support over the years emailing travel agents, booking accommodation, filing paperwork and generally helping with all the practical aspects of my PhD. Also to Cashifa Karriem for always providing friendly support and knowing who to email when practical issues arose.

Finally, this PhD would not have been possible without the support of my family and friends. To my friends Nina P, Conor, Matt, Nina FB and Dylan, thank you for taking my mind off work and filling my weekends and holidays with laughter and good memories. To my three parents Stella, Jon and Elizabeth, thank you for always believing in me and encouraging me to pursue my own interests and passions. I cannot thank you enough for all you've done in the years leading up to this PhD, and for your mental and emotional support throughout the last 4 years.

To Ishana I am endlessly grateful for your love and support, especially during the difficult periods when things where not going as I'd hoped. Thank you for listening to me complain about my model not working countless times, and for helping me manage my stress and find balance over the last 2 years, and particularly the last few months. Thank you for being a source of motivation and confidence, and for giving me the opportunity for self-reflection. I could not have asked for a better partner through this journey.

Contents

List of Figures

List of Tables

Acronyms

AABW	Antarctic Bottom Water
AAIW	Antarctic Intermediate Water
ACC	Antarctic Circumpolar Current
B70	Bellingshausen/Amundsen Seas study region north of 70^o S
BFM	Biogeochemical Flux Model
CDW	Circumpolar Deep Water
chl-a	Chlorophyll-a
Chl:C	Chl-to-Carbon Ratio
CMIP5	Climate Model Intercomparison Project Phase 5
CPT	Atmospheric Circumpolar Trough
ECMWF	European Centre for Medium-Range Weather Forecasts
ESMs	Earth System Models
GI	Growth Initiation
HF	Heat Flux Experiment
ICE	BFM runs with sea ice forcing
LCDW	Lower Circumpolar Deep Water
LIM3	Louvain-la-neuve sea Ice Model

LLA	BFM runs with enhanced low light phytoplankton efficiency
MF	Momentum Flux Experiment
MIZ	Marginal Ice Zone
ML	Mixed Layer
MLD	Mixed Layer Depth
MOC	Meridional Overturning Circulation
NEMO	Nucleus for European Modelling of the Ocean
NOAA	National Oceanic and Atmospheric Administration
NSIDC	National Snow and Ice Data Center
OPEN	BFM runs with no sea ice forcing
PF	Polar Front
PFZ	Polar Frontal Zone
QNS	Non-solar heat fluxes
R75	Ross Sea study region north of 75^o S
REF	Reference run Experiment
SACCF	Southern ACC Front
SAF	Subantarctic Front
SAMW	Subantarctic Mode Water
SAZ	Subantarctic Zone
SBdy	Southern Boundary
SIC	Sea Ice Concentration
SIE	Sea Ice Extent

SIT	Sea Ice Thickness
SOCCOM	The Southern Ocean Carbon and Climate Observations and Modeling
SR	Study Region (58 - 62^o S)
SSH	Sea Surface Height
SSIZ	Seasonal Sea Ice Zone
SSM/I	Special Sensor Microwave Imager
SSMIS	Special Sensor Microwave Imager/Sounder
STF	Subtropical Front
TF	Total Flux Experiment
UCDW	Upper Circumpolar Deep Water
W60	Weddell Sea study region at 60^o S
W65	Weddell Sea study region at 65^o S
XLD	Mixing Layer Depth

Chapter 1

Introduction

1.1 Problem Statement

The Southern Ocean comprises ∼30% of the world ocean, yet has been responsible for ∼43% of anthropogenic carbon and ∼75% of oceanic heat uptake since the industrial revolution, thus partly counteracting the effects of greenhouse gas emissions (Frölicher et al., 2015) [1]. Part of the ability of the region to sequester carbon in the deep ocean is driven by the biological carbon pump, which has been hypothesized to control glacial-interglacial atmospheric CO_2 concentrations (Martin et al., 1990a). The efficiency of the biological carbon pump is strongly related to phytoplankton phenology[2], since the timing of bloom initiation is linked to overall phytoplankton biomass achieved over the growth period (and the overall biomass achieved will strongly influence biomass export). However, our understanding of phenology has been hampered by a distinct lack of observations in the Southern Ocean, especially with respect to the biogeochemical variables.

Nowhere is this lack of data more severe than in the Antarctic seasonal sea ice zone (SSIZ), where satellite data can be missing for half the year or more and in situ observations are generally limited to the spring and summer months. In this region we know that the annual advance and retreat of sea ice strongly affects phytoplankton

[1] For these calculations the authors defined the Southern Ocean as the region south of 30°S. However, in this thesis we will consider the Southern Ocean to be the region south of 40°S, unless otherwise stated. Nevertheless, for the work presented here an exact definition of what constitutes the Southern Ocean is not especially important, since we will focus on specific regions of interest which will be defined in subsequent chapters.

[2] Here phenology refers to the seasonal cycle of growth and decline of phytoplankton, with particular focus on the timing of key biological events such as growth initiation. As such, the use of phenology in this thesis will always refer to phytoplankton phenology, unless stated otherwise. A more in depth discussion of phenology is presented in section 1.3

phenology through its influence on light and nutrient availability (Smith and Nelson, 1985; Sullivan et al., 1988; Taylor et al., 2013; Wang et al., 2014). Under ice in winter, phytoplankton growth rates are presumed to be negligible, even though this has not been explicitly shown, with some studies even showing that substantial blooms can occur under near complete ice cover (Smetacek et al., 1992; Arrigo et al., 2012; Assmy et al., 2017). Such an assumption is probably linked to the fact that sea ice cover in the Arctic generally inhibits pelagic phytoplankton under ice growth (Ji et al., 2013). At the same time, observations over the past decades of Antarctic sea ice have revealed an ice surface quite distinct from its Arctic counterpart, being primarily first year ice comprised of relatively thin small floes (Maksym et al., 2012). This is associated with a much more dynamic ice cover, which may be expected to provide a different set of environmental controls on phytoplankton than is seen in the Arctic.

Despite these clear differences, much of the sea ice physics currently instantiated in models emerged from observations done in the Arctic, resulting in a potential lack of generality [3]. Furthermore, there appears to be widespread consensus of a lack of understanding of the Southern Ocean dynamics (e.g. Watson et al. (2014)), particularly of ice-ocean-atmosphere interactions (Hobbs et al., 2016). This may be connected to the inability of Climate Model Intercomparison Project Phase 5 (CMIP5) models to adequately simulate both the mean historical state and trends in Antarctic sea ice extent (Turner et al., 2013; Mahlstein et al., 2013). However, the source of the discrepancy between modelled and observed sea ice at both seasonal and decadal timescales remains a topic of active research (Purich et al., 2016; Maksym, 2019). A substantial discrepancy also exists between the CMIP5 ensemble Mixed Layer Depth (MLD) and that estimated from observations, with models generally suppressing vertical mixing across the Southern Ocean in historical simulations (Sallée et al., 2013a). Since the seasonal cycle of vertical mixing strongly influences both light and nutrient conditions in the surface ocean, such a bias in model MLD may lead to significant biases in simulated phenology. Similarly, biases in the seasonal cycle of sea ice extent will also negatively affect modelled phenology. Indeed, some authors have already pointed out substantial biases in CMIP5 surface Chlorophyll-a (chl-a) in the summer Southern Ocean (Séférian et al., 2013; Mongwe et al., 2018), although this was not explicitly linked to biases in MLD and sea ice extent.

These biases notwithstanding, substantial progress has been made towards simulating Earth's climate in recent decades, making models invaluable tools for studying

[3]For example, Vancoppenolle et al. (2009) note that the value of h^0 (new ice thickness) in their model is well suited to new ice growth in the Arctic, but is not ideal for the dynamical pancake ice growth seen in the Southern Ocean. More details on ice growth processes are given in section 1.2.2

contemporary, past and future climate. This further motivates research into understanding the sources of model shortcomings, which may improve both the model representation and our understanding of the climate system. Within this context, the work presented here will attempt to advance understanding of the environmental controls on phytoplankton phenology in the Antarctic SSIZ. As such, we will primarily focus on the ways in which sea ice affects stratification and the light environment within the seasonal cycle. A more detailed outline of the aims of the thesis is presented at the end of the Chapter in section 1.4. The rest of this chapter will explore the literature related to the issues raised here, with a view to providing context to the discussion in subsequent chapters. The first part of the chapter will introduce the physical setting of the Southern Ocean, including its large scale circulation, seasonal sea ice and vertical mixing characteristics. This is followed by a review of phenology in the region, with a particular focus on the controls on growth in the SSIZ.

1.2 Physical Environment of the Southern Ocean

The purpose of this section is to describe the major physical features of the Southern Ocean, insofar as they provide context to the topics discussed in the thesis. The description is therefore necessarily restricted, focussing primarily on large scale features and annual time scales. In section 1.2.1, the dominant circulation patterns are discussed, followed by an overview of the seasonal cycle of sea ice and its salient properties in 1.2.2. The section will end with a characterization of the major factors affecting vertical mixing in the Southern Ocean, followed by a discussion of the role that sea ice-atmosphere-ocean exchanges play in such mixing in 1.2.3.

1.2.1 Circulation

Perhaps the most striking feature of the Southern Ocean is it's geography. The opening of the Drake Passage millions of years ago brought about the formation of the largest current in the world ocean: Antarctic Circumpolar Current (ACC). The ACC flows from west to east, extending some 2000 m into the water column and transporting 136.7$\pm$ 6.9 Sv [4] through the aforementioned gap (Meredith et al., 2011). The current is comprised of multiple fronts or jets, regions where horizontal density and Sea Surface Height (SSH) gradients are locally maximised (Rintoul and Naveira Garabato, 2013; Sokolov

[4]This number is based on data from 16 sections occupied between 1993 and 2009, and represents the mean baroclinic volume transport.

and Rintoul, 2007). Three main fronts are commonly identified, the Subantarctic Front (SAF), Polar Front (PF), and the Southern ACC Front (SACCF) (see Fig. 1.1). Two other fronts, the Subtropical Front (Subtropical Front (STF)) and Southern Boundary (SBdy) are also consistent features, but are not zonally continuous and so are often excluded. The fact that each front coincides with strong horizontal gradients makes them readily identifiable from both hydrographic data (Orsi et al., 1995) and satellite derived SSH (Graham et al., 2012).

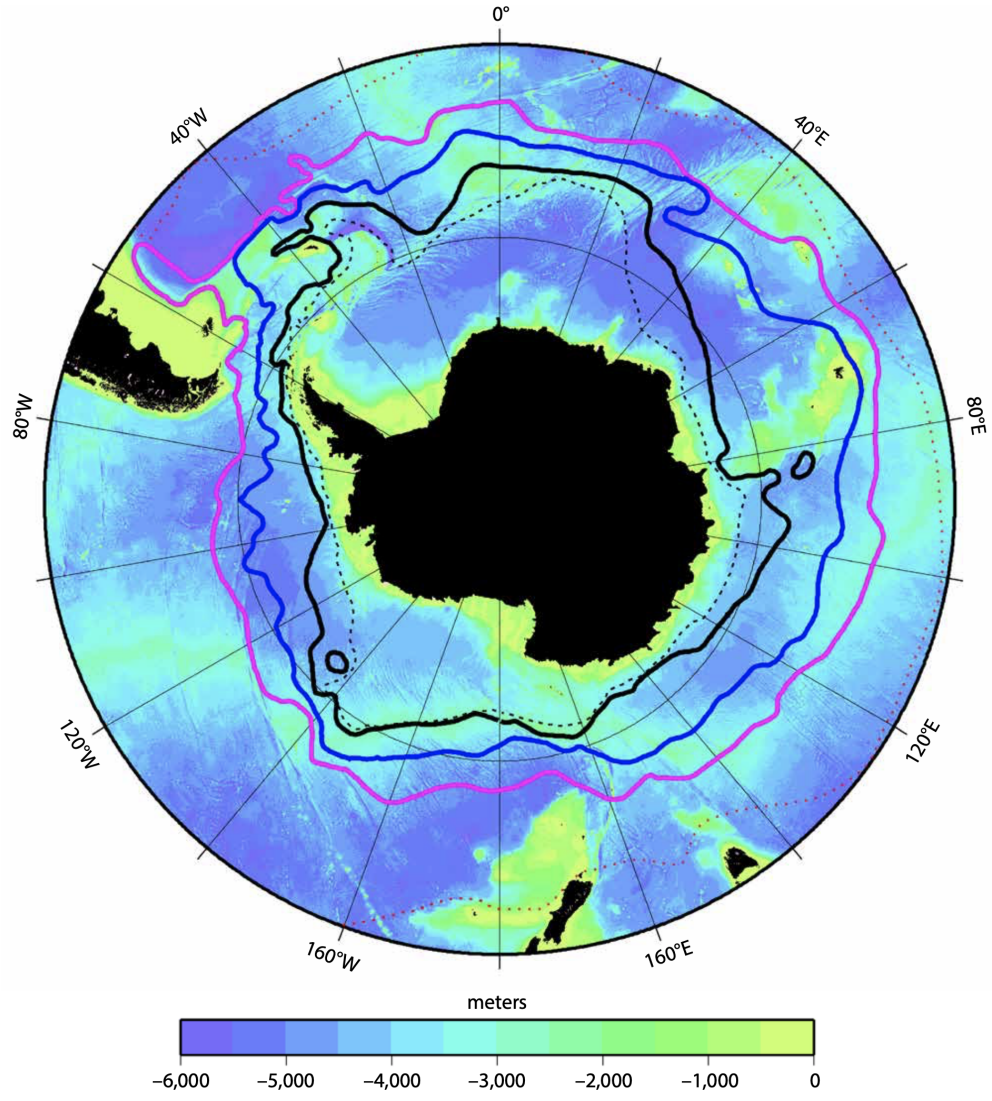

Figure 1.1: Southern Ocean bathymetry overlain with the major fronts of the ACC from Gille et al. (2016). The Subantarctic Front (SAF) is shown in magenta, the Polar Front (PF) in dark blue and the Southern ACC Front (SACCF) in black. The Subtropical Front (STF) is shown by the red dotted line. The frontal positions are those originally determined by Orsi et al. (1995).

Within the frontal structure of the ACC, density surfaces are sharply tilted upwards towards the south, allowing them to outcrop at the surface (see the different coloured

surfaces in Figure 1.2). This creates a pathway between the deep and surface oceans, making the Southern Ocean a key player in the Meridional Overturning Circulation (MOC) and hence global climate (Marshall and Speer, 2012; Rintoul and Naveira Garabato, 2013; Graham et al., 2012). At the same, the zonally unrestricted flow of the ACC mixes water masses from all the major ocean basins, further increasing its importance in the climate system.

The Southern Ocean component of the MOC circulation is depicted schematically in Figure 1.2, which also gives an indication of the major factors maintaining it. In the south close to the Antarctic continent, intense sea ice formation leads the production of the most dense water in the global ocean, Antarctic Bottom Water (AABW). Moving further north, the effect of Ekman divergence associated with the westerly winds becomes important. These strong and persistent winds drive upwelling of Circumpolar Deep Water (CDW), which is partitioned into Upper Circumpolar Deep Water (UCDW) and Lower Circumpolar Deep Water (LCDW) components. Poleward of the site of upwelling, surface water is advected south, where it joins AABW and LCDW to form the lower limb of the MOC. Accordingly, north of the wind stress maxima, UCDW are brought to the surface and transformed by air-sea fluxes before moving equatorward. Following this, they are subducted under warm Subtropical waters to become Antarctic Intermediate Water (AAIW) in the Polar Frontal Zone (PFZ) and Subantarctic Mode Water (SAMW) in the Subantarctic Zone (SAZ), thus forming the upper limb of the MOC.

Thus, large scale circulation patterns in the Southern Ocean are largely driven by the balance of wind and buoyancy forcing, with an additional contribution of poleward moving mesoscale eddies that compensate for the instability created by the equatorward Ekman component. The upwelling of deep waters that have not been in contact with the atmosphere for $\sim$1000 years results in this region being a strong source for natural carbon, while the subduction SAMW and (to a lesser extent) AAIW allows the region to store excess anthropogenic heat and carbon (Marshall and Speer, 2012). Concomitantly, upwelled waters are rich in nutrients needed to sustain primary production, highlighting the importance of large scale circulation in setting both the physical and biogeochemical characteristics of the Southern Ocean.

1.2.2 Antarctic Sea Ice

As with the preceding discussion, our understanding of Antarctic sea ice is fundamentally shaped by the geography of the region. Unlike in the Arctic, where ice

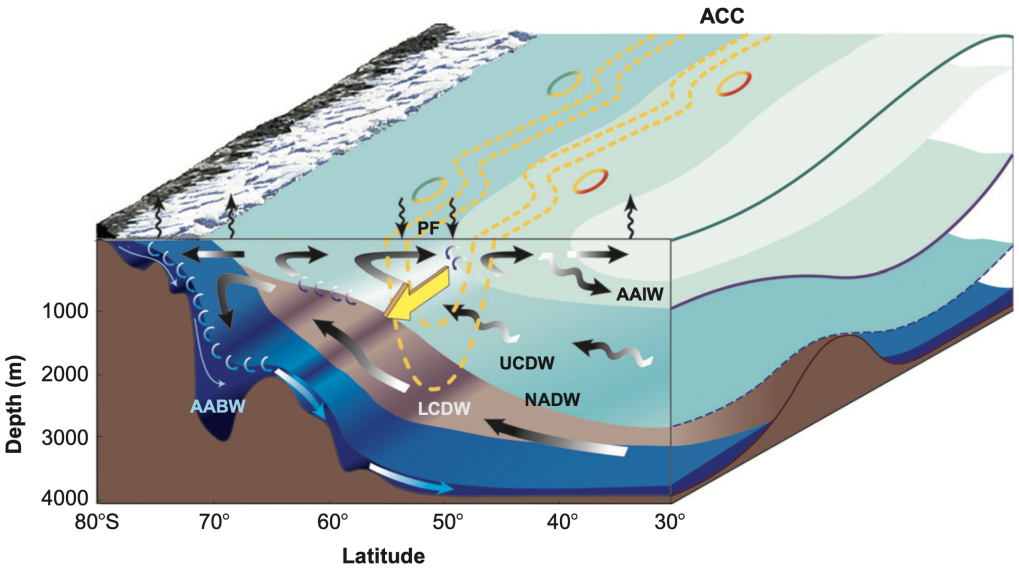

Figure 1.2: Schematic cross-section of the dominant circulation in the Southern Ocean from Rintoul and Naveira Garabato (2013). The Antarctic Circumpolar Current (ACC) is depicted by yellow dashed lines and arrow, while the Meridional Overturning Circulation (MOC) is shown by the dark arrows. Transport occurs mainly along constant density layers, which are shown by coloured surfaces. Wavy black arrows at the sea surface denote air-sea buoyancy fluxes, with down indicating buoyancy gain, up buoyancy loss to the atmosphere. Diapycnal mixing is small arrows between layers.

forms on an ocean protected by surrounding land masses, Antarctic sea ice is exposed to the vast and unbounded Southern Ocean. As a consequence, sea ice reaches much further equatorward in the Antarctic (generally 60°- 70°) than in the Arctic (generally 70°- 90°)[5], leading to a largely seasonal ice cover which almost completely melts each summer (see Figure 1.3). This temporary existence constrains the thickness of the ice cover, allowing for an ice surface which responds much more dynamically to atmospheric and oceanic forcing than its Arctic analogue. Indeed, Worby et al. (2008) estimate the mean ice thickness to be 81 cm, with a standard deviation of 91 cm (based on over 20 000 combined ship and aircraft observations). Furthermore, Antarctic sea ice receives the highest average snowfall on Earth (Massom et al., 2001), which has profound implications for its dynamics, whereas the Arctic is a desert by comparison (based on on the annual amount of precipitation received, see Serreze and Hurst (2000)). Mean snow depth over Antarctic sea ice is estimated at 15 cm (Maksym and Markus, 2008), although substantial spatial variability is seen, with west Antarctica (particularly the Weddell, Amundsen and Bellingshausen seas) generally receiving more snow (see

[5]This statement is meant to refer to the fact that the bulk of Arctic sea ice is found between 70°- 90°N, although there are regions (such as along the coast of Greenland) where sea ice extends further south (as much as 60°N).

Maksym and Markus (2008), their Figure 2).

The unique features of Antarctic sea ice listed above arise from distinct formation and melt processes. In calm conditions, ice forms at the ocean surface in thin continuous sheets called nilas, before continuing to grow vertically into the water column. Such a process leads to congelation-ice growth, and is the dominant formation process in the Arctic (Jeffries et al., 1995). However, in the Southern Ocean the surface is rarely calm, leading to the formation of a large number of fine ice crystals called frazil, which are continually mixed below the sea surface. Through continued stirring of the water/ice mixture, clumps of frazil form and become buoyant enough to remain at the surface. These then begin to consolidate into discs of ice called "pancake ice", which are typically $\sim$1 m in diameter (Lange et al., 1989; Doble et al., 2003). Importantly, even when pancakes are tightly packed together, the spaces between still contain frazil ice mixed with water, allowing the pancakes to move as individual floes (Alberello et al. (2019); see Fig. 1.4A which shows an ice surface comprised of pancakes in a matrix of frazil ice).

The thickness of the pancakes, as well as of Antarctic sea ice in general, is limited by the presence of warm CDW relatively close to the surface. The role this warm deep layer plays in Antarctic sea ice formation and melt processes will be discussed in some detail in Chapter 4. However, it is important to note at this stage that the incorporation of this warmer water into the surface layer can induce a strong oceanic heat flux to the ice, melting it from below and fundamentally limiting its thickness. This is contrasted with the Arctic sea ice, which is protected from this form of melting by a cold halocline layer which prevents warmer deep waters from entering the surface layer (Steele and Boyd, 1998). This, along with the ice formation process outlined above, accounts for the relatively low abundance of columnar over frazil ice seen in Antarctic ice cores (Lange and Eicken, 1991; Jeffries et al., 1997). That is, thermodynamic vertical ice growth (which gives rise to columnar ice in the Arctic) is hindered in the Antarctic, meaning the ice thickening takes place primarily through mechanical processes (discussed below), resulting in much higher frazil concentrations.

Another important component in the ice formation process is the ubiquitous snow layer mentioned above. Due to the very high accumulation rates (defined as the rate at which the snow depth increases, see Maksym and Markus (2008)) and generally thin ice, the weight of the snow can lower the sea ice surface to below sea level. This creates a layer of slush containing brine and seawater, which subsequently freezes to form salty layer of "snow ice" (Jeffries et al., 2001). The contribution of this formation process to the total ice thickness varies spatially and temporally, with estimates of 10% in the Weddell

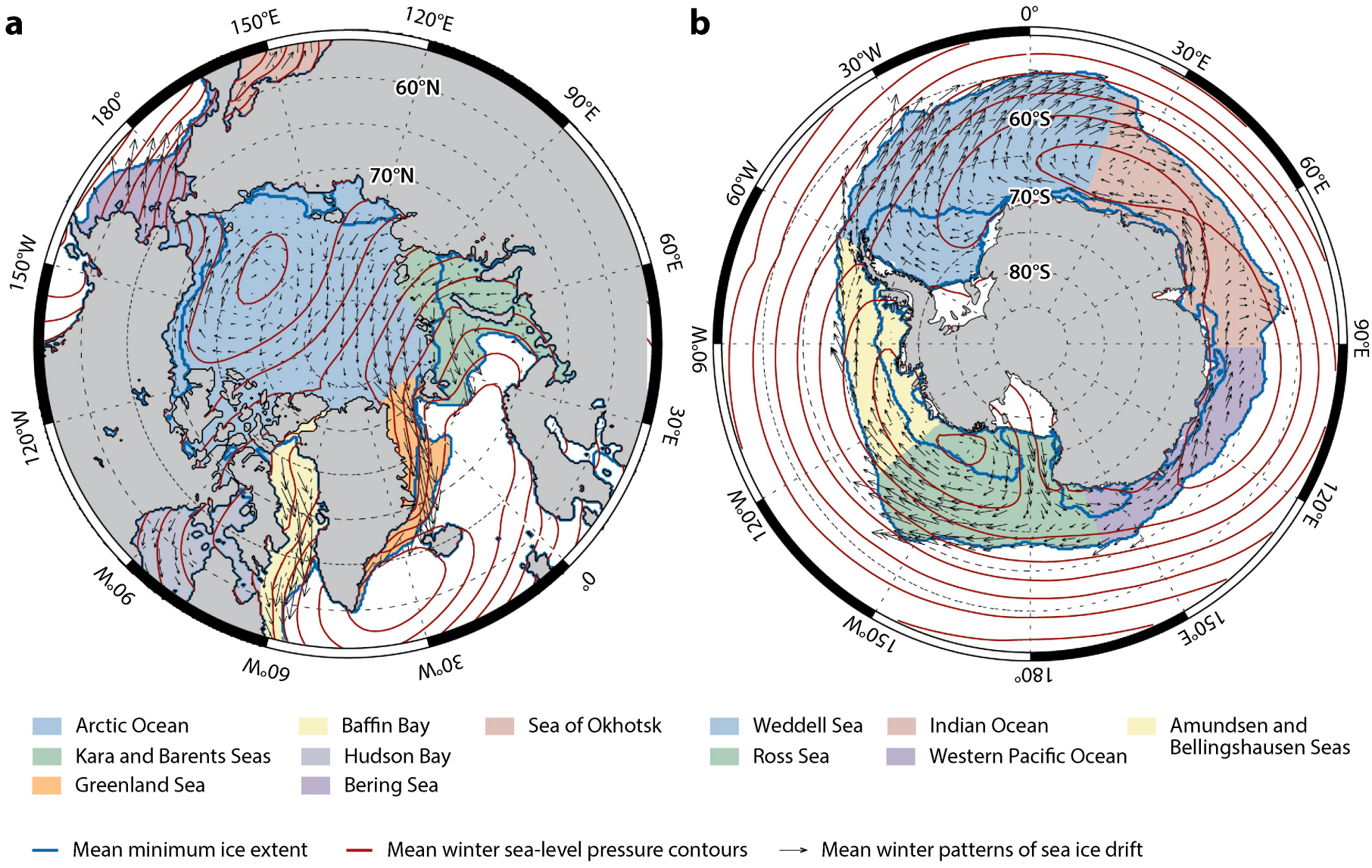

Maksym T. 2019.
Annu. Rev. Mar. Sci. 11:187–213

Figure 1.3: Comparison of major features of Antarctic and Arctic sea ice from Maksym (2019). The region between the two blue lines then depicts the Seasonal Sea Ice Zone (SSIZ), while red lines are the mean winter sea level pressure contours. Black arrows depict mean sea ice drift.

Sea (Lange et al., 1990), to as much as 40% in the Amundsen and Bellingshausen Seas (Jeffries et al., 2001). In extreme cases the snow accumulation rate is high enough to make snow-ice the dominant ice type, since ice formed through freezing of seawater is continually pushed down and melted by the strong oceanic heat flux (Lytle and Ackley, 1996).

The depth of the snow and ice layers is also critical to the transmittance of light into the underlying ocean. Indeed, light transmittance is estimated to decay exponentially with increasing ice thickness and snow depth (Perovich, 2017). Although the ice is generally thin, the presence of even a very shallow snow layer (< 10 cm) greatly diminishes light transmittance to between 1 and 5% of that incident at the surface (Fritsen et al., 2011). In line with this, Arndt et al. (2017) found transmittance to be less the 2% (with the bulk of values falling below 0.5%) from a distribution of snow depths ranging from $\sim$0 - 90 cm and ice thickness between $\sim$0 and 250 cm (see their Figure 4). Since some degree of snow cover is common through-out the year in the Antarctic (Massom et al., 2001), regions of the SSIZ where ice concentration is high would display very little, if any, light penetration into the ocean. The presence of biota within the ice will also further reduce light transmission (Fritsen et al. (2011); this is discussed below in section 1.3.2) This means that the under ice light field in the Antarctic is dominated by high transmittance features such as leads, as well as the spaces between pancakes containing water-ice mixtures discussed above. This is important not only for the heat budget of sea ice and the surface ocean under it (section 1.2.3), but also for phytoplankton residing under the ice (discussed in depth in Chapter 2).

From a dynamic perspective, it is important to understand the interaction of ice field shown in Figure 1.4 with the strong wind and wave action common in the Southern Ocean. Due to the unconsolidated nature of the ice cover, waves are often able to propagate far into the ice before becoming completely attenuated (eg. Kohout et al. (2014)). The region over which wave displacement is still significant is termed the Marginal Ice Zone (MIZ), and is depicted schematically in Figure 1.4B. Although more operationally oriented definitions based on satellite concentration thresholds (Taylor et al., 2013) are commonly used, it is widely recognized that a definition based on wave attenuation more accurately represents the MIZ (Sutherland and Dumont, 2018; Meylan et al., 2014). That is, the presence of waves in the ice surface indicate that open ocean processes such as heat and momentum fluxes remain important, while satellite ice concentration-based definitions of the MIZ tend to artificially reduce its extent (Vichi et al., 2019).

Moving poleward from the outer MIZ in winter we enter what is typically referred

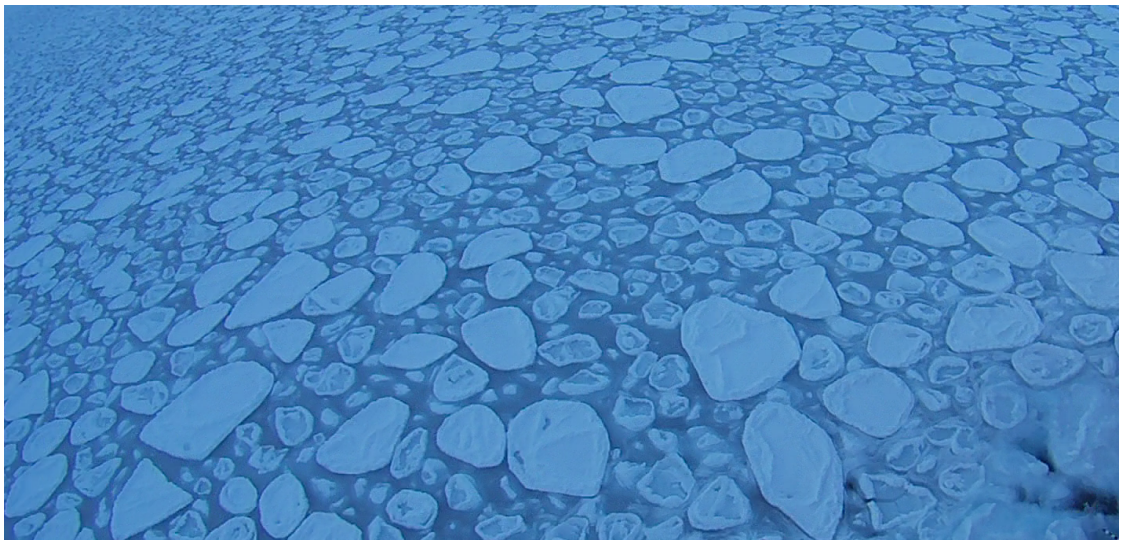

(A)

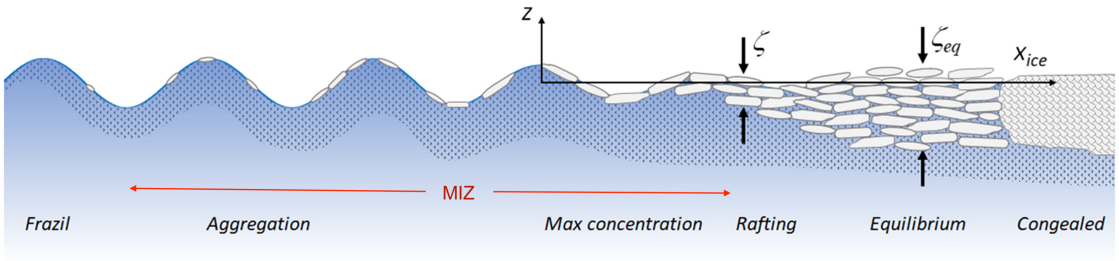

(B)

Figure 1.4: (A): Photograph of a typical pancake ice field taken from on board the SA *Agulhas* II in July 2017 in the Antarctic MIZ (Atlantic sector). **(B)**: Schematic of sea ice wave interaction adapted from Sutherland and Dumont (2018). Frazil ice is illustrated by the stippled region, pancakes by white discs. The various forces acting on the MIZ as depicted by black arrows are not discussed here. The region indicated as the MIZ corresponds to where wave action is still significant.

to as pack ice. In contrast to ice in the MIZ, pack ice is generally consolidated into larger floes ranging in size from 10's to 100's of meters (Paget et al., 2001; Roach et al., 2018b). Such floes are thought to form out of connected pancakes, with thicker ice forming through deformation processes referred to as ridging and rafting. Ridging involves the thickening of ice through the collision of floes, whereby floes are broken into smaller chunks that pile on top of one another. Rapid thickening, however may also occur through rafting. This process was mainly reported in the Weddell Sea (Lange and Eicken, 1991), where individual floes and not fragments "pile up" on top of one another and freeze into a coherent piece as is depicted in Figure 1.4B (Maksym et al., 2012). Although pack ice generally prevents ocean-atmosphere exchanges, cracks and large openings called leads are common, resulting from strain (shear or divergent flow) within the ice arising from winds, waves, currents or internal stresses.

South of the pack ice one may encounter fast ice, which gains its name from being held ”fast” to the coast (as opposed to pack ice which generally drifts with wind and ocean currents). This form of ice may be recurrent at certain locations, where it can be either perennial or seasonal (Giles et al., 2008). Due to its location in near the coast, fast ice is often protected from the strong oceanic heat flux present in the open ocean, allowing it to grow considerably thicker (>5 m Giles et al. (2008)) than pack ice (particularly if it is perennial and the ocean is shallow, see Heil (2006) and citations therein). In regions where snow accumulation is high, snow-ice formation may contribute significantly to the overall thickness (Kawamura et al., 1997). Another common ice type observed in the coastal Antarctic ocean is platelet ice, which consists of an unconsolidated mass of ice crystals (Leonard et al., 2006). These freely drifting ice crystals have been observed to form at depth (as deep as 250 m; Penrose et al. (1994)), after which they may float to the surface and become attached to the sea ice bottom (very commonly to fast ice). When found at the ice-water interface, these thin, fragile plates can have areas of tens of square centimetres, and may form layers several meters in thickness (Arndt et al. (2020) and citations therein). Overall, fast ice, and platelet layer often found beneath, form an important component of the sea ice mass and energy budget in the Antarctic SSIZ.

A final point of discussion relates to the role winds play in the seasonality of Antarctic sea ice. Work by Kimura (2004) has shown that away from the Antarctic coast sea ice motion is characterized by free drift, and so the overall winter extent, as well as it's variability, is controlled to a large degree by wind stress (Stammerjohn and Maksym, 2017; Holland and Kwok, 2012). Indeed, mean winter ice drift patterns shown in Figure 1.3b closely correspond to sea level pressure contours. Strong westerly winds at the ice edge impart a northerly Ekman drift, leading to a divergent ice cover that expands both through ice drift and formation. In the Weddell, Cooperation and Ross seas, persistent southerly winds associated with climatological low pressure systems further accentuates this divergence, leading to a maximum in ice export in these regions (Holland and Kwok (2012); see Figure 1.3b). Along the Antarctic coast strong katabatic winds in winter may lead to the formation of persistently open ocean regions termed latent-heat polynyas. These are distinguished from sensible-heat polynyas in being mechanically driven by ice advection (which is not replaced by upstream flow), rather than thermally driven by upwelling of warm deeper waters (Meredith and Brandon, 2017). The continual exposure of open ocean to the cold atmosphere leads to rates of ice formation far exceeding those of the surrounding ice covered regions ((Tamura et al., 2008); the strong heat loss to the atmosphere is compensated by the latent heat of fusion supplied by ice formation, see Markus et al. (2013)), thus further facilitating equatorward ice export. Indeed, the regions of maximum ice export noted above (Weddell, Ross and Cooperation

Seas) are all associated with coastal latent-heat polynyas (Tamura et al., 2008; Holland and Kwok, 2012).

Apart from these general features, wind-ice interactions have also been invoked to explain the seasonal asymmetry in the duration of advance (7 - 8 months) and retreat seasons (4 -5 months) (Eayrs et al., 2019). The key insight in this regard was that a twice yearly (in autumn and spring) strengthening and poleward shift of the Atmospheric Circumpolar Trough (CPT) results in a predominantly southward Ekman transport of ice in autumn (see Fig. 1.3b), thus inhibiting northward expansion (Gordon (1981); Stammerjohn and Maksym (2017) and citations therein). Conversely, in spring divergent Ekman transport in the outer regions of the ice pack accelerates retreat by creating leads which remain unfrozen due to increased solar radiation. This highlights what is believed to be the major mechanism of spring melting: warming of dark, open ocean regions which results in a strong ocean heat flux, causing lateral and bottom melting (as opposed to the strong surface melting which occurs in the Arctic) (Ohshima and Nihashi, 2005; Nihashi and Cavalieri, 2006; Eayrs et al., 2019). This process then acts as a positive feedback, with lower albedo leads opening and causing increased heat flux, leading to larger open ocean regions and even lower mean albedo.

In this section we have briefly reviewed the major processes controlling the seasonal cycle of Antarctic sea ice. In so doing, ice-ocean-atmosphere interactions have been frequently mentioned, although no specific treatment has been given to them. Accordingly, the specifics of these interactions, and in particular the consequences they have for vertical mixing in the surface ocean, will be the subject of the remainder of section 1.2.

1.2.3 Air-Sea Ice- Ocean Interactions and Implications for Vertical Mixing

Characterizing Mixing in the Upper Ocean

In the uppermost layer of the World ocean properties such as temperature, salinity and density are close to vertically uniform. Such homogeneity is the result of vertical mixing, which itself stems from turbulence in the surface ocean. The extent of this turbulence determines the depth of the mixed layer (MLD), and is controlled by both wind-induced turbulence and buoyancy changes. The mixed layer is of fundamental importance to global climate, controlling the transfer of heat, momentum and climatically important gases (e.g. CO_2) between ocean and atmosphere (Sallée

et al., 2012). In the context of the Southern Ocean, the mixed layer plays an especially important role since it interacts with the MOC (discussed above in 1.2.1) to set the major properties of the ocean's water masses. Furthermore, the seasonality of MLD strongly affects phytoplankton dynamics by modulating both light and nutrient availability (see section 1.3 below).

Since the concept of vertical mixing and the MLD will be referenced frequently in subsequent chapters, a brief overview of the ways in which such mixing is retrieved and defined is presented here (a discussion of the seasonality of vertical mixing in the Southern Ocean is presented next section 1.2.3). Traditionally the Mixed Layer (ML) is measured using vertical profiles of ocean tracers such as temperature, salinity and density. The MLD is then usually defined as the depth at which one or more tracers deviates substantially from values measured above this point. A common metric used to quantify a "substantial deviation" is a density threshold, defined as the depth where density changes by some predetermined amount compared to a reference close to the surface (generally $\delta\rho$= 0.01 - 0.03 kg m^{-3}, de Boyer Montégut et al. (2004)). A more complex method employing multiple MLD estimates derived from profile features is outlined in Holte and Talley (2009). The method generally improves upon purely threshold based methods, but its complexity has limited its adoption in the wider literature.

Nevertheless, all methods used to estimate the MLD are attempting to characterize the extent (i.e. depth) of turbulent mixing in the ocean surface boundary layer. In this regard, a more relevant quantity is the Mixing Layer Depth (XLD), which defines the depth of currently active turbulent mixing (Sutherland et al., 2014). That is, although vertical homogeneity in ocean tracers is the direct result of turbulent mixing, changes in the vertical distribution will lag behind changes in forcing, making the MLD more a record of past mixing than a proxy for the depth to which water parcels may be transported (Franks, 2015; Sutherland et al., 2014). Typical lag times between MLD and XLD can vary greatly from seasonal to daily time scales (Franks, 2015; Sutherland et al., 2014), and is subject to much uncertainly given the lack of observations of XLD (especially time series long enough to capture seasonal changes). This distinction has especially important consequences for phytoplankton phenology (section 1.3), since light availability is related to active mixing through the water column, not necessarily MLD (Franks, 2015).

In this thesis, we will employ the concept of the frequency of buoyant oscillations in the water column to defined the extent of vertical mixing. This buoyancy frequency is derived from a combination of Archimedes' buoyancy principle and Newton's second

law, and gives the frequency of oscillation of a displaced parcel in a stratified fluid (Cushman-Roisin and Beckers, 2007). It is commonly referred to as the Brunt-Väisälä frequency, N (after the two scientist who first emphasized its importance), and is defined as follows:

$$N^2 = -\frac{g}{\rho_0}\frac{d\rho}{dz},$$

where g is the gravitational acceleration, ρ_0 the reference density (a mean value for the ocean) and $\frac{d\rho}{dz}$ the vertical density gradient. The depth of maximum N, or stratification depth, (denoted ND here), is then the region of maximum resistance to mixing. Motivation for employing this metric is provided by a recent study by Carvalho et al. (2017), which showed that the stratification depth was most strongly correlated with the lower boundary of chlorophyll-a (chl-a) profiles across three regions of the Southern Ocean, suggesting it may be a more robust and ecologically relevant measure of vertical mixing than threshold-based MLDs.

Examples of climatological profiles of N are plotted in Figure 1.5 for the winter (1.5C) and summer (1.5D) Southern Ocean MIZ (Atlantic sector), with the value of the stratification depth (ND) overlain in red. Based on the equation above, we can see that N is a function of the vertical density gradient, and so larger values in Figure 1.5C and D denote regions of the water column where density changes rapidly with depth. These rapid density changes are indicative of strong stratification, meaning that the frequency of oscillation (i.e. N) of a displaced fluid parcel will be much higher in these regions (since the fluid parcel will quickly enter a layer with significantly different density, and so will feel a strong recalling force).

From Figure 1.5C and D we can see that even though multiple peaks may be present in the profile, the main peak is at least 3 times larger, implying that far less energy would be required to mix water parcels above ND than through it. What this means is that this layer represents the region of the water column where the greatest energy must be expended to homogenize the water properties (e.g. salinity, chl-a). Also shown in the figure is a comparison to the more traditionally defined MLD discussed above (black horizontal dashed lines). Generally we see that ND is located deeper in the water column, although the difference is small in the winter ($\sim$ 10 m). The exact cause of this discrepancy is beyond the scope of this introduction, although it should be noted that the MLD is very sensitive to the choice of threshold, as well as to the depth of the reference density. Nevertheless, both measures may be used to estimate the extent of vertical mixing, and thus infer the depth to which phytoplankton may be transported (which is of central importance to the work presented in this thesis). This leads us to the (by now conspicuous) question of what exactly are the sources of energy responsible for

turbulence and stratification, and what kind of mixing does this lead to in the SSIZ?

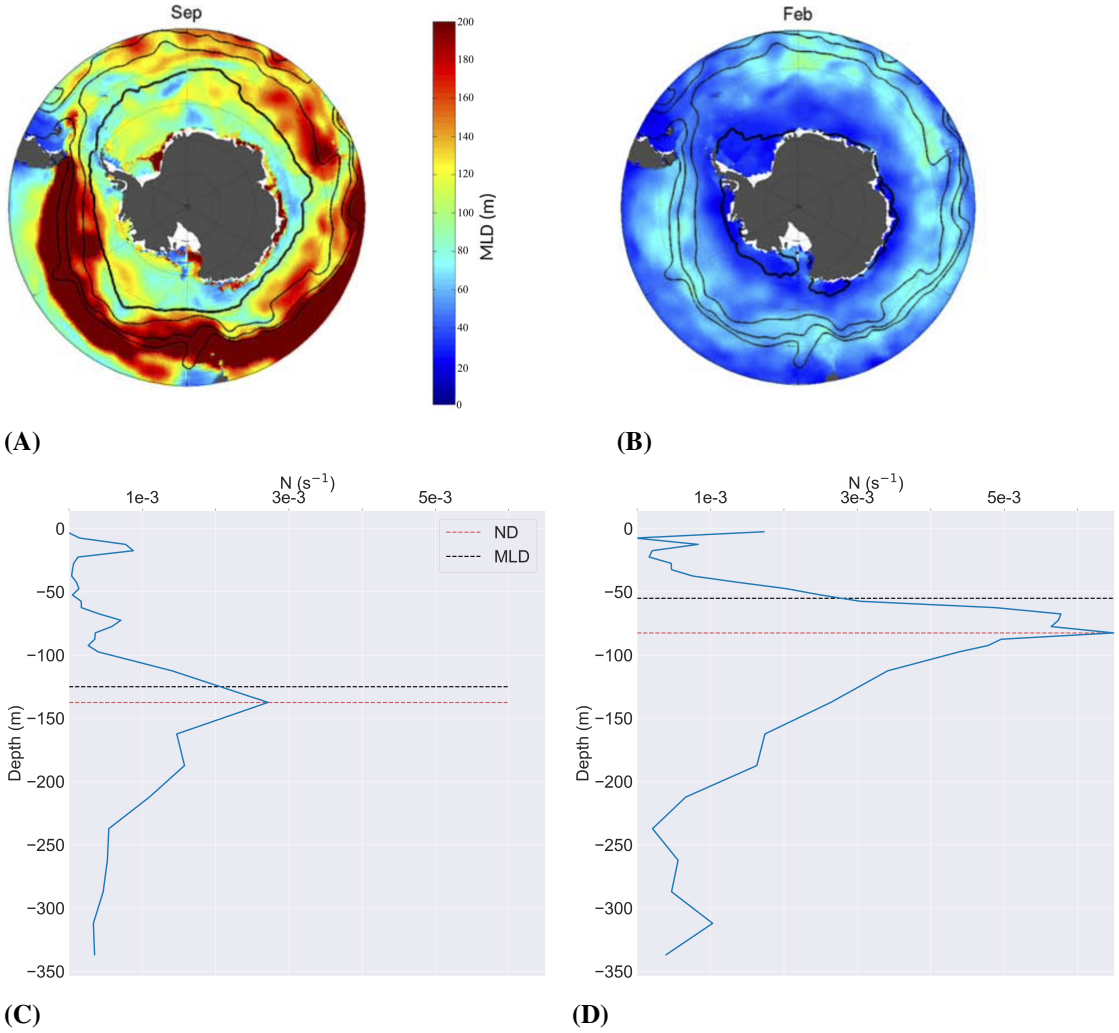

Figure 1.5: Mixed layer depth spatial variability for **(A+(C)**: September and **(B)+(D)**: February. Panels A and B are taken from Pellichero et al. (2016) and plot the spatial variability of the MLD in winter and summer. Panels C and D show the mean profiles of N (see text) in the winter MIZ (averaged over the region 58 - 62°S, 5°W - 5°E) based on WOA2018 data. Horizontal dashed lines show the value of ND (red) and MLD (black). MLD is computed using a potential density threshold value of 0.03 kg/m^3, referenced to the value at 15 m.

Sources of Turbulence and Stratification in the SSIZ

In Figure 1.5(A and B) the large scale spatial patterns of MLD in the Southern Ocean are revealed. The maps are published in Pellichero et al. (2016) and are produced through an optimal interpolation of all available ship-based, elephant seal-derived and Argo profiling float observations. In the winter, the deepest mixed layers (exceeding 200 m) occur north of the ice edge and are primarily associated with the SAF and PF regions of the ACC (see 1.2.1 above), as well as in shelf waters where sea ice production is

especially strong. Within the winter SSIZ (south of the bold black line in Figure 1.5A) under ice MLDs generally exceed 100 m, although fairly substantial spatial variability is evident, with some regions being as deep as 150 m and others as shallow as 40 m in the winter. In contrast, summer MLDs are much more spatially homogenous within the SSIZ (generally 20 - 40 m). This marked shoaling of the MLD in regions that where once ice covered illustrates the characteristic strong seasonal cycle of mixing in the Southern Ocean. This annual cycle is shown in more detail in Figure 1.6, which plots the mean MLD for each month in the ice-free and ice-covered Southern Ocean (the figure is again from Pellichero et al. (2016)). This reveals that both regions have a marked seasonal cycle, with the open ocean MLD shoaling by over 100 m from winter to summer, and the SSIZ shoaling by $\sim$80 m on average. We now turn to a discussion of the primary mechanisms behind this spatial and temporal distribution, with particular focus on the SSIZ and the role of sea ice in vertical mixing.

Fundamentally, the depth of the mixed layer is determined by the balance between the inherent static stability of the water column and the destabilizing forcing (Pellichero et al., 2016). These include both dynamic and thermodynamic forcing, which can act to erode stratification or enhance it. At the large scale, the buoyancy content of the mixed layer within the SSIZ has been shown to be primarily driven by thermodynamic processes associated with formation and melting of sea ice (Abernathey et al., 2016; Haumann et al., 2016; Pellichero et al., 2016). Regionally, the degree of turbulence is also strongly influenced by dynamic processes such as wind, wave and current interaction (Uotila et al., 2000; Maksym et al., 2012; Kohout et al., 2014; Stopa et al., 2018). Although both types of forcing are inevitably at play simultaneously, and interact at various time scales, it is instructive here to discuss each in turn.

Thermodynamic Processes One of the most important ways in which sea ice affects the mixed layer is through fresh water fluxes, as well as through modulation of ocean-atmosphere heat exchange. During much of the year the surface ocean is warmer than the overlying atmosphere, driving a net heat flux from ocean to atmosphere in the Southern Ocean. In fact, as is shown in Figure 1.7, the dominant way the ocean gains heat is through short wave radiative fluxes from October to March. All other components are negative (i.e. fluxes leaving the ocean) on average through the year. A crucial point though, is that because of the properties of the equation of state near the freezing point, the density of seawater near freezing is primarily salinity driven, meaning that sea ice formation and melting processes are the dominant drivers of the vertical density structure in winter (or when the ocean is near to the freezing temperature). Indeed, once the ocean has reached the freezing temperature, further heat loss tends to drive ice

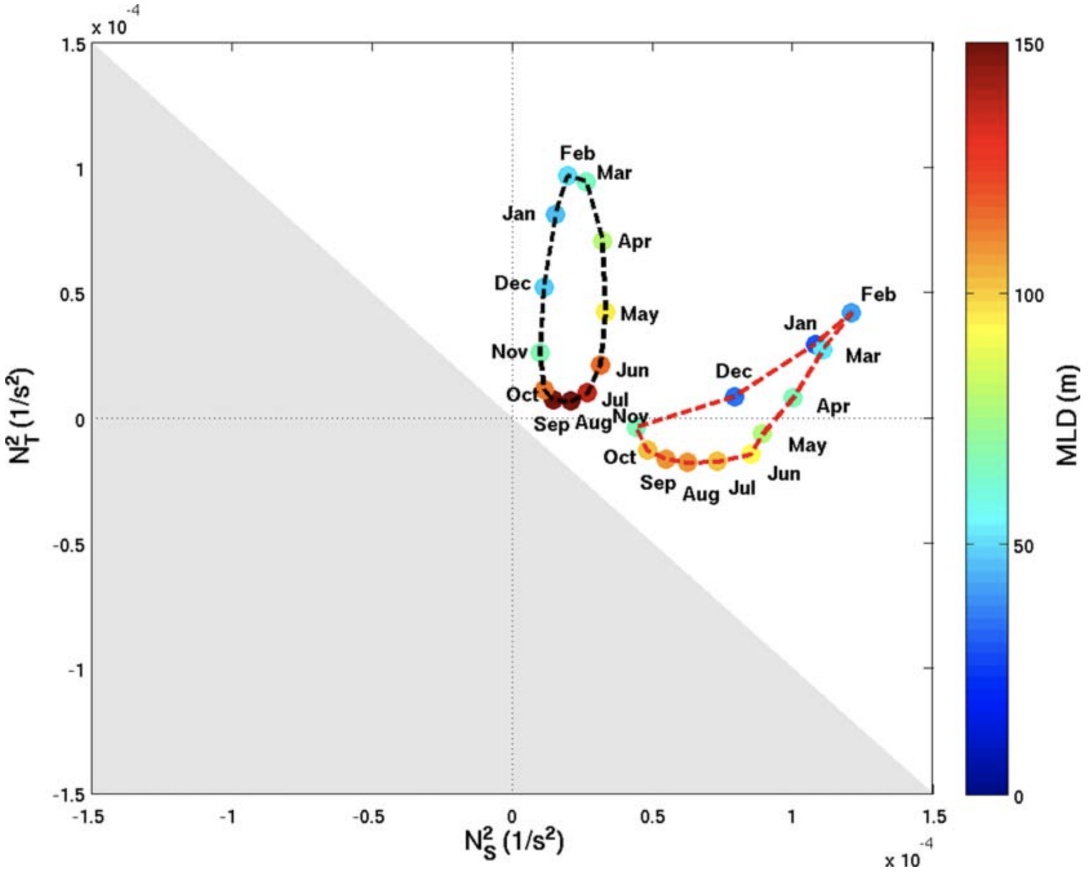

Figure 1.6: Seasonal cycle of stratification at the base of the mixed layer from Pellichero et al. (2016) for the ice covered ocean (red line) and the open ocean (black line). Coloured points represent the mean MLD for a given month. Points are plotted as a function of stratification resulting from salinity (x-axis) temperature (y-axis). This is achieved by decomposing the total stratification frequency (N-see text) into salinity (N_S) and temperature (N_T) components (see citation for more details). Positive (negative) values indicate a stabilizing (destabilizing) gradient. The grey region then corresponds to a gravitationally unstable profile (i.e. increasing temperature or decreasing salinity with depth).

formation rather than temperature reduction. In addition to this, the physical properties of ice and snow also provide a barrier to ocean-atmosphere heat exchange. This is because sea ice, and the snow commonly found on its surface in the Southern Ocean, are highly effective insulators, and so the presence of ice can significantly reduce heat exchange with the atmosphere (Martinson, 1990a; Pellichero et al., 2016).

The effectiveness of insulation is, however, dependent on the type of ice. As was pointed out in subsection 1.2.2, Antarctic sea ice is characterized over large regions by small floes in a matrix of frazil/water (especially during formation, Maksym et al. (2012); Lange and Eicken (1991)). Since the frazil/water mixture does not impede ocean-atmosphere heat exchange, such an ice surface can be expected to be highly permeable

to heat fluxes (ocean-atmosphere heat flux can be as high as $\sim$600 - 300 $W.m^2$ during initial formation - Matsumura and Ohshima (2015)). Furthermore, within the pack ice the presence of leads will also enhance heat exchanges.

Heat loss to the atmosphere can cool the ocean to the point where the surface layer becomes more dense than layers beneath it, a gravitationally unstable situation that leads to convective turbulence. These dense waters will then sink until reaching an equilibrium level, making convectively driven turbulence one of the most efficient means of deepening the mixed layer in the SSIZ (Franks, 2015). Indeed, this is precisely the process which is thought to lead to the deepest MLDs shown in Figure 1.5A north of the ice edge, with relatively shallower MLDs south of the edge resulting from sea ice insulation (the effect of wind stirring is discussed below under "dynamic processes").

In contrast, within the sea ice zone deep mixed layers are primarily formed through ice formation, a process which, due to the ice crystal lattice structure, rejects almost all ions which make up the ocean salinity (Petrich and Eicken, 2016). This process, referred to as brine rejection, therefore injects highly saline brines into the underlying ocean. These brines are significantly more dense than the surrounding ocean (due the equation of state discussed above), thus leading to convective instability and attendant vertical mixing. The very deep MLDs along the Antarctic coast seen in Figure 1.5A are a product of this mechanism, whereby strong katabatic winds continually move ice offshore and allow for large volumes of ice to be formed. Similarly, the relatively deep MLDs of $\sim$120 m seen in the open ocean SSIZ in September (Figure 1.5A, $\sim$60 - 70°S) are the result of ice formation occurring in the preceding months.

Later in the year in spring and summer, the surface heat balance shifts and heat fluxes become positive (i.e. the ocean gains heat on average - see Figure 1.7). In Figure 1.7A we see that this generally occurs in October in the SSIZ (and slightly earlier in September for the open ocean), thus precipitating melting of sea ice formed over the winter. This now releases freshwater into the ocean (sea ice is has very low salinity due to brine rejection, typically $\sim$5 g/kg, Vancoppenolle et al. (2013)), creating a "fresh-water lens" at the surface (Smith and Nelson, 1985) and contributing to sharp vertical density gradients and the high N values close to the surface seen in Figure 1.5D. This buoyant surface layer is then more easily warmed in the spring and summer (since mixing with the cold winter waters below is inhibited by the salinity gradient), further strengthening stratification.

The effect on vertical mixing at the seasonal time scale of both thermodynamic processes discussed here (ice formation/melting and atmospheric heat fluxes) is summarized in Figure 1.6. Here the stratification frequency (N) is decomposed into temperature (N_T,

plotted on the y-axis) and salinity (N_S, plotted on the x-axis) components, where N_T and N_S are a function of the vertical temperature and salinity gradients, respectively (Pellichero et al., 2016). Positive values for N_T and N_S are indicative of a stabilizing gradient, while negative gradients imply destabilization. In the open ocean, stratification at the base of the ML is dominated by the vertical temperature gradient, suggesting that atmospheric heat fluxes play a key role in determining the extent of mixing. Salinity gradients are fairly modest by comparison, with the temperature component being more than 4 times that of the salinity (i.e. the amplitude of changes along the y-axis are 4 times larger than those along the x-axis). However, in the ice covered sector both temperature and salinity components contribute significantly to ML stability, with salinity being the slightly more important factor overall. However, from a seasonal perspective it is clear that the temperature component is only significant from November to May when the ice sector is partially covered and heat fluxes into the ocean become important. During winter the stratification is almost entirely driven by salinity gradients associated with brine rejection.

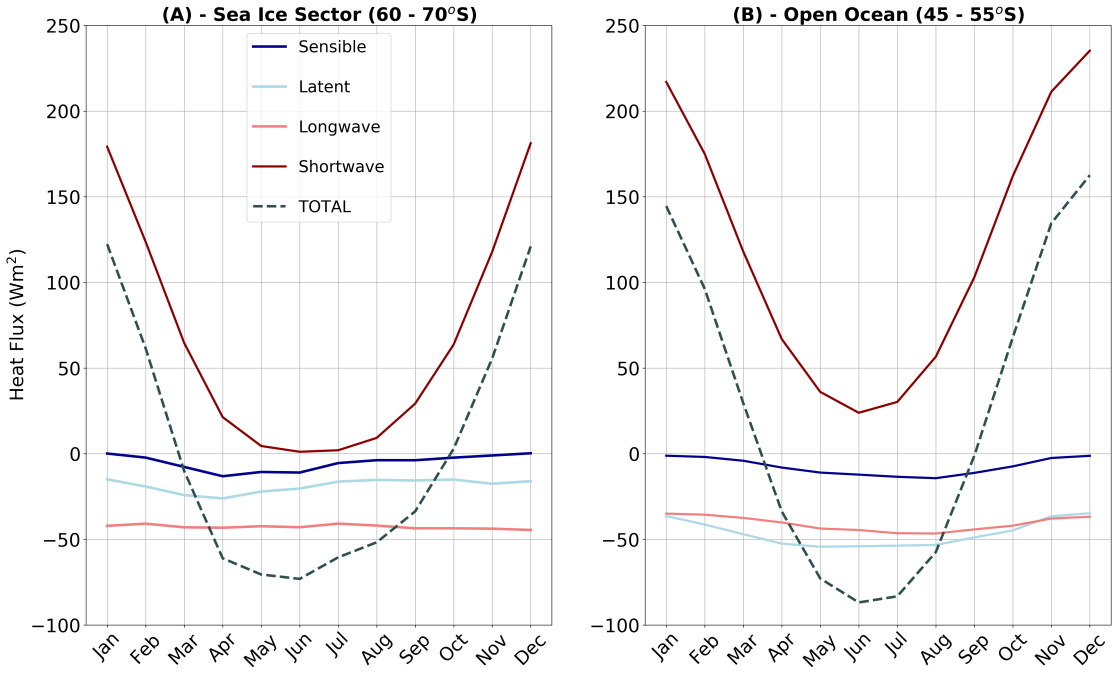

Figure 1.7: Climatological (2014 - 2019) time series of the major fluxes controlling vertical mixing averaged over **(A)** the SSIZ (60 - 70°S) and **(B)** the open ocean between 45 and 55 °S. Shown are shortwave (red) and longwave (light red) radiative fluxes, as well as sensible (blue) and latent (light blue) heat fluxes. Data in are from ECMWF Era-Interim reanalysis product.

Dynamic Processes The primary way in which sea ice affects vertical mixing dynamically is through its motion relative to the underlying ocean. Such differences in

velocity produce shear in the under ice boundary layer, generating turbulent fluctuations in the flow and ultimately mixing tracer properties (McPhee and Morison, 2001). Since relative ocean-ice motion is driven primarily by wind stress, this kind of mixing fundamentally arises from the transfer of momentum from atmosphere to ocean, via sea ice. Both air-ice and ice-ocean stresses are related to the aerodynamic roughness of the ice, given its by roughness length, z_0, which denotes the level at which fluid velocity is zero close to the ice surface (Notz, 2012). In practice, z_0 is expressed in terms of a drag coefficient, C_d, to give a bulk formula used to estimate the atmospheric or oceanic shear stress (McPhee, 2008), τ_s:

$$\tau_s = \rho C_d U^2,$$

where U is the wind or current horizontal velocity and ρ is the air or water density.

Thus, the strength of momentum exchange between atmosphere and ocean is directly related to C_d (both air-ice and ocean-ice drag). In Chapter 4 we will examine in detail the role this quantity plays in vertical mixing through the used of a coupled ice-ocean numerical model. However, it is also important to note that the presence of ice may protect the ocean from wind induced mixing by preventing the generation of surface gravity waves (McPhee and Morison, 2001; Wu et al., 2015). Nevertheless, in regions where the ice surface is highly unconsolidated and floes are able to move considerably under wind forcing, vertical mixing may be enhanced (in comparison to regions where the ice is more consolidated, and thus relative ice-ocean velocity is reduced). As has already been discussed, this kind of condition is common in the Southern Ocean, especially during formation and melting, as well as within the MIZ (Maksym et al., 2012; Doble et al., 2003; Lange and Eicken, 1991; Lange et al., 1989). As such, we will be focussing our attention primarily on these regions where wave-ice interactions are significant. Unfortunately, measurements of C_d in such regions are rare, with most studies focussing on fully consolidated ice conditions, or on Arctic regions where ice concentration is a good indicator of ice type coverage (Martinson and Wamser, 1990; Steele et al., 1989; Tsamados et al., 2014).

In addition to wind and wave forcing associated with the persistent westerly winds, Antarctic sea ice is also strongly affected by intense polar cyclones, which significantly enhance air-ice-ocean interactions during their passage (Vichi et al., 2019; Uotila et al., 2000). Such storms may generate large swells, which are often able to propagate 100's of kilometres into the thin ice cover (Kohout et al., 2014; Vichi et al., 2019). Waves in the ice may break up the ice surface and enhance ocean-atmosphere heat exchange, leading to increased formation and deepening of the MLD during advance, and higher freshwater flux and stratification during retreat. However, in cases where the presence

of ice strongly attenuates wave energy, compacting of the ice field may occur, possibly accompanied ridging and rafting of floes (Stopa et al., 2018). Similarly, on-ice winds, as well as convergent flow regimes may also lead to ice consolidation (Massom et al., 2006). The effect of consolidation on mixing depends again on the season. During the advance phase the ML may shoal (relative to less compacted regions) if ice formation and heat loss to the atmosphere are reduced by the absence of leads. During retreat it may have the opposite effect, hampering the positive feedback (outlined in section 1.2.2 above) involved in sea ice break up and melt, thus inhibiting restratification.

Clearly air-ice-ocean interactions and their impact on vertical mixing in the Southern Ocean are highly complex, requiring further investigation using both models and observations. Accordingly, this issue is of central importance to the work presented in this thesis and will be discussed in some form in all subsequent chapters. In particular, the seasonality of sea ice and vertical mixing strongly influence annual cycles of phytoplankton growth, a topic to which we will now turn our attention.

1.3 Phytoplankton Phenology

The study of phytoplankton phenology is concerned with the timing of biologically significant events (Racault et al., 2012). It has its roots in the desire to quantify both spatial and temporal changes in an ecosystem, in order to make objective comparisons between regions or periods (Platt and Sathyendranath, 2008). In the global ocean, and especially at high latitudes, temporal changes are dominated by the seasonal cycle of growth and decline in phytoplankton biomass. In this sense, phenology is the study of annual cycles of ecosystem change, as well as the environmental and biological processes which drive such change.

Examples of commonly used indices which quantify annual phenological events include the timing of the onset of growth, the timing of rapid accumulation (i.e. bloom onset), the timing of peak biomass and growth termination, as well as the length of the growth period. These events can then be linked to both physical drivers such as light and nutrients, as well as ecological constraints on biomass such as predation. In this thesis we will most commonly use temporal changes in chlorophyll-a (chl-a) concentration as a proxy for phytoplankton growth, which can then be used to estimate phenological indices. The discussion of phytoplankton phenology which follows is separated into two parts. First, a treatment of the major controls on phytoplankton growth will be presented, followed by an exploration of the unique light and nutrient environment present in the Southern Ocean and its seasonally varying ice cover.

1.3.1 Controls on Phytoplankton Growth

Phytoplankton biomass at any point in time is mediated by what has been termed "bottom-up" and "top-down" controls. Bottom-up controls refer to environmental conditions which affect the division rate, μ (day^{-1}), of planktonic cells. Top-down controls are those which directly reduce biomass, and can be summed up as "loss terms" (more detail on this is given below), l(day^{-1}), giving the following simple equation describing the rate of change in biomass Behrenfeld and Boss (2018):

$$r = \mu - l$$

It follows then that changes in biomass result from the balance between gain and loss rates, with rapid accumulation (a "bloom") only occurring when μ is significantly greater than l for a sufficient period (Behrenfeld et al., 2017). It should be noted that this formulation also allows for $r > 0$ even if μ is close to zero or decreasing in magnitude, as long as $\mu > l$. We will return to this detail later in the discussion, focussing at this point on the factors which influence μ and l and ultimately the sign of r through the annual cycle.

Bottom-up controls on μ The division rate of phytoplankton is primarily controlled by light and nutrient availability, and (to a lesser extent) ambient temperature. Apart from annual variability in incident light (driven by solar angle), the primary mechanism limiting light availability in the high latitude open ocean is vertical mixing (we will, of course, discuss the special case of ice cover in section 1.3.2 below). During periods of surface cooling and/or strong wind stress, deepening of the ML and/or increase in turbulence lowers the mean light exposure of phytoplankton cells during the diurnal cycle. This is because light is attenuated with depth in the ocean in an exponential fashion (as show schematically in Figure 1.8B), and so phytoplankton cells are continually transported through this vertical light gradient. The depth of the sunlit layer in the top half of Figure 1.8B is referred to as the euphotic zone, and is typically defined as the depth where photosynthetically available radiation (PAR) has decreased to 1% of its surface value. Therefore, the interplay between the extent of vertical mixing (i.e. the depth to which cells are transported), and the depth of the euphotic zone, largely determines the light available to phytoplankton.

This allows one to construct a conceptually defined depth horizon where gross photosynthesis exactly equals phytoplankton respiration (see Sarmiento and Gruber (2006), Ch. 4 for more details). This depth level is referred to as the compensation

depth (see Figure 1.8A), and implies that net photosynthesis is only possible above this level in a completely stratified ocean (i.e. there is no vertical mixing). This lack of vertical mixing is important, since phytoplankton cells are subject to ocean circulation (i.e. their position in the water column is determined by vertical mixing).

This conceptual framework was first laid out by Gran and Braarud (1935), and later famously extended by Sverdrup (1953) to explain the occurrence of spring blooms in high latitude oceans. The key idea here was that in the real ocean vertical mixing is rarely completely absent, and so a "critical depth" (Z_c) may be defined as the depth to which cells can be mixed such that average diurnal light driven production exactly counters respiration (see Figure 1.8A - in this model the respiration rate is considered constant through the water column). The critical depth is always deeper than the compensation depth, since cells found at the compensation depth at any given time will have spent at least part of their time above it, where light is sufficient for net growth (Sarmiento and Gruber, 2006). In other words, since the critical depth takes into account vertical transport, net positive growth can occur even when cells are mixed below the compensation depth (so long as they receive enough light to counter respiration in the upper portion of the water column). It follows then that $r > 0$ only when $Z_c > MLDorXLD$, that is, biomass may only accumulate when vertical mixing does not exceed the critical depth. It should be noted that the only loss term taken in account here is respiration (Behrenfeld et al., 2017), other factors such as grazing and sinking are not implicitly included as has been incorrectly reported in the literature (e.g. Fischer et al. (2014); Lindemann and St. John (2014)). This is not a value judgement of the critical depth hypothesis, but merely a clarification that Sverdrup intended these other factors to be treated separately.

In relation to phenology and the spring bloom at high latitudes, it is argued that following deep winter mixed and entrainment of nutrients into the ML, surface heating promotes restratification and a shoaling of the ML to above the critical depth. Thus, the timing of bloom initiation may be theoretically deduced from knowledge of the seasonal cycle of Z_c and MLD/XLD, with increasing light exposure (due to increasing incident light as well as decreasing MLD) being the primary trigger of growth. Later in the season nutrient exhaustion is commonly cited as the primary factor controlling the timing of growth termination (Boyd et al., 1999; Buesseler et al., 2003). This paradigm of light limitation and nutrient replenishment in winter, rapid growth in spring, and finally nutrient depletion in late summer/autumn, is the most influential framework used in the current literature to characterize phenology in temperate and polar regions (Behrenfeld and Boss, 2014). While seasonal variability of light and nutrients are no doubt important phenological drivers affecting cell division, factors affecting l (loss rates) may be equally

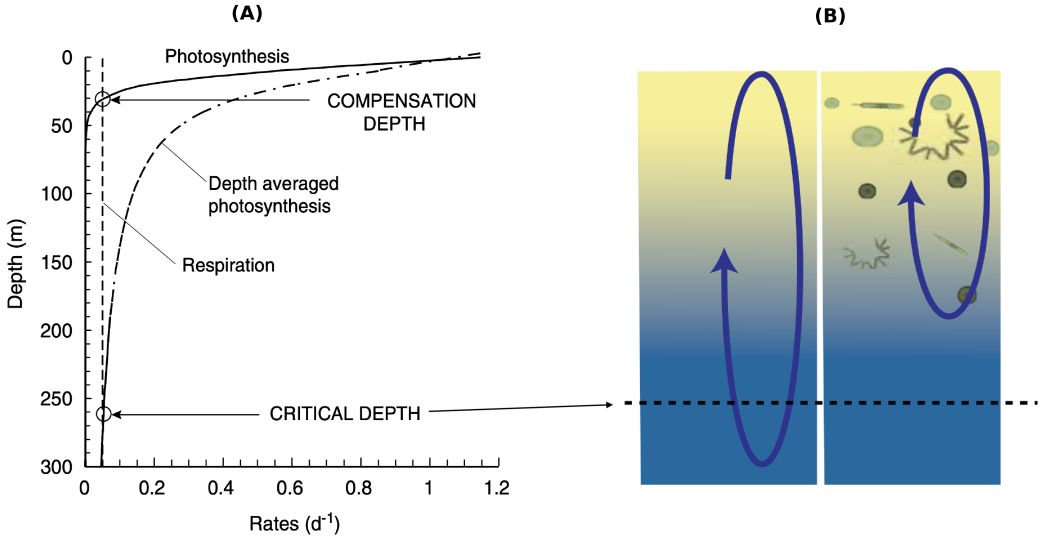

Figure 1.8: Schematic of the compensation and critical depth concepts from **(A)**: Sarmiento and Gruber (2006), Ch. 4 and **(B)** Fischer et al. (2014). In **(A)** the difference between the compensation and critical depths is shown in relation to photosynthesis and respiration as discussed in the text. In **(B)** the vertical light gradient is shown, as well as the vertical transport of phytoplankton cells. Refer to the text for more details.

important.

Top-down controls on l Direct losses to the phytoplankton community come in three main forms: grazing, viral and bacterial losses, and sinking out of the mixed layer. Grazing is the most widely studied top-down control and is typically thought to scale with phytoplankton biomass concentration up to some maximum rate (Rohr et al., 2017; Vichi et al., 2007). However, zooplankton are of course not perfectly efficient at assimilating planktonic carbon, with the rate of uptake depending on factors such as phytoplankton concentration (higher efficiency at higher concentration), temperature, and the size of cells (smaller groups are often preferentially consumed). Losses related to viruses and bacteria are thought to occur through cell lysis (breaking down of the cell wall), which is promoted by viral attack (but may also occur under environmental stress), as well as competition with bacteria for resources (Kirchman, 1999; Buchan et al., 2014). The final loss term represents multiple pathways through which phytoplankton biomass may exit the mixed layer and enter the deep ocean. The two most prominent of these pathways are ”detrainment” (shutdown of convective turbulence from winter to spring drives cells below the new stratification depth into the deep ocean) and direct sinking of individual cells and aggregates (Iversen and Ploug, 2013; Lindemann and St. John, 2014).

Regardless of the exact mechanism, our primary concern here is the effect such loss terms have on phenology. As was stated from the outset, the sign of r results from the balance between μ and l, but studies of phenology generally focus only on abiotic factors affecting μ (e.g. Buesseler et al. (2003); Fauchereau et al. (2011); Taylor et al. (2013); Ardyna et al. (2017)). Despite this, there is increasing recognition of the role played by top-down control, with the work of Behrenfeld and Boss (2014) highlighting factors related to predator-prey interactions. The argument being made is that the depth-averaged biomass accumulation rate is not directly correlated with division rates (see Figure 1.9b), implying that changes in r cannot be explained by invoking increasing μ (Behrenfeld, 2010; Behrenfeld and Boss, 2014; Behrenfeld et al., 2017).

This leads to a view of phenology that expands on the critical depth framework discussed above. Namely, when assessing phenology from the perspective of changes in r it emerges that growth actually initiates in winter during deep mixing and poor light conditions (in the temperate North Atlantic; Figure 1.9a, but also at higher latitudes in both hemispheres Behrenfeld et al. (2017)). Furthermore, peak r occurs during a period of decreasing μ in early winter. This is understood to result from the effect mixing has on predation and viral loss: according to this theory, enhanced turbulence entrains waters low in phytoplankton, thus diluting the mixed layer biomass and reducing encounter rates with zooplankton and viruses (i.e. loss rates are decreasing faster than μ). This is referred to as winter predator-prey "decoupling", which disrupts the otherwise tight correspondence between zooplankton and phytoplankton growth (Figure 1.9c). Later in the season "recoupling" occurs, with both l and μ increasing, until losses outstrip net photosynthesis and accumulation is terminated. This framework has been called the "disturbance-recovery" hypothesis (disturbance referring the decoupling, recovery to the recoupling), and will be discussed again in Chapter 2.

Phytoplankton Physiology One factor affecting phenology which we have not yet discussed is ability of phytoplankton to alter their physiology in response to environmental changes. While a complete overview of physiological responses to seasonal variability is beyond the scope of this introduction, it is necessary to discuss responses to changes in light intensity, since these are also discussed in Chapter 2 and 3. The ability of phytoplankton to alter their physiology in response to changing light intensity is termed photoacclimation, and can be achieved through many changes at the cellular level, including altering pigment concentrations (e.g. chl-a) as well as other components of the photosynthetic machinery (Bellacicco et al., 2016). Changes in pigment amounts are considered most important, and can be measured in terms of the Chl-to-Carbon Ratio (Chl:C). When under light stress (i.e. when light intensity is too

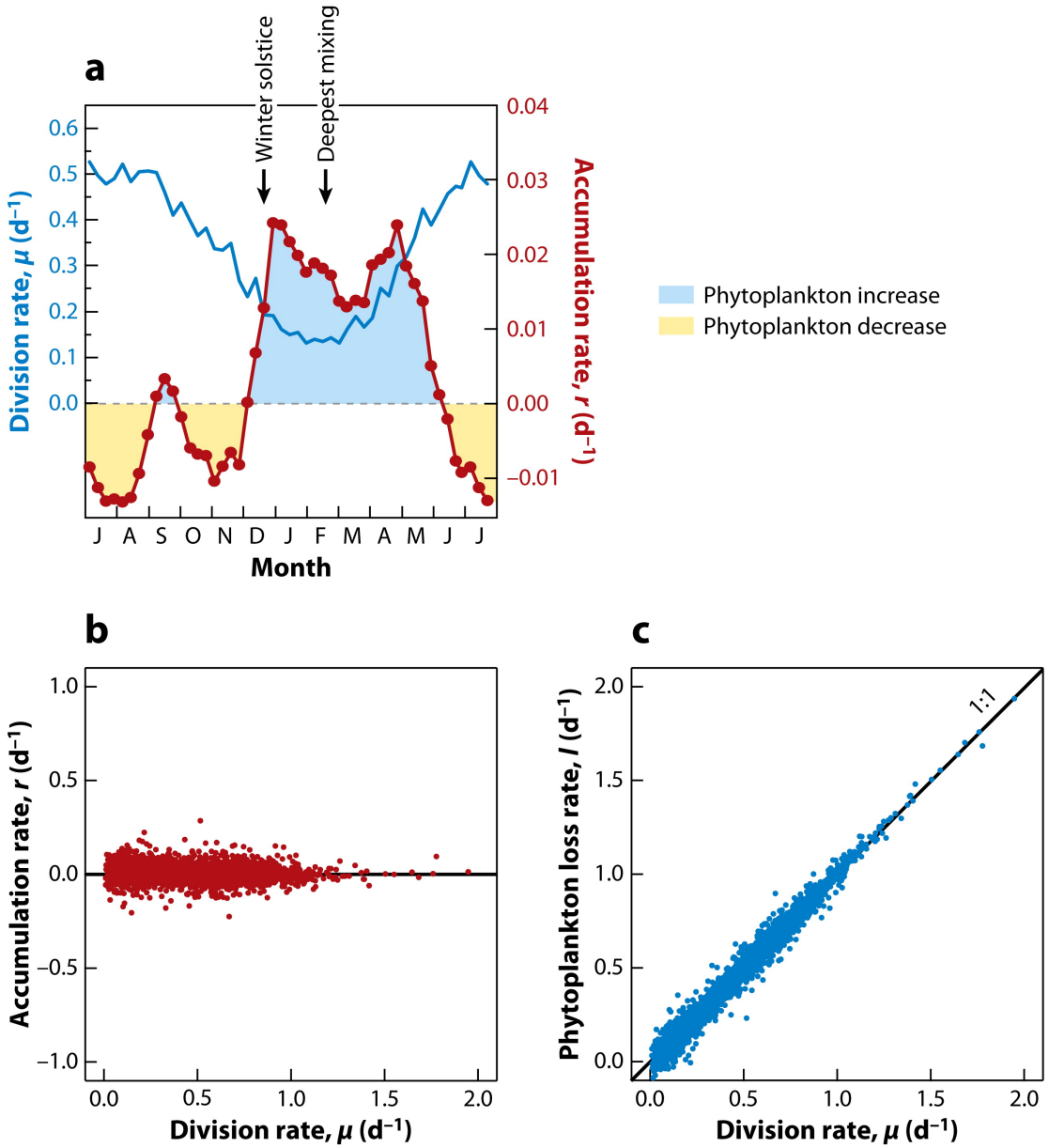

AR Behrenfeld MJ, Boss ES. 2014.
Annu. Rev. Mar. Sci. 6:167–94

Figure 1.9: Evidence of top-down control of phytoplankton in the North Atlantic from Behrenfeld and Boss (2014) (their figure 3). (a) Mean seasonal cycle (July - July; 1998 - 2008) of division rate (μ; blue line) and accumulation rate (r, red line) averaged over the region 45 - 50°N. (b) Relationship between r and μ for all regions and years analysed by Behrenfeld (2010). (c) The same as (b) but for l and μ. r and μ are computed from SeaWiFS phytoplankton carbon concentration (C_{phyt}) and surface chl concentration (Chl_{sat}), respectively. r is estimated by the difference in C_phyt between consecutive 8-day-resolution time bins. μ is computed as the mixed layer net primary production (derived from Chl_{sat} following Behrenfeld (2010)) divided by mixed layer C_{phyt}. l is then simply r - μ (see text).

low or too high), phytoplankton may increase or lower this ratio in order to optimize photosynthesis.

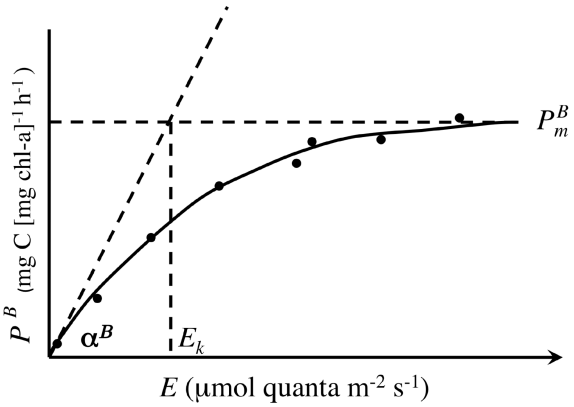

Figure 1.10: A representative P-I curve showing the relationship between the photosynthetic rate (here mg C h^{-1}) and light intensity from Bouman et al. (2018).

This process of altering pigment amounts based in the light environment is typically modelled using a chlorophyll to carbon ratio (Chl:C ratio), although phytoplankton themselves photoacclimate by altering the number of chloroplasts (Dubinsky and Stambler, 2009). In the context of high latitude oceans, optimal Chl:C ratios have been shown to vary considerably at seasonal to subseasonal time scales, which reflects both photoacclimation at the cell level and changes in the community composition (i.e. different species tend to have different Chl:C ratios; Thomalla et al. (2017)). The varying Chl:C ratios between species could be thought of as a form of photoadaptation (i.e. resulting from long time scale evolutionary adaptation; Moore et al. (2006)), although as we have noted there are many other ways in which phytoplankton may vary in their ability to harvest light of differing intensities (e.g. cellular size and shape, number of vacuoles; see Bellacicco et al. (2016) and citations therein). The unique response of different phytoplankton species to light is modelled by the photosynthesis-irradiance curve (PI curve), a hyperbolic function describing changes in the photosynthetic rate with increasing light intensity (Figure 1.10). Assuming negligible photoinhibition[6], the shape of the function can be described by just two parameters: the initial slope, α^B, and the asymptote of the curve, P_m^B, where α^B represents the photosynthetic efficiency at light intensities approaching zero, and P_m^B is the photosynthetic rate at light saturation (see Figure 1.10 dashed lines; refer to Bouman et al. (2018) and citations therein for more details). Thus, given the variability of both photoacclimation and photoadaptation in the Southern Ocean, we can expect physiological changes to provide an additional control on phenology on top of those already discussed (Strzepek et al., 2019).

[6]Photoinhibition is a process whereby plants decrease their photosynthetic rate when exposed to high irradiance Han et al. (2000).

1.3.2 Southern Ocean Phytoplankton Phenology

The unique physical characteristics of the Southern Ocean discussed section 1.2 give rise to an equally distinct biogeochemical region. Early expeditions to the Antarctic waters (Gran, 1931; Hart, 1934; Hendey, 1937) revealed what was termed the "Antarctic Paradox", which related to the condition of high annual nutrient concentrations (Nitrate and Phosphate) but low chlorophyll-a (chl-a) concentrations, implying low productivity. More recently, regions which display this characteristic have been called high nutrient, low chlorophyll (HNLC), with the Southern Ocean comprising the largest of such regions globally (Martin et al., 1990b; Boyd, 2002). The central conundrum here is that in most of the global ocean, nutrients are stripped out of the surface by production, resulting in very low annual concentrations, but in the Southern Ocean there exists a vast pool of unused nutrients.

From the start it was suspected that during periods when light was not limiting, micronutrients, particularly iron, may limit growth (Hart, 1934), although other factors such as temperature, ammonium accumulation and silicic acid where also considered (Boyd, 2002). Indeed, near surface concentrations of dissolved iron rarely exceed 1 *nM* away from coastlines in the Southern Ocean (Tagliabue et al., 2014b). While such low concentrations certainly suggest limitation, the role of iron in controlling growth has now been unequivocally shown by many iron enrichment experiments (in both controlled and natural environments of the Southern Ocean, see for example Martin et al. (1990a); Leeuwe et al. (1997); Coale et al. (2004)). Moreover, comparisons of regions with either enhanced or inhibited iron supply further strengthened the relationship (Martin et al., 1990b; Sokolov, 2008; Tagliabue et al., 2014b).

Spatial Variability Such regional comparisons, when conducted over the whole Southern Ocean, reveal a "patchy" distribution of productivity (in so far as chl-a can be used as a proxy for productivity; Figure 1.11), with distinct seasonal cycle regimes (Figure 1.12). Regions of high productivity are mainly found in coastal seas (shelf regions and polynyas), along ACC fronts, within the SSIZ and in some regions where the ACC interacts with shallow bathymetry (Figure 1.11). In such regions the availability of iron has been implicated as a first-order explanation for increased productivity, although other nutrients such as silicic acid may also be implicated (Boyd, 2002; Sokolov, 2008; Ardyna et al., 2017). The availability of light, as mediated by vertical mixing and seasonal variability, is also thought to control overall productivity (i.e. deep mixing year round can limit biomass accumulation, while strong stratification following mixing can enhance productivity; Smith and Nelson (1985); Ardyna et al. (2017)). This can be

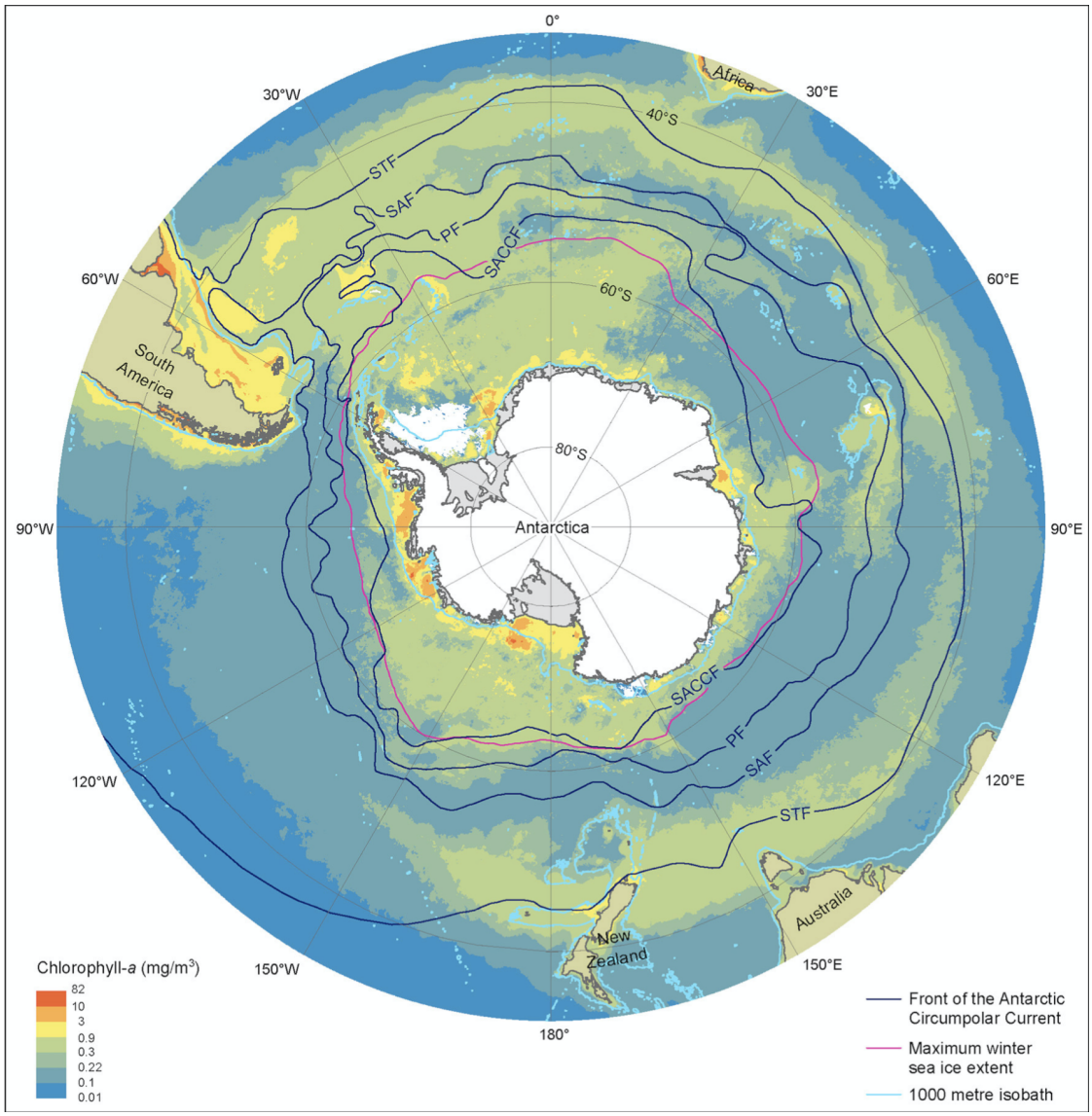

Figure 1.11: Mean surface chl-a concentrations in the Southern Ocean in summer (2002 - 2016) from Deppeler and Davidson (2017). Data are taken from MODIS-Aqua satellite estimates at 9 km resolution. Black lines represent the locations of the major Southern Ocean fronts from Orsi et al. (1995) (see 1.2.1). The red line denotes the approximate location of the winter sea ice edge maximum (averaged over 1978-2008) as estimated from Scanning Multichannel Microwave Radiometer and Special Sensor Microwave/Image satellite data. Light blues lines are the 1000 m isobath computed from General Bathymetric Chart of the Oceans, version 20150318.

seen by comparing figures 1.5A with 1.11 where regions of especially deep mixing (dark red) are correlated with reduced surface chl-a, while regions of higher chl in the open ocean are associated with shallower MLDs in both winter and summer (Figure 1.5B). In line with this, Ardyna et al. (2017) note that a winter MLD of greater than $\sim$150 m can be thought of as threshold where the benefits of increased iron supply are outweighed by decreased light availability, leading to reduced productivity.

Thus, the factors modulating the overall biomass of different bioregions of the Southern Ocean are fairly well constrained. However, the strong spatial variability in phenology evidenced by Figure 1.12a is less well understood, although several promising ideas have been put forward. At the large scale, differences in phenology do appear to follow latitudinal changes in the light regime, with the growing period generally shifting later in the year with increasing latitude (Sallée et al., 2015; Rohr et al., 2017; Uchida et al., 2019). However, at the regional scale simple latitudinal gradients cannot account for the observed distribution of phenology, as seen by the presence of several bioregions in the same latitudinal band in Figure 1.12a (for example, the region around 60°S may be categorized as either bioregion 7,6,5 or 4). Here variability in the seasonal cycle of MLD may again be implicated, with differences in timing of deepening and shoaling affecting light and nutrient availability (Thomalla et al., 2011; Ardyna et al., 2017; Uchida et al., 2019). MLD variability may also affect the timing of decoupling between division and loss rates discussed above in 1.3.1), with consequences for the overall phenology (Rohr et al., 2017; Behrenfeld et al., 2017). Other authors have suggested that the timing of the spring bloom in the open ocean may be related to water mass interactions, whereby such interaction of waters with distinct physical and chemical properties may alter both the light and nutrient regime (Dafner et al., 2003).

Recent work has also suggested that subseasonal variability in mixing, driven for example by synoptic events, may also be an important driver of annual phytoplankton cycles (Swart et al., 2015; Thomalla et al., 2017). This may occur through a variety of mechanisms such as changes in heat fluxes driven by storms (thus affecting vertical mixing; Nicholson et al. (2016)), down front winds (which enhance mixing through cross-frontal Ekman buoyancy flux) and mixed layer eddies (which enhance stratification; du Plessis et al. (2019)). Clearly there are a variety of factors controlling phenology across the Southern Ocean, with different processes dominating in different regions and periods. We now turn our attention to the case of the seasonally ice covered ocean and its unique phenological controls.

Seasonal Ice Zone Phenology The SSIZ comprises a substantial portion of the Southern Ocean, providing a unique habitat for phytoplankton both within and under the ice (see red line in Figure 1.11 for its geographical extent). From a phenological perspective, the bulk of the present literature has focussed on the spring fresh water flux and its role in initiating phytoplankton blooms (Smith and Nelson, 1985; Veth et al., 1992; Sokolov, 2008; Smith and Comiso, 2008; Taylor et al., 2013; Briggs et al., 2017). This stems from early in-situ observations which illustrated how melt waters greatly increased stratification (see 1.2.2), thus allowing phytoplankton to remain close

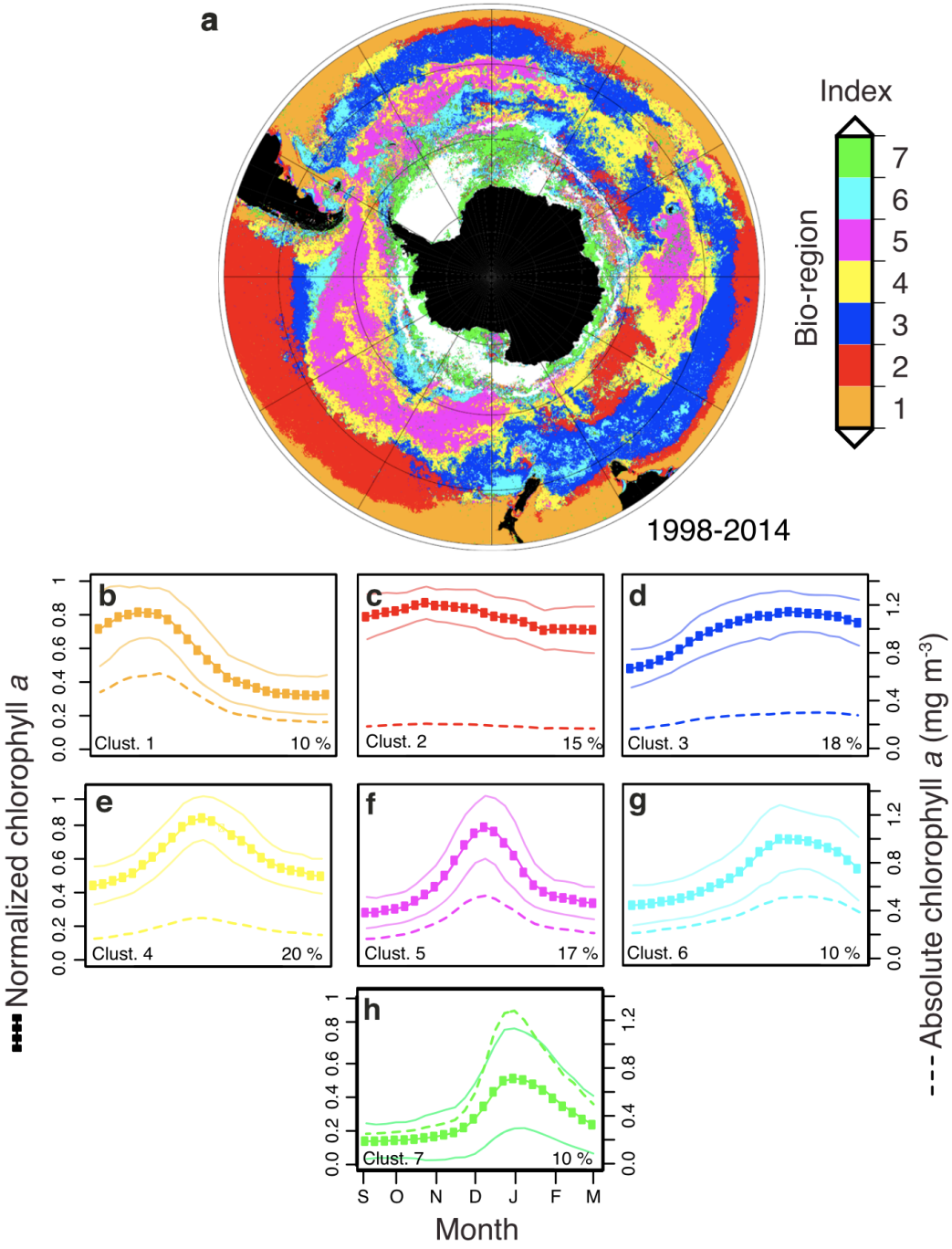

Figure 1.12: Spatial variability of Southern Ocean phenology from Ardyna et al. (2017). Satellite chl-a concentration (GLOBcolour) for years 1998-2014 where clustered into 7 "bioregions" using k-means analysis to give the spatial distribution shown in (a), as well as the time series in b-h. In brief, the technique groups together chl-a time series with similar shapes (and hence similar phenology), from which a representative seasonal cycle can be derived by averaging all time series within a given cluster. Normalized chl-a annual cycles (September - March) and standard deviation are shown in solid lines, dashed lines are the absolute chl-a.

to the surface just when incident light levels where increasing (Smith and Nelson, 1985, 1986; Lancelot et al., 1993). Later satellite-based studies proposed the same mechanism for ice-edge blooms, noting that surface chl-a anomalies tended to occur following the retreating ice edge in spring (Sullivan et al., 1988; Buesseler et al., 2003; Sokolov, 2008; Smith and Comiso, 2008).

In line with this, it was soon hypothesized that sea ice may contain higher concentrations of iron than the underlying ocean, and therefore would relieve both light and iron limitation upon melting. Studies revealed that sea ice did indeed contain iron concentrations 1 or 2 orders of magnitude higher than surrounding sea water, which is thought to arise from a variety of processes including dust interception and accumulation, suspended sediment incorporation (in coastal regions, but then transported into the open ocean by winds and currents - see 1.2.2) and direct entrainment during formation (see Wang et al. (2014); Lannuzel et al. (2016) and citations therein). A further point is that one of the major supply mechanisms for iron away from coasts is deep winter mixing driving entrainment into the ML (Tagliabue et al., 2014b), and so ice formation may be expected to occur during the period of highest dissolved iron concentrations. Finally, some authors suggested that algae residing in the ice itself (sympagic phytoplankton) may ”seed” the spring bloom upon their release (Garrison et al., 1987; Kuosa et al., 1992; Mangoni et al., 2009; Riaux-Gobin et al., 2011), providing a further mechanism explaining the high biomass observed in the wake of the receding ice.

Thus, as with phenology in the broader Southern Ocean, a paradigm emerged which sought to explain the timing of bloom initiation in terms of the release of melt waters. As may be anticipated, this framework leaves out some important considerations, most obviously conditions in autumn and winter. This is perhaps understandable given the logistical constraints of in-situ observations during this period, as well as the distinct lack of satellite data coverage (Cole et al., 2012). Nevertheless, new observational techniques including floats (Uchida et al., 2019), buoys (Hill et al., 2018) and ship-based monitoring (Assmy et al., 2017), as well as advances in modelling of sea ice and sympagic phytoplankton (Tedesco et al., 2019), are beginning to unveil the character of the full annual cycle of phytoplankton in the SSIZ. Some of the major themes which are emerging include the role of light penetration through sea ice (and leads), variability in vertical mixing processes under ice (especially in winter), as well as potential interactions between pelagic and sympagic communities.

Sympagic Phytoplankton Phenology Indeed, sympagic, or ice associated phytoplankton, are an important component of the overall seasonal dynamics of the SSIZ (Van Leeuwe et al., 2018). Much of this phytoplankton community is found in the lower 20 cm of the sea ice, although there other communities found deeper within the ice, as well as near the surface (Arrigo, 2017; Arrigo and Thomas, 2004). However, the relatively higher abundance found in the lower portion is due to the greater availability of nutrients, which often restricts growth in the upper sections of the ice. These nutrients are derived from a tight coupling with the underlying ocean, which, especially during winter in the Southern Ocean, tends to be fairly nutrient replete. Thus, the primary advantage of this unique environment is its ability to suspend phytoplankton close the surface where light is sufficient and nutrients are not limiting. The sea ice may also afford some projection from grazers due the limited space (Arrigo, 2017).

In terms of phenology, the onset, climax and decline of the sympagic community tends to precede that of their pelagic counterparts. In a recent review, Arrigo (2017) found that pan-Antarctic peak ice algal production occurred in November, one month before the water column peak production. However, this average value likely masks significant spatial variability due to differences in ice and snow thickness, nutrient availability and light regime (Meiners et al., 2012; Vancoppenolle et al., 2013). This earlier growth cycle is the result of adaptation to extreme low light environments, allowing sympagic phytoplankton to bloom under very low irradiance (Tedesco et al., 2012; Meiners et al., 2012). The fate of the sympagic community upon melting, as well as its potential role in seeding pelagic phytoplankton blooms, remains unclear (Van Leeuwe et al., 2018). Although some studies have found that sympagic phytoplankton can adapt to ice-free waters (Garrison et al., 1987; Kuosa et al., 1992), others have found that only a few taxa exhibit this trait (Riaux-Gobin et al., 2011). Nevertheless, the sympagic community plays an important role in the phenology of the SSIZ by providing a significant biomass of primary producers whose seasonal dynamics are distinct to that of the pelagic community.

1.3.3 Marine Biogeochemical and Ecosystem Modelling

The discussion up to this point has focussed on the foundational concepts and knowledge needed to understand phytoplankton phenology in the Antarctic SSIZ. However, central to our understanding of these topics is the use of marine biogeochemical models. This involves constructing a set of mathematical equations which attempt to capture the essential functioning of the various components of the ocean ecosystem (phytoplankton, zooplankton and higher tropic levels), as well as the cycling various biochemical

materials (inorganic and detrital matter). All of these processes are influenced to varying degrees by the physical environment (ocean, atmosphere and sea ice), which can either be explicitly modelled or simply provided as input to the biogeochemical model. The use of either biogeochemical or ecosystem model reflects a focus on either biogeochemical cycling (e.g. of nutrients and carbon) or the interactions of organisms (e.g. predation, viral lysis). Despite this delineation, both sets of models require at least some representation of both biogeochemical cycling and ecosystem interactions, since the processes involved are intrinsically linked (Sarmiento and Gruber, 2006; Dutkiewicz, 2020).

In this thesis, Chapters 2, 3 and 4 all include some form of numerical modelling of the Southern Ocean SSIZ. In Chapter 2 we will employ a biogeochemical model to investigate the phenology of under ice phytoplankton. In this case the physical environment will be prescribed as input to the model, while in Chapters 3 and 4 these components are explicitly modelled through their own sets of mathematical equations. In particular, ocean dynamics can be represented mathematically (to a good approximation) by the primitive equations, which describe the temporal evolution of fluid velocity, pressure and density (Gill, 1982; Cushman-Roisin and Beckers, 2007). This allows for a physically meaningful simulation of the three-dimensional ocean circulation, as well as of vertical and horizontal mixing occurring through turbulent processes. Surface boundary interactions can be taken into account either through the coupling of an ocean model to other dynamical models (e.g. atmospheric, sea ice models) or by prescribing a fixed external forcing (e.g. atmospheric winds, temperature, short wave radiation etc.).

Indeed, in Chapter 4 we present a set of experiments conducted with a coupled ocean-ice model. This model, and others like it, simulate much of the ocean-ice processes discussed above in sections 1.2.2 and 1.2.3. This involves representing both the ice thermodynamics (snow/ice growth and decay, vertical heat diffusion, new ice formation in open water, brine drainage and ice ageing) and dynamics (momentum balance, transport and mechanical redistribution through ridging, rafting and divergence) (Vancoppenolle et al., 2009). This allows for a reasonably realistic simulation of the large-scale distribution of ice thickness, concentration and circulation (Rousset et al., 2015; Blockley et al., 2020), making these models invaluable tools for studying ice-ocean dynamics and feedbacks, a central topic of Chapter 4.

For an even more realistic simulation of all aspects of the Earth's climate system, the modelling community has developed Earth System Models (ESMs). These generally include an explicit representation of the atmosphere, oceans, sea ice and land surface, as

well as both terrestrial and oceanic biogeochemical processes (Flato, 2011). Crucially, each component is dynamically coupled to several other components, thus simulating the complex interactions between physical, biological and chemical processes which characterize Earth's climate. In the context of the work presented here, ESMs can simulate the air-ice-ocean dynamics of the Southern Ocean discussed above, as well as the influence this has on phytoplankton phenology (Séférian et al., 2013; Rohr et al., 2017). Accordingly, an analysis of these models and their representation of Southern Ocean SSIZ phenology is presented in Chapter 3.

A final important point relates to how and why models are used in this thesis. One of the primary motivations for using models to study climate is the ability to synthesize knowledge, and therefore perform experiments on the climate system (or some aspect of it) that would otherwise be impossible. Certainly, there are specific processes which are amenable to traditional laboratory experiments. However, the complex interaction of many processes at meaningful spatial and temporal scales ($\sim$10's to 1000's of kilometres, years to decades and even millennia) requires the use of computer simulations (Flato, 2011). In the context of the Southern Ocean SSIZ models are especially useful, since the region is both highly complex and generally poorly understood (Turner et al., 2013; Mahlstein et al., 2013; Purich et al., 2016; Maksym, 2019). The region also suffers from a distinct lack of observations, making models useful tools for enhancing understanding of the region. However, it is important to note that models are only approximations of reality, and contain many sources of uncertainty (e.g. subgrid-scale parametrizations, processes not included or not well resolved). Nevertheless, so long as these limitations are taken into account, one can use models to pose scientific questions simply not possible with other techniques.

One way in which models can be used to investigate processes is by altering features of the model (e.g. changing parameter values, removing or adding processes) and comparing the resulting model output with a reference simulation where no changes are made. For example, Goosse and Fichefet (1999) investigated the role sea ice salt fluxes (i.e. freshening from melting, salinification from formation) play in global ocean circulation by comparing a simulation where ice salt fluxes are removed with a reference run where fluxes are included. This general technique of comparing model runs where changes have been made to particular processes is employed in chapters 2 and 4. More details on the specific models used and the experiments conducted can be found in the respective chapters. In Chapter 3 we take a slightly different approach, comparing the output from 11 ESMs that formed part of CMIP5. While this approach still compares model simulations, the differences between them are less controlled in this case, since they reflect different choices made by the various modelling groups. The aim is then to

identify mechanisms which can account for the differences between models, as well as between models and observations (Sallée et al., 2013a; Bracegirdle et al., 2013; Mongwe et al., 2018).

1.4 Aims and Outline

1.4.1 Research Aims

Now that the importance of the particularities of Antarctic sea ice and its influence on vertical mixing and phenology have been established, the primary aims of the thesis can be outlined. **The overarching objective is to further understanding of the role Antarctic sea ice modulation of surface fluxes (light, heat, momentum, buoyancy etc.) play in controlling phytoplankton phenology.** This high level objective is then parsed into the following research aims:

1 Due a distinct lack of data in the Southern Ocean in general, and especially under sea ice, very little is know about the complete annual cycle of phytoplankton in the region. Therefore, the first aim of the thesis is to characterize phenology in the Antarctic SSIZ using the best available data (floats and satellite data). Once observational estimates of phenology have been conducted, comparisons to fully coupled Earth System Models (ESMs) can be made.

2 With under ice phenology characterized in observations and models, the logical next step is to understand the drivers of under ice phenology. In particular, what are the mechanisms controlling the timing of growth initiation in the SSIZ? For this I intend to use a simplified biogeochemical box model forced by under ice float data.

3 Several shortcomings with regards to Southern Ocean phenology and vertical mixing have been identified in modern ESMs. I aim to diagnose the mechanisms behind these shortcoming with respect to the representation of seasonal sea ice, in particular the winter ice cover.

4 Another symptom of the lack of observations in the Antarctic SSIZ are the poorly constrained air-ice-ocean fluxes, which may contribute to the model bias in vertical mixing mentioned above. The relative abundance of such observations in the Arctic has lead to model implementations which favour that environment (e.g. Vancoppenolle et al. (2009)). As such, I aim to better understand the

role of the more dynamic Antarctic ice cover in modulating surface fluxes such as heat, momentum, freshwater and light, as well as the consequences this has for the surface mixed layer. To address this, an ice-ocean model will be used to run several experiments which test the sensitivity of the under ice mixed layer to imposed changes in heat and momentum fluxes. Furthermore, regional comparisons of the model mixed layer response to the imposed changes can be performed. The aim of studying the mixed layer is in relation to it's control of seasonal light and nutrient availability, which strongly effect phytoplankton phenology.

1.4.2 Thesis Outline

Following the introduction presented above, the remainder of this thesis is organised into three main chapters and one synthesis chapter:

Chapter 2 provides the first ever comprehensive characterization of under ice phenology for the winter and early spring period using Bio-Argo float data. The drivers of phenology in the Antarctic SSIZ are then investigated through several biogeochemical box model experiments. This chapter is published as: Hague, M. & Vichi, M. (2020). Southern Ocean Biogeochemical Argo Detect Under Ice Phytoplankton Growth Before Sea Ice Retreat. *Biogeosciences*, 17, 1–14. https://doi.org/10.5194/bg-17-1-2020

Chapter 3 explores the representation of Southern Ocean phenology in 11 CMIP5 models (Climate Model Intercomparison Project phase 5) and its relation to the seasonal cycle of sea ice and vertical mixing. The output from the models is compared to satellite data, objectively analysed fields (such as World Ocean Atlas) and an assimilative model (Southern Ocean State Estimate). The analysis is focussed on a study region, which corresponds roughly to the multi-model ensemble MIZ between July and September. This chapter is published as: Hague, M., & Vichi, M. (2018). A link between CMIP5 phytoplankton phenology and sea ice in the Atlantic Southern Ocean. *Geophysical Research Letters*, 45. https://doi.org/10.1029/2018GL078061

Chapter 4 investigates the role sea ice plays in modulating atmosphere-ocean heat and momentum fluxes and their impact on vertical mixing. A regional numerical ocean-ice model (NEMO) of the Atlantic sector of the Southern Ocean is described, from which experiments testing the sensitivity of mixed layer to enhanced heat and momentum fluxes are performed. Detailed analysis of two regions of interest is presented, one corresponding to the study region described in Chapter 3, the other being slightly further north and representing the winter MIZ as simulated by the model. This allows for

comparison to the results of Chapter 3, as well as between regions with different degrees of seasonal ice cover (the study region becoming completely covered in winter, while the MIZ has only partial coverage).

Chapter 5 draws together the results of the previous three chapters within the context outlined in Chapter 1. The research objectives presented above in section 1.4.1 are addressed in light of the findings of each of the three main chapters. This is followed by a discussion of some of the limitations which arise from the data sources and methodology used in the thesis. A final section provides recommendations for future research based on the findings and limitations of the thesis.

Chapter 2

Drivers of Under Ice Phytoplankton Phenology

Abstract

The seasonality of sea ice in the Southern Ocean has profound effects on the life cycle (phenology) of phytoplankton residing under the ice. The current literature investigating this relationship is primarily based on remote sensing, which often lacks data for half the year or more. As discussed above in Chapter 1, one prominent hypothesis holds that following ice retreat in spring, buoyant melt waters enhance available irradiance, triggering a bloom which follows the ice edge. However, an analysis of BGC-Argo data sampling under Antarctic sea ice suggests that this is not necessarily the case. Rather than precipitating rapid accumulation, we show that melt waters enhance growth in an already highly active phytoplankton population. Blooms observed in the wake of the receding ice edge can then be understood as the emergence of a growth process that started earlier under sea ice. Indeed, we estimate that growth initiation occurs, on average, 4-5 weeks before ice retreat, typically starting in August and September. Novel techniques using on-board data to detect the timing of ice melt were used. Furthermore, such growth is shown to occur under conditions of substantial ice cover ($>$90% satellite ice concentration) and deep mixed layers ($>$100 m), conditions previously thought to be inimical to growth. This led to the development of several 0D model experiments in which we sought to investigate the mechanisms responsible for such early growth. The results of theses experiments suggest that a combination of higher light transfer (penetration) through sea ice cover and extreme low light adaptation by phytoplankton can account for the observed phenology.

2.1 Introduction

The annual advance and retreat of Antarctic sea ice is the largest seasonal event on Earth, covering some 15 million km^2 (Massom and Stammerjohn, 2010). Such considerable seasonal changes have profound effects on the phenology of phytoplankton residing under the ice. However, the exact character of such effects is currently unknown, primarily because studies investigating phenology in these regions have relied on satellite data, which are unable to retrieve information for half the year or more. In particular, the winter and early spring periods at the higher latitudes are not taken into account, despite the important role they play in both the overall phenology and subsequent summer production.

This chapter presents the first ever comprehensive characterization of under ice phenology for this period. This is achieved by leveraging under ice data collected by ARGO profiling floats equipped with a suite of biogeochemical sensors, deployed as part of the The Southern Ocean Carbon and Climate Observations and Modeling (SOCCOM) project (https://soccom.princeton.edu/). Of primary interest to us here are the mechanisms controlling the timing of phytoplankton growth initiation in the unique environment of the Seasonal Sea Ice Zone (SSIZ), introduced in Chapter 1. A dominant idea in the literature with regards to such mechanisms holds that following ice retreat in spring, buoyant melt waters tend to enhance average light availability by rapidly shoaling the mixed layer. This alleviation of light limitation (coupled perhaps with iron input from melting ice) is then used to explain why blooms are often observed in the wake of the receding ice edge (Smith and Nelson, 1985; Smith and Comiso, 2008; Briggs et al., 2017; Sokolov, 2008). The implication here is then that, prior to the release of melt waters, growth rates remain low, only increasing substantially in response to melting. Hence, a prediction of the hypothesis (which we may term the ”melt water hypothesis”) is that the timing of melting should precede the timing of rapid growth. This is a somewhat subtle point, since the relevance of melt waters is usually brought up to explain the presence of blooms, and so is often not explicitly linked to phenology (e.g. Taylor et al. (2013); Uchida et al. (2019)). Nevertheless, the hypothesis implicitly assumes that phenology is strongly affected by the release of melt water.

However, there is increasing evidence that this is not necessarily the case. In an early study, Smetacek et al. (1992) documented an intense bloom under pack ice conditions in early spring (before melting) in the Weddell Sea ice shelf region. More recently in the Arctic (Barents Sea) a similarly intense phytoplankton bloom was observed in the Chukchi Sea under complete ice cover (ponded) ranging from 0.8 to 1.3m thick (Arrigo et al., 2012). Although this bloom was observed in summer, Assmy et al.

(2017) have recently shown that under ice blooms may develop even earlier in the Arctic due to the presence of leads in spring. Notably, the composition of the phytoplankton population was distinct in these two blooms, with diatoms dominating in the Chukchi Sea and Phaeocistys in the Barents Sea (Arrigo et al., 2012; Assmy et al., 2017). In the Southern Ocean, evidence is emerging of earlier than expected growth in deep mixed layers within the SSIZ (based on under ice fluorescence and backscatter from profiling floats; Uchida et al. (2019); Prend et al. (2019)). The important feature of these studies for the present discussion is that high growth rates have been observed prior to melting and under complete (or near-complete) ice cover. However, the present literature has left several issues related to under ice phenology unresolved.

Firstly, studies focus almost exclusively on spring and summer and hence miss any potential growth occurring in winter. Indeed, it is assumed that such growth is negligible even though this has not been explicitly shown. Second, much attention is paid to regions of high biomass (i.e blooms as inferred either by high average satellite chl-a or through in-situ observations; refer to Figure 1.11 and in text discussion) and their associated environmental conditions. Although these regions are no doubt of great interest (perhaps particularly for carbon export, e.g. Buesseler et al. (2003)), their study does not necessarily contribute to an understanding of the mechanisms controlling phenology in general. This is especially true in the Southern Ocean where large spatial variability is common (Thomalla et al., 2011). Third, the bulk of present literature is based on studies of Arctic under ice phenology. Antarctic sea ice is distinct in being generally thinner and more dynamic (see section 1.2.2), as well as having much more snow year round that does not form melt ponds (Vancoppenolle et al., 2013). This means that seasonal variations of light and nutrients are likely very different, motivating special attention to this unique environment.

2.1.1 Aims and Questions

This chapter will first characterize under ice phenology using the unique Bio-ARGO dataset discussed above, with the aim of address research objective 1 outlined in section 1.4.1. Particular attention is paid to the early period of growth and its relation to the timing of the seasonal melting of ice. Following this, the mechanisms controlling under ice phenology will be investigated using simple biogeochemical box-model experiments forced by the float data (research objective 2). Thus, the chapter seeks to address the following fundamental questions:

1. Can the proposed melt water hypothesis explain under ice phenology derived from in-situ Bio-ARGO data?

2. What are the physical and biological drivers of under ice phenology?

2.2 Methods

The work presented here employs several novel techniques to detect the timing of phenological events in the seasonally ice covered Southern Ocean. This, coupled with a suite of simple model experiments, affords a unique perspective on the phenology of the region. As is discussed above, our primary concern is the winter and early spring period when traditional data sources provide little or no information.

In particular, the use of profiling float data to detect both the timing of melt and growth initiation avoids several of the shortcomings inherent to satellite and ship-based studies which characterize the present literature on under ice phenology. First, if in-situ data are used, they are limited in space and time and are usually compared to satellite products as a consequence. However, direct comparisons of this kind are often associated with large uncertainties stemming from the coarse spatial resolution of satellite products, as well as differences in the measurement technique used to produce in-situ and satellite data. By using a consistent observing platform we largely overcome these issues, while still achieving good spatial and temporal coverage at seasonal time scales (see Section 2.3.1). Another clear advantage of the SOCCOM dataset is the availability of depth information (profiles), allowing us to simultaneously compare the seasonal evolution of temperature, salinity, stratification and mixed layer chlorophyll-a. We now move on to a more detailed discussion of the methodology used to detect melt water release and growth initiation. Following this we will describe the biogeochemical model experiments used to investigate the drivers of under ice growth.

2.2.1 Detection of Phenological Events

Under Ice Detection

The first step in our investigation of under ice phenology was to determine which profiles could be classified as sampling under ice. Since many of floats deployed in the SOCCOM project are intended to sample under ice, an ice avoidance algorithm is utilized onboard. The ice-sensing algorithm simply compares the median temperature

between ∼50 m and 20 m during ascent to a threshold temperature of -1.78°C. If the observed value is lower than the threshold, it is assumed that sea ice is present overhead. The float then terminates its ascent, stores the profile data and returns to its parking depth (Riser et al., 2018).

Since the freezing point of sea water depends both on temperature and salinity, we chose to include near-surface salinity measurements in our revised under ice detection algorithm. That is, for each profile the freezing temperature, based on the salinity closest to the surface, is computed and compared to the temperature measured at the same depth. It is important to note that the depth of these near-surface measurements will vary from ∼20 - 25 m in winter, to ∼0 - 5 m in summer. This is because of the on-board ice avoidance algorithm described above: in winter the temperature threshold is generally exceeded, and so sampling ceases ∼20 m from the surface, while in other months this condition is generally not met and so floats are able to sample much closer to the surface. Therefore, since the on-board ice avoidance algorithm is intentionally conservative, it may assume there is ice present when in fact melting has already occurred.

While the fact that winter profiles generally only sample up to 20 m may seem unimportant, it actually has significant bearing on the under ice detection algorithm used in this study. This is because at 20 m in winter, water is generally above its freezing point (if salinity is taken into account). Therefore, in order to delineate under ice from open ocean profiles, one has to assume some degree of cooling from the last measurement in the profile to the surface. Since the degree of cooling over this winter surface layer cannot be observationally constrained, we tested several values and the corresponding effect they had on the main result is shown in Figure 2.6. The orange and green curves in this Figure depict the change in the probability density function when increasing and decreasing the amount of cooling by 20%, respectively. The blue curve and associated histogram depicts the chosen value of 0.1°C used in this study (i.e. we assume a decrease of 0.1°C from ∼20 m to the surface). We would note that the essential features of the distribution remain unchanged in this sensitivity test.

In addition to the above testing, two further checks were performed to assess the validity of using an assumed rate of cooling to detect under ice profiles. The first approach is shown in figure 2.1, which plots the distribution of distances of under ice profiles to the satellite ice edge. Here the ice edge is defined by the 15% sea ice concentration contour, following previous satellite-based studies (e.g. Stroeve et al. (2016)) We found that the vast majority of profiles where located 100 km or more south of the ice edge, with 13.6% being north of the edge. It is important to point out here that while sampling under ice, floats do not communicate their location, since they are prevented from surfacing.

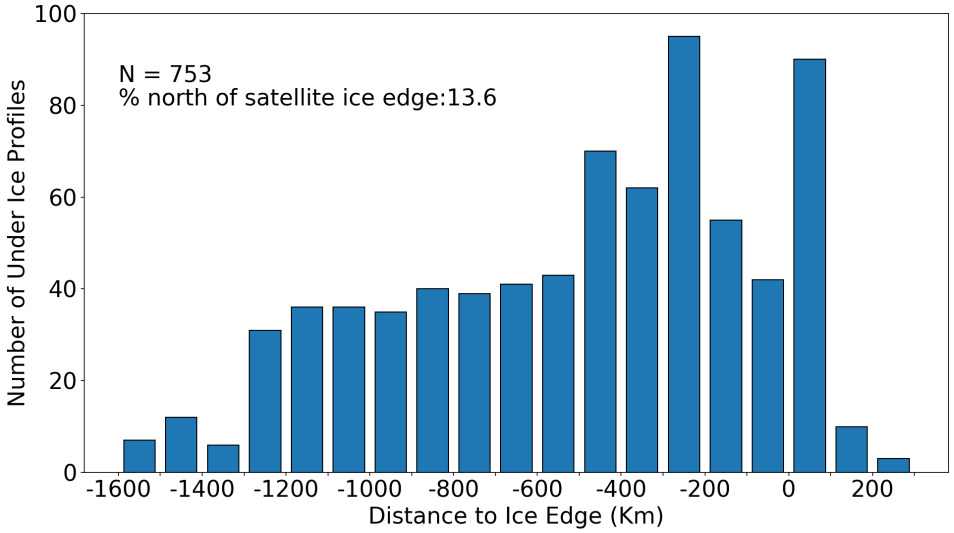

Figure 2.1: Distribution of great-circle distances of under ice profiles to the estimated satellite sea ice edge (latitude of 15% sea ice concentration contour). Negative values indicate that the profile is poleward of the ice edge. Great-circle distances refer to the shortest distance between 2 points on the Earth's surface (measured along the spherical surface), assuming a perfect sphere. Here the Haversine Formula is used, see **?**.

A simple linear interpolation is used to estimate the location of the under ice profiles (based on the relative time stamp difference), with an approximate maximum error of 100 km as reported by Riser et al. (2018). It is precisely because of this uncertainty that we chose to use on-board data, as opposed to satellite, to detect under ice profiles (as well as to detect melting). The distribution shown in Figure 2.1 is included to illustrate that there is broad agreement between the two methods.

The second approach used to assess the under ice detection method involved visual inspection of time series of temperature and salinity like those shown in Figure 2.2A. This consisted of comparing the timing of the transition from under ice to open ocean (depicted by the black vertical line in Figure 2.2A), with the associated changes in temperature and salinity. By inspecting a subset of floats sampling under ice, we found good agreement between the timing of the transition and the corresponding warming and freshening of the surface ocean. The best agreement is achieved by assuming a relative temperature difference (between the last winter measurement and the surface) 0.1°C as described above, which is why this value was chosen over other candidates. A sample of time series for floats other than that shown in Figure 2.2A is provided in additional Figures 2.12 and 2.13.

Ice Decay Onset Detection

Once a transition from ice cover to open ocean has been established, our algorithm then verifies that these changes are associated with melting. This is done by computing time derivatives of surface temperature and salinity at the time of transition (data are taken from measurements closest to the surface). In order to be classified as an ice decay onset, the temperature derivative must be positive (i.e increasing temperature) with a negative salinity derivative that is persistent for 1 month following transition. More formally, ice decay onset is detected at time t if:

1. $\left.\frac{dS}{dt}\right|_{t,t+1,t+2} < 0$
2. $\left.\frac{dT}{dt}\right|_{t} > 0$
3. $T\Big|_{t+1} > T_f\Big|_{t+1}$

Where S and T are near surface salinity and temperature time series, respectively, and T_f is the freezing temperature. An example of such a ice decay event is shown in Figure 2.2A (black vertical line), where salinity (blue lines) decreases gradually for $\sim$1 month prior to transition, while temperature (red lines) begins to steadily increase after remaining consistently below freezing. At least three consecutive under ice profiles (equivalent to $\sim$1 month since profiles are at 10-day frequency) are needed to detect a melt event. In cases where multiple transitions occur in one season, the transition with the strongest signal (i.e steepest time derivative) of warming and freshening is chosen. This enables us to filter out transitions which occur as a result of local advection or high frequency warming associated with synoptic variability. This also highlights the important point that we are detecting the most prominent melting signal associated with a substantial reduction of the ice cover and shoaling of the mixed layer (as well as warming of the surface ocean - Ohshima and Nihashi (2005)). We recognize that there may be low levels of melting prior to the detected ice decay onset date, which are probably due to bottom melting arising from the entrainment of warm deep waters into the mixed layer. However, as is shown in Figure 2.11A, such melting does not significantly lower the near surface salinity compared to the more significant melting seen after the detected ice decay onset (in the majority of cases).

Apart from the three criteria discussed above (transition from under ice to open ocean, positive temperature derivative, negative salinity derivative), additional inspection of time series of stratification depth (ND introduced above in section 1.2.3) was performed on a subset of the dataset. As is discussed in Section 1.2.3, the release of melt waters

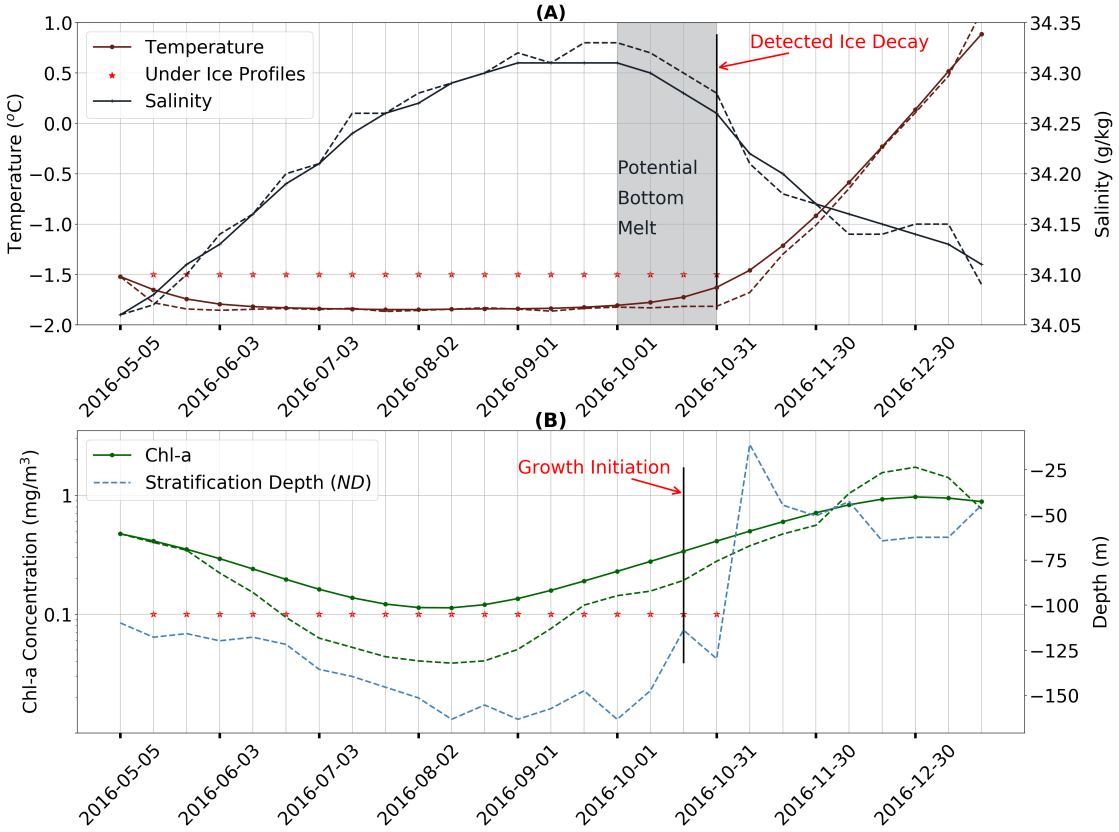

Figure 2.2: Time series of key properties illustrating the methodology used for melt and growth detection. **(A)**: Mean near surface temperature (dark red) and salinity (dark grey/black) from May to December 2016 in the Ross Sea sector (∼65°S - Float 5904768, see first entry in table 2.3). Red stars indicate profiles flagged as under ice (near surface temperature is within 0.1 °C of the freezing point - see 2.2.1, "Under Ice Detection"). Solid lines with markers are filtered time series (higher frequencies have been removed), dashed are raw data. The black vertical line indicates the estimated timing of ice decay onset. The grey shaded region denotes the period of weak freshening which may be the result of bottom melting as discussed in section 2.2.1 - "Ice Decay Onset Detection." **(B)**: Mean mixed layer chlorophyll-a (dark green) and mixed layer depth plotted for the same period as in (A). The black vertical line indicates the timing of growth initiation (GI). Note that the timing of GI always occurs between the local minimum and maximum values of the filtered time series (solid green curve), while the actual location of GI is determined by the raw signal (dashed green curve). For more information refer to 2.2.1.

tends to stratify the surface ocean, and so ND should rapidly decrease following the detected melt event. In Figure 2.2B we show an example of such a time series of ND (in blue), with profiles flagged as under ice shown with red stars. One can clearly see that ND shoals rapidly at the point of transition from under ice to open ocean, providing further confidence in the melt detection algorithm. Additional figures which were used to verify the algorithm are provided in Figures 2.12 and 2.13, which show similar results. Indeed, in Figure 2.11B, we show that ND is generally much shallower immediately after the detected melt than before, indicating that the algorithm positions the ice decay onset at the time of rapid shoaling of the mixed layer (in the majority of cases).

Phytoplankton Growth Initiation (GI)

Our main metric for assessing the relationship between melting and phenology is termed growth initiation (GI). It is defined here as the point at which the time derivative of mean mixed layer chl-a exceeds the median time derivative computed for the growth period in question. These time derivatives, here taken as a proxy for growth rates, are only computed over the period of positive growth. This period is determined from a filtered time series of mean mixed layer chlorophyll-a used to remove variability at the 10-day sampling frequency (the actual value of the median is computed from the raw signal). A first-order, low-pass Butterworth digital filter is employed with a cut-off frequency of 0.1 Hz. An example of the resulting filtered time series is shown in Figure 2.2B (solid green curve) and compared to the original raw signal (dashed green curve). Also shown in the figure by the black vertical line is the timing of GI for this particular season. The distance between the 2 black vertical lines in panels A and B in Figure 2.2 then denotes the timing difference between melting and GI as shown in Figure 2.6 for all float data. In summary, the growth period is determined by the filtered time series of mean mixed layer chl-a, while the exact timing of GI within this period is based on the raw, unfiltered time series.

Initially our choice of metric may seem unjustified, considering the metrics commonly used in the literature. Following Racault et al. (2012), early stages of growth are usually quantified using a metric termed bloom initiation, which is defined as the time at which chlorophyll-a concentration first exceeds the long term median plus 5%. However, this method is unsuitable in this study for several reasons. First, our time series are, at most, 4 years long, and on average only 2 years long, precluding an estimation of any long term threshold value. Second, our focus is on the conditions which trigger *growth*, not necessarily a *bloom*, which again implies that a comparison to some longer term value must be made. Finally, we believe a metric based on growth rates (as opposed to an

absolute threshold value) to be more appropriate, since it avoids any biases in the median which may be created by long periods of close to zero chlorophyll-a concentration under ice (followed by a rapid increase). Similar metrics (using a relative quantities rather than absolute) developed for high latitude phenology are discussed in Tedesco and Vichi (2014), where anomalies (chl-a concentration minus its standard deviation) are used to compute various phenological indices for ice algae.

Furthermore, using growth rates allows us to say something about the stock of the phytoplankton community under ice, without being anchored to a particular concentration value. That is, we can determine at what time growth becomes *stronger* than average, which can then be compared to the associated environmental conditions. We now move on to a brief description of the biogeochemical model used in this study, as well as the model experiments conducted.

2.2.2 Model Experiments

A biogeochemical box model is employed in this study to investigate the drivers of under ice growth. The model is based on the Biogeochemical Flux Model (BFM) framework, for which documentation can be found in Vichi et al. (2015). Our particular configuration is a ”0.5D” box model where all the major components of the marine biogeochemical system are simulated, namely, phytoplankton, zooplankton, organic and inorganic matter, nutrients and bacterioplankton. The model is termed ”0.5D” due to the fact that light transmission into the water column is taken into account. The depth of the box is able to vary to simulate the effect of vertical mixing, which decreases light exposure with increasing mixed layer depth.

A schematic of the various interactions of the marine biogeochemical system ,as simulated by the BFM, is shown in Figure 2.3. The components of the model are defined by functional groups, which together seek to represent the major processes governing marine biogeochemical cycling. Within BFM these are the Chemical Functional Families (CFF) and Living Functional Groups (LFG) (Vichi et al., 2015). In terms of the LFGs, three major groups are defined: producers (phytoplankton - light green box Figure 2.3), consumers (zooplankton - dark purple box Figure 2.3) and decomposers (bacteria - olive green box Figure 2.3). These groups then interact both between each other and with the CFFs (inorganic and non-living components) through the various processes shown in Figure 2.3 (photosynthesis, grazing, remineralization etc.).

In this study, the major process of interest is photosynthesis by phytoplankton, the energy source for which is the downwelling incident radiation at the ocean surface. Only

a portion of this incident radiation is utilized for growth, the Photosynthetically Active Radiation (PAR), which we denote here as E_{PAR}. In the model, irradiance is integrated over the depth of the box (Δz, given by the float derived mixed layer depth), and is given by:

$$E_{PAR} = \frac{E_{PAR}}{\lambda \Delta z}(1 - exp(-\lambda \Delta z))$$

, where λ is the total light extinction coefficient, taking into account both extinction by suspended particles and the background value of water (Vichi et al., 2015).

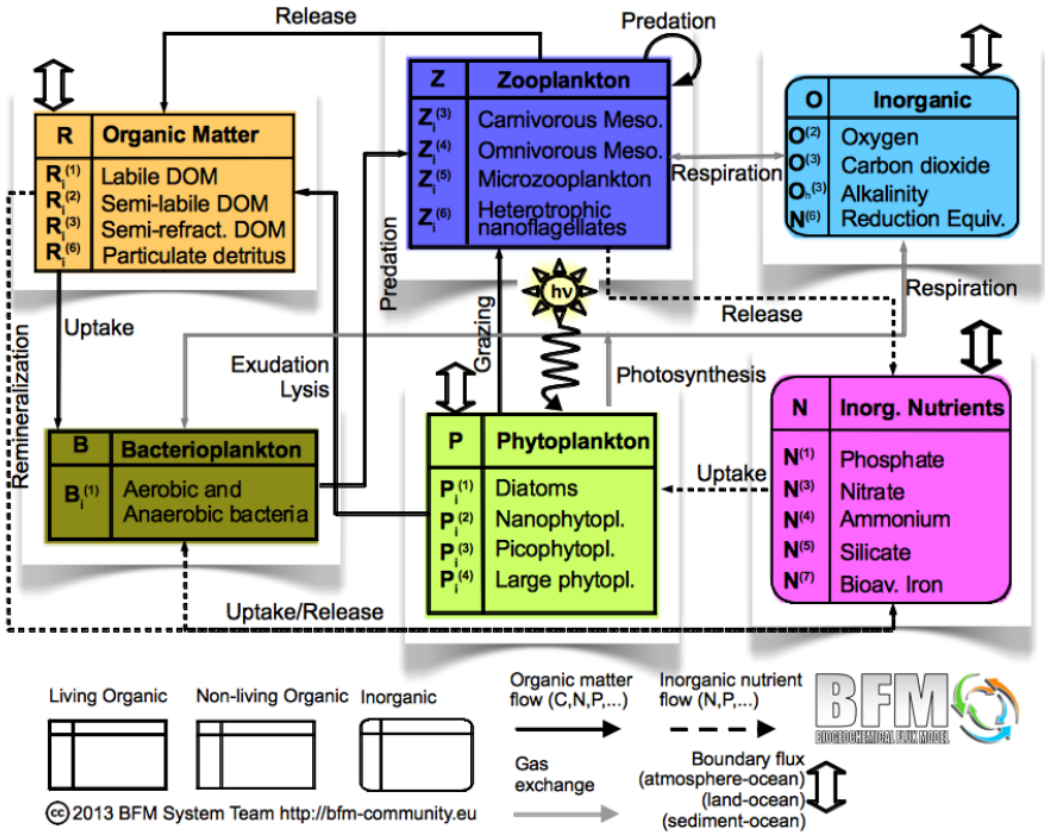

Figure 2.3: Schematic of the state variables of the BFM model, as well as pelagic interactions between the various components of the system. Living components are shown in square boxes (purple, light green and dark green), while inorganic components are shown in rounded boxes (light blue and pink). Non-living components are shown by the orange box.

Since our study is process-oriented, focussing on photosynthesis in the under ice environment, we chose to simulate only 1 phytoplankton (Diatoms) and 2 zooplankton groups (Omnivorous Mesozooplankton and Heterotrophic Nanoflagellates). In terms of nutrients, all those standard in biogeochemical models are included, as well as silicate and iron. Initial nutrient conditions where chosen to be representative of the Southern Ocean south of $\sim$60°S, with non-limiting concentrations of Nitrate (31.8

$mmol/m^3$), Phosphate (2 $mmol/m^3$) and Silicate (40 $mmol/m^3$). An initial dissolved iron concentration of 0.3 $\mu mol/m^3$ is applied to all experiments, which gave the most realistic magnitude of summer growth when compared to float data. This compares well with data published in Tagliabue et al. (2014a) for the Southern Ocean south of ~60°S, where values range between 0.1 and 0.5 $\mu mol/m^3$ in the top ~100 m of the water column (their Figure 8).

The model is forced daily with solar radiation, satellite sea ice concentration, float temperature and salinity, as well as mixed layer depth derived (estimated by ND) from float data (refer to Section 2.2.3 for data sources). Light available at the surface is scaled by the sea ice concentration by simply multiplying the incident radiation by the percentage of open ocean. Following this scaling, downwelling irradiance is prescribed as per the above description.

Experiment Design

Three core experiments were conducted in 4 study regions, with each run having a spin-up time of 10 years to allow for adjustment to a repeating annual cycle (although in most cases adjustment took only a few years). In Table 2.1 we provide an overview of the available float data in each study region. For every complete time series of float observations we performed the set of three core experiments. First, 2 sets of experiments were run to test the effect of sea ice cover on phytoplankton phenology: a run with no ice (OPEN) and a run with imposed satellite sea ice concentration (ICE). A third experiment sought to test the combined effect sea ice cover and increased low light adaptation by phytoplankton had on phenology (LLA). This was achieved by increasing the initial slope of the Photosynthesis-irradiance curve by a factor of 10, thus enhancing photosynthetic efficiency at light levels close to zero (generally > 1 $\mu Em^{-2}s^{-1}$). This value is equivalent to what is commonly used for sea ice algae (Tedesco et al., 2010).

2.2.3 Data Sources

Float data used in this study is made available by the SOCCOM project, and can be downloaded at https://soccompu.princeton.edu/www/index.html. Analysis was done on all available floats, which, at time of writing, spanned from 2014 to 2019. All profiling BGC-Argo floats used in this study are capable of measuring temperature, salinity, pressure, chlorophyll fluorescence, optical backscatter and nitrate, using CTD and various bio-optical sensors. In addition, pH and O_2 sensors are also included in all floats, although this information is only used in the appendix of this chapter.

Table 2.1: Number of floats sampling in each year for the 4 study regions. This number then corresponds to the number of model runs done in each region for each of the three core experiments discussed in the text. W60 = Weddell Sea region at ∼60°S; W65 = Weddell Sea ∼65°S; B70 = Bellingshausen/Amundsen Sea ∼70°S; R75 = Ross Sea south of 75°S.

	2015	**2016**	**2017**	**2018**	Float ID
W60	1	1	1	1	5904397
W65	2	2	2	2	5904468; 5904471
B70	0	0	2	2	5904859; 5905075; 5905080
R75	0	0	3	2	5904858; 5904857; 5904860

Only quality controlled data flagged as good are used here (quality control flag 0 for SOCCOM float data). In general, performance of the biogeochemical sensors has been found to be satisfactory for the majority of floats, although detailed discussion of this topic is presented in Johnson et al. (2017).

Satellite sea ice concentration for the period January 2015 to April 2019 is taken from the NOAA/NSIDC Climate Data Record (version 3), which makes use of 2 passive microwave radiometers: the Special Sensor Microwave Imager (SSM/I) and the Special Sensor Microwave Imager/Sounder (SSMIS). The data are downloaded at daily resolution on the NSIDC polar stereographic grid with 25 x 25 km grid cells. Finally, incident solar radiation at sea level used to force the model simulations is taken from European Centre for Medium-Range Weather Forecasts (ECMWF) ERA-Interim reanalysis dataset. The data resolution is daily on a 0.75^o x 0.75^o regular grid.

2.3 Results

The results presented here fall under two general categories. In the first section we will characterize Southern Ocean under ice phenology in relation to spring melting through an analysis of BGC-ARGO float data. Here the main focus is on testing the melt water hypothesis outlined in Section 2.1, by comparing the timing of growth initiation (GI) with that of sea ice retreat. Following this we will present results from a set of simple model experiments in an attempt to account for the observed phenology. In these experiments we investigate the role sea ice cover and low light adaptation (by phytoplankton) play in controlling winter/spring growth. By placing the experiments in

4 distinct study regions we also utilize the spatial and temporal variability available in the float dataset to force our simulations, thereby increasing the robustness of the results.

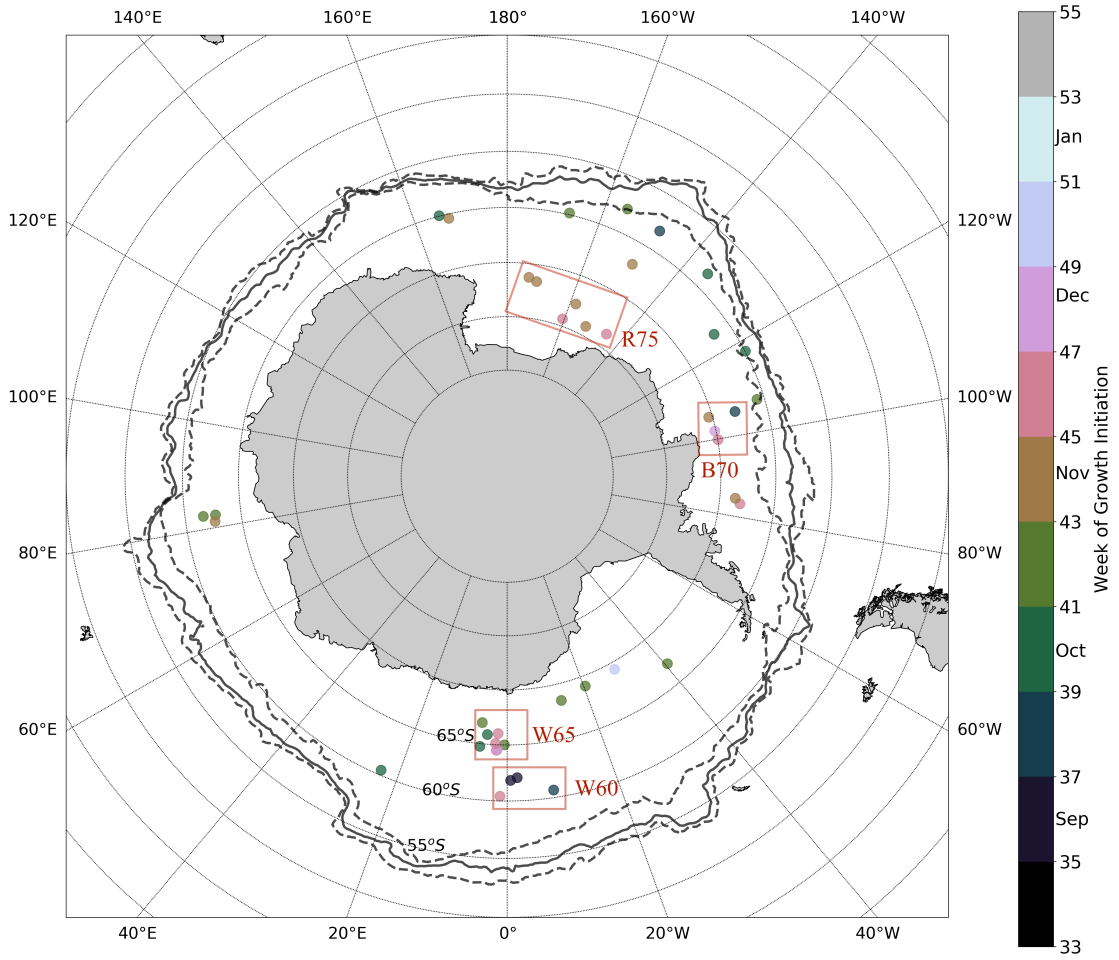

Figure 2.4: Approximate locations of melt events identified in the under ice Bio-Argo dataset. The solid black line represents the mean maximum extent of the 15% sea ice concentration contour for the period 2015 - 2018, while dashed lines represent the interannual variability. The colour of each point represents the timing of growth initiation (GI) in weeks of the year. Red boxes refer to study regions discussed in the text.

2.3.1 Observed Under Ice Growth

The results discussed in this section are summarized in Figure 2.4, which plots the approximate mean location of the 42 melt events captured in the Bio-Argo dataset. From this map it is clear that a fairly broad spatial distribution is achieved, with all the major ocean basins sampled. However, the Atlantic and Pacific oceans are better represented, with the Weddell, Bellinghausen and Ross Seas having the highest concentration of sampling. Meridionally, floats sample between approximately 60 and 70°S, and cover

Table 2.2: Summary of properties of under ice Bio-Argo dataset. GI = Growth Initiation.

Total Floats	99
N Floats Under Ice	20
N Profiles Under Ice	753
N Melt events	42
Mean Time series length	27 months
Mean timing of GI	Week 42 (Mid-October)
Mean timing of melt	Week 49 (Early December)
Mean mixed layer Chl-a at GI	0.13 $mg.m^3$
Mean peak mixed layer Chl-a	2.31 $mg.m^3$

the period 2015 to 2018. Based on this spatial and temporal distribution, we can expect a large variability in oceanographic conditions. This in turn leads to the large spread observed in the timing of GI (from September to January), represented by the colours of the points in Figure 2.4. While there is some indication of the expected progression towards later GI as one moves south (lighter colours), large interannual variability is observed where points are clustered together in space but still have very different GI values.

In Figure 2.5A we show more explicitly the relationship between growth initiation timing and latitude. Here we find a statistically significant correlation (p = 0.001) of -0.47, implying that $\sim$22% of the variance in GI may be explained by variability in latitude alone. Conversely, the relationship between GI and the timing of melt water release is insignificant at the 5% level (p = 0.07) with a lower correlation of 0.27 (Figure 2.5B).

In Figure 2.6, we plot the distribution of the difference in timing between GI and melting. For the majority of the observed events, GI occurs well before the release of melt waters (the mean timing difference is 4.5 weeks before ice decay onset). The mean growth rate (as estimated by the time derivative of mean mixed layer chl-a) over the period from GI to ice decay onset is 0.09 $chl-a/10days$ (this is only for cases where GI occurs before ice decay onset). This growth rate is generally supported by changes

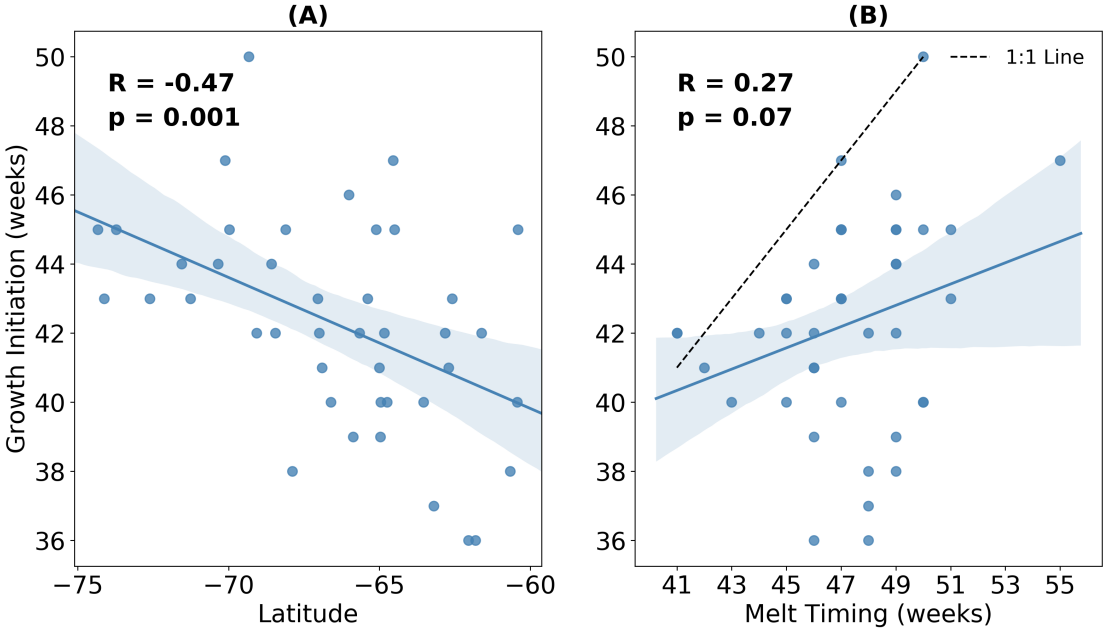

Figure 2.5: Timing of growth initiation (GI) plotted against **(A)**: timing of sea ice melt and **(B)** : average latitude for each of the 42 melt events shown in Figure 2.4. Overlain in blue is the linear regression with the 95% confidence intervals for 1000 bootstrapped resamples shaded in light blue.

seen in nitrate, dissolved oxygen and DIC (computed over a 30-day period from 10 days before GI to 10 days after), shown in Figure 2.15. That is, in 55% of cases dissolved oxygen is increasing at GI, with nitrate and DIC drawdown occurring in 60.5% and 65% of cases, respectively.

We would note that our definition of GI is likely to be more conservative than methods employing a threshold value (i.e likely to delay growth initiation). The timing differences shown here should be interpreted with this in mind. Refer to Section 2.2.1 for a description of how this timing difference is determined. The significance of GI preceding melting is discussed below in Section 2.4.

In terms of vertical mixing, average stratification depth (ND) at GI is $\sim$128 m, with a standard deviation of 51 m. In Figure 2.16 we show the value of ND at GI for all 44 events, as well as the relationship between ND and GI. We found that ND generally ranged between $\sim$75 and $\sim$160 m at the timing of growth initiation, with no correlation between ND and GI. Furthermore, this measure of the depth of the mixed layer has been shown to be more ecologically relevant in the Southern Ocean than other more traditional methods involving density/temperature thresholds (Carvalho et al. (2017); see also section 1.2.3).

In summary, we have shown that prolonged under ice phytoplankton growth prior to

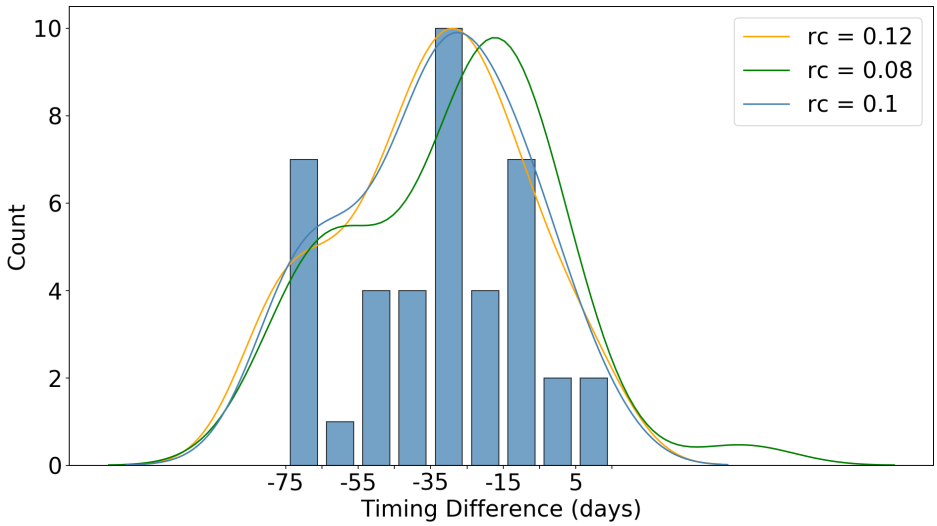

Figure 2.6: Distribution of the difference in timing between GI and melting (for all floats sampling under ice). Curved lines represent the fitted probability density functions for several values of the assumed rate of cooling (rc) in the upper ∼20 m of the water column. Refer to Section 2.2.1 for a discussion of the methodology used to produce the Figure.

retreat is typical of the Southern Ocean SSIZ. While the results discussed up to this point incorporate data from all available under ice floats, in Figure 2.7 we focus on 3 select floats which sampled in close proximity to each other in the Ross Sea. This allows for a clear comparison of the seasonality of chlorophyll-a and sea ice, serving as a good example of how phytoplankton are able to sustain growth under near complete ice cover. Indeed, in this particular case average satellite sea ice concentrations were consistently above 90% until late November, by which point chlorophyll-a has already been steadily increasing for 2-3 months. Examples of other regions can be found in Figure 2.14.

2.3.2 Regional Modelling of Under Ice Growth

In order to further investigate the findings detailed above, we conducted several simplified model experiments in 4 study regions (refer to Figure 2.4 for the locations of each region and section 2.2.2 for more details on the model setup and forcing). These areas where chosen because they represented a good spread in space and time (from 60 to 74°S, 2015 to 2018), allowing us to run each experiment under a variety of forcing conditions. Three core experiments were run for each region, with separate runs for each year available in the float data. The results of all experiments are shown in Figure 2.8 and compared to the phenology obtained from float data. The objective here is to determine which experiments most closely resemble the observed seasonality of mixed

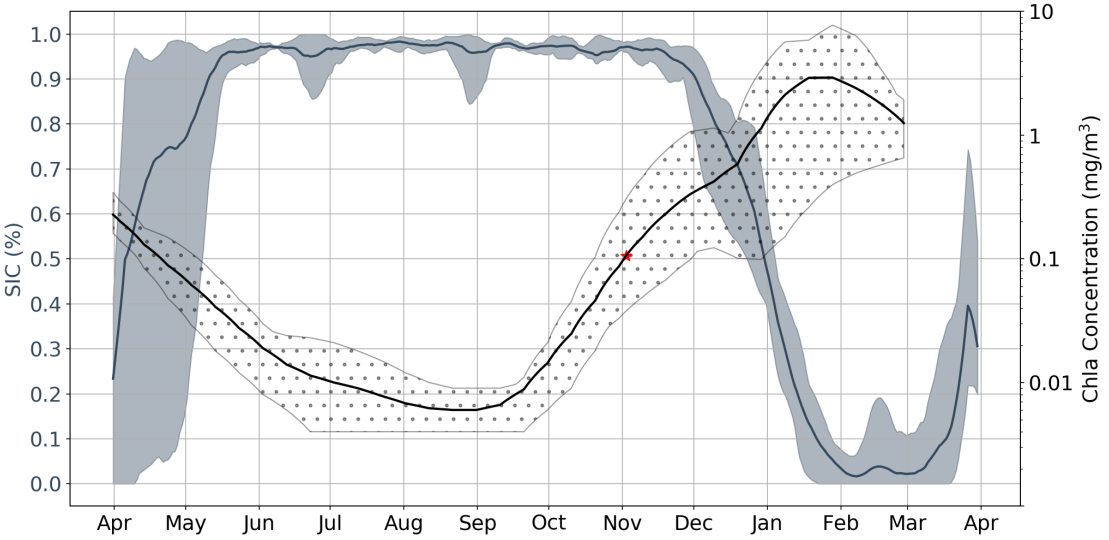

Figure 2.7: Satellite sea ice concentration versus chlorophyll-a for the region R75 (float derived). Shaded regions around each line represent both the spatial and temporal variability present in each dataset. That is, each bold line plots the mean value of 5 time series which are associated with a specific melt event. Events are separated in space and time; in this particular case 2017 and 2018 were sampled by 3 floats, which resulted in 5 time series (2 each, with one of the floats only sampling in 2017). The red star represents the mean value of GI.

layer chlorophyll-a, thereby inferring which factors may be important in promoting under ice growth.

The results indicate that winter and spring phenology is most closely captured by LLA experiments in the Ross and Bellinghausen/Amundsen seas (regions R75 and B70), while in the Weddell Sea (regions W65 and W60) a combination of OPEN and LLA experiments can account for the phenology of this period. That is, in the Weddell Sea the timing of the transition from negative to positive derivative in chl-a is better represented by OPEN experiments, while the subsequent rate of growth in spring is more closely simulated by LLA experiments. In almost all cases, the ICE experiments overly dampened growth in winter and spring, with the switch from negative to positive mixed layer chl-a derivative occurring significantly later than observations.

In Figure 2.9 we provide a more quantitative view of the light availability in each of the four study regions. Here we show both the light (PAR) incident at the surface (yellow curves), as well as the light available to phytoplankton once attenuation by suspended particles, transport through the MLD and ice cover have been taken into account (green curves). The figure also gives an indication of MLD forcing that is applied to each study region, with generally deeper mixing as we move further south in regions with greater ice formation (and therefore more convective mixing driven by brine rejection). Here the mean light experienced by phytoplankton is averaged over this MLD, assuming an

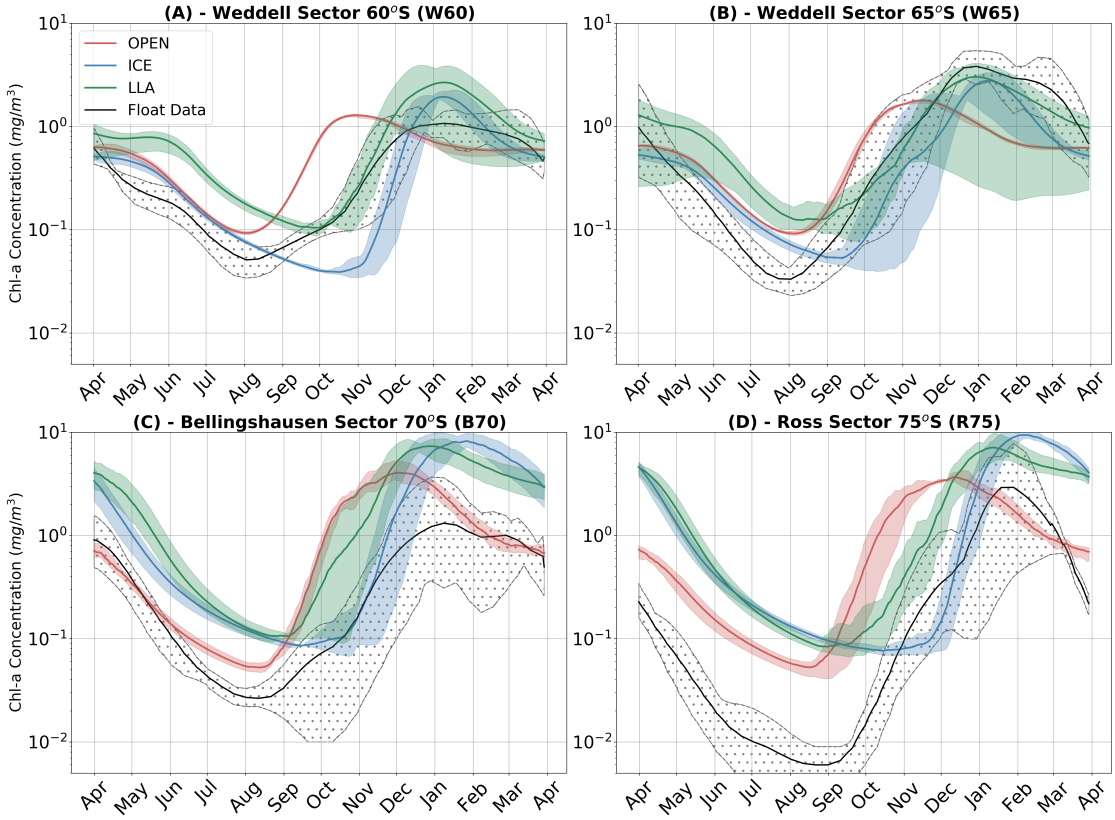

Figure 2.8: Time series of mean mixed layer chlorophyll-a for each of the 4 regions discussed in the text. In each panel the observed values (black) are compared to 3 model experiments; runs with no sea ice are shown in red (OPEN - irradiance calculated as if there was no ice), runs with ice in blue (ICE), and runs with both ice and enhanced low light efficiency by phytoplankton are plotted in green (LLA). The shaded regions for each curve represent the spatial and temporal variability present in each dataset as in Figure 2.7.

exponential decay as a function of the water attenuation and absorption and scattering by suspended particles (as described above in section 2.2.2).

An interesting comparison can be made between the two study regions in the Weddell Sea (W60 and W65, Figure 2.9A and B), which display generally similar incident light (yellow curves) and MLD forcing. The much greater under ice PAR (green curves) present in the W65 is largely due to the emergence of an open ocean polynya in 2017 associated with the Maud Rise seamount (Jena et al., 2019). Indeed, Figure 2.14B reveals that ice concentrations in the W65 region dropped as low as 40% in mid-September of 2017, while in other years concentrations are generally above ∼90% until retreat in late November. This substantial reduction in ice cover greatly increases under ice PAR in 2017, thus biasing the mean PAR high in Figure 2.9B. This is why we also show the mean time series with 2017 removed (green dashed curve in Figure 2.9B), which shows values more typical of the region. However, even with this anomalous year removed, the W65 region still shows greater under ice PAR in September/October than W60, despite being further south. Quantitatively, mean September under ice PAR is more than 4 times greater in W65 (0.43 $\mu Em^{-2}s^{-1}$) than in W60 (0.09 $\mu Em^{-2}s^{-1}$). Similarly, the mean October under ice PAR in W65 is almost double that in W60 (0.91 and 0.55 $\mu Em^{-2}s^{-1}$, respectively).

Moving further south into the Bellingshausen Sea sector at ∼70°S (B70 - Figure 2.9C), we see that under ice PAR is also high compared to W60, with a mean value of 0.77 $\mu Em^{-2}s^{-1}$ for September. This is again primarily driven by anomalously low sea ice concentrations in 2017, associated with the location of float 5905075 (mean location 68.9°S, 102.8°W - see table 2.3). If this anomaly is removed, mean September under ice PAR is in B70 reduced by 62% to just 0.29 $\mu Em^{-2}s^{-1}$. In the most southerly region, R75, under ice PAR is below 1 $\mu Em^{-2}s^{-1}$ until late November. Also notable in R75 are very deep winter mixed layers, which further contribute to light limitation in this set of experiments.

We would note that these under ice PAR values agree well with the available observations of the region. Arndt et al. (2017) provide data of under ice irradiance for the Weddell Sea at 60.78°S and 26.36°W, with values generally ranging from 0 to 1 $W.m^2$ over the period 18 to 26 September 2013. This converts to an under ice PAR range of 0 - 0.77 $\mu Em^{-2}s^{-1}$ (using conversion method in Vichi et al. (2015), page 20), which corresponds well to the mean September value 0.43 $\mu Em^{-2}s^{-1}$ for the W60 experiment (Figure 2.9A). In addition, Fritsen et al. (2011) measured under ice PAR from early October to early December at ∼70°in the Bellingshausen Sea, reporting values generally below 1 $\mu Em^{-2}s^{-1}$ (although with some intermittent increases up to

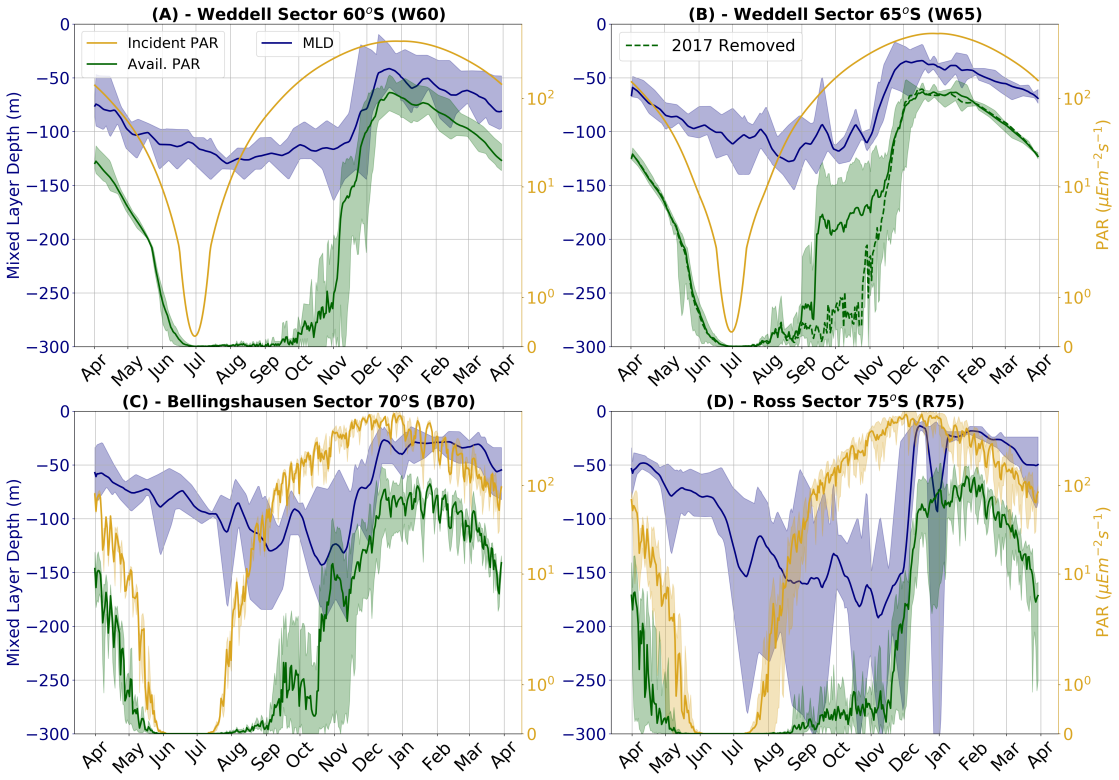

Figure 2.9: Time series of PAR (green and yellow curves) and MLD (estimated by ND - blue curves) for each of the 4 model study regions. The total PAR available at the surface is shown in yellow, while the green curves show the PAR which is actually available to phytoplankton after the effects of sea ice cover and light attenuation through the mixed layer are taken into account. The shaded regions around each curve represent the variability present in each study region, just as in Figure 2.8. Note that the PAR axis is log scaled to allow for small increases in light in late winter/ early spring to be seen.

6 $\mu Em^{-2}s^{-1}$). This again compares well to our modelled values in the corresponding study region, B70, which has values ranging from 0 - 10 $\mu Em^{-2}s^{-1}$ for the period October to December.

In Figure 2.10 we show the timing of GI for each region and experiment, providing a more quantitative view of the relative changes in phenology (each point in the figure represents a separate year or location). While the LLA set of experiments generally performs best at reproducing GI, there are notable exceptions in each of the 4 study regions. In the W60 region the observed GI occurs between early September and mid-October, with OPEN experiments having growth too early and LLA experiments too late. Moving further south to W65, we see that only LLA is able to capture the observed variability in GI, but that in some cases OPEN provides the best fit to data. Continuing south and west, both B70 and R75 contain cases where GI is best described by ICE simulations. In the following section we will bring together both the observational and modelling results discussed thus far, thereby shedding light on the possible mechanisms leading to under ice growth in the Antarctic winter and spring.

2.4 Discussion

Relationship between Melting and Growth

The central question of the present study relates to what conditions are necessary to trigger phytoplankton growth in the Antarctic SSIZ. As has been outlined in Section 2.1, a popular hypothesis holds that the release of buoyant melt waters following sea ice retreat shoals the mixed layer, relieving light limitation and triggering rapid growth. In contrast to previous studies relying on incomplete satellite data or models, we were able to thoroughly test this hypothesis by utilizing a unique in-situ dataset of under ice profiles. In particular, we were able to test two predictions of the hypothesis; first, that at least part of the variability in the timing of growth initiation (GI) may be explained by the timing of sea ice melt, and second, that GI should either be synchronous with or occur after the release of melt waters.

Based on the data analysed here, we do not find evidence which convincingly supports either claim. In Figures 2.6 and 2.7, we show that phytoplankton are clearly able to sustain net growth before significant freshening of the surface ocean. It is important to reiterate here that GI is based on the rate of growth exceeding the median rate, and so the predominantly negative values in the difference between GI and melting in Figure 2.6 suggest a highly active phytoplankton population exists under ice prior to melting.

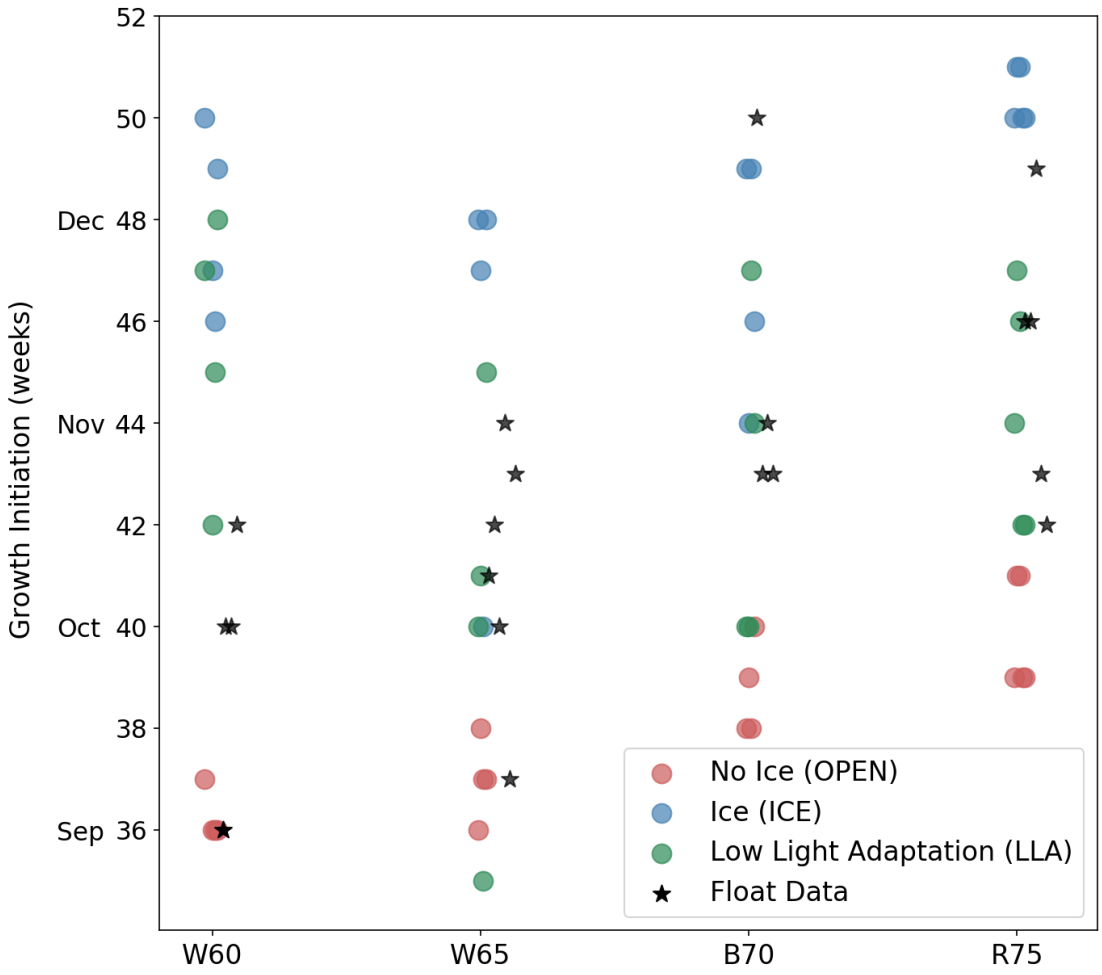

Figure 2.10: Timing of GI for each study region (horizontal axis) and model experiment (coloured points). Corresponding values from float data are indicated by black stars.

This explains why GI and melting are not strongly correlated in time (Figure 2.5B); the release of melt waters does not appear to relieve light and/or iron limitation and so variability in melt timing cannot account for variability in GI. GI is instead correlated more strongly with latitude, suggesting that phytoplankton are responding to changing incident light conditions rather than sea ice related fresh water fluxes.

In a complementary analysis, we performed the same correlation, but replaced GI with a proxy for bloom initiation (BI - see Figure 2.17), which we estimated using the timing of the maximum growth rate (based on the mean mixed layer chl-a, as for GI). As could be expected, BI occurs later in the year and is more strongly correlated with the ice decay onset (Figure 2.17B, R = 0.37 for BI, but R = 0.22 for GI). Bloom initiation also generally occurs after ice decay onset, suggesting that melt water release may be associated with the peak growth rate (as opposed to triggering growth). Despite the higher correlation coefficient of BI (when compared to GI) with ice decay onset, BI is still more strongly correlated with latitude (R = -0.39, Figure 2.17A), with a lower p-value (p = 0.007). Furthermore, for $\sim$57% of the observed melt events, BI occurs one month or more after the ice decay onset, suggesting that conditions only become optimal for growth several weeks after significant melting.

Also noteworthy is the extent to which GI occurs prior to melting (Figure 2.6). For 35% of the events, GI is observed more than 35 days before melting, with a further 25% preceding melting by 25-35 days. Only 10%, or 4 events, occur either at the same time as or after sea ice retreat. As is discussed in 2.3.1, our float dataset samples in a wide variety of environmental conditions, which exhibit very different sea ice and vertical mixing regimes. This suggests that the results presented here are fairly representative of the SSIZ as a whole, rather than being biased by a particular region or time period.

These findings are broadly in agreement with those presented by Uchida et al. (2019), who analysed the same dataset and found that early growth initiated in August/September in the region south of $\sim$60°S. However, our findings are contrasted with those of Briggs et al. (2017), who concluded that respiration dominated during the ice covered period based on nine under ice floats deployed in 2014 and 2015 in the Ross and Weddell Seas. Importantly, the ice covered period was estimated by the ice avoidance algorithm, which is purely temperature based. Here we have included salinity data in our estimation of the melt timing, thus providing a more robust constraint on ice covered period. Furthermore, our interest has been the period of initial growth when overall biomass is still generally very low, but growth rates are substantial. Briggs et al. (2017) note that nitrate, oxygen and dissolved inorganic carbon (DIC) changes during the ice covered period are consistent with net respiration, however the modest

phytoplankton standing stock present at GI (which occurs at the end of the ice covered period) may not be sufficient to appreciably reduce nitrate and DIC concentrations and increase oxygen values (see Table 2.2).

Indeed, as is shown in Figure 2.15, only 55% to 65% of cases show dissolved oxygen, nitrate or DIC changes that are consistent with net production at the timing of GI (note that each ”case” here refers to an instance where GI was retrieved with valid data for at least one of the other 3 variables, namely, oxygen, nitrate or DIC). In the end, higher resolution data are needed to more precisely determine the timing of net production.

It is also interesting to note that these results can be interpreted as supporting the ”disturbance-recovery” hypothesis discussed above in section 1.3.1. Using this framework Behrenfeld and Boss (2014); Behrenfeld et al. (2017) have argued that growth/bloom initiation occurs much earlier in the year in winter at high latitudes than previously thought, a very similar conclusion to that arrived here. However, as will be discussed below, the winter growth shown here does not necessarily require that ecological interactions be invoked to explain it. Although the role played by such interactions is not ruled out here, it is argued that the observed growth can be accounted for by a revision of our understanding of the under ice light environment, as well as the physiological response by phytoplankton to this.

Growth Under Extreme Light Limitation

We now move on to the question of how phytoplankton are able to sustain such high growth rates under such poor ambient light conditions. Recall that the average stratification depth at the time of GI is around 130m, and that satellite data suggest near complete ice cover. Although the timing of GI in October would allow for ample light in open ocean conditions, previous studies suggest that light transmittance through typical consolidated ice would be just 1- 5% of that incident at the surface (even with a thin snow layer, Fritsen et al. (2011); Arndt et al. (2017)). Indeed, as was discussed in section 1.2.2, the Antarctic under ice light environment is likely controlled by high transmittance features such as leads and ice-water mixtures (e.g. grease) found between floes. Two possible explanations for growth under these conditions are then apparent: one, light is more readily available in ice covered environments than previously thought, and two, phytoplankton are more adapted to extreme low light than previously thought. Hence, the phenomenon can be accounted for by both physical factors (such as sea ice and vertical mixing conditions which alter light availability) and biological ones (such as phytoplankton physiology).

Both factors are likely operating simultaneously. Indeed, the very presence of growth indicates light levels above zero, suggesting a revision of our current understanding of under ice environments. It may also be possible that sea ice algae are entering the water column through bottom melting, although observations of successful seeding events are rare (see section 1.3.2; Riaux-Gobin et al. (2011); Van Leeuwe et al. (2018)). While we would not rule out the potential role of seeding in explaining early growth, the lack of evidence of this occurring in the Antarctic leads us to favour alternative explanations discussed above.

In our regional box model experiments we explore both physical and biological factors. The fact winter and spring phenology is brought closer to observations when low light efficiency is enhanced by an order of magnitude certainly suggests a role for phytoplankton adaptation (Figure 2.8 - LLA experiments). Certainly, growth by sea ice algae under the extreme low light conditions presented in Figure 2.9 has been observed on several occasions (Fritsen et al., 2011; Hancke et al., 2018). However, these are observations of ice algae, which are known to be capable of sustaining growth under irradiance lower than 1 $\mu Em^{-2}s^{-1}$ (Fritsen et al., 2011; Hancke et al., 2018). The irradiance requirements for growth by phytoplankton in the water column are generally assumed to be much higher, at least >1 - 5 $\mu Em^{-2}s^{-1}$ (e.g. Nelson and Smith Jr. (1991); Hill et al. (2018)). As was mentioned above in section 2.2.2, the value used for the initial slope of the P-I curve in LLA experiments is close to that commonly used for sea ice algae (Tedesco and Vichi, 2014). Thus, the ability of the LLA simulations to reproduce the early spring growth seen in the float data suggests that SSIZ phytoplankton are able to grow under irradiance lower than 1 $\mu Em^{-2}s^{-1}$, as has been observed for sea ice algae (Fritsen et al., 2011; Hill et al., 2018; Hancke et al., 2018).

However, the interpretation is complicated somewhat by the fact that under certain conditions phenology may be best described by simulations with no ice (OPEN) or with ice but standard physiology (ICE). For example, in the Weddell Sea (Figure 2.8A and B) early growth in August is best captured by OPEN experiments, but subsequent spring growth rates (October-November) more closely align with LLA simulations. The inference here would be that in this region sea ice is unconsolidated and highly permeable to light, allowing growth to initiate as soon as incident radiation is sufficient. This corresponds well with the correlation between GI and latitude shown in Figure 2.5A. This is despite the apparently near 100% sea ice concentration suggested by satellite data (see Figure 2.14A+B). Indeed, at these latitudes we may actually be in the MIZ (as defined by dynamical considerations such as wave propagation, not satellite concentration), which would explain the higher light permeability. Yet, this is not to say that sea ice has no effect, later in the season growth rates are slowed by its presence,

explaining why LLA experiments perform better here.

Further south in the Bellinghausen and Ross seas, sea ice is expected to be more consolidated in winter and spring, and so phenology is better captured by LLA simulations. However, in two cases the timing of GI most closely matches ICE experiments (see Figure 2.10, regions B70 and R75). This may be accounted for by especially thick snow and ice layers in those cases, which lead to delayed growth. This highlights the importance of the particularities of ice morphological features and their effect on the light environment, something which does not seem to be captured by satellite sea ice concentration.

Thus, it is both the character of ice and snow overhead, and the physiological response to severe light limitation that may address the question raised at the start of this section. A crucial point here is that 100% sea ice cover as seen from satellite does not necessarily imply a completely consolidated ice surface (Vichi et al., 2019). While the ocean may indeed be completely ice-covered, the ice itself may be unconsolidated, being primarily composed of pancakes loosely connected by grease or brash ice. Such a condition is common in the Southern Ocean, and is maintained by wind and wave action far from the ice edge. Waves are known to propagate several hundred kilometres into the ice, effectively preventing the formation of pack ice-like conditions (Kohout et al., 2014; Meylan et al., 2014). Wind forcing is also known to be highly effective in causing ice break-up and motion, with intense synoptic events in the Weddell and Eastern Indian oceans occurring frequently (Vichi et al., 2019; Uotila et al., 2000). Such events, along with interactions with the westernly wind belt, drive the formation of leads within the MIZ, as well as within pack ice. Therefore, the highly dynamic nature of Antarctic sea ice may lead to a general enhancement of light availability in the underlying ocean. The presence of even a tiny amount of light may be expected to induce adaptation in primary producers, thereby explaining why the model configurations presented here which take this into account produce a more realistic phenology.

Conclusions

This study has characterised under ice phytoplankton phenology using a unique dataset of Bio-ARGO profiles, complemented by a set of process-oriented biogeochemical model experiments. We have shown that rather than acting as a trigger as postulated in previous studies, the release of melt waters enhances growth in an already highly active phytoplankton population. Such unexpected early growth (under presumed severe light limitation) may be accounted for by a combination of low light adaptation by phytoplankton and sea ice permeability with respect to light. We argue that such

permeability is related to the turbulent state of the Southern Ocean, which together preserve an unconsolidated ice morphology that is not captured by current satellite sea ice concentration algorithms.

However, our investigation has not been exhaustive of all possible mechanisms leading to under ice growth. Future research directions could include an examination of potential discrepancies between the timing of shoaling of the mixed layer and that of active turbulent mixing (e.g. Carranza et al. (2018); Sutherland et al. (2014)). An earlier reduction in mixing would increase ambient light, and help explain the observed under ice growth. Other ecological factors could also be explored, such as potential interactions between pelagic and sympagic communities, which are known to be highly efficient at low light intensities (Tedesco and Vichi (2014) and citations therein). Nevertheless, the findings presented here have important implications for our understanding how the biogeochemistry of the region may change in the future. With possible earlier sea ice retreat, as well as a generally thinner and more dynamic ice in some regions, we may expect even earlier growth than reported here, which would likely alter the seasonal air-sea carbon flux and thus the biological carbon pump.

2.A Additional Figures

The additional figures shown here either for other regions or using a slightly different methodology. Figure 2.11 is intended to provide further validation of the ice decay onset detection method described in section 2.2.1. Note that the marked early decrease in sea ice concentration shown in Figure 2.14B is due to the formation of an open ocean polynya associated with the Maud Rise seamount 2017 only (Jena et al., 2019), all other years have concentrations above $\sim$90% until retreat in late November.

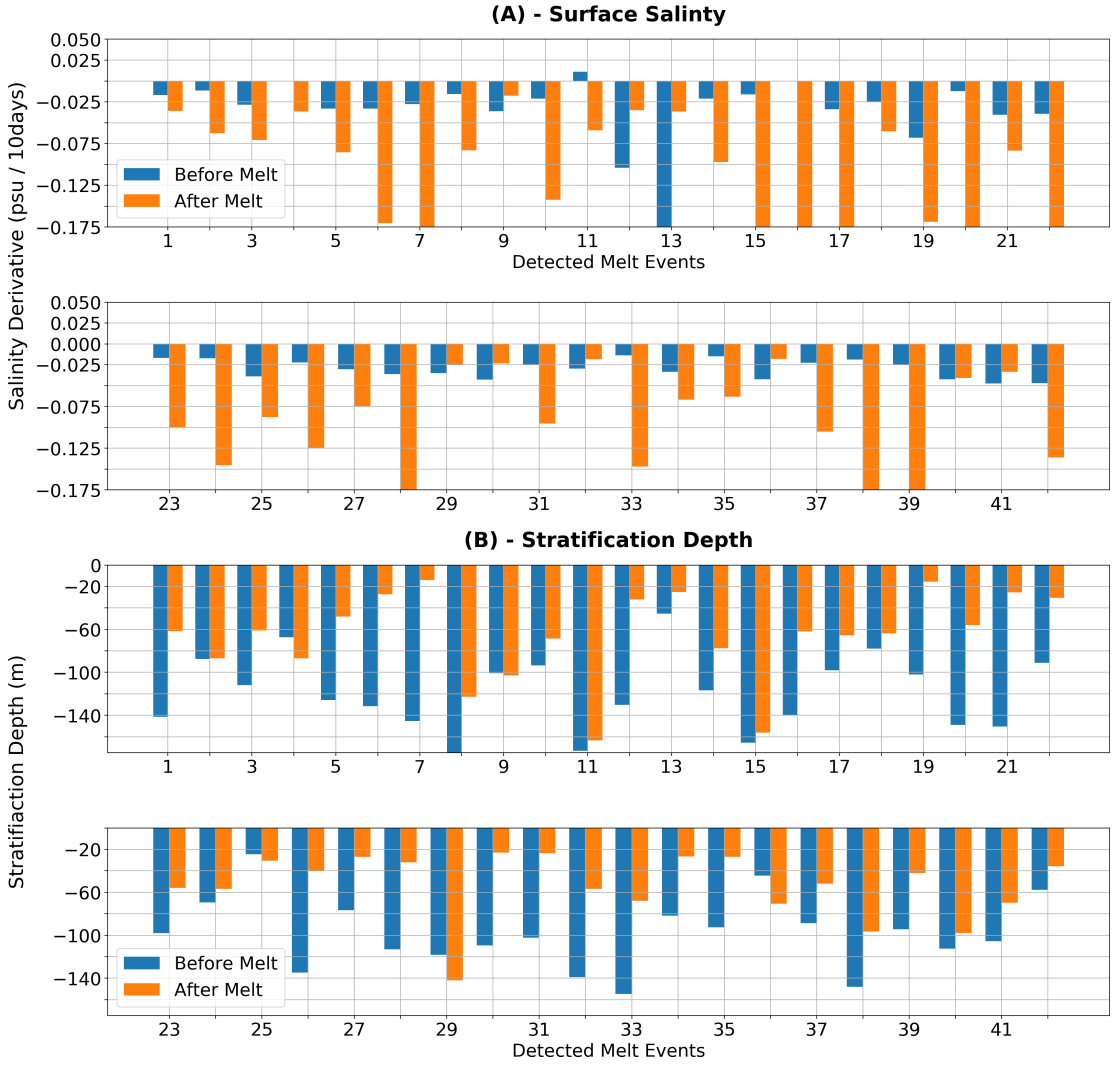

Figure 2.11: Comparison of **(A)** mean salinity derivatives and **(B)** mean stratification depth 20 days before and 20 days after the ice decay onset date (as detected by the algorithm described in section 2.2.1). Values are the mean over the 20 days before and after the ice decay onset. Each pair of bars represents one melt event, with blue showing values before the ice decay onset date and orange after (42 events in total, split over 2 plotting regions). In panel **(A)**, negative values indicate a freshening (salinity decrease) of the near surface ocean. Therefore, larger negative values indicate a stronger freshening signal. In panel **(B)** larger values indicate a deeper stratification depth associated with a deeper mixed layer depth.

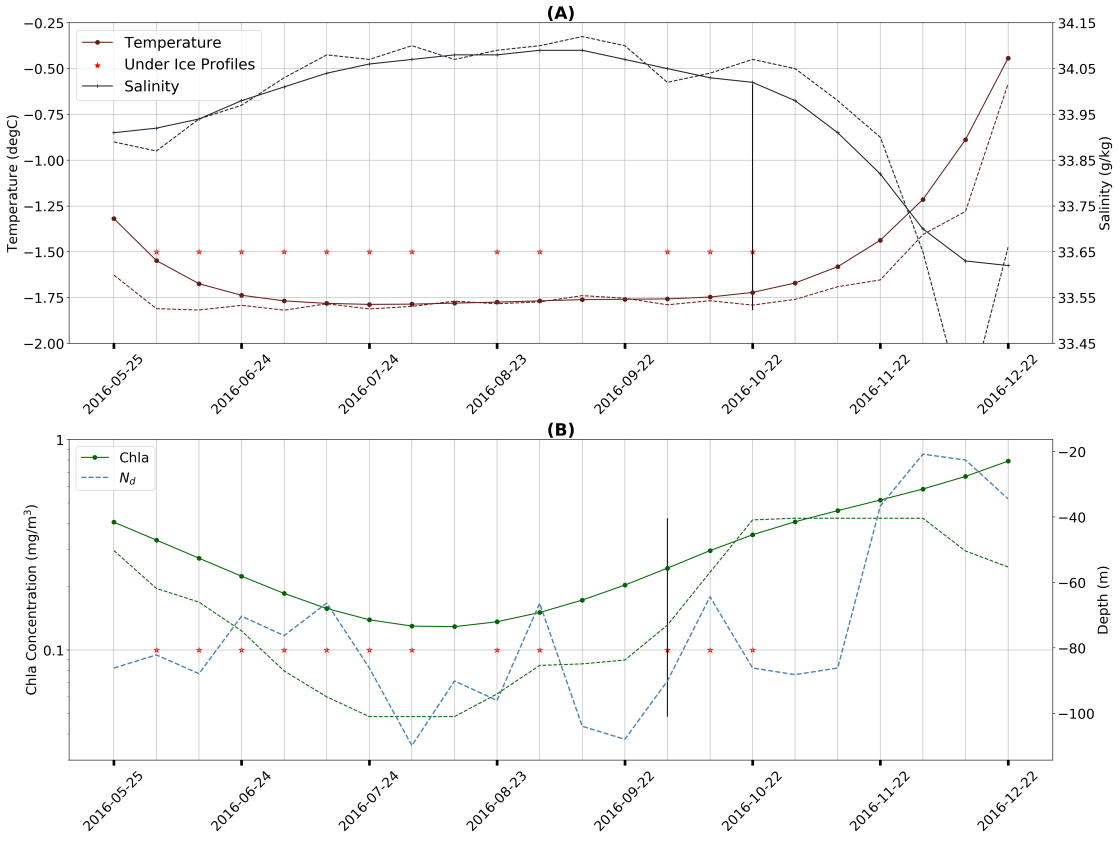

Figure 2.12: Additional time series of key properties as in Figure 2.2, but for a float in the Indian Ocean sector at ∼63°S.

Table 2.3: Table of all floats used in this study, including both the WMO ID and MBARI ID (for identifying floats on the SOCCOM website). The years of data which where used are shown, although there may be more available data at the time of reading. Mean locations for each float are also shown based on the time interval used for calculations.

WMO ID / MBARI ID	Years Sampled	Mean Latitude	Mean Longitude
5904768 / 0570SOOCN	2016	64.8°S	166.7°W
5904671 / 0507SOOCN	2016 2017 2018	62.3°S	82°E
5905636 / 12754SOOC	2018	67°S	149.4°W
5905078 / 12371SOOC	2017	66.6°S	124.4°W
5904858 / 12551SOOC	2017 2018	73.9°S	148.7°W
5904184 / 9091SOOCN	2014	61.4°S	147.4°W
5904469 / 9096SOOCN	2018	60.4°S	23.2°E
5904767 / 0568SOOCN	2016 2018	63.2°S	145.5°W
5904859 / 12549SOOC	2017 2018	70.2°S	104.3°W
5904857 / 12381SOOC	2017 2018	72.8°S	167.2°W
5905100 / 12361SOOC	2017 2018	65.2°S	166.3°E
5904860 / 12541SOOC	2017 2018	72.1°S	164.8°W
5905075 / 8501SOOCN	2017 2018	68.9°S	102.8°W
5904472 / 9275SOOCN	2015 2016 2017 2018	68.5°S	25.9°W
5904855 / 12559SOOC	2017 2018	68.3°S	83.8°W
5905077 / 12379SOOC	2017	65.7°S	107.1°W
5904468 / 9099SOOCN	2015 2016 2017 2018	65°S	2.3°E
5904471 / 9094SOOCN	2015 2016 2017 2018	65.7°S	4°E
5904397 / 9125SOOCN	2015 2016 2017 2018	61.2°S	2.4°W
5905080 / 12366SOOC	2017	65°S	117.7°W

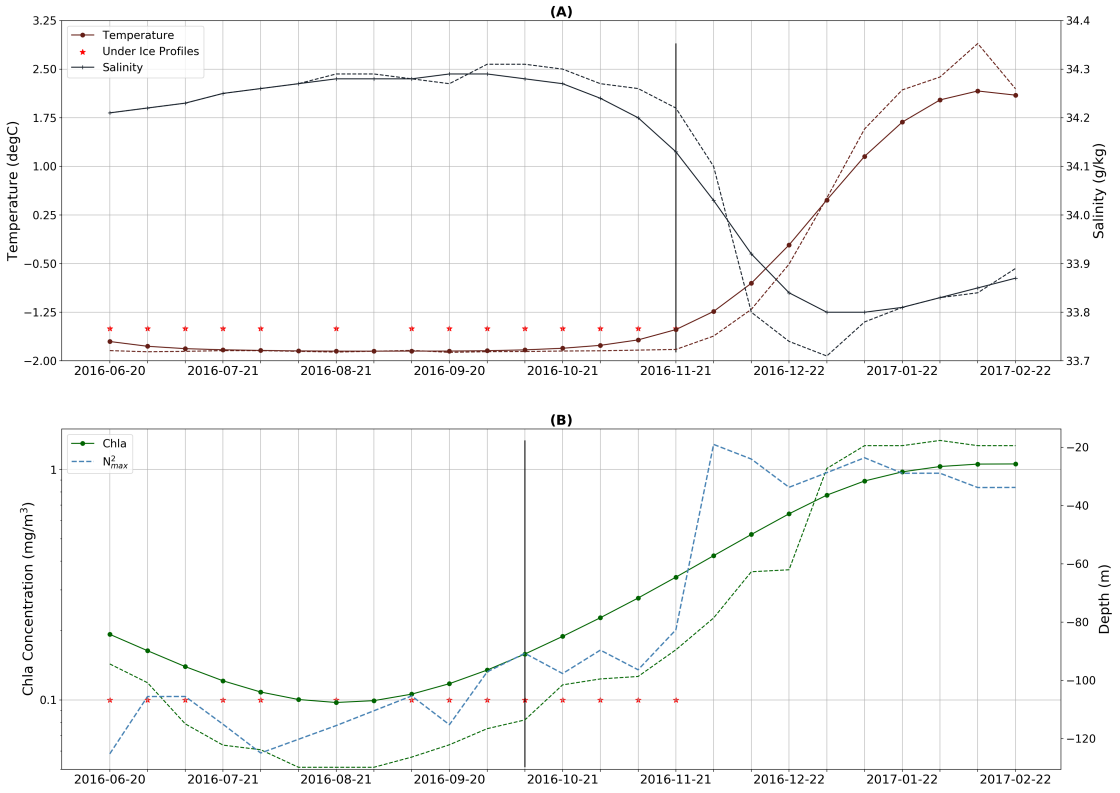

Figure 2.13: The same as Figure 2.12, but for a float in the Weddell Sea at ∼60°S in 2016.

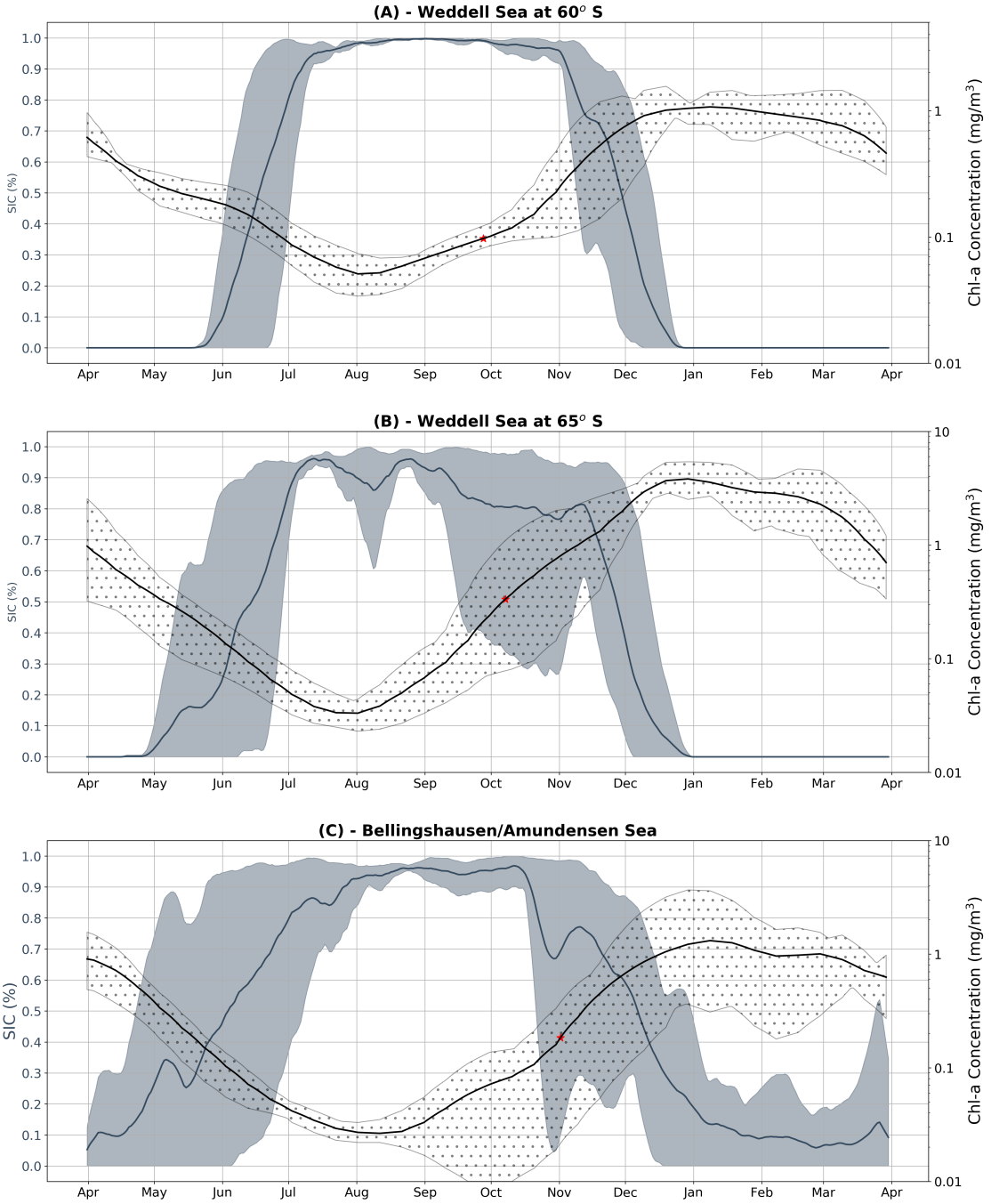

Figure 2.14: Time series of satellite sea ice concentration versus float mixed layer chl-a as in Figure 2.7, except for regions **(A)**: W60 , **(B)** W65 and **(C):**B70.

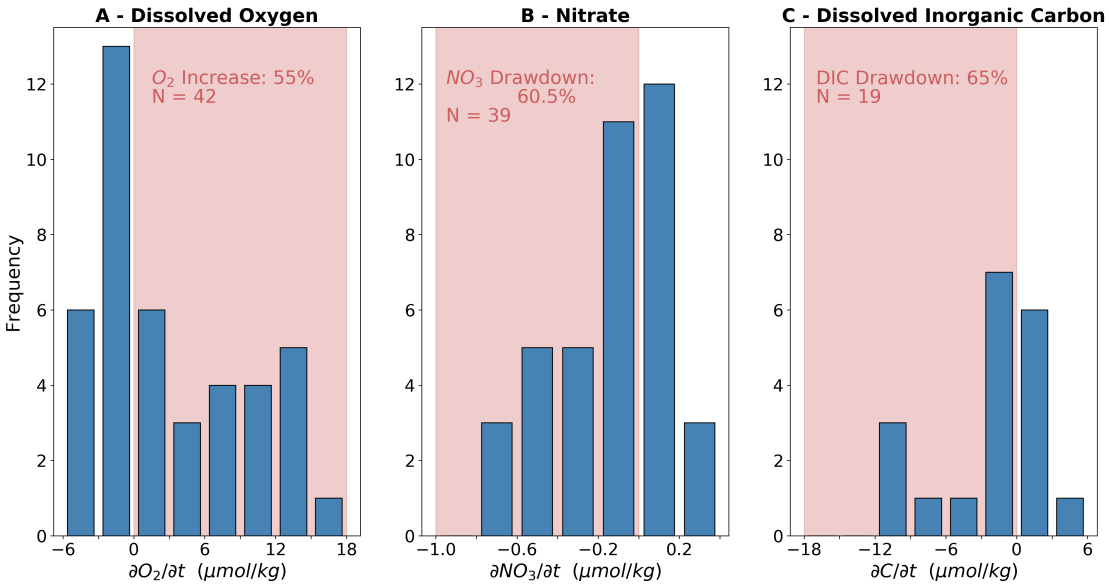

Figure 2.15: Distribution of time derivatives of mean mixed-layer **(A)** dissolved oxygen, **(B)** Nitrate and **(C)** dissolved organic carbon (DIC). Derivatives are computed over a 30-day period from 10 days before GI to 10 days after, and then averaged to give the values shown in the figure. The derivatives therefore show the mean change over GI, taking into account information both before and after the estimated growth initiation. The red shaded region denotes the portion of the distribution where the sign of the derivatives are indicative of net photosynthesis (i.e. increasing oxygen, NO3 and DIC drawdown). In **(A)**, positive values indicate that mean dissolved oxygen is increasing in the mixed layer at GI, which occurs for 55% of the 42 events captured. In **(B)**, negative values indicate that mean nitrate concentration is decreasing, which occurs in 60.5% of the 39 events captured (valid nitrate data was not available for all 42 events where GI was captured). In **(C)**, negative values indicate that mean DIC is decreasing, which occurs in 65% of the 19 cases captured (unfortunately valid DIC data were much more rare than chl-a).

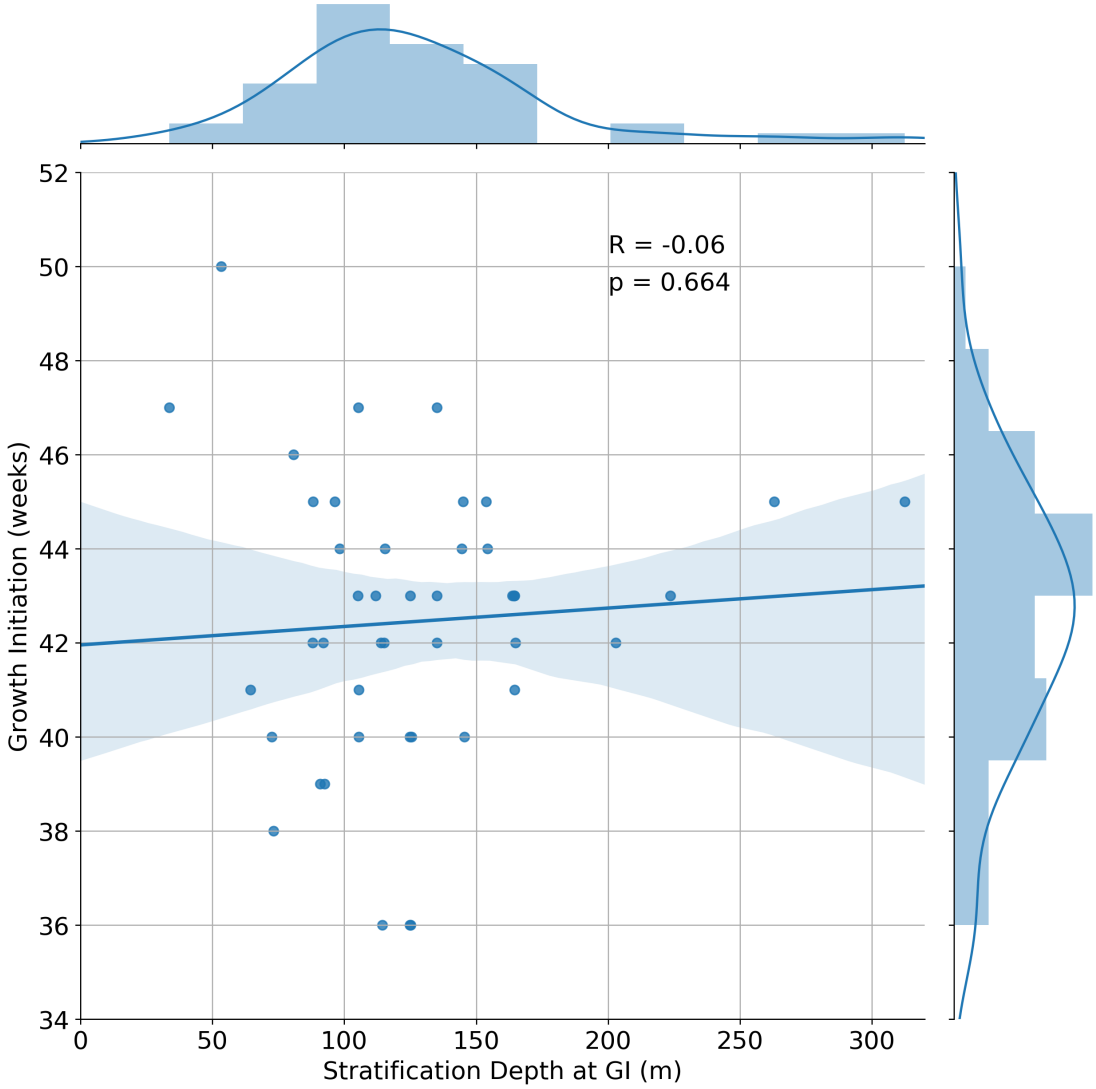

Figure 2.16: Stratification Depth at the timing of GI plotted against GI for each of the 44 melt events detected. Overlain in blue is the linear regression with the 95% confidence intervals for 1000 bootstrapped resamples shaded in light blue. Histograms and PDFs of each variable are shown along the edge of the axes.

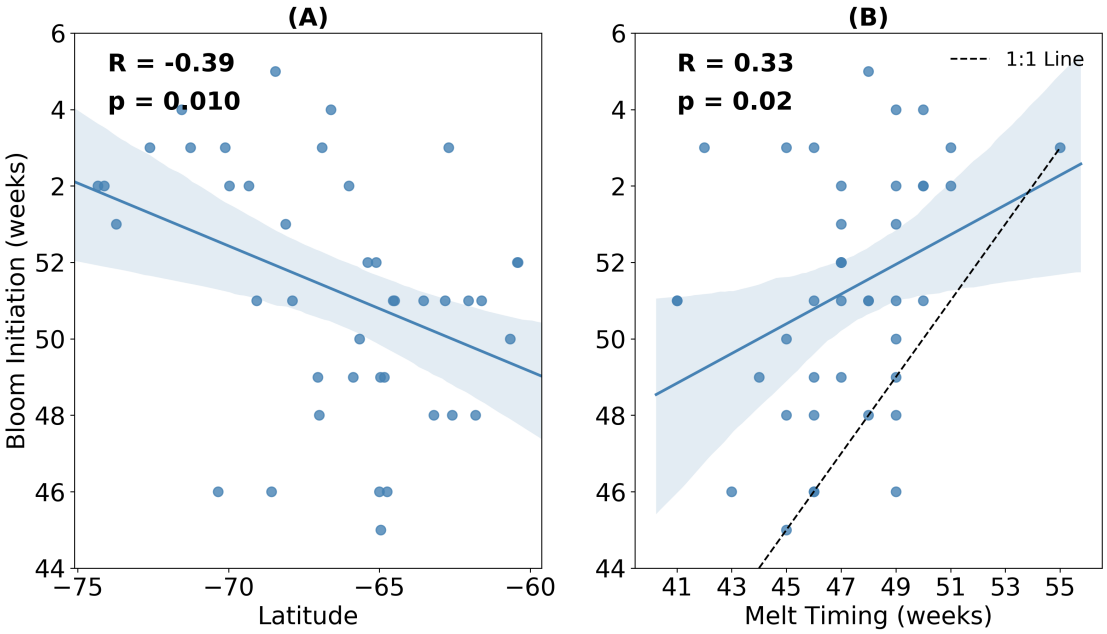

Figure 2.17: Timing of bloom initiation (BI) plotted against **(A)**: timing of sea ice melt and **(B)** : average latitude for each of the 42 melt events shown in Figure 2.4. Overlain in blue is the linear regression with the 95% confidence intervals for 1000 bootstrapped resamples shaded in light blue. The Pearson correlation coefficient (R) and corresponding p-value are shown for each regression.

Chapter 3

Sea Ice Phytoplankton Phenology in Climate Models

Abstract

[1] Earth system models from the Climate Model Intercomparison Project phase 5 (CMIP5) are strongly biased in Southern Ocean phytoplankton phenology, especially in the marginal ice zone. In this study we describe the mechanisms driving CMIP5 models to misrepresent seasonal primary production in the Atlantic marginal ice zone during late winter. We link subsurface light availability during this period to simulated early growth, arguing that a combination of ice cover and deep winter mixing prevent biomass accumulation in the real ocean, while in models this combination of factors is not present. Furthermore, we find a statistically significant correlation across the model ensemble between vertical stratification and the location of the ice edge; whereby the more equatorward the ice edge is, the closer to the surface stratification occurs. We argue that models may be grouped according to how strongly they express two major controls on their phenology, namely, the location of the ice edge and the degree of stratification present in the water column in late winter. We find that models with small biases in just one of these controls (but large biases in the other) are able to simulate bloom initiation close to observations, while models with significant biases in both controls initiate growth 2–4 months early.

[1]The following chapter is published as Hague, M., & Vichi, M. (2018). A link between CMIP5 phytoplankton phenology and sea ice in the Atlantic Southern Ocean. Geophysical Research Letters, 45. https://doi.org/10.1029/2018GL078061

3.1 Introduction

In recent years much attention has been paid to trends in the Antarctic sea ice. Of particular concern has been the apparent inability of CMIP5 models to reproduce the observed weak trend in sea ice extent (SIE), instead virtually unanimously simulating a negative trend (Turner et al., 2013). A related and equally important discrepancy exists between the modelled and observed mean state, with the majority of models simulating far too little historical sea ice (Turner et al., 2013; Mahlstein et al., 2013; Meijers, 2014).

Despite the recognized importance of sea ice for biogeochemical processes in the Southern Ocean (for example Cavanagh et al. (2017); Wang et al. (2014)), the implications of this bias have not been addressed in the literature. Accordingly, this study seeks to investigate the effect misrepresentations of seasonal sea ice have on simulated phytoplankton phenology in the Southern Ocean in CMIP5 models. We have chosen to focus on the Atlantic because it not only has the highest average surface chlorophyll concentrations, but also large spatial intra-seasonal variability (Thomalla et al., 2011).

Within the Atlantic, we focus on the marginal ice zone (MIZ), which can be defined as a region where some degree of ice cover is found, but nevertheless exchanges of heat, momentum and radiation between ocean and atmosphere are significant. As introduced in Chapter 1, this region has long been recognized as an area of enhanced primary productivity, with many early studies pointing to the role melt waters play in stabilizing the water column following ice retreat. (Smith and Nelson, 1985, 1990; Lancelot et al., 1993). Biomass is then able to accumulate in this stable fresh layer where light conditions are favourable. While there are other factors which could promote growth in the MIZ such as iron input (that is, iron contained within sea ice) (Wang et al., 2014) and seeding by ice algae (Arrigo and Thomas, 2004; Tedesco et al., 2012), these processes are not included in CMIP5 models.

Substantial fresh water and mixed layer depth biases have also already been identified in the CMIP5 Southern Ocean (Sallée et al., 2013b,a). Sallée et al. (2013a) showed that a year round shallow bias in the mixed layer across models was related to excess fresh water input at the surface, which tended to prevent deep winter convection. Such lack of mixing has important consequences for the simulation of phytoplankton phenology since both light and nutrient conditions are controlled to large degree by the amount of mixing present in the water column (Boyd, 2002; Fauchereau et al., 2011; Carranza and Gille, 2014).

3.1.1 Aims and Questions

The overall aim of this chapter is to first characterize and then investigate the drivers of Antarctic MIZ phenology in CMIP5 climate models. Since substantial biases have already been identified in the representation of sea ice and vertical mixing in these models, we will further investigate whether these play a role in explaining potential biases in the annual cycle of phytoplankton. Accordingly, we will attempt to address the following research questions, which are linked to point 3 in section 1.4.1:

1. How well do CMIP5 models reproduced the observed phenology of the Antarctic MIZ?
2. What are the drivers of Antarctic MIZ phenology in CMIP5 models?
3. What is the relationship between sea ice and vertical mixing in CMIP5 models at seasonal time scales?

3.2 Materials and Methods

3.2.1 Data

Data from 11 CMIP5 earth system models where assessed in this study (see Table S1), focussing on the historical simulations for the 30-year period 1976-2005. The variables considered include: total chlorophyll mass concentration at surface, sea ice area fraction, sea water salinity and sea water potential temperature. Two satellite products are used in this study: chlorophyll-a from the European Space Agency Climate Change Initiative's Ocean Colour (ESACCI-OC level 3, version 1.0; 1998 - 2011, 1°resolution) and sea ice concentration from the National Snow and Ice Data Centre (NSIDC) using Nimbus-7 SMMR and DMSP SSM/I-SSMIS Passive Microwave Sensors (downloaded at monthly 0.25°resolution). In addition, temperature and salinity were downloaded from three observationally based products for comparison to model data: World Ocean Atlas 2013 Version 2 (WOA-2013, 1°), Monthly Isopycnal / Mixed-layer Ocean Climatology (MIMOC) and the Southern Ocean State Estimate data assimilation model (SOSE, 1/6°). For a description of each of the models analysed, please refer to Table **??** (Chylek, P. et al., 2011; Vichi et al., 2007; Voldoire et al., 2013; Séférian et al., 2013; Dunne et al., 2013a,b; Romanou et al., 2013; Collins et al., 2011; Ilyina et al., 2013; Adachi et al., 2013). These 11 models are chosen to represent a broad range of modelling groups,

and therefore capture a variety of approaches to simulating sea ice-ocean-atmosphere interactions, as well as ocean biogeochemistry.

3.2.2 Methods

As a first step, all CMIP5 data presented here are regridded onto a regular 1°x 1°grid in order to ease comparison. However, in the vertical the original model grids are used except when computing the ensemble. The domain spans from 20°W to 20°E for all figures except 3.1A-C.

In this study we define the MIZ as the region between the 15% and 80% sea ice concentration contours, following operational estimates based on satellite data as well as many previous studies (see, for example Stroeve et al. (2016) and citations therein and Taylor et al. (2013) for other ways in which one may define the MIZ). We term the latitude of the 15% sea ice concentration contour the ice edge location, representing the northern edge of the MIZ. Since the location of the MIZ varies greatly between models, we extract a common region of analysis (Figures 3.1D and 3.4A-C) in which the majority of models simulate an average sea ice concentration between 15% and 80%. The region extends from 58 to 62°S, corresponding roughly to the multi-model ensemble MIZ between July and September (JAS), as well as containing the observed MIZ in JAS (see Fig. 3.2L and M). We refer to this region as the study region (SR). This ensures that meaningful comparisons are made between models with similar incident light, as well as similar atmospheric fluxes, but not necessarily similar ice concentrations.

The main phytoplankton phenology diagnostic used here is bloom initiation, defined as the month where surface chlorophyll concentration passes a threshold of 5% greater than the climatological median following Racault et al. (2012). This differs from the metric used in Chapter 2, which was more tailored to the profile data analysed in that case. Here we use 30-year climatologies where threshold methods are more suited, as well as more utilized in the literature. Furthermore, the results of Chapters 2 and 3 can now be compared to highlight the differences between threshold and rate of change based approaches (in Chapter 2 growth initiation is defined based on rate of change in chl-a). The bloom peak is simply the month of maximum chlorophyll concentration. We also use the time derivative of surface chlorophyll as an indicator of phenology, employing a forward in time numerical derivative.

Institution	Model	Horizontal Resolution	Vertical Resolution	Biogeochemical Component	Reference
Canadian Centre for Climate Modelling and Analysis	CanESM2	0.9°x 1.4°	40 levels	NPZD	Chylek, P. et al. (2011)
Centro Euro-Mediterraneo Sui Cambiamenti Climatici	CMCC-CESM	0.5-2°x 2°	21 levels	PELAGOS	Vichi et al. (2007)
Centre National de Recherches Meteorologiques Centre Europeen de Recherche et de Formation Avancee en Calcul Scientifique	CNRM-CM5	1°x 1°	42 levels	PISCES	Voldoire et al. (2013); Séférian et al. (2013)
Geophysical Fluid Dynamics Laboratory	GFDL-ESM2G/M	0.3 - 1°x 1°	59 (2G) / 50 (2M)	TOPAZ2	Dunne et al. (2013a,b)
NASA Goddard Institute for Space Studies	GISS-E2-R-CC	1°x 1.25°	32 levels	NOBM	Romanou et al. (2013)
Met Office Hadley Centre	HadGEM2-CC/ES	0.33-1°x 1°	40 levels	Diat-HadOCC	Collins et al. (2011)
Institut Pierre-Simon Laplace	IPSL-CM5A-MR	0.5-2°x 2°	31 levels	PISCES	Séférian et al. (2013)
Max Plank Institute for Meteorology	MPI-ESM-MR	0.4°x 0.4°	40 levels	HAMOCC5.2	Ilyina et al. (2013)
Meteorological Research Institute	MRI-ESM1	0.5°x 1°	51 levels	NPZD	Adachi et al. (2013)

Table 3.1: Description of the 11 CMIP5 models analysed in this study.

3.3 Results

3.3.1 Seasonality

Substantial model spread exists in the reproduction of the seasonal cycle of surface chlorophyll and the ice-edge location as shown in Figure 3.1. Indeed, the initial impetus for the study stemmed from the need to account for the poor representation of surface chlorophyll-a in CMIP5 models across the entire Southern Ocean, as shown in Figure 3.1A - C. In Figure 3.1E we show the same seasonal cycle, but averaged over the study region 58 to 62°S, revealing remarkably similar biases in the timing and intensity of growth. In terms of sea ice, models which are fairly close to observations during advance and retreat tend to have an equatorward bias in winter (CanESM2, CMCC-CESM and MRI-ESM1), while the majority of other models have strong poleward biases through most of the year.

Despite limited winter coverage, satellite observations of surface chlorophyll shown in Figure 3.2M reveal that growth should be modest ($\Delta chl/\Delta t < 0.1$ mg Chl m^{-3} $month^{-1}$) until October/November in the region south of 55°S. However, our results indicate that half of the models simulate strong positive growth in surface chlorophyll close to the ice edge, as well as under ice in August and September. Generally, this feature extends northward indicating simultaneous growth from the sub-Antarctic into ice covered regions. In the other half, the magnitude of the rate of change is within the observed range, but the issue of early growth remains, occurring as early as autumn in CNRM-CM5 and IPSL-CM5A-MR at ∼65°S.

It is interesting to note that satellite phenology shown here differs somewhat from the float derived phenology shown in Chapter 2. In particular, floats sampling in the SR reveal substantial growth in the August/September period at ∼60°S (see Figure 2.8A, black curve) when satellite data show growth rates close to zero. There are many potential sources for this discrepancy, with a full investigation being beyond the scope of this thesis. However, it can be reasonably hypothesized that since satellites only capture the surface chl-a signal in ice and cloud free regions of the SR, a significant sampling bias may be present in the data. Ice free regions may then have deeper mixed layers due to enhanced heat loss and new ice formation (as will be demonstrated in Chapter 4), thus either inhibiting growth or diluting the chl-a signal retrieved from space. The satellite data in the late winter/spring is also biased towards the northern region of the SR. It should also be noted that the satellite data shown here is a monthly mean, while the float data of the previous chapter samples at 10-day frequency. Furthermore, the comparison is perhaps further complicated by the fact that satellite data is averaged over the entire

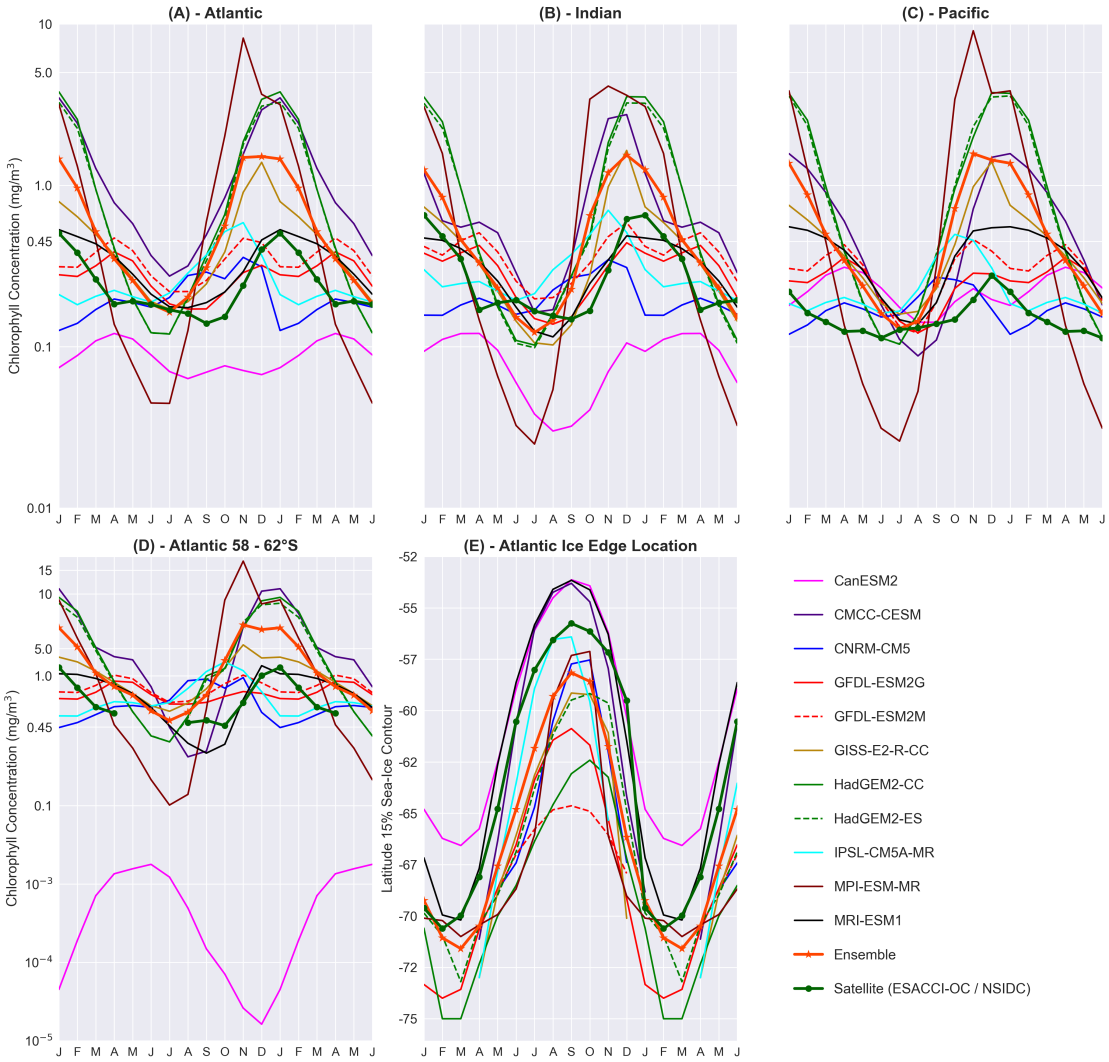

Figure 3.1: Seasonal cycle of (a–d) surface chlorophyll and (e) the location of ice edge for 11 Climate Model Intercomparison Project phase 5 models and satellite products. For each of the major Southern Ocean basins (a–c), concentrations are averaged meridionally from 45°S to 70°S, where as in panel (e) the average is taken over the region 58–62°S. For the Atlantic (a, d, and e) zonal averages are taken from 20°W to 20°E, the Indian (b) from 60°E to 100°E, and the Pacific (c) from 90°W to 130°W. Refer to section for more details.

SR and spans 14 years, while floats only sample a small part of the SR and cover 4 years that do not overlap with satellite data presented here.

In Figure 3.3 we investigate the seasonal cycle of vertical stratification and its relation to surface chlorophyll in the study region. The region of the water column where maximum energy is required to achieve mixing (the stratification depth, ND Gill (1982)) is shown by the solid black line. Most striking is a clear bias toward shallow ND, with only the GFDL and HadGEM2 models producing a realistic breakdown of stratification in winter. In addition, models such as CNRM-CM5 and IPSL-CM5A-MR simulate growth

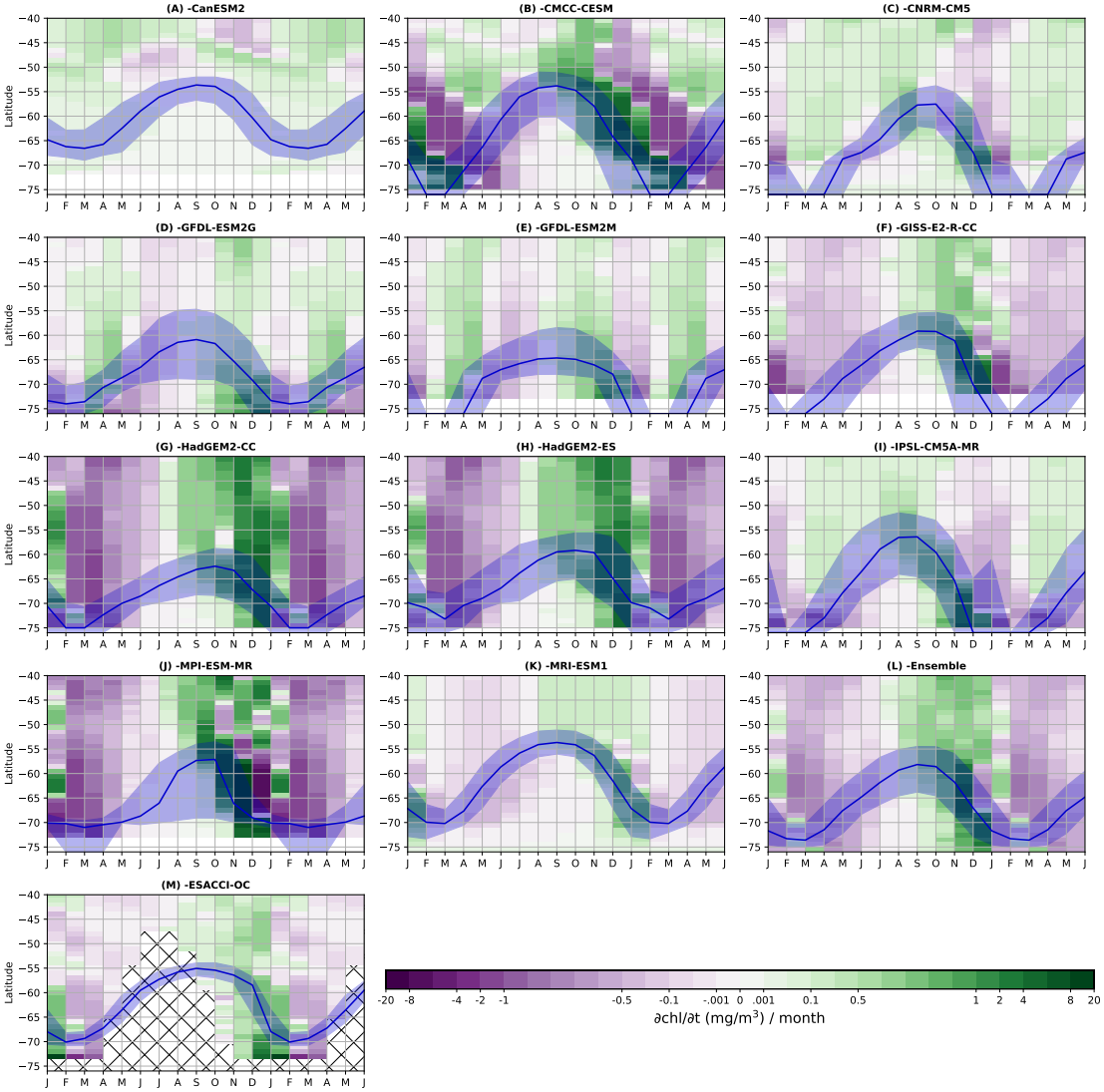

Figure 3.2: Hovmöller plot showing the zonal average of the time derivative of surface chlorophyll in the Atlantic. Hatched regions indicate missing data, which is somewhat exacerbated by using the derivative. The bold blue line represents the ice edge as in previous figures (15% contour). The top (northern-most) edge of the shading delineates the transition from open ocean to very low ice cover (0% contour), while the bottom edge is the 80% contour. The shaded region between the bold blue line and bottom edge then represents the MIZ.

in response to a deepening (or flattening at a deep level) of ND in winter, while in observations, growth coincides with a sharp shoaling of ND in October. Inspection of the ensemble in Figure 3.3L reveals that the late winter carries the largest biases in both phenology and vertical mixing.

3.3.2 Late Winter Diagnostics

Figure 3.4A illustrates the combined effect of both ND and the ice edge location on phytoplankton phenology in late winter. We note that overly stratified models with a poleward (i.e. negative) location of the ice edge simulate an early bloom initiation of between 2 to 4 months. This condition characterises the ensemble mean, which, due to error compensation, results in an artificially reduced bias of one month. On the other hand, the most stratified models, which nevertheless have a small bias in the ice edge location (such as CMCC-CESM and MRI-ESM1), simulate bloom initiation close to observations. CanESM2 stands out being the only model with delayed growth of 3 months.

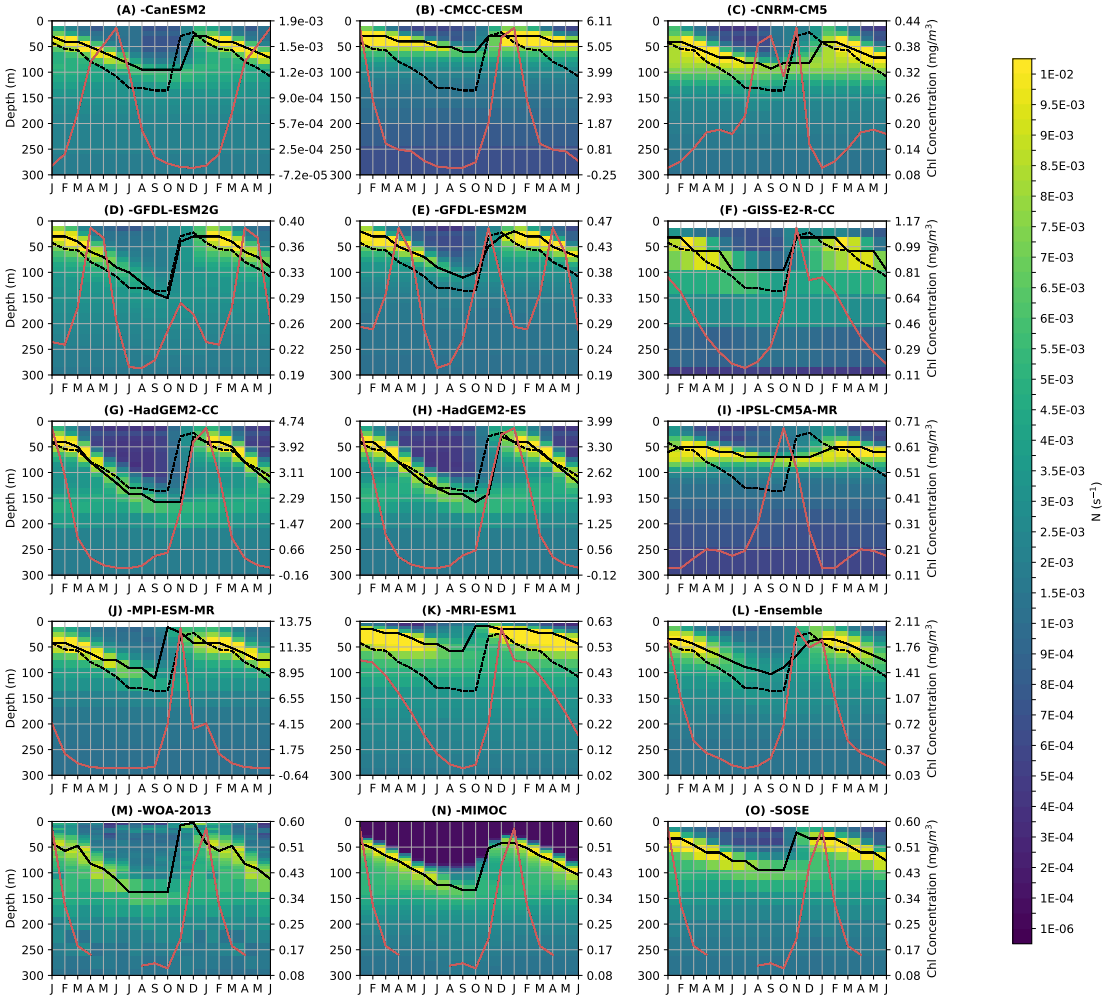

Figure 3.3: The seasonal cycle of the Brunt-Väisälä frequency (N) over the top 300 m of the water column in the study region (58 - 62 °S). Overlain in red is the average surface chlorophyll concentration in the same region, while the solid black line indicates the depth of the maximum frequency (stratification depth, ND) over this depth range. The dashed black line in each of the model panels is the average ND of the WOA-2013 and MIMOC products.

Figure 3.4B relates phenology to the latitude of the ice edge. The line length indicates the duration of the positive phase of the bloom (see Sec. 3.2.2) and the slope indicates whether it occurs during the ice retreat or advance. The simulated starting of the bloom in the study region has no evident relation with the latitudinal location of the ice edge. Further, the bloom generally starts and peaks when the sea ice is more poleward than observations, with the growth phase generally being longer than observed.

A significant linear relationship instead exists between the location of the ice-edge and ND in the study region across all models (Figure 3.4C), whereby the more equatorward the ice is found, the shallower ND is. The correlation is robust, with the ice-edge location accounting for 50% of variance in ND (with a confidence interval of roughly 6% around this). Significant correlations within each model domain further strengthen this link (coloured lines through each model cluster). Interestingly, the observations show the opposite relation, with more equatorward ice being associated with deeper stratification.

3.4 Discussion

This study has assessed CMIP5 models ability to simulate phytoplankton phenology in the Southern Ocean MIZ. We find that the later winter (July-September) presents the most significant biases in both phenology and vertical mixing, with models generally simulating early growth and shallow ND. While we largely show results from the region 58 to 62°S (Sec. 3.3.2), we also performed the same analysis in regions both north and south of this, the results of which are consistent with what has been shown here.

Figure 3.4A summarizes the key findings of this study and the grouping of models according to two major controls on their phenology in the study region. The first control simply refers to the modulation of light penetration by sea ice cover (Tedesco and Vichi, 2014), while the second is concerned with the nature of vertical stratification present in the late-winter water column. Hence, both controls are related to light availability in late winter and so affect the timing of phytoplankton growth. The first control is most strongly expressed by group 1 models, which have three important characteristics as shown in Figure 3.4A: pronounced biases in ND (stratification occurs too close to the surface), equatorward ice edge locations (higher average sea ice concentrations in the study region) and either small bloom initiation biases (CMCC-CESM and MRI-ESM1) or late growth (CanESM2). This is especially convincing of the role of ice cover, since we expect that in the absence of ice cover light conditions would favour early growth considering how strong stratification is in these models.

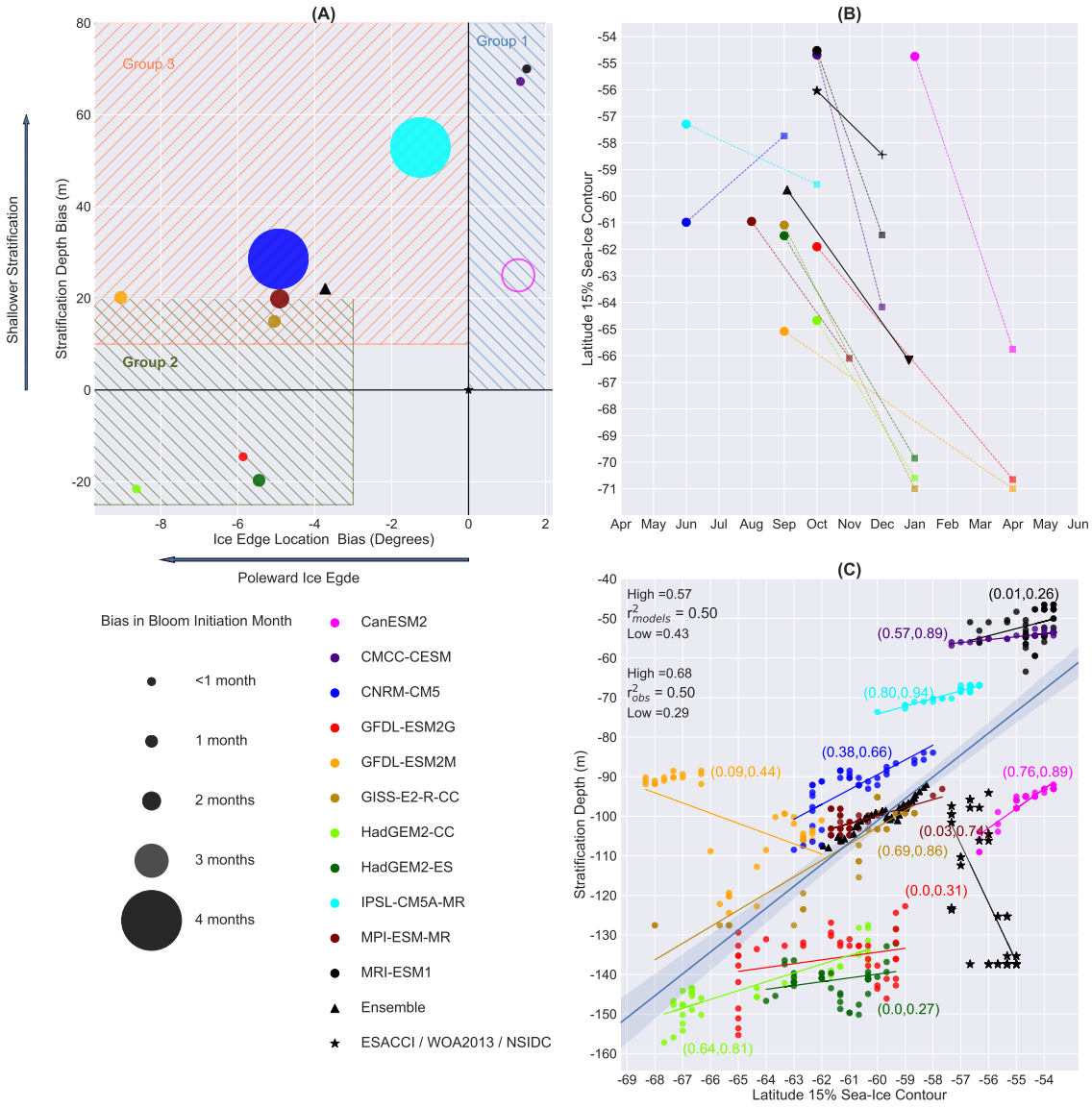

Figure 3.4: Property-property plots of the key variables in the study region (58 - 62 °S) in late winter (JAS). **(A):** Model bias in ND, ice edge location and bloom initiation month. The size of the markers is proportional to the bias in the bloom initiation month. The marker representing CanESM2 is unfilled to denote that the bias is positive i.e. the bloom occurs later than is observed. **(B) + (C):** Latitude of the ice edge versus **(B)** phytoplankton phenology diagnostics and **(C)** ND. **(B):** Circles represent the month of bloom initiation (see section 3.2.2), squares the month of maximum chlorophyll concentration (bloom peak). Similarly, the black star and upright triangle represent the bloom initiation for the observations and the ensemble, respectively, while the black cross and reversed triangle represent the bloom peak for the observations and the ensemble. **(C):** Relation between ND and ice edge location within and across the model ensemble. Overlain in blue is the linear regression with the 95% confidence intervals for 1000 bootstrapped resamples shaded in light blue. Printed in the top left is the percentage of variance explained by the regression (r^2), as well as the high and low confidence intervals shown by the shading. Each data point shown represents a different degree of longitude (40 in total) for each model as well as the ensemble means and observations (excluded from the regression). 2-tuples next to each model cluster are high and low confidence levels for r^2.

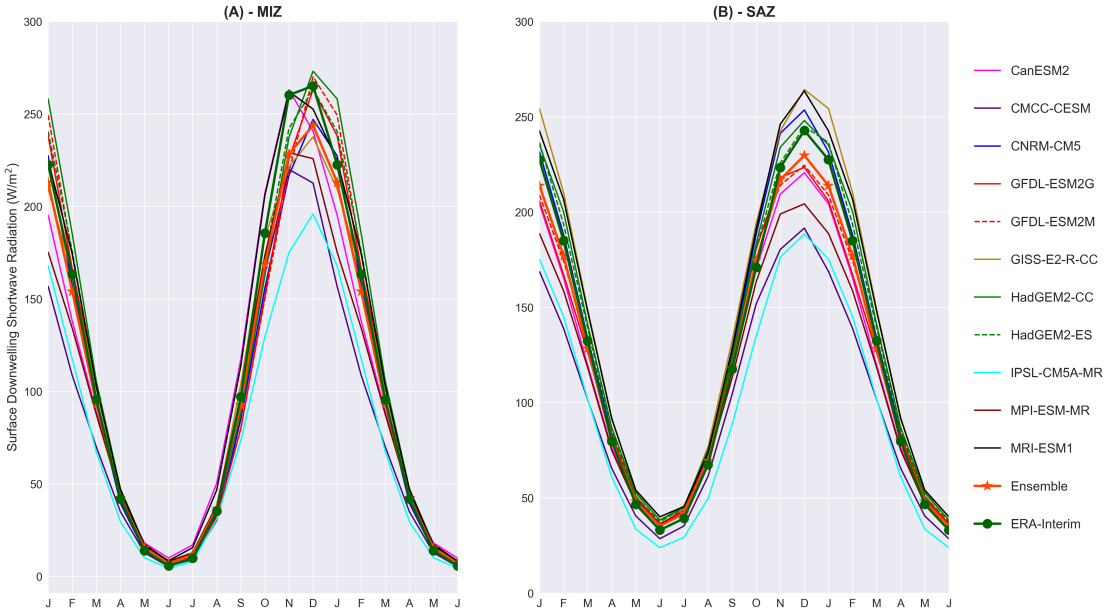

Figure 3.5: Climatology of surface downwelling shortwave radiation averaged over the study region (MIZ, 58 - 62°S) and the Subantarctic Zone (SAZ, 46 - 48°S) for 11 CMIP5 models and the ERA-Interim reanalysis product.

The second major control on phenology is exemplified by group 2 models, which are characterized by low average sea ice concentrations in the study region (poleward ice edge location). At the same time, these models are also the most well mixed in the surface layer (deep ND values) and have small bloom initiation biases. We would argue that this provides strong evidence that poor light conditions, this time related to deep winter mixing, delay the onset of growth in these models. Bloom initiation in group 2 models is then controlled by the onset of spring stratification, coupled with increasing daylight hours, a situation more typical of an open ocean environment such as the Subantarctic. This distinction between the mechanisms regulating light in the surface ocean (deep mixing versus ice cover) is then what separates groups 1 and 2. Interestingly, this seems to lead both groups to simulate later growth closer to observations, even though they have completely different ice and mixing regimes.

This is in contrast to group 3 models, which generally have large bloom initiation biases. We hypothesize that this results from the simultaneous expression of both controls, that is, significant biases in both the amount of sea ice coverage (i.e poleward biases in ice edge location) and in stratification (stronger and shallower stratification than is observed). In this way, highly favourable light conditions are sustained through the winter since mixing is suppressed and ice cover is limited. In summary, group 1 and 2 models have their bloom initiation brought close to observations (delayed) by limiting light, while group 3 models have neither deep enough mixing nor sufficient

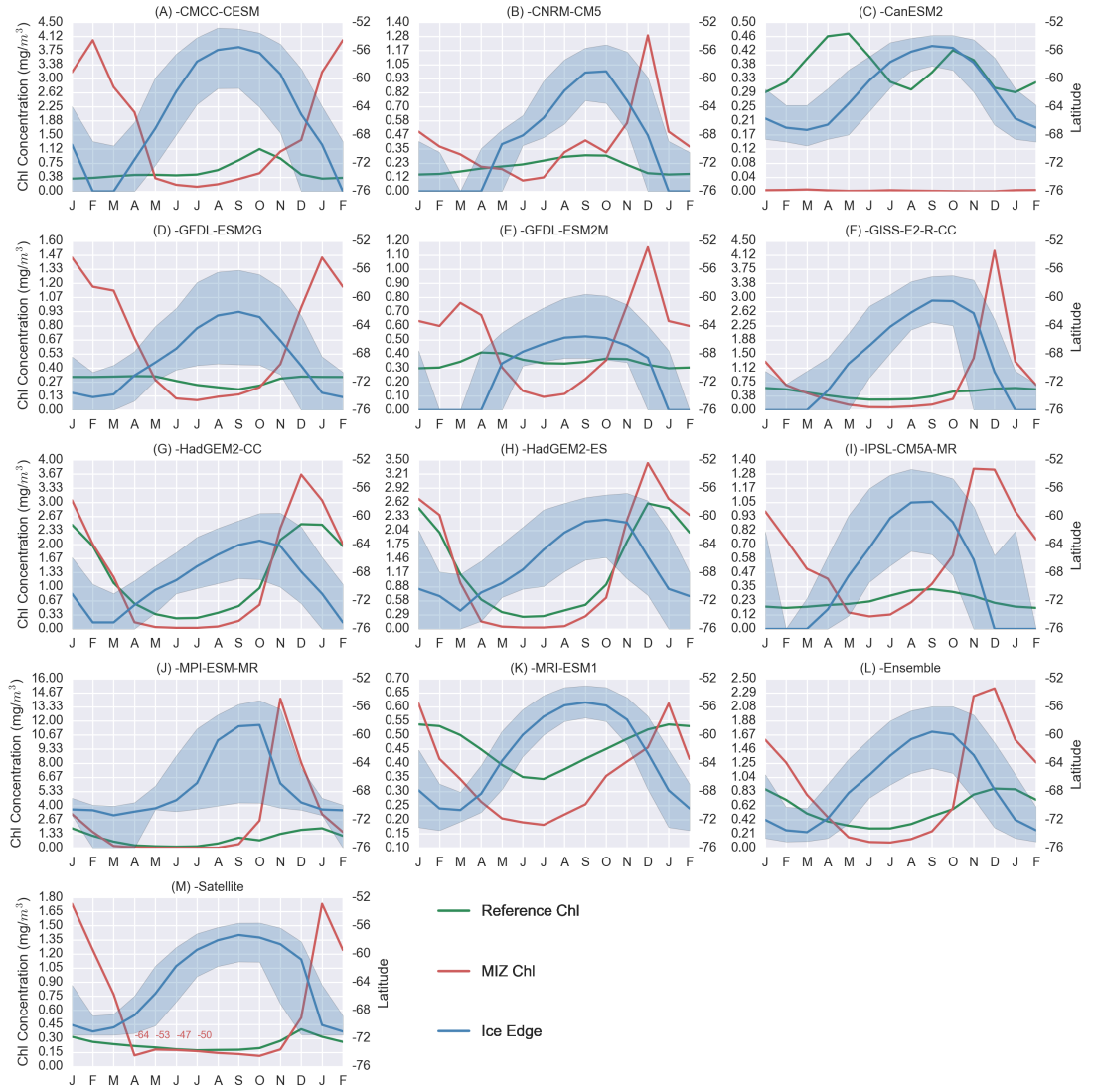

Figure 3.6: Seasonal cycle of the marginal ice zone (MIZ) in the Atlantic sector of the Southern Ocean for 11 CMIP5 models and satellite data. The blue line is the average latitude of the 15% sea ice concentration contour, while the shading around this line gives an indication of the region cover by marginal ice. The top (northern-most) edge of the shading delineates the transition from open ocean to very low ice cover (0% contour), while the bottom edge is the southern-most extent of the marginal ice zone (80% contour).The region between the thick blue line and the bottom edge of the shading can then be said to represent the MIZ under our definition. Overlain in red is the surface chlorophyll-a concentration following the MIZ, that is, for each month the average concentration is taken over grid cells which have a sea ice concentration between 80% and 15%. This means that in each month a different region is selected, as opposed to the green line where concentrations are fixed to the region between 46 and 48°S, representing the Subantarctic Zone.

ice cover to prevent extremely early growth. In the case of CNRM-CM5 and IPSL-CM5A-MR which exhibit growth in exceptionally low light conditions (see Figure 3.2), over-parameterized light acclimation may also play a role. The fact that these models also have the same biogeochemical model is telling in this regard.

A final point regarding model groupings is the overlapping region between groups 2 and 3. Models in this region express both controls, but the ice edge location bias is much stronger than the stratification bias and so the phenology bias is reduced.

In a complementary analysis, we also considered the role biases in simulated downwelling short wave radiation may play in phenology shifts in late winter, but only found significant biases in the summer and autumn months (Figure 3.5). Furthermore, the only models which have a slight ($\sim$20 W/m^2) positive bias in winter (CanESM2 and MRI-ESM1) both do not simulate early growth, supporting our hypothesis that sea ice inhibits growth during this period. Even more interesting is IPSL-CM5A-MR, which is the only model with a large negative bias in surface radiation in late winter/ early spring, and yet is still able to sustain growth and bloom far earlier than observations. This again points to a role for the parametrisation of light acclimation in accounting for some model biases.

Moreover, an analysis of phenology following the seasonal MIZ (as opposed to selecting a region as we have done here) reveals that even in models where the MIZ is much more poleward than is observed (as in GFDL and HadGEM2 models), growth can still occur in late winter even though satellite chlorophyll is actually decreasing during this period (Figure 3.6). This supports not only the idea of over-acclimation in models, but also that sub-surface light availability as mediated by sea ice cover and vertical mixing is systematically misrepresented within the MIZ.

While the discussion so far has focussed on phenology biases, the strong correlation between the ice edge location and stratification shown in Figure 3.4C warrants an explanation. It is important to stress however, that our conclusions regarding phenology do not rest on an explicit demonstration of the role sea ice plays in altering the vertical structure. Nevertheless, one plausible explanation for the correlation is that models with equatorward sea ice also simulate an equatorward westerly jet, resulting in lower average wind speeds over the study region, less momentum flux and shallower stratification. Although we do find a significant correlation between the wind induced momentum flux and mixing in models (models with higher average zonal wind have deeper stratification - see Figure 3.7), the westerly jet location is correlated with neither ND nor the ice edge location (Figures 3.8). This suggests that variability between models in the location of the jet cannot account for variability in the ice edge location or ND.

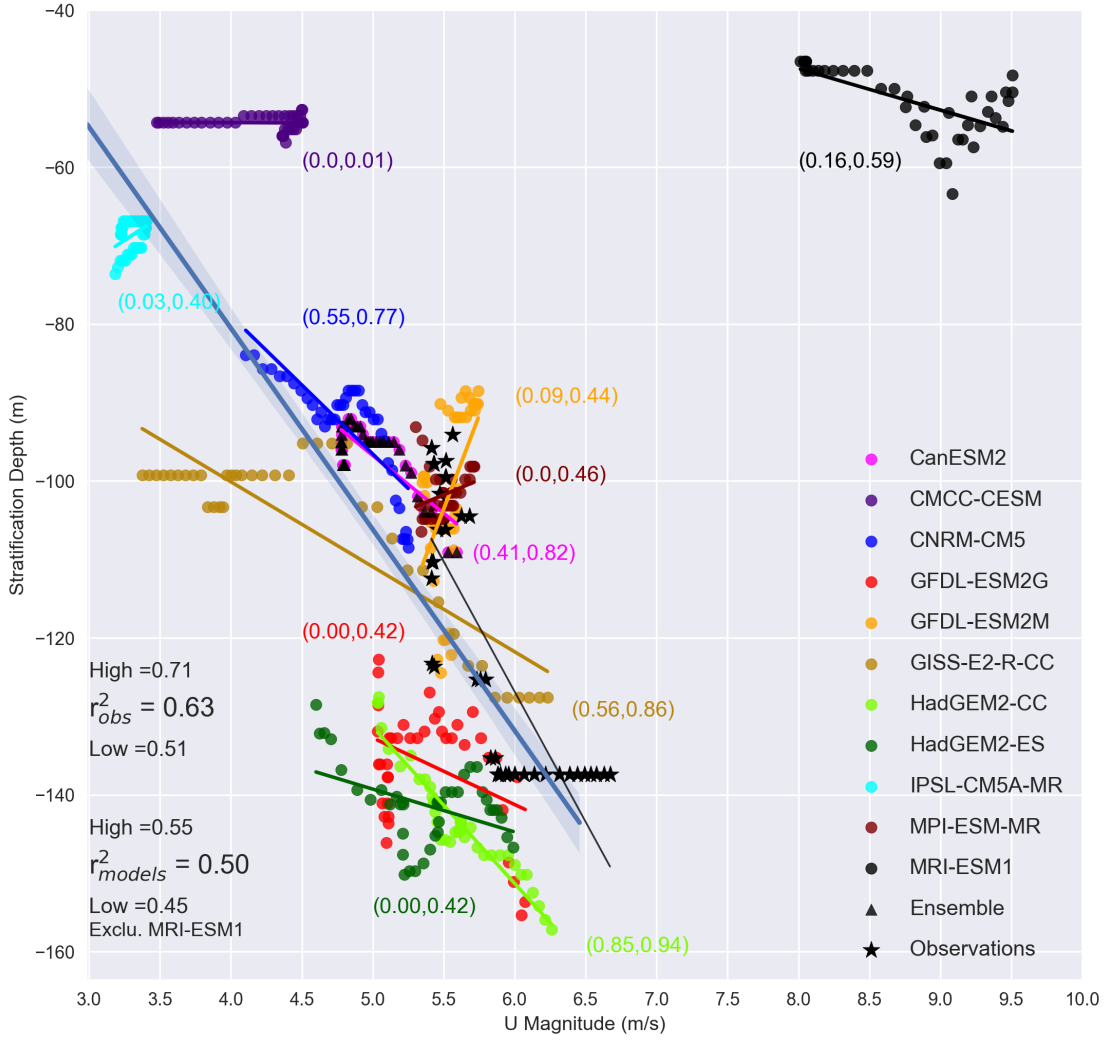

Figure 3.7: Zonal wind magnitude versus ND in the study region in JAS. Note that MRI-ESM1 is removed from the regression shown. The blue line surrounded by shading is the linear regression of the model super-ensemble, with the shading representing the 95% confidence intervals for 1000 bootstrapped resamples. Printed in the bottom left is the percentage of variance explained by the regression (r^2), as well as the high and low confidence intervals shown by the shading. Each data point shown represents a different degree of longitude (40 in total) for each model as well as the ensemble means and observations (excluded from the regression). 2-tuples next to each model cluster are high and low confidence levels for r^2).Observed sea ice concentration is the same as previous figures, while observed winds are taken from a blended product of Metop/ASCAT measurements which can be found at `ftp://ftp.ifremer.fr/ifremer/cersat/products/gridded/MWF/L3/ASCAT/Daily/` . Satelitte winds were downloaded at daily, 12km resolution, but averaged to give monthly means for this comparison.

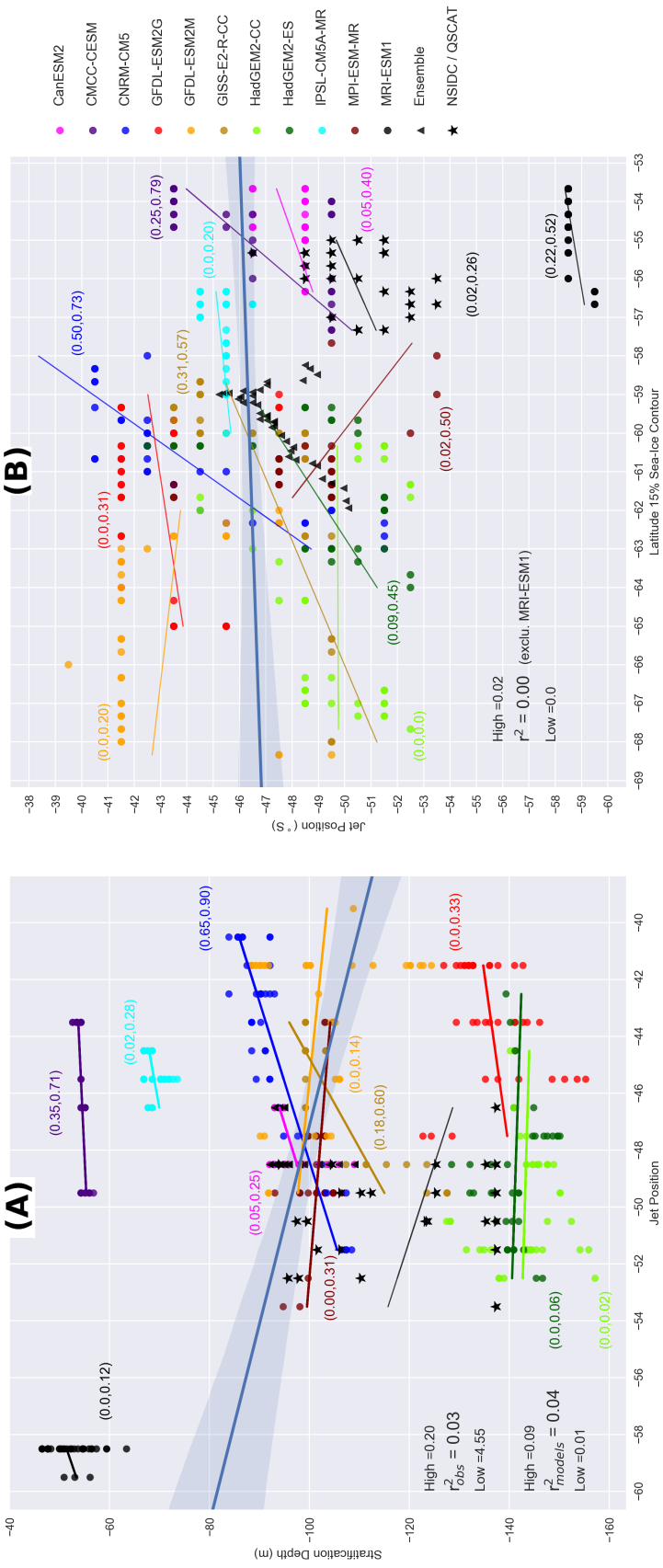

Figure 3.8: Climatological location of the westerly jet (defined as the latitude of maximum westerly wind magnitude) plotted against **(A)**: ND and **(B)**: the ice edge latitude for all models and satellite observations in the study region during late winter (JAS).

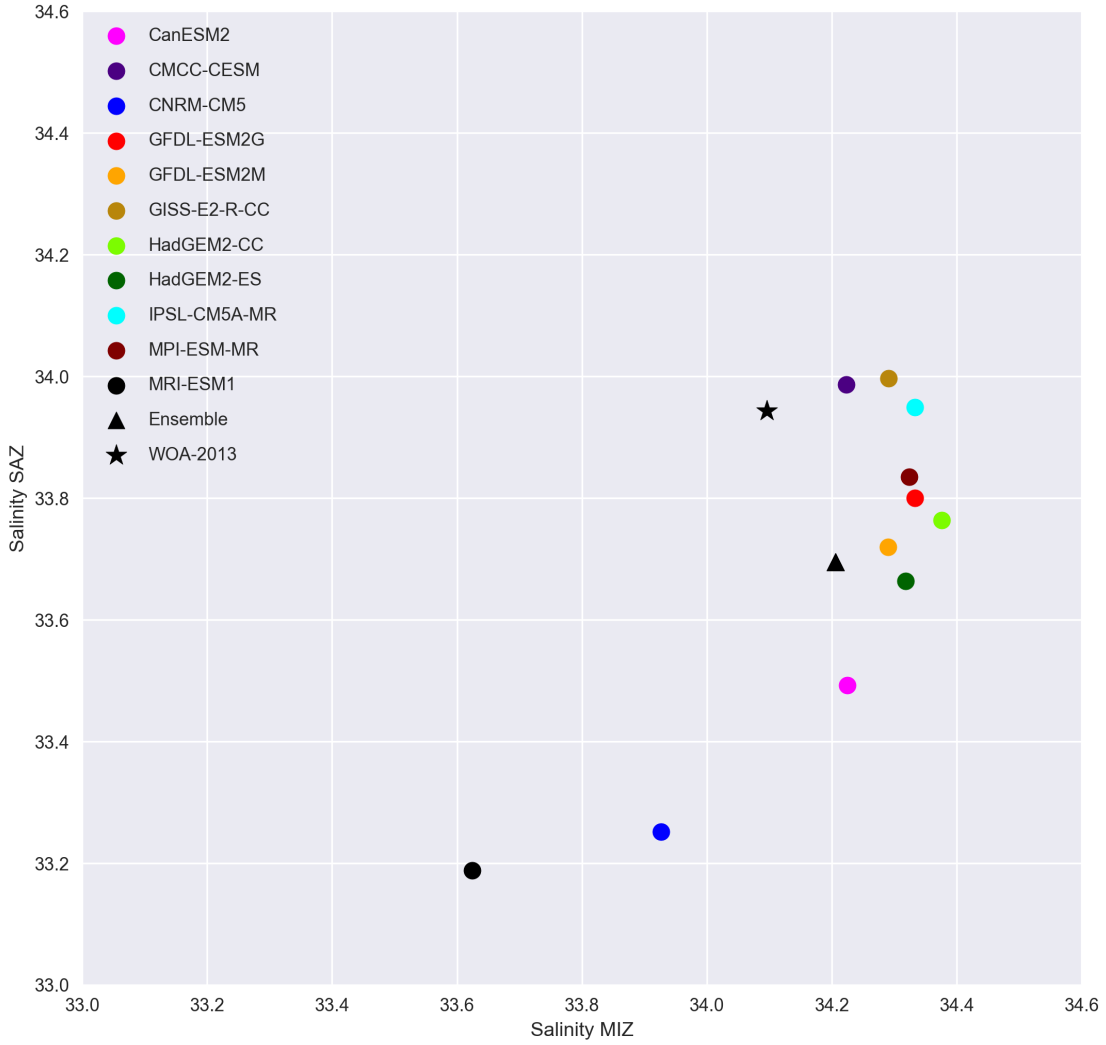

Figure 3.9: Average salinity in the MIZ versus in the SAZ for late winter. Note that the MIZ is defined dynamically as in Figure 3.6, that is, salinities are extracted from grid cells which have sea ice concentration between 15% and 80%.

The other possibility is that models with more sea ice tend to misrepresent surface buoyancy fluxes in the study region. We found that all models except CNRM-CM5 and MRI-ESM1 slightly overestimate salinity in late winter (Figure S6), suggesting that brine rejection is present, but does not enhance mixing enough to produce a vertical structure resembling observations. While mean salinity is underestimated in the Subantarctic Zone (SAZ), these findings imply that biases in the study region result from a combination of a lack of heat loss to the atmosphere, and lack of wind induced momentum transfer. Consequently, it appears that models with an equatorward ice edge, and hence more sea ice in the study region, dampen both the momentum and the long wave radiative fluxes such that stratification is enhanced. A striking example of this is seen in MRI-ESM1, which overestimates zonal wind speeds by roughly 4.5 m/s (Figure 3.7), but nevertheless has the strongest stratification bias in our ensemble (Figure 3.4A). On the other hand, in models with a poleward ice edge and very little sea ice, the surface ocean is exposed to both these fluxes, resulting in higher rates of heat loss and momentum transfer, and therefore deeper ND values.

In connection with this is the fact that the presence of sea ice may enhance the roughness of the sea surface (Hiraike and Ikeda, 2009; Elvidge et al., 2016), thereby increasing the momentum exchange and degrading stratification. Crucially, the nature of such exchanges of momentum depend on both the sea ice concentration and the type of ice present (pack ice, pancake ice, ice thickness, leads etc.). Moreover, the type of ice may also alter surface heat fluxes, suggesting that models will also need to take this into account. Indeed, this provides the impetus for a more in-depth exploration of sea ice mediated fluxes in Chapter 4. Since CMIP5 models have only relatively simplistic representations of sea ice Roach et al. (2018b) which do not encompass the variety of sea ice features found in the Southern Ocean, we expect that this will limit their ability to simulate mixing in the region strongly affected by sea ice. This is indeed hinted at in Figure 3.4C, where equatorward ice edge locations are associated with deeper stratification in the observations (black stars). The fact that models display the opposite relation further supports the idea that both momentum and heat fluxes are artificially suppressed by sea ice in the Southern Ocean, making this connection an interesting topic for further investigation.

In contrast to the situation in the study region (where the observed MIZ is found), the SAZ is characterized by significant fresh biases in the majority of models (8 out the 11 models - Figure 3.9). Sallée et al. (2013a) discuss the sources of this fresh bias in detail, concluding that it is mainly associated with air-sea and Ekman buoyancy fluxes which tend to overly stratify the water column and prevent deep convection. In Figure 3.10 we show how models tend to overestimate the northward propagation of salinity anomalies

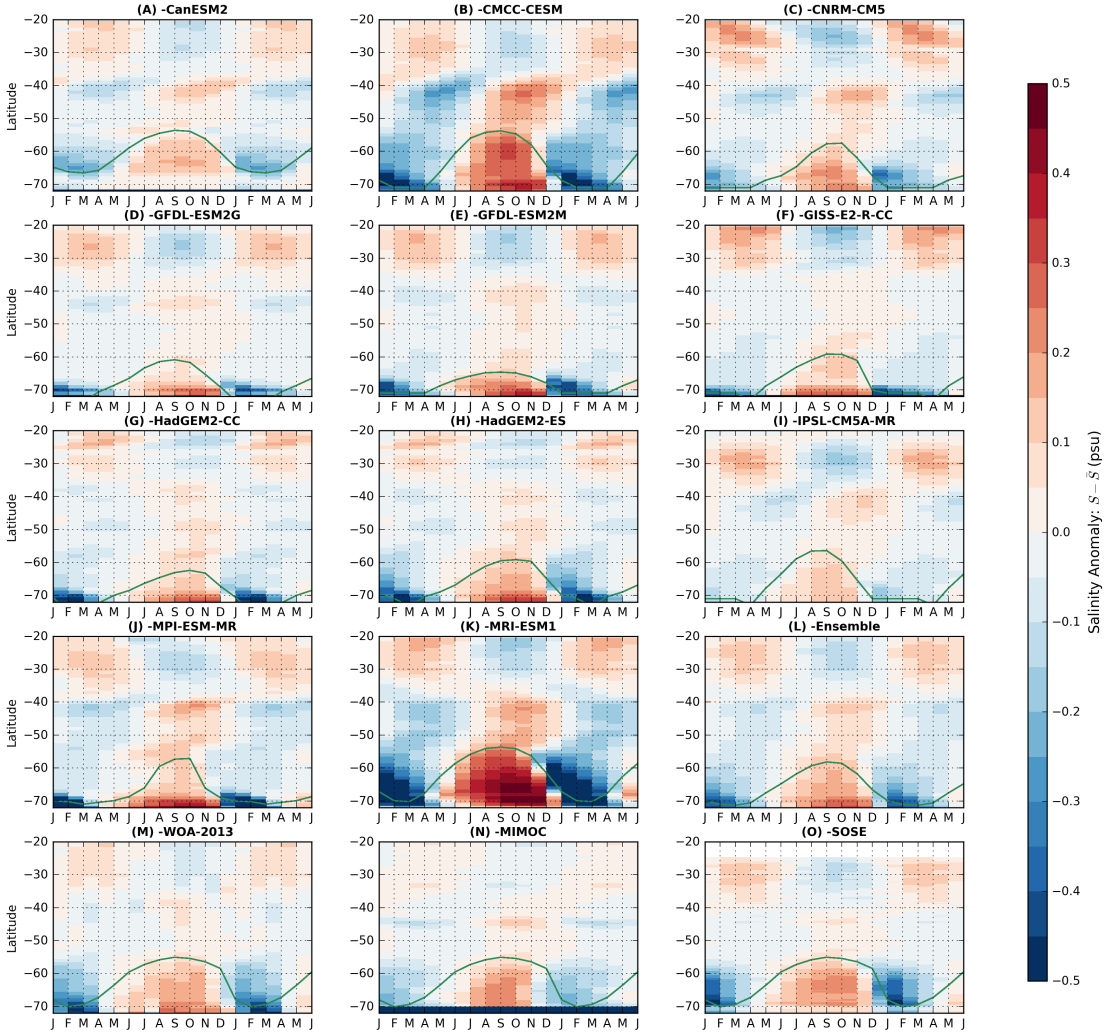

Figure 3.10: Zonally averaged (from 20°W to 20°E) surface salinity anomalies (with respect to the annual mean) plotted as a function of time for all models **(A - K)**, the ensemble mean **(L)** and 3 observationally based products **(M - O)**. Anomalies are shown for the region from the Antarctic coast to 20°S. The green line in all figures is the location of the ice edge, as defined previously. Note that the ice edge for SOSE is the same as for WOA-2013 and MIMOC.

originating from the sea ice, which would contribute to the Ekman component of this buoyancy flux. We leave detailed considerations of the role of sea ice in stratification in the SAZ for further analysis, although a preliminary analysis of the possible drivers is presented in Chapter 4. However, we would note that shallow stratification biases in the SAZ (as shown in Figures 3.11 and 3.12) have a similar effect on phenology as they do in the MIZ, largely resulting in early growth in autumn and winter (see Figure 3.2). These phenology biases may have major implications for future climate change projections, since phenology modulates the seasonal air-sea carbon flux in the Southern Ocean, which is known to be out of phase (Lenton et al., 2013; Anav et al., 2013; Mongwe et al., 2018). Furthermore, biases in both the timing and intensity of phytoplankton blooms would modulate surface dissolved inorganic carbon (DIC) concentrations and the suppression of vertical mixing models may underestimate entrainment of DIC rich deep waters.

3.5 Conclusions

In the real ocean, our results suggest that a combination of ice cover, deep winter mixing and associated light limitation prevent biomass accumulation until the late spring when melt waters introduce some stability and improve light conditions. This is in contrast to the results of Chapter 2, which showed earlier growth occurring in late winter. Nevertheless, none of the CMIP5 models assessed here reproduce both realistic sea ice and vertical mixing, and so the resulting phenology tends not to resemble observations. Further, this combination of physical forcings makes it difficult to investigate possible shortcomings within biogeochemical models, since one cannot be sure of the exact source of a particular bias. This highlights the importance of constraining the physical environment as much as possible, allowing us to further our understanding of the complex interactions characteristic of the MIZ and Southern Ocean as a whole.

3.A Additional Figures

Figures 3.11 and 3.12 depict the seasonal cycle of stratification in the 11 CMIP5 models analysed here, compared to observational estimates. The figures are the same as Figure 3.3, but provide a comparison to regions further north where seasonal sea ice is absent but may still influence the water column structure (i.e. the Polar Frontal and Subantarctic Zones).

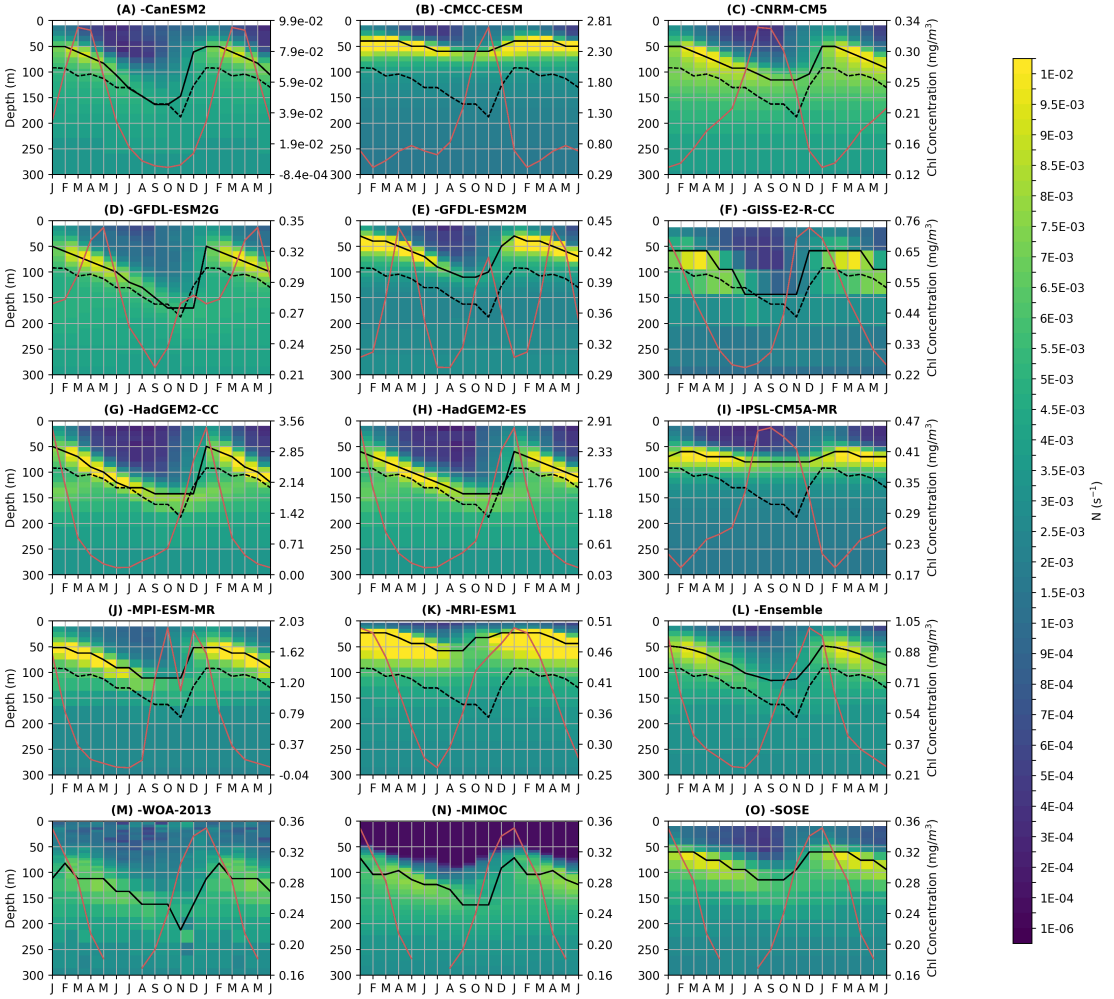

Figure 3.11: Seasonal cycle of the Brunt-Väisälä frequency (N) over the top 300 m of the water column in the Atlantic Polar Frontal Zone, 54 - 52°S for 11 CMIP5 models and observational estimates. All details of the figure are the same Figure 3.3

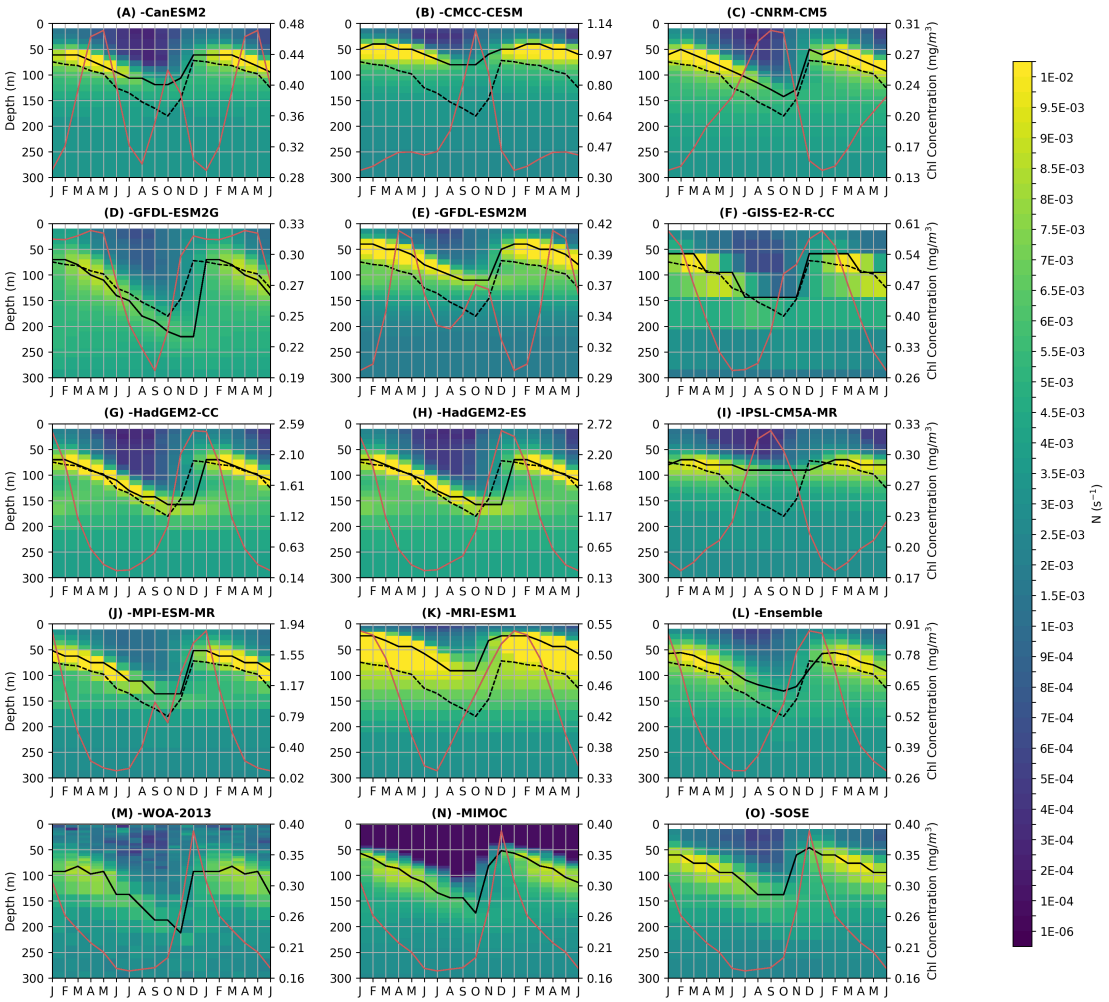

Figure 3.12: The same as Figure 3.11, but for the Subantarctic Zone, 48 - 46°S.

Chapter 4

Sea Ice Modulation of Heat and Momentum Fluxes: Mixed Layer Response in an Ice-Ocean Model

Abstract

In this Chapter a state of the art ocean-ice model was utilized to investigate the effect heat and momentum fluxes have on vertical mixing in the Southern Ocean SSIZ. Two sensitivity experiments were conducted, one aimed at heat exchanges in the SSIZ (HF experiment), the other at momentum transfer from atmosphere to ocean, via sea ice (MF experiment). For the HF experiment, ocean-atmosphere heat exchange in ice covered regions (where ice concentration > 0) was increased by 10%, while the MF experiment enhanced the momentum flux by increasing the air-ice drag coefficient by $\sim$50%. In both cases the sensitivity of the winter under ice mixed layer to the imposed perturbation is investigated through comparison to a reference experiment (REF). In general, the model was more sensitive to the HF perturbation, which was associated with a northward expansion of the winter ice cover. This was driven by reduced ice thickness in the retreat phase, thus leading to a more mobile ice pack during the advance phase. The ice cover expansion led to increased freshwater transport into the outer SSIZ (58 - 55°S), thus enhancing stratification. In contrast, further south in the study region (62 - 58°S) the increase in heat loss caused increased ice production, thereby eroding stratification through brine rejection. The model response to the MF perturbation was more spatially variable, which was linked to the underlying vertical structure of the water column. Regions of deeper vertical mixing in the REF experiment (linked to higher ice formation

rates) tended to entrain warm CDW waters into the mixed layer under MF. This leads to a negative feedback, whereby the enhanced turbulence (arising from the increased momentum exchange) deepens vertical mixing, which leads to warm water entrainment and bottom melting of sea ice, thus enhancing stratification. Conversely, in regions where the mixed layer is relatively shallow, warm water entrainment is limited or absent, and so the MF perturbation deepens the stratification depth. These results highlight the importance of the specificities of the Antarctic sea ice in controlling vertical mixing.

4.1 Introduction

Sea ice plays a critical role in the seasonal variability of vertical mixing in the surface ocean. Formation and melting processes are the dominant drivers of surface ocean salinity in the high latitude Southern Ocean (Haumann et al., 2016; Pellichero et al., 2016). Since density changes in the polar oceans are primarily salinity driven (see section 1.2.3), formation and melting of sea ice is also the dominant driver of seasonal changes in vertical mixing. Sea ice also acts as an intermediary between ocean and atmosphere, thereby modulating fluxes of heat and momentum, as well as other climatically important molecules such as CO_2 (Vancoppenolle et al., 2013; Maksym et al., 2012). However, the mechanisms by which this modulation occurs, as well as quantification of its effect on mixing, have remained elusive due in large part to a lack of observations (Swart et al., 2019). This has led to a relatively poor representation in the Southern Ocean of both vertical mixing and sea ice in climate models, as was discussed at length in Chapter 3. It was suggested in section 3.4 that the location of the winter ice edge may be linked to the pronounced stratification seen in some models, with the presence of ice overly damping atmospheric exchange. In Chapter 2 we also presented evidence for enhanced light availability near-complete ice cover in winter, this time employing under ice float data which showed earlier than expected phytoplankton growth.

Therefore, the results presented thus far suggest that sea ice is more permeable to both heat and momentum fluxes than previously thought (particularly in winter). Further evidence for this suggestion is found in the literature, although heat and momentum fluxes are generally dealt with separately. With regards to heat exchanges in the SSIZ, Matsumura and Ohshima (2015) have shown that climate models likely underestimate this quantity since they do not take into account frazil ice, which does not substantially affect ocean-atmosphere heat flux. In line with this, Maksym et al. (2012) (and citations therein) reports that between 20% and 60% of Southern Ocean sea ice may be composed

of frazil based on ice core data. Ship-based observations also confirm the relatively high abundance of this ice type (Lange and Eicken, 1991; Alberello et al., 2019; Vichi et al., 2019). Notably, this ice type is not distinguished from others in current satellite algorithms, as has been done in the Arctic (Ye et al., 2016), which leads to a bias towards a more consolidated ice field.

Furthermore, a substantial oceanic heat flux (typically 15 - 35 Wm^2) driven by upwelling of warm and salty CDW tends to prevent vertical growth, leading to thinner ice cover and enhanced heat loss to the atmosphere (Maksym et al., 2012). The upwelling of CDW may also lead to the accumulation of salt in the surface layer (the excess heat is generally lost to the atmosphere), thereby further eroding the stability of the winter water column (Gordon and Huber, 1984, 1990). Conversely, diffusive and entrainment heat fluxes into the mixed layer tend to enhance stability by sharpening the thermal gradient (Martinson, 1990a,b). Indeed, there exists a negative feedback associated with sea ice formation and vertical mixing in the Southern Ocean. Formation leads to brine rejection, which tends to enhance mixing and the entrainment of heat, which then dampens further ice growth by reducing the net heat loss to the atmosphere (Martinson, 1990a,b). It is therefore the balance between this oceanic heat gain and atmospheric heat loss which ultimately determines whether there is net ice growth, with attendant consequences on the mixed layer evolution.

In a large scale modelling context, the importance of sea ice mediated heat, momentum and salt fluxes for vertical mixing was already highlighted some 20 years ago by Goosse and Fichefet (1999). Indeed, several idealized experiments similar to those performed in this study were conducted in a coupled ice-ocean global model. One such experiment removed the salt flux associated with ice formation and melting, which had the effect of completely suppressing convective mixing in some regions of the Southern Ocean. Another set of experiments significantly lowered the ocean-ice heat exchange, which increased the annual mean ice area in the Antarctic by more than 20%, but had a much weaker effect on the Arctic ice area (13% increase in one experiment, 2% in another). These results again underscore the importance of the oceanic heat flux and its interaction with sea ice in Antarctic waters.

Evidence for enhanced momentum flux in ice covered regions comes mainly in the form of increased air-ice aerodynamic drag. This drag ultimately induces ice motion, which then generates drag between the ice and underlying ocean, enhancing turbulence and mixing. The effect of drag on the overall stress is typically parametrized by the drag coefficient, C_d (see section 1.2.3). However, there is little consensus on a representative value for air-ice C_d in the Southern Ocean, with values based on in-situ measurements

ranging from 0.9x10^{-3} to 8.5x10^{-3} under different conditions (Bing et al., 2013). Global coupled climate models tend to use a single value for C_d between 1x10^{-3} and 1.5x10^{-3}, although this is based almost entirely on studies of Arctic ice conditions. A key point which is often missed though is that momentum is only effectively transferred from atmosphere to ocean if ice is free to drift over large distances. This point was highlighted by Hiraike and Ikeda (2009), who argued that momentum exchange would be locally maximised in the MIZ where partial ice coverage guarantees free drift. Given the thin and highly unconsolidated nature of Antarctic sea ice, as well as the intense wind field, free drift over vast distances is a common phenomenon (Holland and Kwok, 2012; Kimura, 2004; Uotila et al., 2000). Thus, we can expect momentum exchange to be underestimated by current climate models, which utilize a constant value for C_d, as well as largely underestimate wind speeds over ice (Elvidge et al., 2016; Mahlstein et al., 2013).

4.1.1 Aims and Questions

In this chapter we will more closely examine the role sea ice plays in regulating vertical mixing in the Southern Ocean SSIZ. In particular, we will investigate the effect enhancing heat and momentum fluxes associated with sea ice has on vertical mixing. We will attempt to address the following key scientific questions using a coupled ice-ocean numerical model in line with the research objectives outlined in section 1.4.1:

1. How sensitive is the mixed layer depth to changes in heat and momentum flux in the SSIZ, and do each contribute equally?
2. Are there different responses in different sea ice zones? i.e partially vs. more fully covered regions
3. Can small increases in these fluxes reduce model shallow bias in vertical mixing?

4.2 Data and Methods

4.2.1 Data

The atmospheric forcing fields are taken from the European Centre for Medium-Range Weather Forecasts (ECMWF) Era-Interim Reanalysis product, downloaded at 0.75^o horizontal resolution (see section 4.2.2 for temporal resolution of various fields). For

both the initial and boundary conditions the GLobal Ocean ReanalYSis (GLORYS2V4) product was used, which were made available on the original model grid (exactly matching the grid used in this model) by Mercator Ocean upon request. This reanalysis is also forced with Era-Interim data, allowing for consistency when comparing model results to this data set. The model results are also compared to World Ocean Atlas 2018 (WOA2018) temperature and salinity (used to derive ND), as well as satellite sea ice concentration from NOAA/NSICD Climate Data Record (version 3; see 2.2.3 for more details). WOA data are also assimilated into the Era-Interim reanalysis product.

4.2.2 Model Description

In this Chapter we perform numerical model experiments using the Nucleus for European Modelling of the Ocean (NEMO) platform, in particular the ocean (Océan Parallélisé - OPA) and sea ice (Louvain-la-neuve sea Ice Model - LIM3) components. The model domain roughly covers the Atlantic sector of the Southern Ocean, spanning from the Drake Passage (70°W) to the eastern edge of the Weddell Gyre (20°E), and from the Antarctic coast to 40°S (see Figure 4.1). The model grid is part of the ORCA family of global tripolar grids (Madec and team, 2016), of which a portion has been selected at $1/4^o$ resolution (i.e. the ORCA025 grid - see Bernard et al. (2006)). In the vertical the model has 75 depth levels implemented using z-coordinates, with the resolution increasing with decreasing depth to $\sim$1 m in the top 10 m.

In terms of forcing, the model uses an offline atmosphere, with the major fluxes at the ocean-ice-atmosphere interface determined by the CORE bulk formulae (Large and Yeager, 2004). Winds, 2m air temperature and humidity are provided at 6-hourly intervals, precipitation at 12-hourly, and short and longwave radiative fluxes at daily intervals (see section 4.2.1 for data sources). Both the air-ice and water-ice stresses are determined using the same quadratic formula shown in equation 1.2.3, but with different values for drag coefficients and fluid densities (see 4.2.3 below). Although the model does include heat fluxes from ice to ocean, the overall heat exchange between atmosphere and ocean in ice covered regions is dominated by air-water fluxes in leads (except when ice formation or melting is occurring; Lytle and Ackley (1996); Vancoppenolle et al. (2009); Eayrs et al. (2019)).

While an in-depth description of LIM3 is beyond the scope of this thesis (see Vancoppenolle et al. (2012)), some salient features may be highlighted here. Most importantly, the model takes into account both dynamic (advection, ridging, rafting, internal stresses and strains) and thermodynamic (vertical diffusion of heat, snow/ice

formation and decay, new ice formation in open water, brine drainage and ice ageing) processes. Five thickness categories are included, each with their own set of state variables, as well as two ice and one snow layer, allowing for a representation of subgrid-scale variability. Sea ice rheology is represented by an elastic-viscous-plastic (EVP) material following Hunke and Dukowicz (1997), where ice flow has a visco-plastic behaviour at the time scale of wind forcing, but uses damped elastic waves at shorter time scales.

The model has a semi-realistic setup with two open lateral boundaries at the Drake Passage and along the eastern boundary, with the northern boundary closed. Given the dominance of the zonal flow of the ACC at the seasonal time scale of the model experiments, it is unlikely that an open northern boundary would significantly affect the results presented here. At the open boundaries the model temperature and salinity are relaxed to the prescribed value over a 10 grid point region (adjacent to the boundary) following the Flow Relaxation Scheme (FRS - see Madec and team (2016) pp. 171). The barotropic velocities at the boundaries are defined by the Flather Radiation Scheme (Flather, 1994), and are computed based on monthly means of external SSH and velocity data (tracers are also at monthly resolution). The monthly averaging of lateral boundary data, coupled with the use of the FRS for tracer data, mitigates against the production of numerical instabilities associated with high frequency variability and strong spatial gradients common in the ACC. The model does not include baroclinic velocities from external data at the boundaries.

4.2.3 Experiment Design

As is suggested by the aims outlined in section 4.1.1 above, the model experiments presented here are designed to investigate the processes regulating vertical mixing under ice. The approach taken was to simulate only one year, focussing on the sea ice formation period given the results discussed in previous chapters. As such, model experiments where run for 10 months from January 1st to October 31st 2014, starting from realistic (reanalysis) tracer, SSH and velocity fields, as well as using reanalysis data at the open boundaries (see section 4.2.1). Reanalysis ice concentration, thickness and velocities where also used as initial conditions. This allowed for as much realism as possible, while still having dynamical ocean and sea ice components. That is, the model starts from reanalysis ocean and sea ice fields, is relaxed to these at the lateral boundaries, and is forced by an atmospheric reanalysis the surface boundary, thus providing realistic constraints to the dynamical components. The choice of 2014 is arbitrary in this case, since our aim was to have a realistic year prior to the sea ice

extent decline observed after 2014 (Parkinson, 2019). Model output is saved at 5-day frequency, which is displayed in all time series unless stated otherwise.

Once a fairly realistic reference simulation (REF experiment) had been conducted, two separate adjustments to the heat and momentum fluxes in ice covered regions where performed. In the case of heat fluxes, the concept of an "effective" Sea Ice Concentration (SIC) was employed, whereby the concentration value used in the flux calculation was reduced by 10% compared to the one computed by the model (HF experiment). This essentially means that we assume the ice cover to be slightly more permeable to heat fluxes than is presumed by the standard climate models. This is applied everywhere and at all times, which is certainly unrealistic when consolidated pack ice with a thick snow layer is present (in these cases we would not expect ice to be permeable to heat fluxes). However, this can be justified by the fact that the analysis is focussed on the outer band of sea ice in winter (i.e. the regions of interest shown in Figure 4.1) where sea ice is expected to be more permeable.

This increase in permeability with respect to heat exchanges is intended to encompass several specificities of the Antarctic sea ice that are currently unresolved in models and may result in heat exchange errors. This includes features such as ice-water mixtures found between floes (in particular between pancakes as shown in Figure 1.4A), which are known to have different thermodynamic properties (Smedsrud and Martin, 2015). In addition, the effects of waves propagating through sea ice are not currently resolved, which could enhance ice break-up and therefore increase heat exchange through lead opening (Kohout et al., 2014). This process is not taken into account in the current model formulations and at the scales typical of coarse resolution simulations. Climate models have also been shown to simulate too much highly compact ice (in the 90-100% concentration range) during the winter months which are of interest here (see Roach et al. (2018a), their Figure 5c and d).

The experiment is further motivated by the results of Chapter 3, which showed that models with higher sea ice concentrations (more in line with observations) tended to also have the strongest biases in vertical mixing (Figure 3.4C). This suggests that the presence of ice in later winter is overly damping heat exchange, thus inhibiting ice formation and brine rejection.

With regards to the momentum flux, an increase in air-ice drag coefficient from $1.4\text{x}10^{-3}$ to $2.0\text{x}10^{-3}$ ($\sim$50% increase) was implemented across the model domain and at all times (MF experiment). Again this is not realistic for all ice conditions, but a similar argument can be made that in the regions of interest (as well as in most of the domain when MIZ conditions are present) the dynamic and unconsolidated ice surface may

be expected to respond more readily to wind forcing. The value of $1.4\text{x}10^{-3}$ for C_d is the default one used for global ocean simulations in NEMO, and so represents a compromise between values observed in both hemispheres, as well as between differing ice conditions (e.g. MIZ vs pack ice). The asymmetry between the imposed flux changes in each sensitivity test (10% increase for heat, $\sim$50% for momentum) is also not meaningful, although is partially linked to the uncertainty of the two factors (e.g. Bing et al. (2013); Matsumura and Ohshima (2015)). The value of ice-water drag is much higher by default at $5.0\text{x}10^{-3}$, and is constant for all experiments.

Furthermore, since a primary goal of the model experiments is to test the sensitivity of the under ice mixed layer to changes in heat and momentum fluxes, the validity of the exact value chosen for C_d or the effective SIC is not as important as the model response to these imposed changes. That is, even though it may not be true that sea ice is at all times more permeable to heat fluxes or more responsive to wind stress (than is currently modelled), the important point is that based on the literature and results presented in previous chapters, we can expect this condition to occur over large portions of the SSIZ. With this in mind, the model experiments are then designed to address the question of what effect this will have on the winter mixed layer (and hence on phenology). A final experiment combining both fluxes is performed to asses the relative sensitivity of enhanced heat and momentum fluxes (TF experiment), giving a total of four model experiments (REF, HF, MF and TF).

4.2.4 Model Diagnostics

In this Chapter we will use various diagnostics to analyse the model experiments, including the ice edge location, stratification depth (ND) and ice-ocean shear. The first two of these diagnostics remain unchanged from previous chapters (see section 3.2.2 and 1.2.3), while the ice-ocean shear requires introduction here. Shear refers to the difference in velocity between the ice and the underlying ocean ($\mathbf{U}_{ocean} - \mathbf{U}_{ice}$), and is computed for both u and v components. The magnitude of the shear is then computed for the MF and REF experiments to give the difference map shown in Figure 4.13.

Much of the analysis is focussed on two regions of interest, the study region (SR), corresponding to the same region analysed in Chapter 3, and the winter (JAS) model MIZ, which refers to the region dominated by partial ice coverage during winter months in the model (see Figure 4.1). The SR is analysed for comparison to the results presented in Chapter 3, where as the model MIZ represented a region where in-situ ice growth is small compared to advection of ice into the area. This is in contrast

to the SR which has regions of strong ice formation, allowing for a comparison of different processes affecting the ML below sea ice (these are discussed below in sections 4.3). The positioning of the two regions also allows for a comparison of latitudinal differences in atmospheric fluxes. Other diagnostics include sea ice concentration, volume and freshwater flux, all of which are computed online by LIM3 and documented in Vancoppenolle et al. (2012).

4.3 Results and Discussion

The results presented here are split into four sections covering different model experiments. Much of the focus is on two of these, where heat (HF experiment- section 4.3.2) and momentum (MF experiment - section 4.3.3) fluxes where enhanced over the region covered by sea ice. However, discussion of the results obtained from these experiments is preceded by a brief treatment of the reference run sea ice representation (section 4.3.1), and is followed by discussion of the final experiment combining both heat and momentum flux enhancements (TF experiment - section 4.3.4). The structure of this chapter differs slightly from the previous two in that the presentation of results for each experiment is accompanied by a discussion of their significance and interpretation of mechanisms explaining the response of the model. This is done for practical reasons, since separating the presentation of the results from the interpretation would lead to a fairly disjointed analysis. At the end, insights from all the experiments are brought together in section 4.4.

4.3.1 Reference Run Sea Ice Representation

In Figure 4.1A the mean winter (JAS) distribution of sea ice concentration (SIC) is shown for the REF experiment, with 2 regions of interest highlighted by red boxes. These regions correspond to the study region (SR) discussed in Chapter 3 (solid box) and the model winter MIZ (dashed box - 58 - 55°S). Immediately evident are the differing sea ice regimes in the two regions: in the SR, winter conditions can be thought of as pack ice, with concentrations consistently over 90%, where as in the MIZ region contains a range of concentrations from 0 to over 90%. Also striking is how concentrated the pack is south of $\sim$60°S, with concentrations uniformly over 90% (time series of SIC, not shown, for a range of grid points reveals that concentrations increase rapidly in the advance phase, then vary between 90 and 100% for the winter period). Analysis of satellite data for the same period reveals the same pattern (see Figure 4.1B),

suggesting that the model is performing well (when compared to many of the CMIP5 models discussed in Chapter 3). Some model discrepancies are evident though, such as the overestimation of ice cover in the SR (overestimation of ice in the 90-100% concentration range), as well as the polynya-like feature at the eastern boundary. This is likely caused by the location of the boundary at the edge of the Weddell Gyre. The model also overestimates ice concentration in the MIZ (especially in the southern portion of the MIZ - see Figure 4.1), although these biases are small compared to the CMIP5 model biases. Our study region is located against the boundary in order to be consistent with the analysis in the previous chapter. In the case of the CMIP5 models, the SR corresponded to roughly the multi-model ensemble MIZ between July and September (JAS), in contrast to the much higher average concentrations seen during the same period in Figure 4.1.

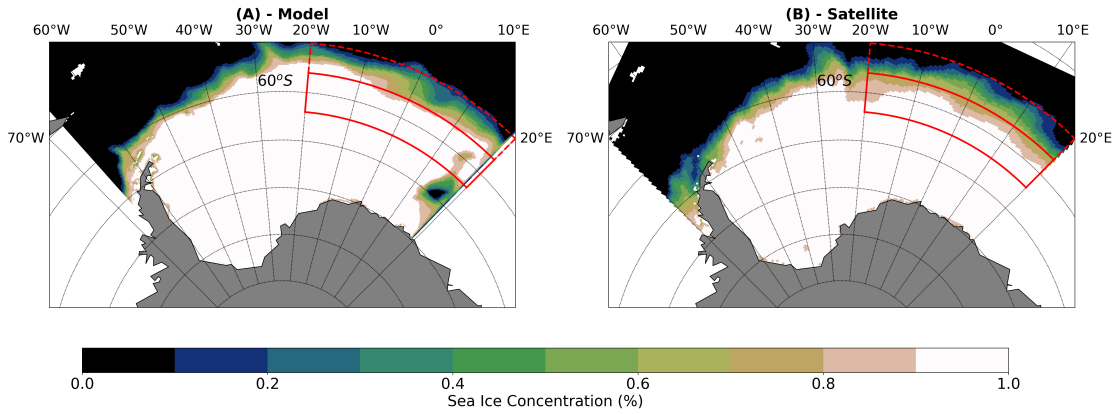

Figure 4.1: Sea ice concentration for **(A)** REF run and **(B)** satellite data, averaged over July to September. The solid red box denotes the study region, while the dashed box is the region defined as the MIZ in the model.

Furthermore, Figure 4.2 reveals that the seasonal evolution of the ice edge location is also well captured by the model when compared to satellite estimates and the original reanalysis field. Also shown in the figure by the shaded regions is the zonal variability of the ice edge within the SR, which gives a sense of the east-west asymmetry in ice advance. Here we see the model also performs fairly well, although there are some notable differences when compared to the reanalysis during February/March when the model has greater variability, and during June/July when the reanalysis produces a slow down (and even retreat) of the ice advance in some places. This retreat is not seen in the mean location of the ice edge (bold dark brown line), but rather in the bottom edge of the shaded region of Figure 4.2, which indicates that the retreat only took place in some regions of the SR. This feature is not seen in satellite observations (see Figure 4.23), so the model actually performs better than the reanalysis in this case.

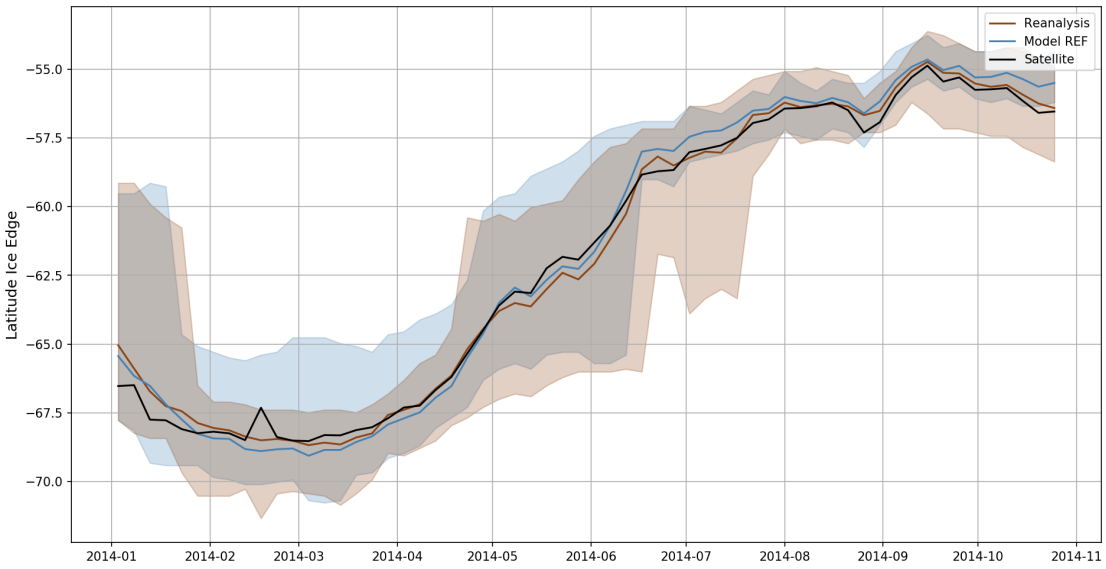

Figure 4.2: Mean location over the study region of the ice edge (15% concentration contour) for REF run (blue), Reanalysis (red), and satellite data (black). Shaded regions denote the zonal variability of within the study region (20°E to 20°W).

In Figure 4.3 we show the mean winter sea ice thickness spatial distribution, with the ice circulation patterns overlain. In general, the ice circulation matches that shown in Figure 1.3 (which is based on satellite observations), with western sector of the model domain displaying equatorward ice transport, which then shifts to strongly eastward as ice encounters the ACC and westerly wind belt to the north. The figure also shows a general correlation between thinner ice and faster velocities, with the ice field becoming more mobile as one moves north and east in the model domain. Such a pattern is also clear in Figure 1.3, as well as in other works investigating Antarctic sea ice circulation (Holland and Kwok, 2012).

An important point to make here is that although it could be said that the model reproduces the observed seasonality well, this does not necessarily imply that ocean-atmosphere fluxes in the SSIZ will be well represented (with important consequences for the ML). Indeed, a major aim of this chapter is to verify the hypothesis that even with the seasonal evolution of the ice cover well constrained (at least to a far greater degree than in the ESMs discussed in Chapter 3), one still tends to underestimate the winter MLD under ice. We now move on to a discussion of the potential role played by heat fluxes through ice cover.

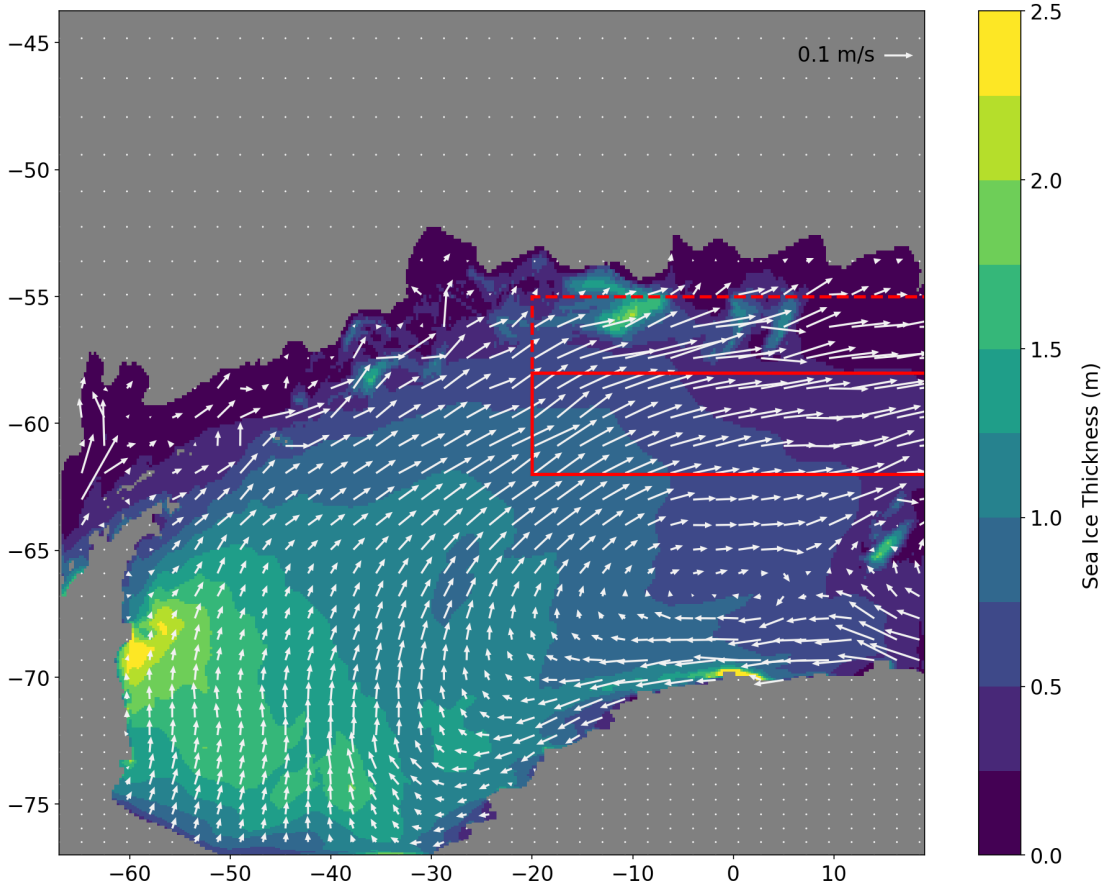

Figure 4.3: Mean winter (July - September) sea ice thickness for the REF experiment, with sea ice velocity vectors overlain. As in Figure 4.1, the regions of interest are shown by red boxes.

4.3.2 Heat Flux Experiment

In this experiment, the concept of an effective sea ice concentration was utilized to allow an increase of 10% in surface heat fluxes across the SSIZ (refer to section 4.2 for more details). It should be emphasized that the increased heat loss imposed in this model experiment is motivated by the ubiquity of frazil ice in the Southern Ocean, which does not substantially alter the ocean-atmosphere heat exchange. Thus, when we refer to sea ice permeability in this section, we mean the inability of particular ice types to hinder heat exchanges.

The effect this has on the overall seasonality of the ice edge location in the study region is shown in Figure 4.4, along with a comparison to the REF run and a satellite estimate. Although the overall change in the location of the ice edge is minor (i.e the mean seasonality is not strongly affected), the amplitude of the seasonal cycle is enhanced. That is, in late summer the ice edge location shifts south of the REF simulation, while in winter there is an amplification of the northward advance. The magnitude of the

enhancement is on the order ∼100 km, based on the difference between the mean ice edge locations shown in Figure 4.4. This seems to be caused by a thinning of the ice during retreat (late summer in this case, January to mid-March), driven by enhanced warming of ice covered regions, which then subsequently makes the ice more mobile during the advance phase, leading to a greater northward expansion (see Figure 4.6). This interpretation is further supported by the ice circulation patterns shown in Figure 4.3, which illustrates the predominantly northward ice motion in winter over much of the model domain. As was noted above in section 4.3.1, the figure also shows a general correspondence between thinner ice cover and greater ice velocity (thus explaining the greater northward ice velocities shown in Figure 4.6C).

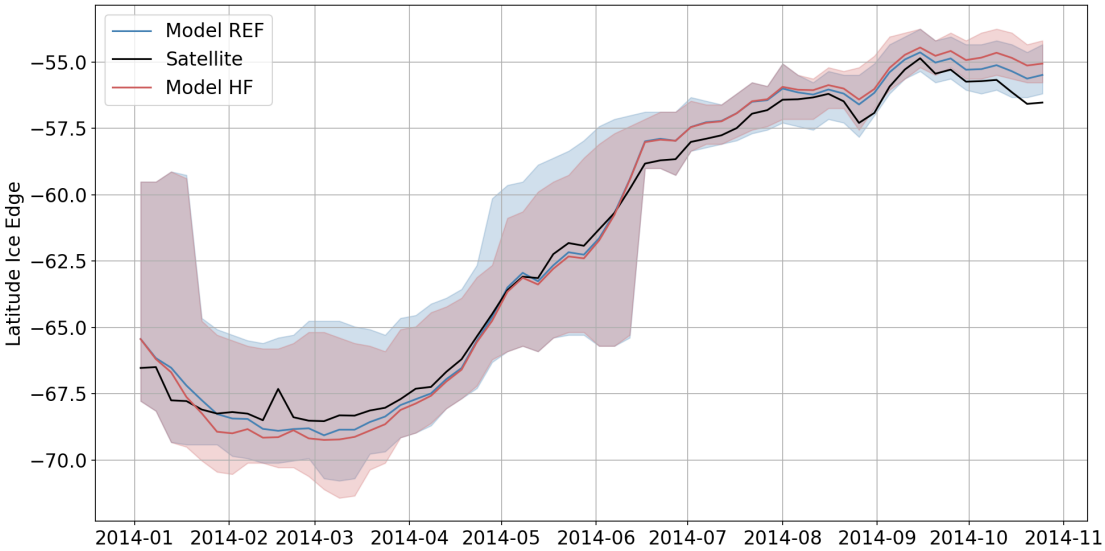

Figure 4.4: Mean location over the study region of the ice edge (15% concentration contour) for REF run (blue), HF run (red), and satellite data (black). Shaded regions denote the zonal variability of within the study region (20°E to 20°W).

As was stated from the outset, the primary aim of the modelling experiments presented here was to test the winter mixed layer response to ice-mediated heat and momentum fluxes in the SSIZ. As such, we will be focussing on the mean July-September (JAS) response in vertical mixing, corresponding to the same late winter period analysed in Chapter 3. Since the majority of ice formation occurs prior to this, analysis of this period also allows us to integrate the surface layer processes occurring during the advance phase. In the HF experiment, the introduction of additional heat exchange through ice had contrasting effects on mixing, with ND generally deepening in the SR (solid red box Figure 4.5) and shoaling in the MIZ (dashed red box Figure 4.5). West of the regions of interest the pattern is broadly similar, with a band of localized shoaling at the outer edge of the SSIZ (dark blue patches in Figure 4.5), followed by deepening of ND south of this where the ice is more consolidated.

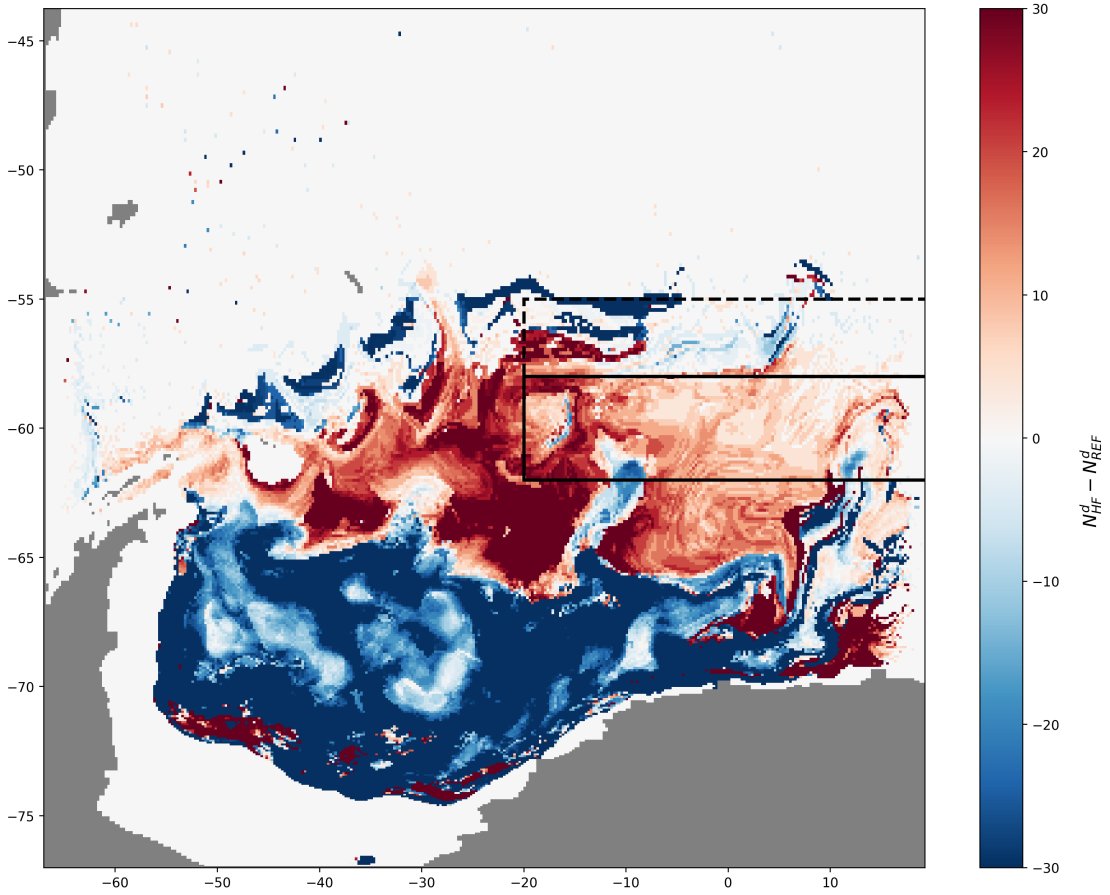

Figure 4.5: Change in mean winter (JAS) stratification depth (ND) in the HF experiment compared to REF run. Red shading denotes a deepening of the stratification depth, blue a shoaling. The solid and dashed boxes demarcate the study region and model MIZ, as in figure 4.1.

Accounting for this pattern requires a more detailed analysis of the seasonal evolution of various properties within the regions of interest. In the model MIZ, as well as across the entire domain, mean winter SIC is increased in the HF experiment (Figure 4.7), in agreement with the observed northward expansion of the ice edge discussed above. However, the effect is much more prominent in the MIZ, with mean JAS concentration increasing by as much as $\sim$20% in some places, while in the SR increases are on the order 2-5%. Comparison of figures 4.5 (change in ND) and 4.7 reveals that regions with the greatest increase in SIC coincide with regions of shoaling of ND (dark blue in Figure 4.5) in the MIZ (i.e. in the northwest corner of the dashed box, as well as in other regions of shoaling at the outer edge of the ice pack). This suggests that the additional ice cover in the MIZ reduces heat loss to the atmosphere in winter, inhibiting further ice formation and decreasing vertical mixing.

However, closer examination reveals that is not the case: there is no significant difference in the oceanic heat loss in the MIZ between REF and HF runs (Figure 4.8,

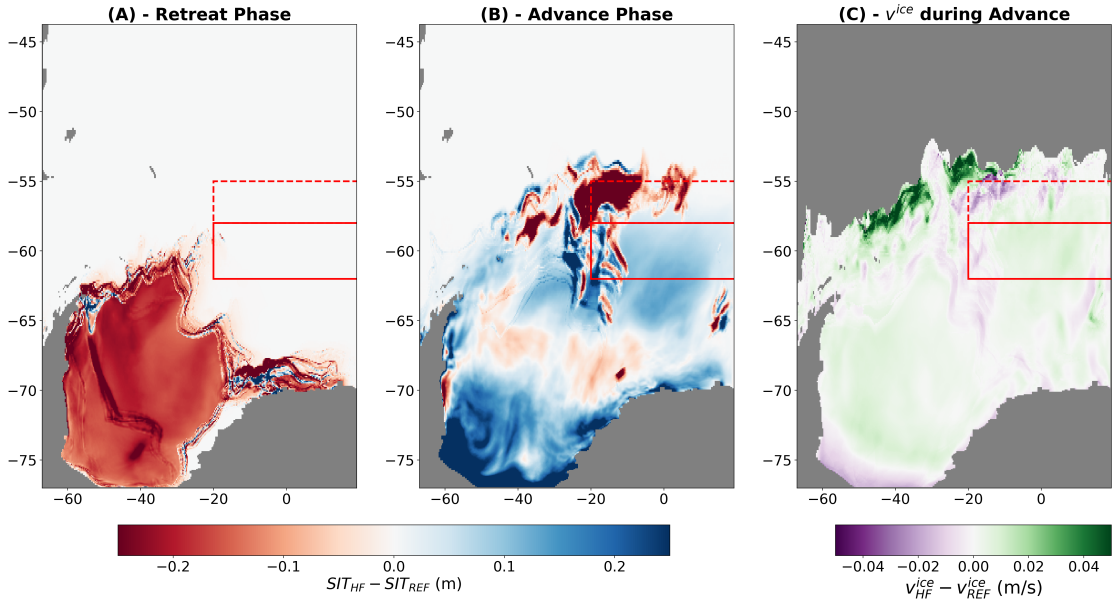

Figure 4.6: Sea ice thickness during **(A)**: late retreat phase (January - March 15th) and **(B)**: the advance phase (March 15th - September 15th). Plotted in **(C)** is the mean difference between meridional ice velocity in the HF and REF runs during the advance phase.

dashed lines). One possible explanation for this is that even though there is more ice cover, the ice is now more permeable, so any reduction in heat flux (due to concentration increases) is counteracted by increased heat loss through the ice. Indeed, the winter SIC increases are on the order 10-20%, similar to the imposed ice permeability of 10%. This highlights an important negative feedback mechanism present in the model: the imposed heat loss increases mean ice concentration (Figure 4.7), which acts to reduce the ocean-atmosphere heat exchange. This therefore acts to dampen the model response in winter when there is a net heat flux out of the ocean. When the sign of this heat flux reverses later in the year, we may expect the perturbation to enhance the positive feedback associated with melting (mentioned in section 1.2.2): warming of dark ocean regions leads to a strong ocean-ice heat flux, precipitating melting and the exposure of more open ocean and further melting.

Therefore, the mechanism of shoaling of ND in the MIZ appears instead to be driven by melting of the excess ice advected into the region (through the mechanisms discussed above). This is clearly shown in Figure 4.9, where surface ocean has a stronger freshening signal during melting in HF when compared to REF (dashed lines). The presence of excess ice in HF is also shown in Figure 4.27, which plots the time series of ice volume in the MIZ and SR. Figure 4.9 also shows that the MIZ is not a region of strong ice formation, since surface salinity increases are modest compared to the SR slightly further south. The figure also shows that the HF perturbation does not significantly increase ice formation in the MIZ (since mean salinity increases are nearly

identical), suggesting that the net effect is to freshen the surface ocean.

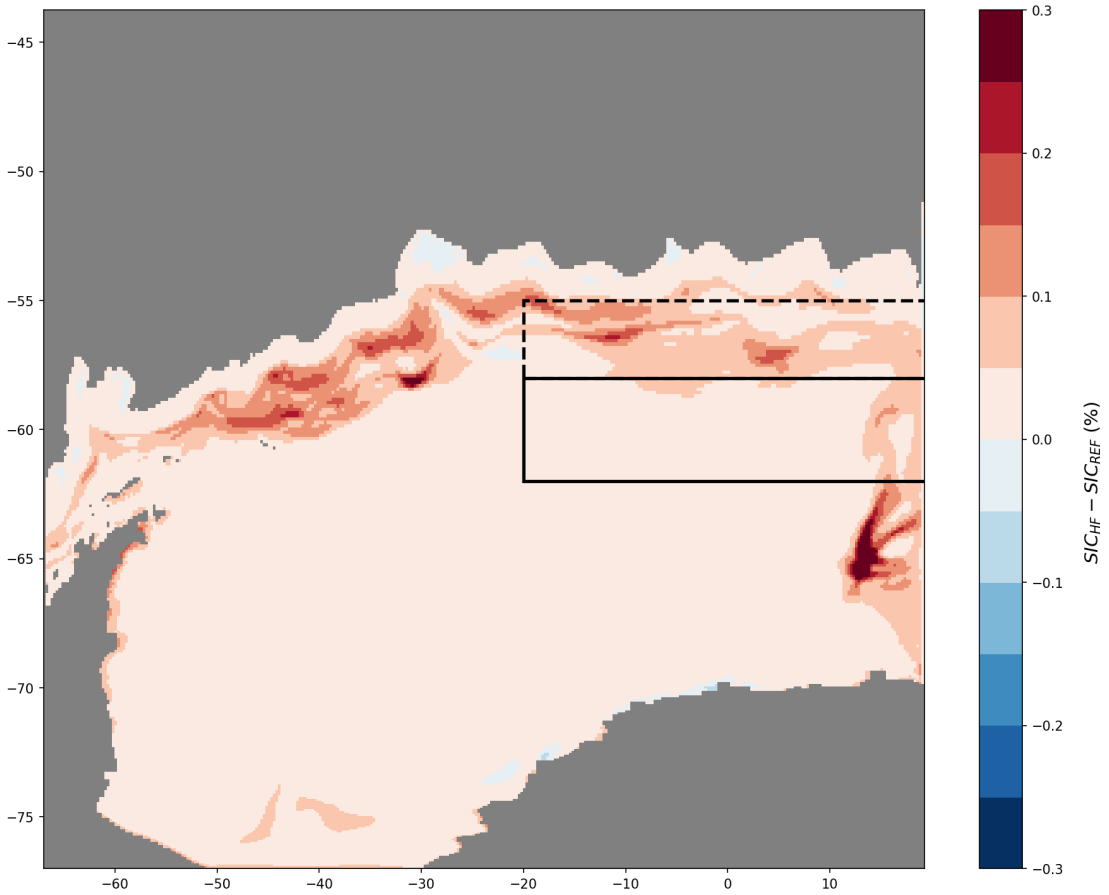

Figure 4.7: Difference in mean JAS sea ice concentration between the REF and HF runs. Red shading indicates an increase in sea ice concentration under increased heat flux. Black solid box denotes the study region (SR), black dashed box is the MIZ.

Various lines of evidence therefore support the idea that under increased permeability ice becomes thinner in summer, which then enhances the winter northward expansion, leading to more ice in the outer regions of the winter pack. This excess ice in the MIZ is then more readily melted in the spring, since warming of the ocean will proceed faster in the HF experiment, leading to an increase in the freshwater flux and associated stratification (thus shoaling ND). Note that the melting of excess ice occurs in August/September, but the shoaling of ND is apparent in the mean JAS field (Figure 4.5). This can be clearly seen in Figure 4.10B, where freshwater fluxes associated with melting are enhanced under HF in August/September.

If we now shift the focus further south to the SR (solid black box in Figure 4.5), we see that winter ND is generally enhanced, in some regions by more than 30 m. When compared to the MIZ, the SR has much higher mean SIC (Figure 4.1), and is also a region of strong ice formation (Figure 4.9 solid lines). The model response to

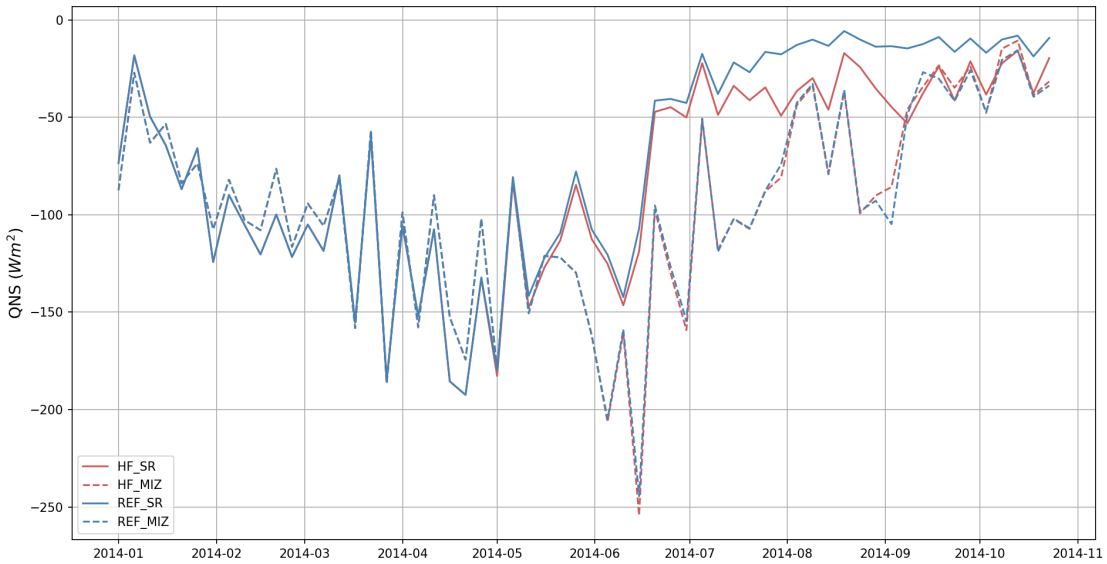

Figure 4.8: Mean non-solar heat fluxes (QNS) in the SR (solid curves) and MIZ (dashed) for the HF (red) and REF (blue) model runs. Note that for the MIZ only regions which display a decrease in N^d (reduced mixing, blue areas in figure 4.5) of at least 15m are shown.

increased heat flux through ice is perhaps more intuitive in this case: the enhanced winter heat loss drives increased ice formation and thickening, which enhances brine rejection and thus convective mixing. This can be seen in Figure 4.8 (solid lines), where heat loss is significantly higher in HF when compared to REF during winter, as well as in Figure 4.9 where surface salinification (associated with brine rejection) is enhanced in HF. Figure 4.10A provides further evidence for this interpretation: ice formation (shown in the figure by negative freshwater fluxes) events are greatly enhanced under the HF perturbation (in the SR). However, the figure also reveals that melting events are similarly enhanced by the increased heat exchange. Indeed, in mid-August the HF experiment produces a significant melting event which is completely absent from the REF run. Nevertheless, it appears that the increased formation dominates in the overall response, leading to a deeper mean stratification depth.

Interestingly, oceanic heat losses in the SR begin to match those in the MIZ by early September in the HF experiment (Figure 4.8, two red curves overlap), which is exactly the condition which has been suggested by the results of previous chapters. Namely that 100% SIC does not necessarily imply an end to MIZ-like conditions where atmosphere and ocean still exchange heat through the interface. This suggests that, at least in winter in this region, MIZ-like ocean-atmosphere exchanges may be facilitated through a simple parametrization which assigns higher permeability to particular ice types (such as thin ice). In relation to this, Smedsrud and Martin (2015) incorporated grease ice (mixture of frazil and water found in the early stages of sea ice formation) into an ocean-

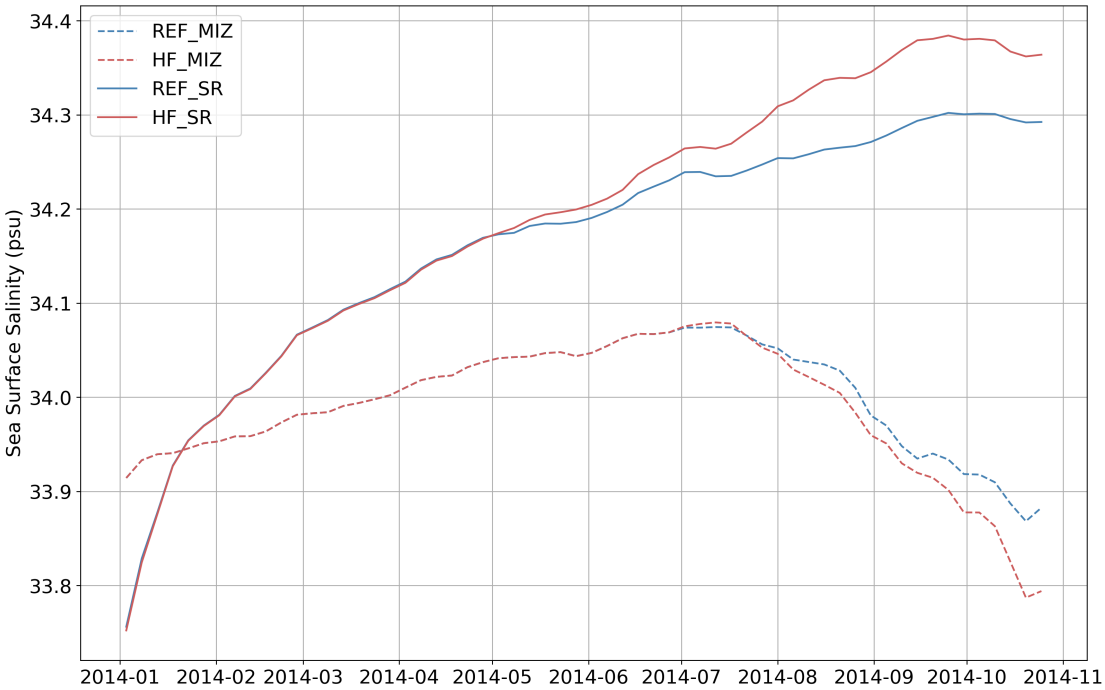

Figure 4.9: Comparison of mean sea surface salinity in the study region (solid lines) and the model MIZ (dashed lines), for REF (blue) and HF (red) experiments. Note that for the MIZ only regions which display a decrease in N^d (reduced mixing, blue areas in figure 4.5) of at least 15m are shown.

ice model, and found that its inclusion increased Arctic Ocean heat loss by 10-30% when compared to a reference simulation.

In summary, we have found that enhancing sea ice permeability with respect to heat exchanges has contrasting effects on the winter mixed layer in the MIZ and further south in more consolidated conditions (the SR in our case). A reduction in winter vertical mixing in the MIZ is driven by melting of additional ice advected into the region (as opposed to formed in-situ), while an increase in mixing in the SR is driven by increased ice formation resulting from enhanced heat loss. The excess ice in the MIZ is linked to a thinning of the ice cover during the retreat phase (January - March), which then created a more mobile surface which expanded further north during the advance phase (March - September). It should be emphasized that these are the winter (JAS) mixed layer responses, and that responses in other seasons may be different. The focus on the winter period also means that density changes are primarily salinity driven, with temperature only becoming important later in the year. So while we have enhanced the winter heat loss in this experiment, we would stress that the changes in vertical mixing discussed here are driven by changes in ice formation and/or melting and the associated fresh waters fluxes.

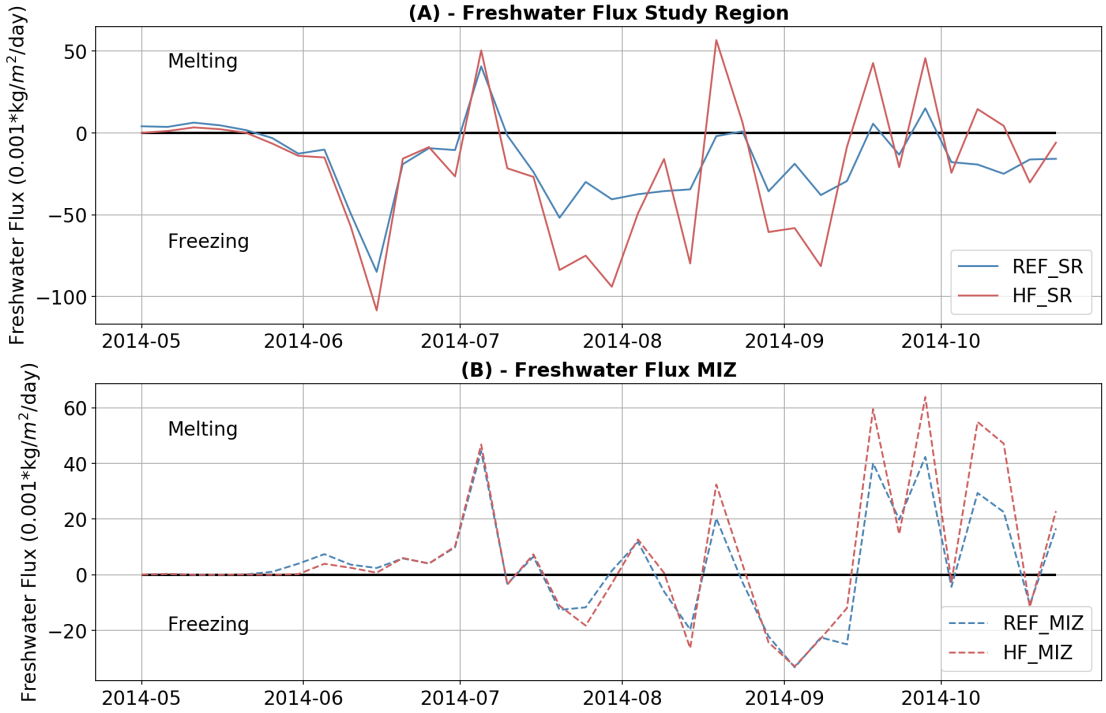

Figure 4.10: Total sea ice freshwater flux averaged over the study region **(A)** and the MIZ **(B)** . Negative values indicate flux out of sea ice associated with brine rejection and ice formation.

4.3.3 Momentum Flux Experiment

The other key component controlling vertical mixing in the SSIZ is the flux of momentum from atmosphere to ocean, as mediated by ice cover. As with previous sections, we show the effect of enhanced momentum flux (achieved by increased air-ice drag - see section 4.2) on the annual cycle of the ice edge location in Figure 4.11. In contrast to the HF experiment, the increased air-ice drag does not significantly alter the overall evolution of the ice edge location. This despite the fact that mean ice velocities are increased, as one would expect given the increased shear stress imposed in the experiment. This lack of response is an interesting finding, although an analysis of why this occurs is beyond the scope of this thesis. However, a reasonable explanation could be that the increase in northward ice drift is compensated by increased melt as ice is advected north into warmer waters (as was seen above for the HF experiment).

As in the previous section, the model mixed layer response to the imposed increase in flux is regionally dependent, with contrasting behaviour in different areas. However, unlike in the previous section, the overall pattern is reversed, with vertical mixing being generally enhanced in the model winter MIZ, and reduced across much of the SR (Figure 4.12). Furthermore, there is significant spatial variability in the response within the SR, with some areas displaying a deepening of ND, others a shoaling, and some no response.

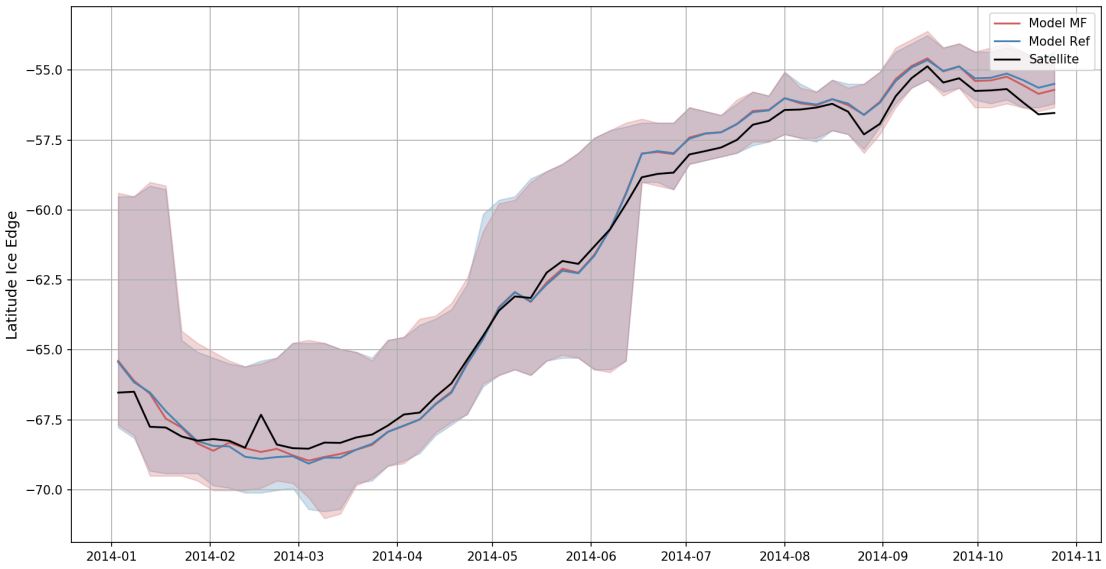

Figure 4.11: Mean location over the study region of the ice edge (15% concentration contour) for REF run (blue), MF run (red), and satellite data (black). Shaded regions denote the zonal variability of within the study region (20°E to 20°W).

Study Region Response Particularly intriguing is the shoaling of ND in the SR, since within context of the MF experiment, we expect that mixing will be enhanced by increasing the air-ice drag coefficient. This should lead to greater variability in sea ice velocities (since ice will more readily respond to high frequency wind forcing), and so the shear between ice and ocean will increase. Indeed, this is precisely the response we see in Figure 4.13, which plots the difference in ice-ocean shear between the MF and REF runs. The increased shear will then enhance turbulence in the upper ocean, deepening ND. However, the increase in shear seen in Figure 4.13 is surprisingly uniform across the SR, and so cannot be used to account for the variability in response seen in Figure 4.12.

Closer examination reveals that this variability in the response of the stratification depth can be accounted for by differences in sea ice formation rates across the SR. Indeed, regions which display a shoaling of the stratification depth are regions of strong ice formation, while regions have a deepening response have relatively weak ice formation rates. This is clearly illustrated by the comparison of sea ice associated freshwater flux between the two regions shown in Figure 4.14. In regions where ND shoals (panel A), strong formation events (negative flux values indicating release of brine into the surface ocean) are observed in June and July, but are largely absent in regions which deepen (panel B). Also compared in this figure are the differences between the MF (green) and REF (blue) model runs. Although these differences are small, the MF experiment consistently inhibits ice formation and enhances melting (negative values in figure 4.14

are closer to 0 and positive values are larger). Notice that this is the case for both regions considered (shoaling and deepening of ND).

This enhanced melt water production under increased turbulence may be linked to an ice-ocean negative feedback mechanism introduced above in section 4.1. Here the deepening of the mixed layer may be entraining warm upper CDW waters, thus enhancing the oceanic heat flux to the ice bottom and driving melting. This freshwater flux may then account for the differing response we see in the stratification depth in Figure 4.12 (changes in ND under MF).

In order to investigate whether this mechanism can account for the shoaling of the stratification depth, we start by looking at the upper ocean heat content changes imposed by the increased ice-ocean stress. By comparing regions with contrasting responses in the mixing, we found that there is a slight increase in the heat content of the upper 180 m in the regions where ND shoals (only in August - Figure 4.15). Conversely, in regions

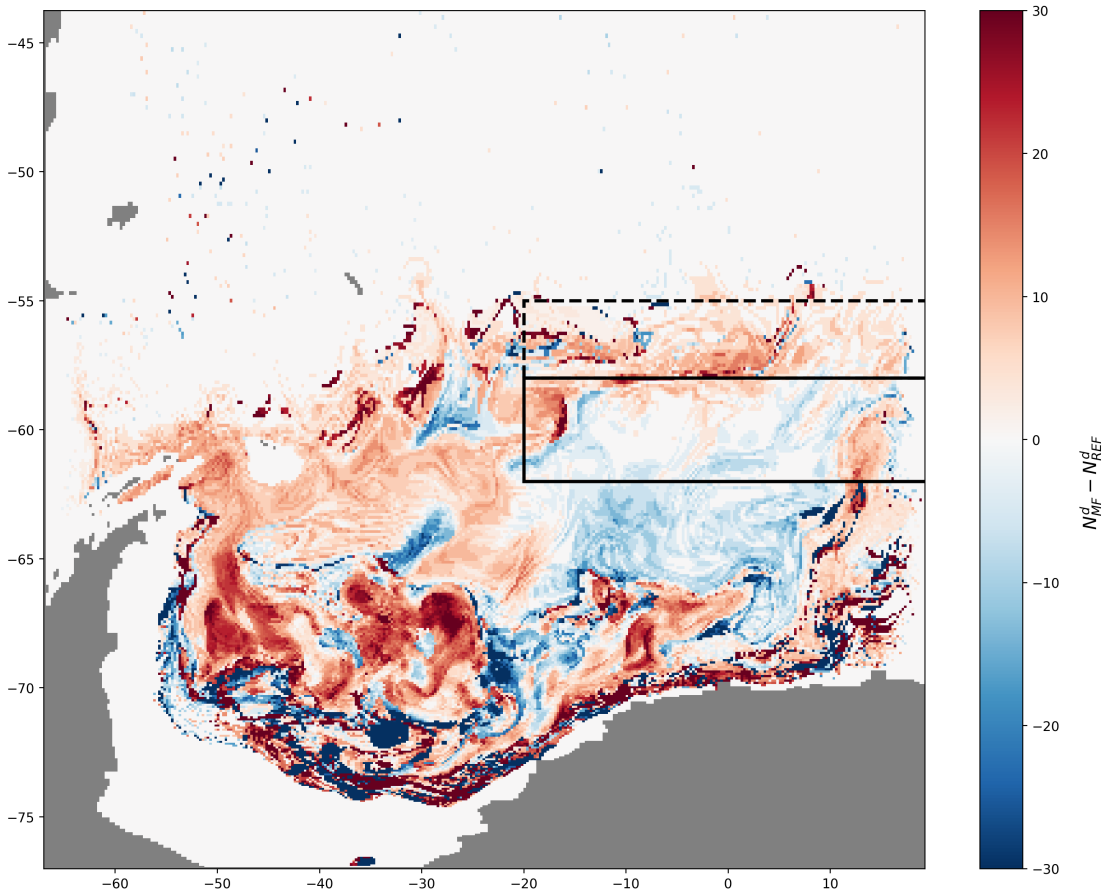

Figure 4.12: Change in mean winter (JAS) stratification depth (ND) in the MF experiment compared to REF run. Red shading denotes a deepening of the stratification depth, blue a shoaling. The solid and dashed boxes demarcate the study region and model MIZ, as in figure 4.5.

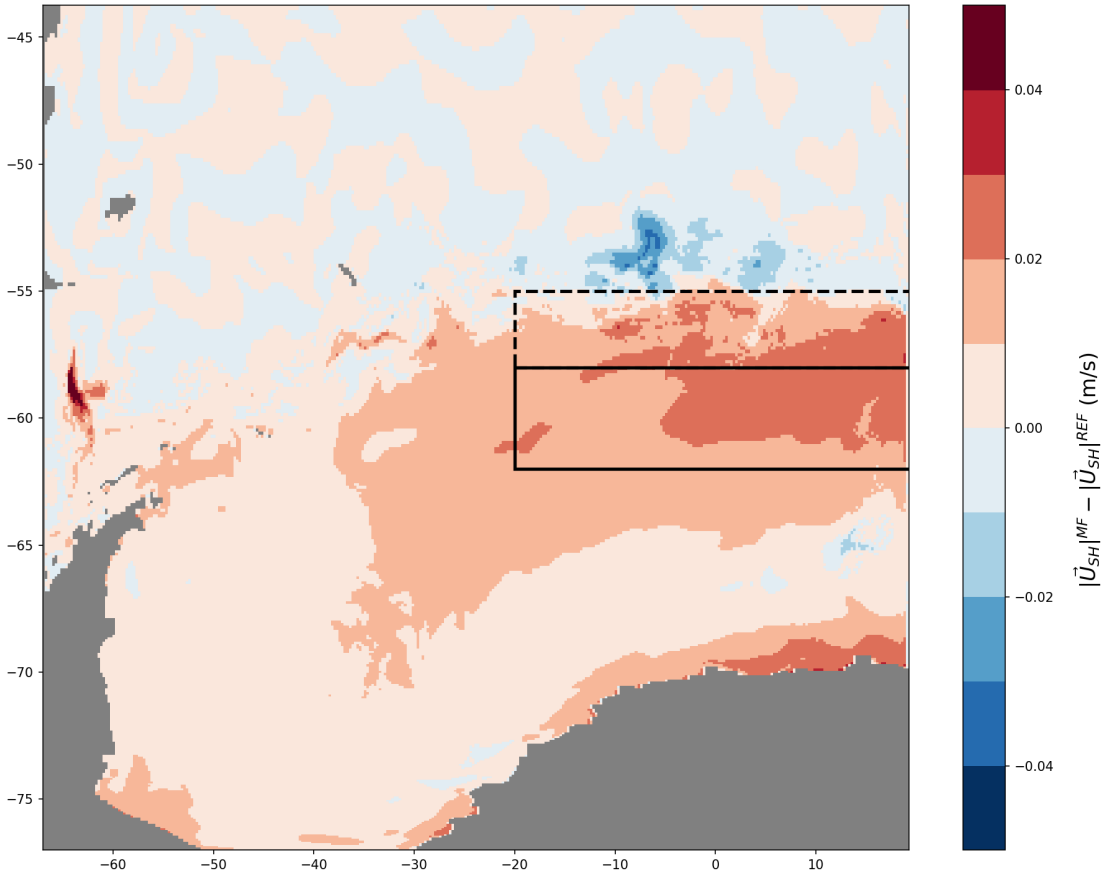

Figure 4.13: Difference in the magnitude of ice-ocean shear between MF and REF runs. Red shading indicates an increase in shear. Regions of interest are denoted as in previous figures.

which deepen the upper ocean heat content is reduced.

This can be clearly seen by looking at temperature profiles averaged over the shoaling and deepening regions (Figure 4.16A). The upper mixed layer is actually deepened by the increase in turbulence and resulting mixing with the cold waters close to the surface. The warming takes place below 100 m within the thermocline. The difference between the shoaling and deepening regions is that the shoaling regions already had a much deeper ML to begin with (due to greater ice formation), so the perturbation leads to an overall increase in heat content through mixing with the warmer deeper waters. Conversely, in the deepening regions the increase in turbulence leads to a much stronger cooling of the upper 100 m, which dominates in the overall heat content change. The increase in turbulence warms the thermocline in both regions, which causes the maximum temperature gradient to move towards the surface. This is what the black arrows in Figure 4.16A are showing, the raising of the thermocline under the MF experiment, thus enhancing stratification at the base of the mixed layer.

However, in order to understand the overall changes in stratification, the vertical salinity

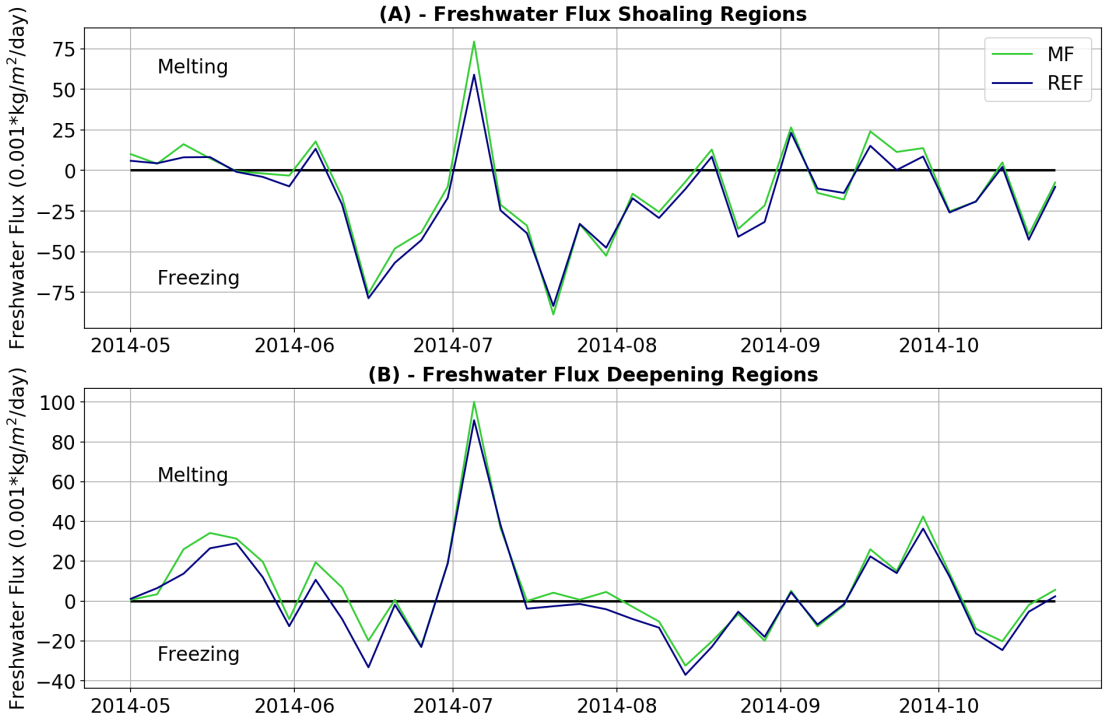

Figure 4.14: Total sea ice freshwater flux for regions where ND deepens and shoals (as in figure 4.24). Negative values indicate flux out of sea ice associated with brine rejection and ice formation.

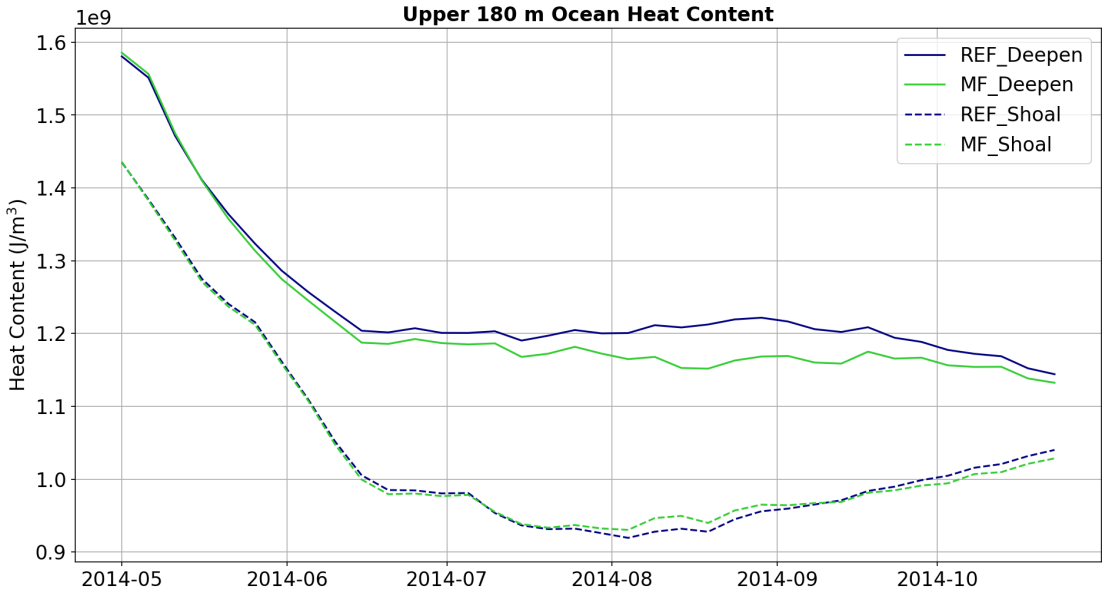

Figure 4.15: May to October upper ocean (180 m) heat content for the MF (green) and REF (blue) experiments. Regions where ND shoals within the SR are shown in dashed lines, while regions where ND deepens are plotted in solid lines.

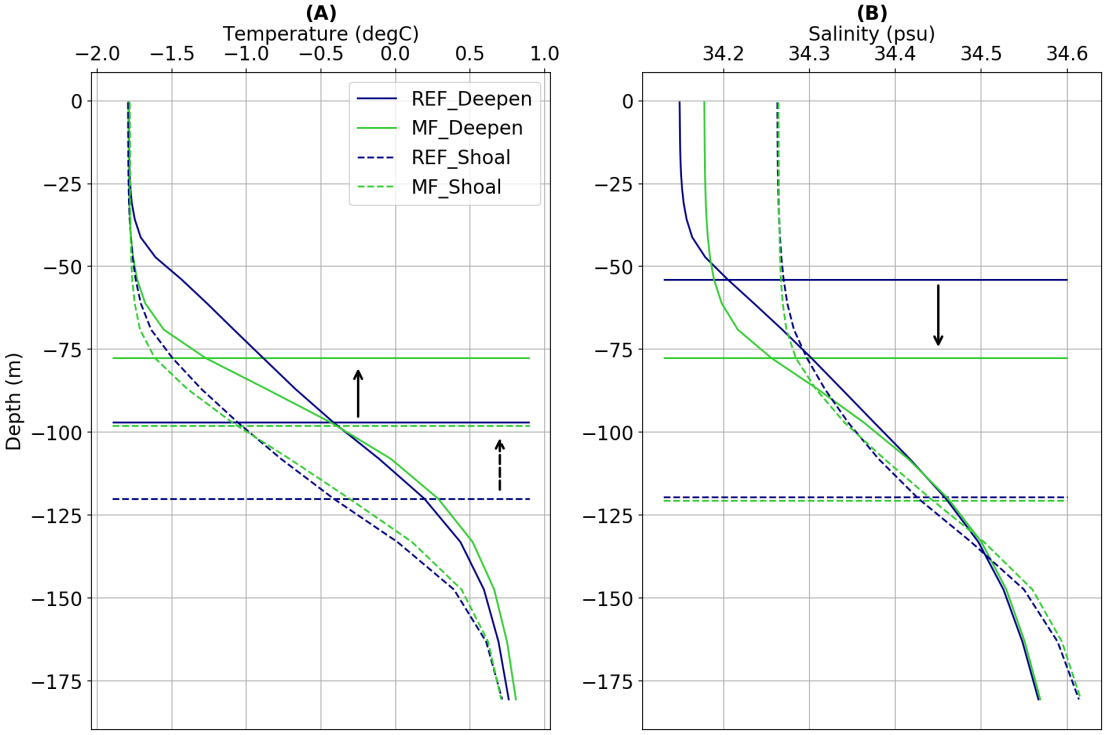

Figure 4.16: Mean winter (July - September) profiles of **(A)** temperature and **(B)** salinity over the top 180 m, averaged over regions where ND shoals (dashed lines) and deepens (solid lines) within the study region. The MF and REF experiments are shown in light green and blue, respectively, as in previous figures. The horizontal lines indicate the depth of the maximum gradient for each profile, thus estimating the depth of the thermocline for **(A)** and the halocline for **(B)**. The black arrows denote the direction of change (either deeper or shallower) in these measures of stratification when going from REF to MF. Note that panel A the blue solid and green dashed line occupy the same depth index, but have been shifted slightly to allow for ease of identification (the same has been done in panel B for the two dashed lines).

structure must also be taken in account (Figure 4.16B). Here we see that in the deepening regions the halocline is shifted downwards, while there is no change in the shoaling regions. Thus, in the deepening regions the net effect is to shift the density gradient downwards, since at these temperatures density is primarily controlled by salinity. In the case of the shoaling regions, the deeper mixing entrains higher salinity upper CDW into the halocline, which offsets the freshening seen higher up in the water column (around 75 m). The mean depth of the halocline is therefore unaffected (two dashed horizontal lines Figure 4.16B are the same) and the shoaling of the thermocline discussed above drives the overall shoaling of ND in these regions.

Now that we have characterized the changes to the vertical density structure, we move on to investigating the effect this has on ice growth and melt processes. Figure 4.17 plots the July - October oceanic heat flux which results in the melting of the bottom of the ice, again comparing regions where the stratification depth deepens or shoals. It is clear

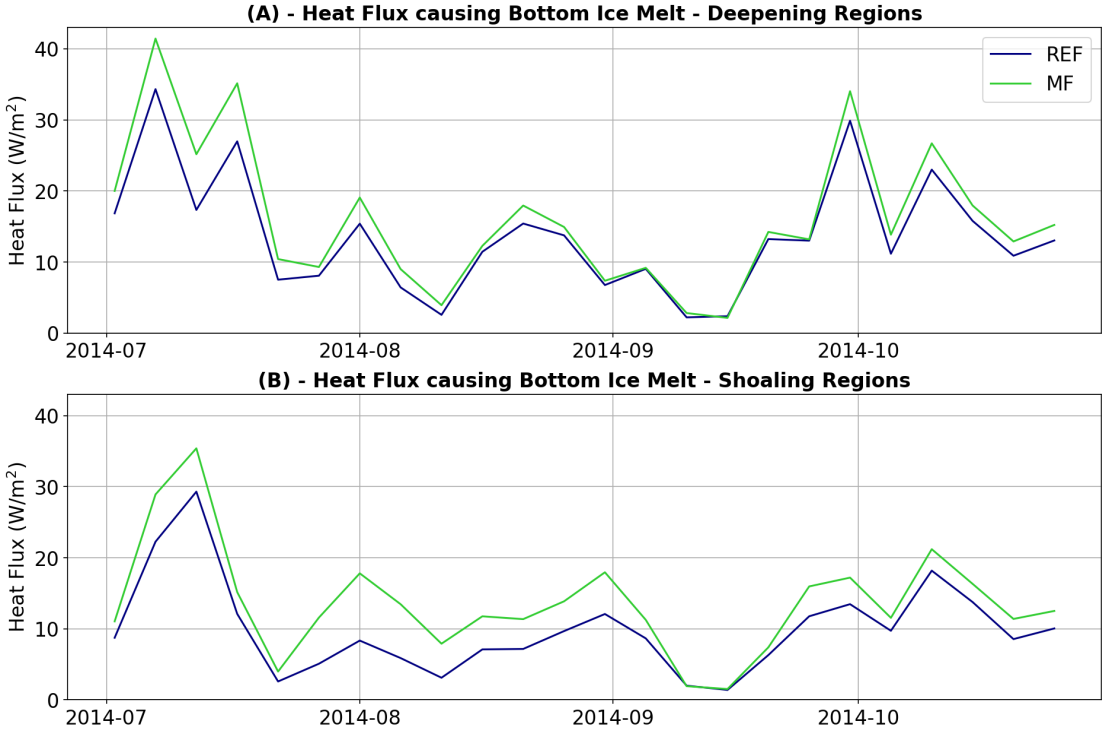

Figure 4.17: July to October mean oceanic heat fluxes which result in bottom ice melt. Compared are regions where the stratification depth (ND) deepens **(A)** and where it shoals **(B)**. The REF experiment is shown in blue, the MF in light green as in previous figures.

from this figure that the feedback discussed above is indeed active - the perturbation enhances the heat flux in both regions, but the effect is almost twice as strong in the shoaling region (a mean increase over JAS of 4.1 W/m^2 as opposed to 2.6 W/m^2). This then causes the ice to thin, again in both cases, but with an enhanced response in the shoaling regions. This is shown in Figure 4.18, which plots the change in sea ice thickness between the MF and REF experiments, contrasting the changes that occur in deepening (purple) and shoaling (green/blue) regions. The mean winter (JAS) thinning of ice in the shoaling regions is roughly twice that of the deepening regions (1.3 cm compared to 2.6 cm), however in late August/ early September the difference is greater (1.9 cm compared to 4.7 cm).

Therefore, the shoaling of the stratification depth seen in some regions of the SR can be attributed to an ice-ocean feedback whereby the initial deepening of mixing enhances the oceanic heat flux, thereby driving increased bottom melt and stratification of the water column. Although this feedback is also present in regions where the stratification depth deepens, the relatively shallow mixed layer prevents significant bottom melting. This shallow mixed layer may also be more readily deepened by the turbulence imposed in the MF experiment, compared to the already deep mixed layer present in other regions.

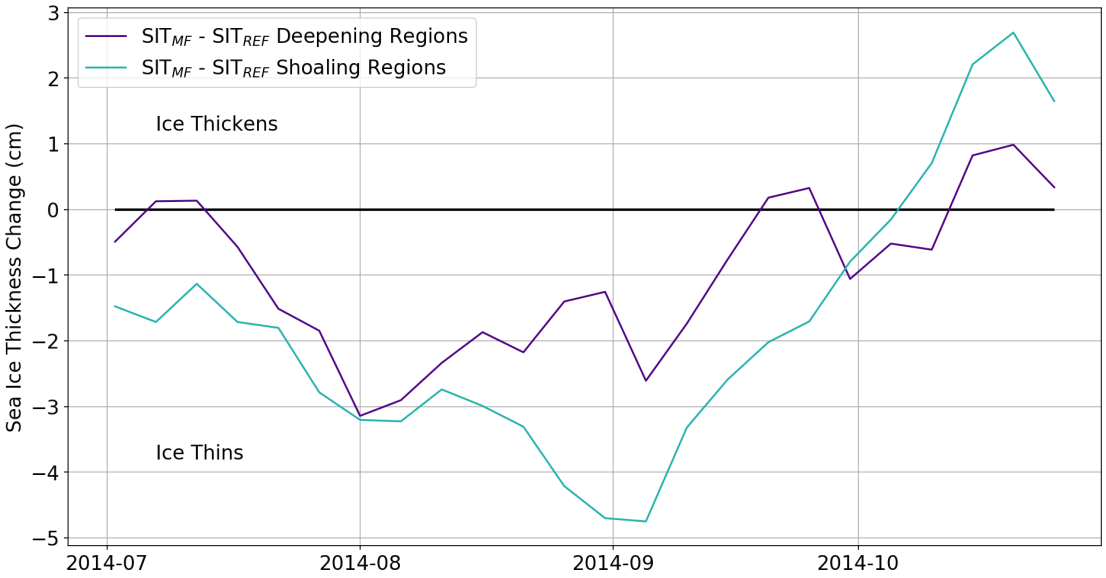

Figure 4.18: Change in mean sea ice thickness (SIT) between MF and REF experiments over July - October. Regions where ND deepens are plotted in purple, shoaling regions in blue/green. Negative (positive) values indicate a thinning (thickening) of sea ice under the MF experiment.

Marginal Ice Zone Response Moving now to the model MIZ, we found that enhanced mixing across much of the region is more straightforwardly related to enhanced ice-ocean shear associated with increased ice velocities in the MF experiment. Since this region also displays weak rates of ice formation, the same reasoning as before can be applied, namely, that ND deepens as a result of the enhanced shear. However, the vertical density structure is somewhat different in the MIZ than in the SR. This can be seen by comparing Figure 4.19 with 4.16: the water column in the MIZ is much more weakly stratified than in the SR, thus allowing the MF perturbation to more readily deepen ND (note that we only show the deepening regions in Figure 4.19 since this is the primary response across the MIZ - see Figure 4.12). In this case the weak stratification also means that ice-ocean feedback discussed above has limited effect, since the deepening perturbation will entrain relatively cooler waters (i.e. warmer waters are found deeper in the water column).

It appears then that the model response to enhanced momentum flux is very sensitive to the initial state of the vertical density structure. In the study region, warm and salty CDW is located close to the surface mixed layer, creating the potential for significant heat and salt entrainment. In contrast, in the MIZ these waters are found at greater depth, reducing such potential. Thus, even though the mixed layer is relatively deep in the MIZ, the entrainment of warm CDW is limited. This sensitivity of the under ice mixed layer to initial conditions was also suggested by early observational work documented in Gordon and Huber (1990). More recently, work by Schultz et al. (2020) found that an increased

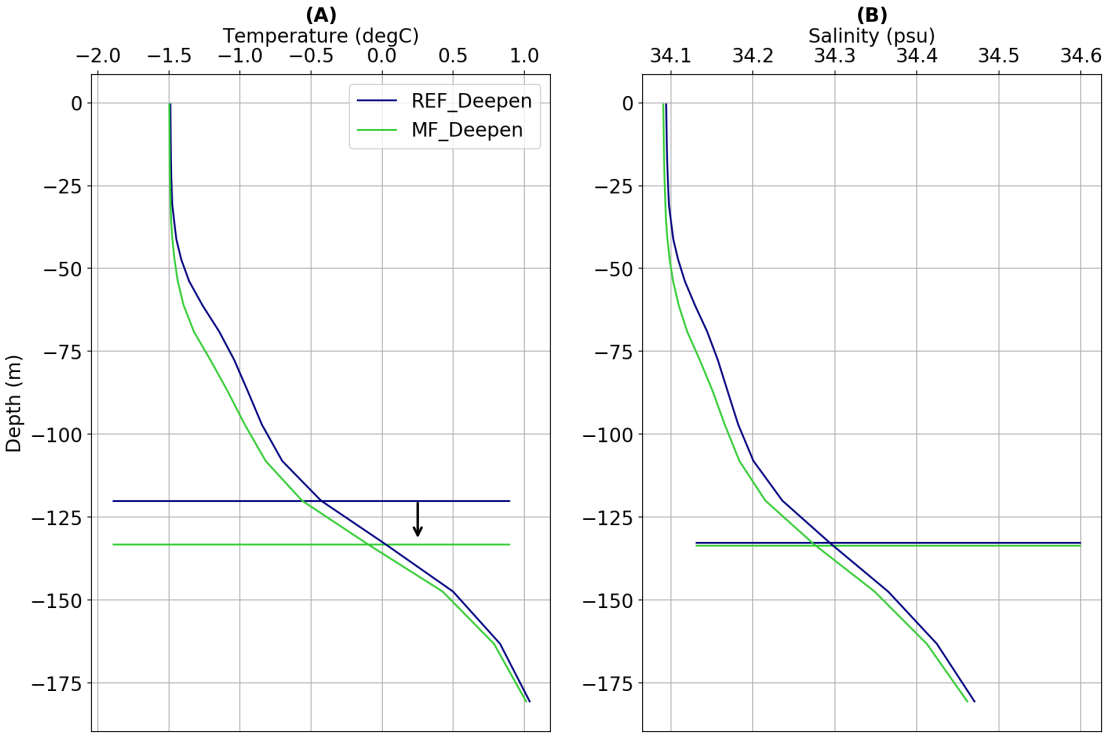

Figure 4.19: Mean winter (July - September) profiles of **(A)** temperature and **(B)** salinity over the top 180 m, averaged over regions where ND deepens in the model MIZ. The MF and REF experiments are shown in light green and blue, respectively, as in previous figures. The horizontal lines indicate the depth of the maximum gradient for each profile, thus estimating the depth of the thermocline for **(A)** and the halocline for **(B)**. The black arrows denote the direction of change (either deeper or shallower) in these measures of stratification when going from REF to MF.

air-ice drag coefficient had similar effects on the winter vertical structure (their figures S4 and S5) in a model of the West Antarctic Peninsula region. Furthermore, in their experiments the deepening effect was stronger when the MLD was relatively shallow, such as during ice retreat. This mirrors the model response seen here, where regions with a shallow mixed layer were more prone to deepen under an enhanced air-ice drag.

4.3.4 Combined Effects

In this section we compare the seasonality of ND in all model runs to observational estimates and the original reanalysis product. The main goal here is to assess the relative contributions of the HF and MF perturbations in the seasonal cycle of vertical mixing in the regions of interest, as well as to summarize and highlight the overall effect of each experiment. In line with this, the seasonal cycle of ND in the final run, the TF experiment, is compared with the other three experiments in the SR in Figure 4.20. Here we see that when running the model with both enhanced heat flux through ice and

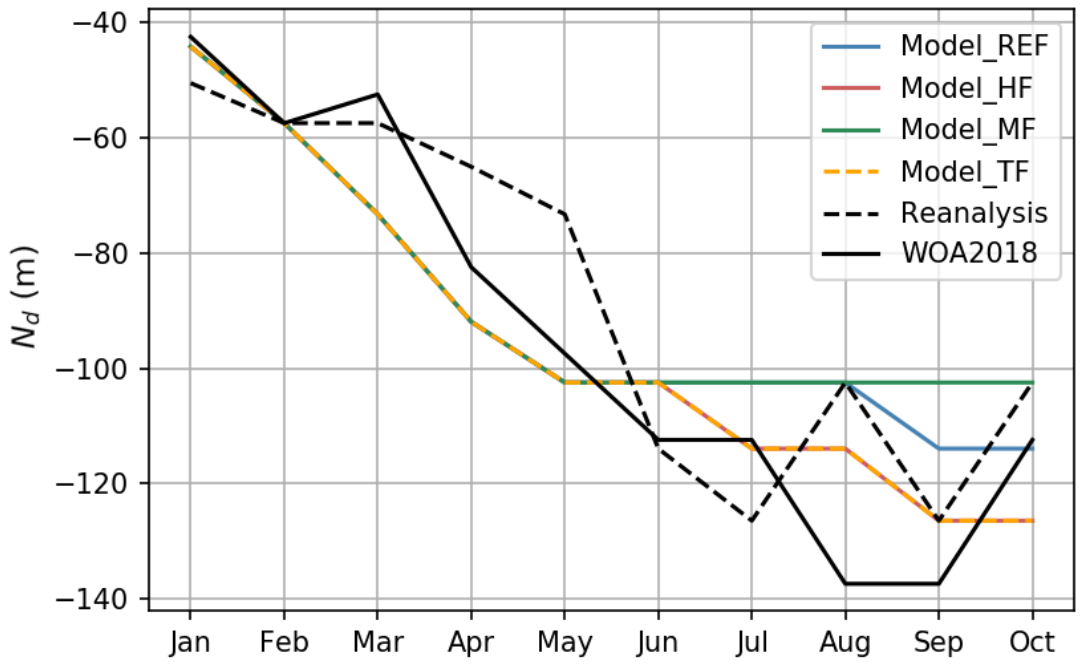

Figure 4.20: Seasonality of the ND for all experiments, WOA2018 observations and Reanalysis, averaged over the study region. Note that the time series is monthly means for the sake of comparison to WOA2018. Note that the red line for the HF experiment is hidden under the orange line.

air-ice drag, the thermodynamic effects of the former completely dominate the resulting mixing regime. This is illustrated by the fact that HF and TF experiments simulate the same mean ND across the SR, with MF simulating a shallower mixed layer. Indeed, comparison of figures 4.5 and 4.12 shows that the mixed layer response is generally greater in the HF experiment, which is also in agreement with the observationally-based work of Pellichero et al. (2016) discussed in section 1.2.3 (the authors showed that the under ice MLD is controlled by sea ice related buoyancy fluxes).

Another important consideration is the high average SIC found throughout winter in the SR (see Figure 4.1). This condition will tend to favour a buoyancy controlled mixed layer, where the effect of winds in winter are diminished (in the model that is). Accordingly, further north in the MIZ we see that the mixed layer is more strongly affected by the enhanced air-ice drag, especially during melting in October (Figure 4.21), a result which again agrees with the work of Schultz et al. (2020) described above. This is seen by the suppression in TF and MF of the strong stratification present in October in the HF experiment, suggesting that the additional ice present in the MIZ under enhanced heat flux leads to the generation of excess melt water (as was seen in section 4.3.2). Interestingly, comparison of late winter/early spring surface freshening (in the MIZ) in HF and TF runs shows only slightly lowers salinity values in

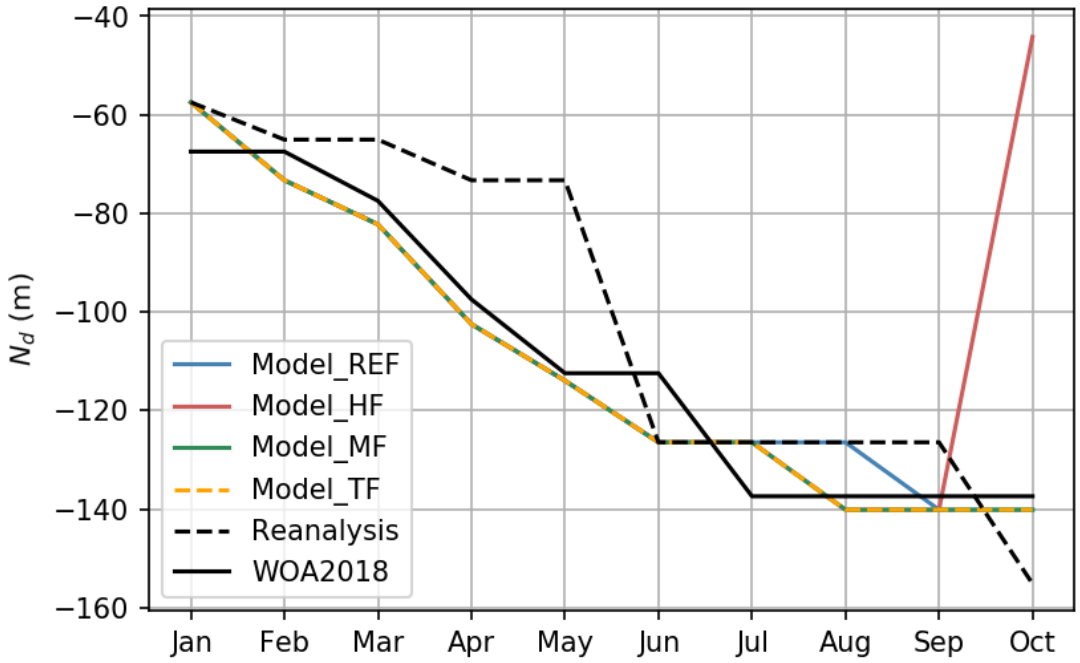

Figure 4.21: The same as figure 4.20, but the model MIZ from 58 - 55°S.

TF (suggesting that TF still exhibits excess melt water generation), which may indicate that enhanced turbulence brought about by ice-ocean shear (the MF component of TF) erodes the freshwater stratification (see Figure 4.28).

An aspect of Figures 4.20 and 4.21 that we have not discussed yet is the comparison of the model ND to observational estimates. Here we see that in general the HF and MF alterations deepen ND closer the observed (WOA2013) winter values, although MF does not seem to have much of an effect in the SR. Yet we know from the discussion in section 4.3.3 above that this lack of an overall effect is probably the result of the opposing deepening and shoaling of ND in the SR. This highlights the fact that the regional averages presented here may conceal substantial variability, and should therefore be interpreted with caution.

Another constraint of Figures 4.20 and 4.21 is that they plot monthly means (in order to be comparable to WOA2018), which can also obscure variability and potentially bias results. Accordingly, plotted in Figure 4.22 are higher resolution diagnostics of vertical mixing for all four model runs, computed online and saved at the 5-day frequency of the model run. Included are two separate measures of the extent of vertical mixing: the turbocline depth (or the mixing layer depth, shown in top panels A and B - see section 1.2.3), here defined as the depth where the vertical tracer diffusivity is lower than or equal a background value of 5x10^{-4} m^2/s, and the more classical MLD defined with a density threshold criterion (depth where density deviates by 0.01 kgm^{-3} compared to

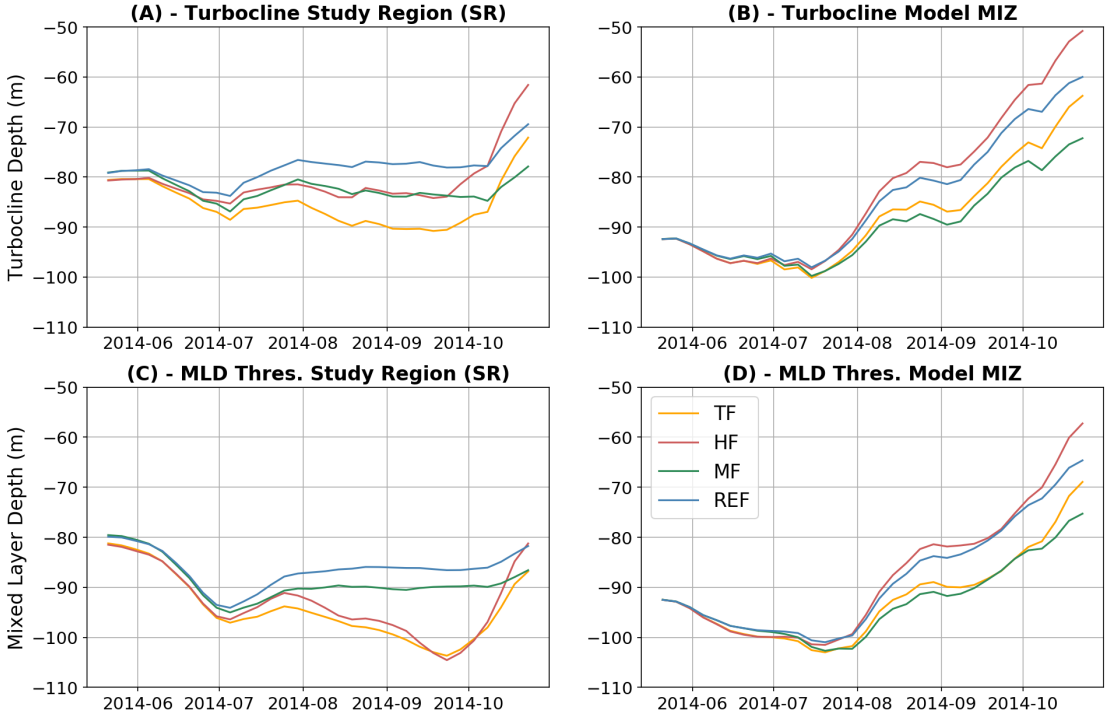

Figure 4.22: Comparison of all model runs May - October turbocline and mixed layer depths for the regions of interest.

the 10 m value, shown on bottom panels C and D). This allows for smaller differences in the seasonality of mixing between model runs to be resolved, something that is evidently averaged out in Figures 4.20 and 4.21.

Immediately we see in Figure 4.22A that the turbocline depth does not show the same model response as monthly means of ND in the SR. Both heat and momentum flux perturbations contribute roughly equally to deepening the turbocline in winter, with cumulative effects apparent in the TF experiment (which displays the deepest winter turbocline). If we compare this to the classical MLD (panel C), we see a very similar result to that shown in Figure 4.20: the heat flux component again dominates the overall winter mixing regime in the SR, with very little contribution from the MF component.

Moving to the MIZ, the results align closely with previous figures, indicating a much more prominent role of the momentum flux in the region. As estimated by both the turbocline and the classical ML depth, the MF experiment simulates the deepest winter mixing, confirming the speculation above that the inclusion of enhanced air-ice drag in the TF run counteracts the melt water induced stratification present in HF in October (Figure 4.22B+D). Overall, the more detailed picture provided by Figure 4.22 implies that while the MF experiment does enhance turbulence in both regions of interest (indeed as is suggested by Figure 4.13), the effect on the vertical density structure is regionally

dependent, a similar conclusion to the one arrived at in section 4.3.3. In contrast, the model response to increased heat flux through ice appears more linear: deeper mixing in winter, enhanced melting and stratification in spring. Such a difference could be a consequence of active turbulence (generated by ice-ocean relative motion) in the SR not penetrating below the base of the ML, the depth of which is likely set by buoyancy fluxes (heat loss in autumn and brine rejection in winter). Indeed, the turbocline is generally shallower than the MLD, but the difference is much smaller in the MIZ, implying that strong wind mixing events in the region are enhancing turbulence close to the base of the ML.

Before moving on to conclude this chapter, a brief discussion of the implications of its findings for phytoplankton phenology in the Antarctic SSIZ is warranted. The fact that the winter mixed layer is brought closer to observations in both sets of experiments is certainly encouraging, given that in Chapter 3 we saw that shallow biases in the stratification depth contributed to pronounced early growth in some CMIP5 models. The implication here is that deeper winter mixing may delay the onset of growth by limiting light availability (as has been shown in the ice free Southern Ocean in Vichi and Masina (2009)), although it is crucial that this be coupled with a realistic winter ice cover. In line with this, we saw in Chapter 2 that an ice cover characterised by 100% satellite concentration may still be permeable to light, in much the same way that we assumed some degree of heat permeability in this chapter. The results of Chapter 2 also showed that phytoplankton may be adjusted to very low light intensities, suggesting that changes to physiological parameters may also be necessary. Thus, enhancing both heat and light permeability in climate models may improve the representation of phenology, but only if the ice cover is realistically simulated and the physiological response taken in account. However, changes to permeability should be linked to the ice type and not applied universally as was done here. Similarly, changes to air-ice drag should also be linked to sea ice physical features (e.g. Andreas et al. (1984)), which, based on the results presented here, would also affect phenology by enhancing turbulence during winter and late spring, thus altering the mean light exposure.

4.4 Summary and Conclusions

In this Chapter we have investigated the effect heat and momentum fluxes have on vertical mixing in the Southern Ocean SSIZ. To this end, we have performed several sensitivity experiments using a numerical ice-ocean model of the Atlantic sector of the Southern Ocean. In total four experiments where conducted (REF, HF, MF and TF), in

which several processes related to under ice vertical mixing where investigated. These processes included changes in ice cover, oceanic heat flux, formation and melting of sea ice (brine rejection and freshwater fluxes), and ice-ocean shear produced by relative motion (turbulence driven by momentum transfer from atmosphere to ocean, via sea ice).

In the HF experiment, we enhanced the ocean-atmosphere heat exchange in ice covered regions (where ice concentration > 0). This induced a northward expansion of the winter ice cover, which was associated with reduced ice thickness in the preceding retreat phase, thus leading to a more mobile ice pack during the advance phase (since the ice was thinner at the start of the advance phase and therefore more mobile). While this northward winter expansion increases the ice concentration and volume in the MIZ, it is not associated with significantly higher rates of ice formation in this region. Therefore, the overall effect is to shoal the late winter (JAS) stratification depth in the MIZ, since the excess ice leads to greater fresh water flux from melting. In contrast, further south in the SR ice formation rates are significantly increased by the HF perturbation, leading to enhanced brine rejection and deeper stratification depths.

In the MF experiment, we increased the air-ice drag coefficient by $\sim$50%, thus enhancing the atmosphere-ocean momentum exchange. Here the model response was much more spatially variable, especially within the SR. We found that this variability is related to differences in the vertical density structure present in the reference experiment (REF). Regions of deeper vertical mixing (due to higher ice formation rates) tended to entrain warm CDW waters into the mixed layer under MF. This leads to a negative feedback, whereby the enhanced turbulence (arising from the increased momentum exchange) deepens vertical mixing, which leads to warm water entrainment and bottom melting of sea ice, thus enhancing stratification. Conversely, in regions where the mixed layer is relatively shallow, warm water entrainment is limited or absent, and so the MF perturbation deepens the stratification depth (ND).

A final experiment (TF) combined both the thermodynamic (HF) and dynamic (MF) effects of the previous two experiments. A key finding is that the thermodynamic effects are dominant in the SR, while in the partially ice covered MIZ the dynamic effects also play a role. In particular, the strong September/October stratification seen in the HF MIZ is not present in TF, suggesting that the enhanced momentum flux is able to erode the fresh water lens created by the HF perturbation. This points to the potential role heat and momentum flux enhancements may have in addressing the climate model biases in vertical mixing discussed in Chapter 3. Namely, that heat fluxes may be more important in the high ice concentration regime (such as the

SR in this study), while momentum exchange may play a greater role in the MIZ. Furthermore, the model experiments conducted here highlight the importance of the close coupling between dynamic and thermodynamic processes in the Southern Ocean SSIZ. Indeed, a relatively small thermodynamic perturbation in the HF experiment led to a significant dynamic response (thinner and more mobile sea ice). Similarly, the dynamic perturbation imposed in the MF experiment can induce changes in the oceanic heat flux, with associated consequences for the ice thermodynamics.

As a final point, it should be emphasized that the methodology used here is in no way prescriptive. For example, the argument is never made that sea ice is at all times and places permeable to heat fluxes, even though this is what is employed in the model. Similarly, the choice of air-ice drag coefficient in the MF experiment is not meant to be physically realistic for all conditions. Indeed, examples of more sophisticated approaches which attempt to improve fluxes in the SSIZ are available in the literature (e.g. Tsamados et al. (2014); Smedsrud and Martin (2015) and Schultz et al. (2020), under review), and will be discussed below in section 5.3.

Rather than attempting to realistically parametrize the relevant processes, the approach taken here was to ask *what effect would a more permeable and dynamic ice cover have on the mixed layer beneath it?* The motivation for assuming such an ice surface is provided by the results of chapters 2 and 3, which we can now consider in relation to the insights of this chapter.

4.A Additional Figures

Figure 4.23 the spatial variability of satellite ice edge location is shown (black shading) for comparison to the model REF run (in previous figures only spatial variability for model runs is shown). Figures 4.24, 4.25 and 4.26 compare regions where ND deepens and shoals in the MF experiment, providing further information to that shown in section 4.3.3. Figure 4.27 plots the mean ice volume for the regions of interest, comparing HF and REF runs. Finally, Figure 4.28 compares surface salinity in the MIZ between model runs, illustrating the stronger freshening signal seen in runs with enhanced heat flux through ice.

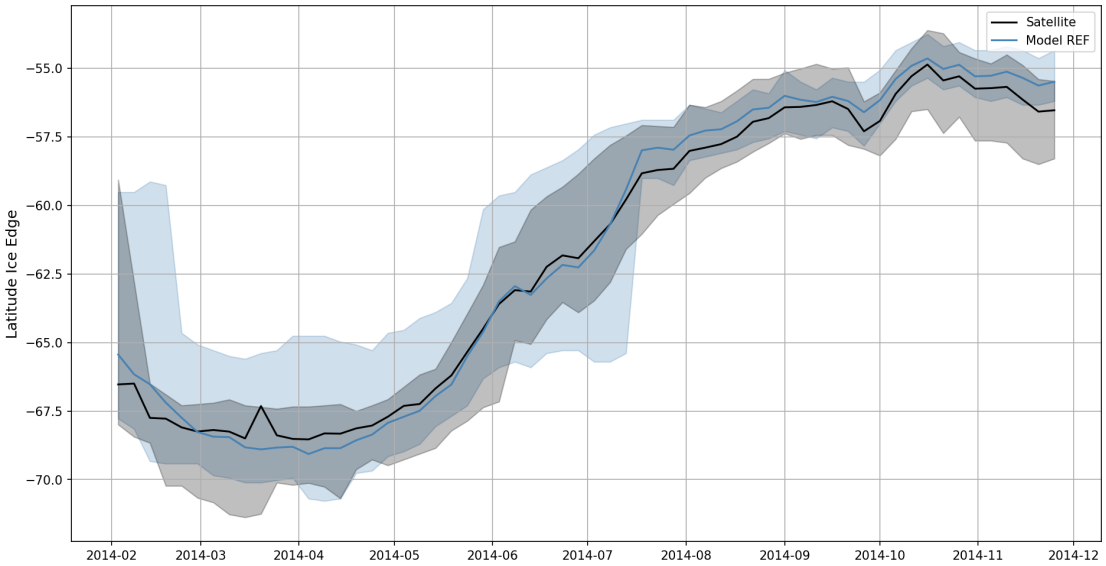

Figure 4.23: Ice edge location for the REF run and satellite data as in Figures 4.2 and 4.4.

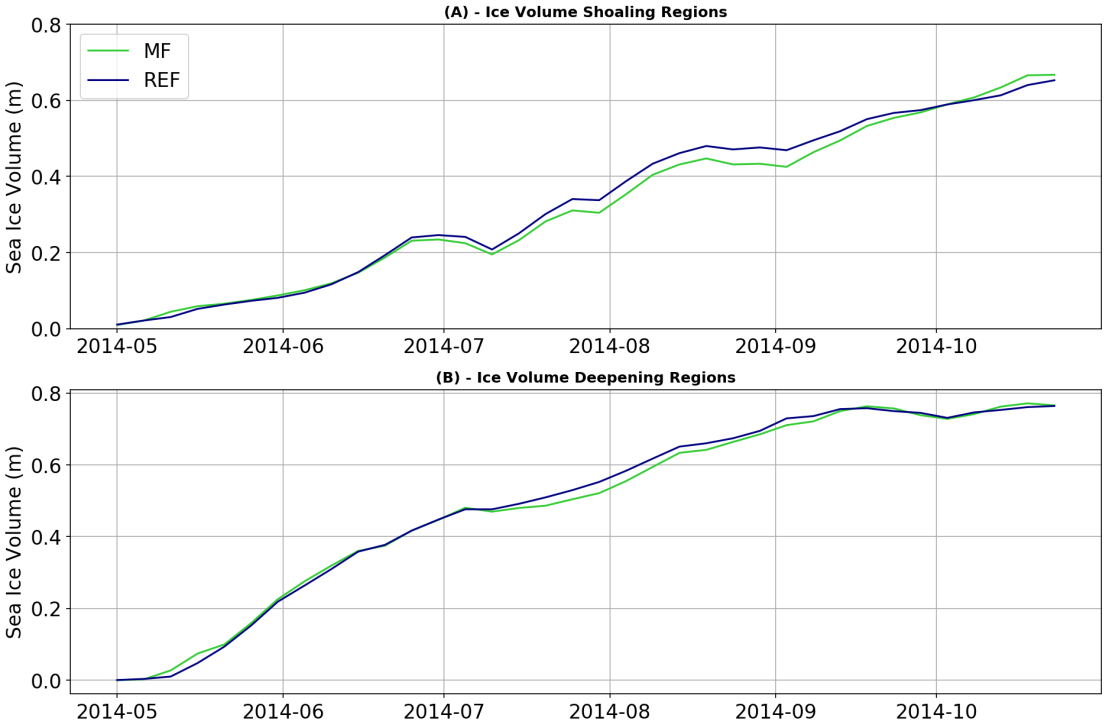

Figure 4.24: Comparison of mean sea ice volume changes from May to October in regions where ND deepens **(A)** and shoals **(B)** for the REF (blue) and MF (green) experiments.

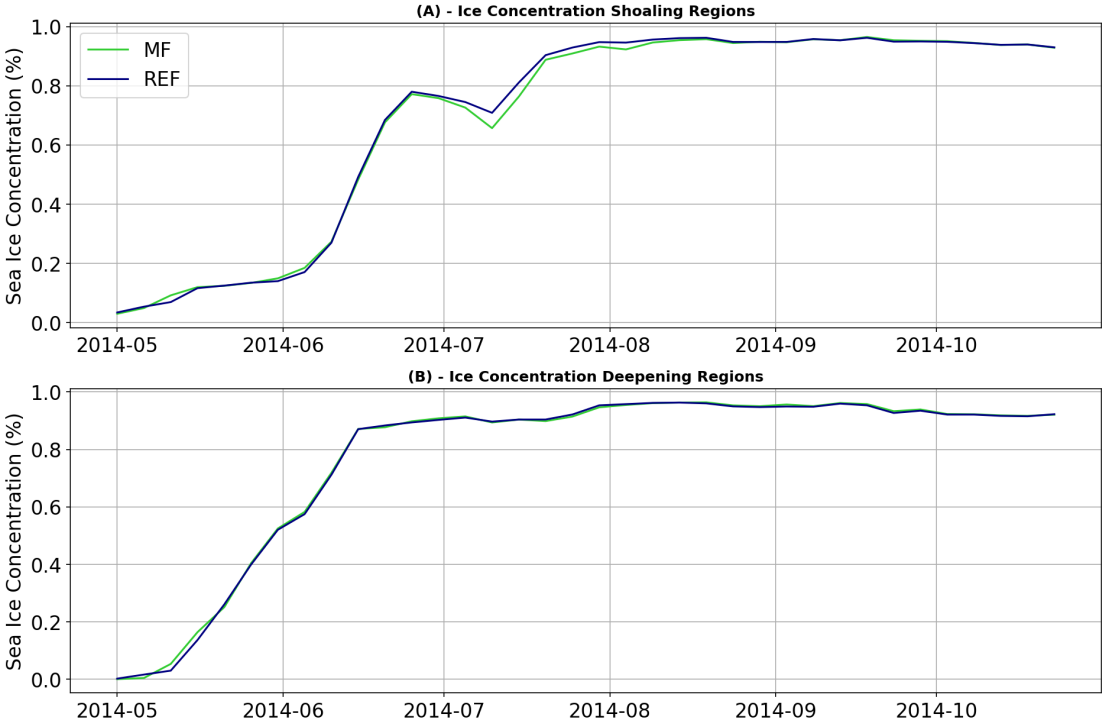

Figure 4.25: Comparison of mean sea ice concentration in regions where ND deepens **(A)** and shoals **(B)** for the REF (blue) and MF (green) experiments.

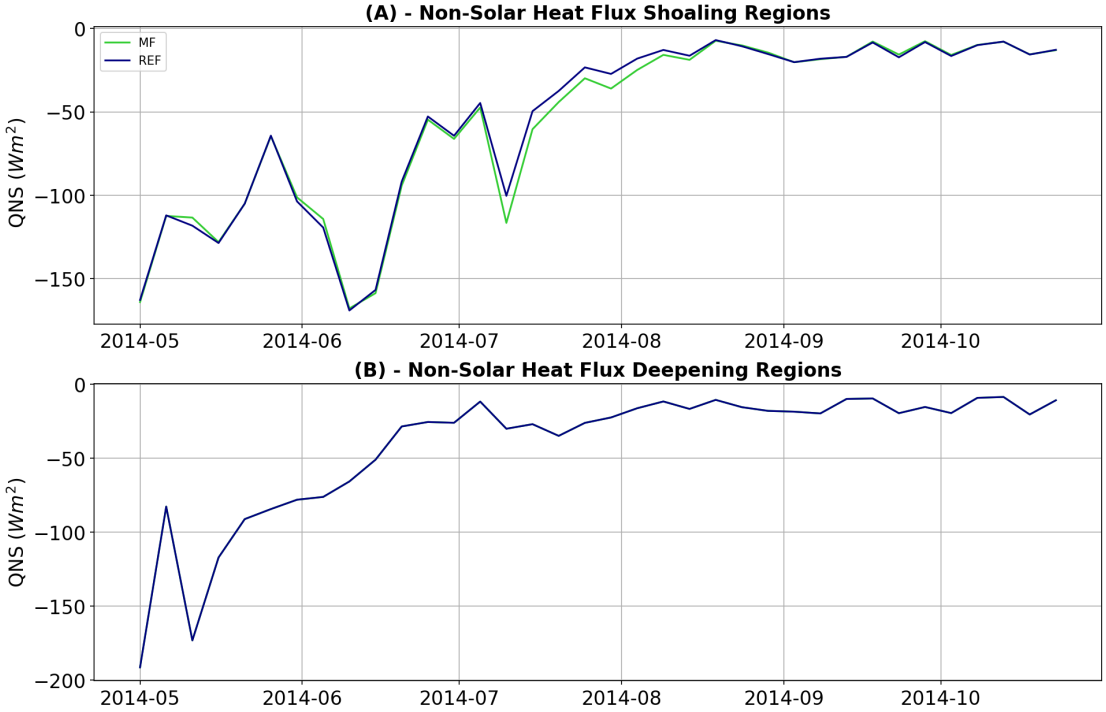

Figure 4.26: The same as figures 4.24 and 4.14 except plotting total non-solar heat fluxes at the sea surface (ocean component).

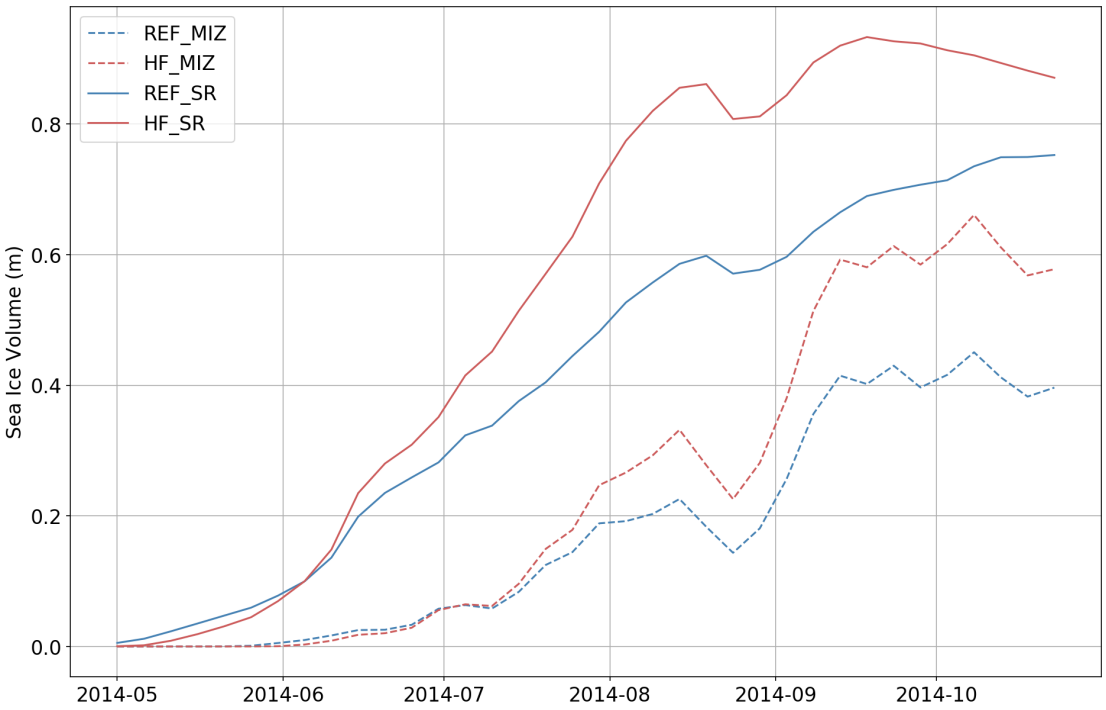

Figure 4.27: Mean ice volume averaged over the SR and MIZ for the HF experiment.

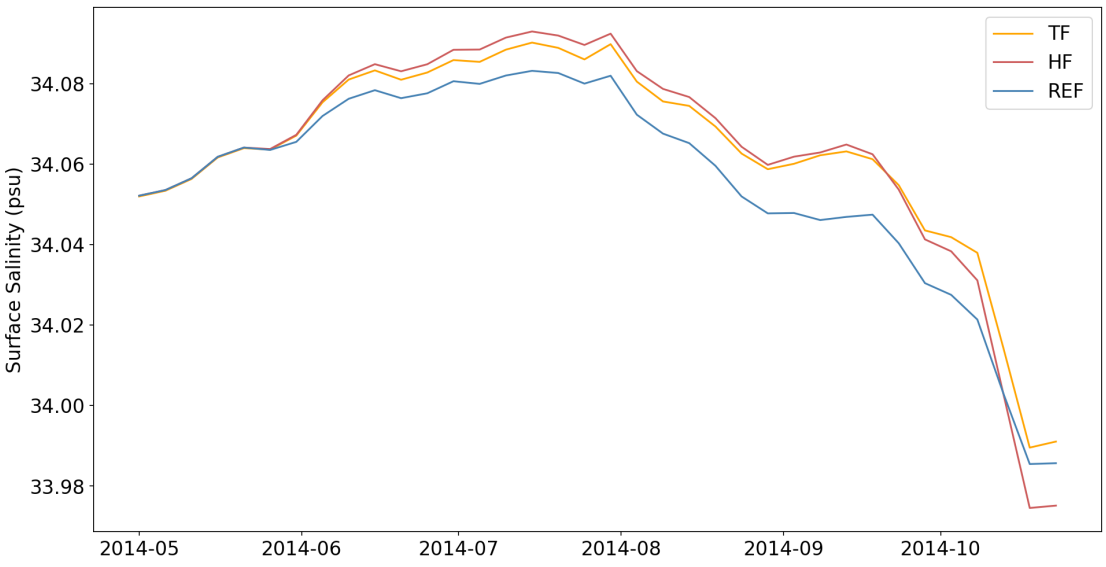

Figure 4.28: Mean surface salinity in the MIZ (55 - 58°S) for the HF, TF and REF runs from May to late October.

Chapter 5

Synthesis

The annual advance and retreat of Antarctic sea ice has profound effects on the primary producers in the region. Some of the most prominent of these effects are connected to the influence sea ice has over the seasonal deepening and shoaling of the mixed layer, thus regulating the light and nutrient available to phytoplankton. Sea ice also more directly affects phenology by strongly (in many cases completely) attenuating light transmission into the surface ocean, as well as by acting as a source of dissolved iron upon melt.

Many studies have sought to characterize Antarctic SSIZ phenology and the drivers of the timing of key biological events such as bloom initiation, peak and decline (Smith and Nelson, 1985; Racault et al., 2012; Taylor et al., 2013; Rohr et al., 2017; Briggs et al., 2017; Uchida et al., 2019). However, such studies rarely utilize more than one or two data sources, generally relying on either satellite or model data, and in some cases in-situ observations from ship-board measurements or autonomous platforms (primarily floats). Furthermore, a large proportion of the present literature is focussed on regions and periods of high productivity (e.g. coastal and shelf regions in summer, recently melted regions in the open ocean in spring). While these regions are no doubt important for, say, carbon export, their study does not necessarily contribute to an understanding of the fundamental drivers of phenology and its spatial variability across the Southern Ocean.

Finally, I am unaware of any studies of phenology which take into account the unique character of Antarctic sea ice cover as discussed in Chapter 1 (section 1.2.2). In particular, strong wind and wave action, coupled with upwelling of warm CDW, maintains a thin and dynamic ice cover which is likely highly permeable to heat and light, with important consequences for the mixed layer and phenology (Uotila et al., 2000; Kohout et al., 2014; Vichi et al., 2019). In this thesis I have used a combination

of models and observations to understand the phenology of the SSIZ, employing both a simple box model and a more complex 3D model (which was used to study the mixed layer in the SSIZ), as well as various observational approaches (satellite, floats, assimilative models and objectively analysed data). In this final chapter I will first bring together the findings of the thesis in section 5.1, after which a discussion of the limitations of the approach taken (section 5.2), as well as an outlook on future research is presented (section 5.3).

5.1 Findings and Conclusions

In this section the main findings of the thesis are used to address the research objectives outlined in section 1.4.1:

1 **Characterize the Antarctic SSIZ phytoplankton phenology using the best available data and compare to climate model (ESM) representation.**

In Chapter 2 we presented the first comprehensive characterization of under ice phenology using a unique bio-ARGO dataset. This dataset of under ice profiles allowed us to overcome many of the shortcomings inherent to satellite and ship-based studies by providing both physical and biological information down to 2000 m, as well as covering the full seasonal cycle. The characterization is focussed on the initial period of growth, the timing of which was determined by the derivative of mixed layer chlorophyll concentration exceeding the median rate.

Based on this it was shown that growth initiation (GI) occurred much earlier than previously estimated from satellite data. Moreover, the results presented here indicate that phytoplankton are able to maintain growth under near complete ice cover and deep mixed layers, conditions previously thought to be inimical to growth. The overall phenology of the Antarctic SSIZ is then one where growth first exceeds losses ($\mu > l$) in August/September, after which the condition is maintained until peak mixed layer chl-a is reached in January/February (giving a growth period of between $\sim$4 and 6 months). This finding broadly agrees with results presented by Uchida et al. (2019), who used the same dataset to more generally characterize phenology over the entire Southern Ocean (although a different conclusion was reached about the drivers of phenology in the SSIZ). However, the findings are in conflict with an earlier study by Briggs et al. (2017), who analysed data from nine floats sampling under ice and concluded that respiration dominated during ice covered periods. This discrepancy is most

likely due to methodological differences, as well as the fact that Briggs et al. (2017) analyse respiration rates for the entire under ice period. Here the focus is on the later winter period when biomass is still very low (but the rate of growth is significant), making it difficult to detect changes associated with production (e.g. a decrease in nitrate concentration).

Interestingly, even though different methodology and data where used to analyse phenology in satellite and float data, similar results for growth initiation timing where obtained for the eastern Weddell Sea region at $\sim$60°S, which is within the study region (58 - 62°S). This is despite the fact that the annual cycles of chl-a are qualitatively very different, with satellite derived growth rates close to zero for July-September, but consistently positive in the float data. While an in-depth analysis of this discrepancy was beyond the scope of the thesis, a reasonable explanation may be argued for involving the sampling bias of satellite data in ice covered regions, as well as the limitations introduced by monthly averaging.

In Chapter 3 we presented a detailed analysis of phenology in a study region which displayed varying degrees of seasonal ice coverage across 11 CMIP5 models. Comparison of phenology in this region revealed several discrepancies with respect to the observed phenology discussed above. Most notable though was the extremely early growth observed in some models, with growth beginning in June and peaking in September/October. In other models phenology was closer to observations, while in one model growth period was from January to April, highlighting the large spread of simulated phenology across CMIP5. It should be noted though that the physical conditions (especially vertical mixing and ice coverage) present in the models were generally unrealistic, an issue which will be discussed further in objective 3 below.

2 Contribute towards an understanding of the drivers of under ice phenology.

A key finding of Chapter 2 was that growth initiation (GI) precedes the release of fresh waters by melting sea ice. This observation contradicted many previous studies, which either implicitly or explicitly endorsed the view that the release of freshwater relieves light and/or nutrient limitation, thus triggering the spring bloom (Smith and Nelson, 1985; Smith and Comiso, 2008; Taylor et al., 2013; Briggs et al., 2017; Uchida et al., 2019). This view, which I termed the ”melt water hypothesis”, implies that variability in the timing of growth should be linked (at least in part) to variability in the timing of melting. Put another way, regions where ice retreats earlier should have growth initiation earlier. However, results presented in Chapter 2 showed that the variability in GI was more strongly

correlated with latitude than with melt timing, indicting that the meridional shift in light regime is more important for SSIZ phenology than melting and associated stratification.

These findings then led to the obvious question of how such early under ice growth could be achieved. Through the use of several biogeochemical box model experiments, we where able to show that both physical and biological factors may be invoked to explain this phenomenon. From a physical stand point, it was shown that one had to assume some level of sea ice permeability with respect to light in order to simulate a phenology close to float observations. Indeed, in some cases simulations with no ice forcing best described the early phases of growth in August/September. On the other hand, later stages of growth in the spring where better captured by models which enhanced phytoplankton low light efficiency, suggesting a role for biological factors such as physiological responses and/or community composition changes.

Furthermore, the relative importance of physical and biological factors showed some dependence on latitude, with ice light transmission becoming more prominent as one moves north into less consolidated ice, and low light adaptation being more important in poleward regions with longer ice seasons and more congealed surfaces. The view which then emerges is one where SSIZ phenology is strongly affected by the type of ice surface present at the start of the growing season. In the outer regions of the SSIZ, strong wind and wave action promote the maintenance of a surface characterized by pancakes embedded in a matrix of frazil ice. Since frazil is highly permeable to light, early growth stages can be effectively modelled by assuming a large fraction of incident light penetrates through the ice. Nevertheless, subsequent growth rates in spring are still hampered by the presence of ice, coupled with relatively deep mixed layers, necessitating an increase in the light harvesting capability of phytoplankton. In regions where the winter ice cover is more consolidated, and light penetration more strongly attenuated, growth can only commence once the ice surface is broken in spring and leads begin to open. Our results indicate that low light efficiency may then allow growth to occur even when lead fractions are less than 10%.

This is in contrast to under ice phenology in climate models, where the presence of ice and deep winter mixing generally inhibit growth. This is discussed in greater detail below in research objective 3.

3 Contribute towards a mechanistic understanding of Antarctic SSIZ phenological biases in ESMs.

In Chapter 3 we sought to understand the mechanisms responsible for the pronounced biases in Southern Ocean phenology present in CMIP5 models. Working from the fact that biases in the seasonality of sea ice extent (Mahlstein et al., 2013; Turner et al., 2013; Purich et al., 2016; Schroeter et al., 2017)) and vertical mixing (Sallée et al., 2013a; Meijers, 2014) had already been identified in the CMIP5 ensemble, we where able to show that a connection existed between these three sets of model shortcomings. The nature of the connection is well summarized by the fact that models where only able to simulate a phenology close to observations if they had either unrealistic seasonal sea ice or biased vertical mixing, but not both.

In the case of sea ice representation, we diagnosed the models based on the mean location of ice edge in winter in the study region, finding that models simulated either far too little winter ice, or slightly too much. In models with pronounced poleward biases in the ice edge location, the lack of ice cover induced stronger heat loss and wind stress, deepening the winter mixed layer and delaying the initiation of growth closer to satellite estimates. On the other hand, models with a slight overestimation of the winter ice extent (equatorward bias) tended to also be highly stratified year round, yet their bloom initiation was similar to those models with strong poleward biases in ice edge location. In this case, the presence of high ice concentrations ($>$80%) severely limits light availability (despite a relatively shallow mixed layer), again delaying growth initiation. A final group of models with both too little ice cover and shallow mixed layers, predictably simulated bloom initiation far earlier than is observed (June instead of September).

Another key finding of Chapter 3 was a robust correlation between the ice edge location and the stratification depth, ND, which suggested that the presence of ice in the study region tended to inhibit mixing. Indeed, observational estimates indicated that the mean winter value of ND varies between $\sim$100 m and 140 m, while CMIP5 models with high winter ice concentrations simulated ND between $\sim$50 m and 100 m. Given the evidence for high light permeability provided in Chapter 2, this correlation suggested that model sea ice artificially dampened winter heat and momentum fluxes in the SSIZ, leading to shallow biases in ND. This then provided the motivation to study sea ice modulated fluxes in greater detail in Chapter 4.

4 Improve understanding of sea ice modulation of heat and momentum fluxes and their impact of the surface mixed layer in the Antarctic SSIZ.

The primary tool used to address this research objective was a numerical ice-

ocean model, from which we conducted several experiments altering the sea ice modulation of heat and momentum exchanges between atmosphere and ocean (Chapter 4). This allowed us to test the sensitivity of the mixed layer to the imposed changes, and thus to asses the relative contribution of heat and momentum fluxes, as well as regional variability in the response (i.e. in regions with differing ice regimes).

In the first experiment, ocean-atmosphere heat fluxes in ice covered regions where uniformly increased by 10%. This lead to an amplification of the seasonal cycle, with more ice retreat is late summer and more northward expansion in winter (compared to the reference run). This was associated with an approximately zonally banded response in the model winter stratification depth (ND), with dampened mixing in the outer MIZ, contrasted with enhanced mixing further south. In the MIZ, shoaling of ND was driven by enhanced melt water production in August/September associated with the aforementioned northern expansion. Deepening of ND further south was associated with increased heat loss through the winter, which drove increased ice (brine) production, thus enhancing convective mixing.

The second experiment enhanced the momentum flux by increasing the air-ice drag coefficient by $\sim$50%, which, based on theoretical considerations, should enhance turbulence and deepen the mixed layer. The model response in this case was less pronounced and more spatially heterogeneous than in the heat flux experiment, with a more complex interpretation of the underlying mechanisms. In essence, it was found that although the increased momentum transfer did enhance turbulence in the mixed layer, this did not lead to an increase in the depth of the mixed layer or the value of ND in all regions. This variability in model response was linked to an negative ice-ocean feedback, whereby the enhanced turbulence deepened vertical mixing, leading to warm water entrainment and bottom melting of sea ice, thus enhancing stratification. Regions where ND shoaled under increased air-ice drag where characterized by this feedback, while in regions where ND deepened, vertical mixing was insufficiently deep to entrain warm CDW waters. Thus, the feedback did not operate in these regions and the stratification depth was shifted deeper into the water column by the enhanced turbulence.

In summary, we found that the model mixed layer was highly sensitive to the imposed changes in ice mediated fluxes, although the response also displayed high spatial variability. The results also showed that the model was more sensitive to heat fluxes changes than momentum, suggesting that the climate

model mixed layer biases reported in Chapter 3 may be due to underestimated sea ice permeability (with respect to ocean-atmosphere heat exchange). Moreover, we hypothesized in Chapter 4 that the deepened mixed layer associated with a more permeable and dynamic ice surface may improve climate model representation of phenology (if implemented more realistically than is done here) by delaying the onset of late winter/spring growth. However, it must be noted that this would have to be accompanied by a realistic sea ice seasonal evolution, something which most models are missing. In addition, the physiological response of the phytoplankton community to the unique under ice environment discussed in Chapter 2 also warrants consideration. In the end, it could be argued that incorporating all the model alterations performed in this thesis (enhanced sea ice heat and light permeability, increased air-ice drag and higher phytoplankton low light efficiency) would improve modelled phenology, given that each have a direct impact on the annual cycle of growth and decline. How each of the factors would combine to affect the overall phenology remains a topic for future research.

5.2 Limitations

Following the preceding discussion, the limitations of this thesis can be similarly grouped by the four primary research objectives. This will then lay the foundation for the discussion of future research in section 5.3. In terms of characterizing SSIZ phenology, the major challenges are related to the scarcity of under ice winter data. Even though our analysis of the available under ice float data represents a significant improvement, the overall spatial and temporal coverage is still relatively poor. Given the high spatial variability of the Southern Ocean (Thomalla et al. (2011)), the 42 seasonal cycles analysed in Chapter 2, while representative of a diverse set of environmental conditions, are certainly not sufficient for a fully comprehensive characterization of phenology. Moreover, the float dataset is only available from 2014 to present, with 2017 and 2018 containing the bulk of the available data in the analysis. Another limitation of the data is the 10 day sampling frequency, which introduces some uncertainty in the estimation of the timing of growth initiation and sea ice melt. This uncertainty is further amplified by the monthly frequency of the CMIP5 output analysed in Chapter 3, which was then compared to monthly averages of satellite data.

Understanding of the drivers of under ice phenology is also limited by the scarcity of data. In particular, the under ice floats do not sample the upper $\sim$20 m of the water column in winter, thus missing any productivity occurring there as well as any early

melting. It is unclear whether such near surface signals would be mixed into deeper layers, and so this limitation may introduce uncertainty into our estimation of the timing difference between melting and growth initiation. Furthermore, since the exact location of the float is unknown while under ice, the corresponding values of satellite sea ice concentration used to force the box model experiments of Chapter 2 may contain errors. The magnitude of the errors will be related to the spatial variability of ice concentration in the vicinity of the floats, along with error associated with the retrieval algorithm itself (Brucker et al., 2014).

The major limitations related to the diagnosis of climate model biases where the monthly resolution of the output mentioned above, as well as the methodology used to asses the CMIP5 ensemble. Specifically, much of the conclusions drawn from Chapter 3 are based on correlations between spatially averaged properties such as the ice edge location, ND and month of bloom initiation. This kind of analysis is common, and is very useful in forming hypotheses about the mechanisms driving phenomena in complex climate models, such as the control of light availability by sea ice cover, which then affects phenology. However, an explicit demonstration of the relationship between processes usually requires more specialized model experiments to be conducted. That is, the attribution of model biases to particular processes can be made explicit by comparing simulations where features of the model have been intentionally changed, as was done in Chapters 2 and 4.

The investigation of sea ice mediated fluxes and their impact on vertical mixing was the primary goal of Chapter 4. Here several model sensitivity experiments where conducted, which looked at the response of the mixed layer to enhancements of heat and momentum fluxes through sea ice. A major caveat of the study though was the implementation of these flux alterations, which where not linked to physical characteristics of the ice surface. There is also reason to believe that the sea ice model does not adequately represent the ice surface characteristics, since it does not take into account the unique frazil/pancake formation process typical of the Southern Ocean (Doble, 2009). Similarly, the fairly simplistic implementation of sea ice modulation of light in the box model experiments stands in contrast to the known differences in the light penetration properties of different ice types (Perovich, 2017). A final limitation which we can highlight here is the focus on purely physical processes without the inclusion of a biogeochemical model in Chapter 4. Although this can be justified by the many unknowns involved, in including an adequate representation of plankton physiology and ecology in ice-covered regions, this would have allowed for an in depth investigation into the effect sea ice mediated heat and momentum fluxes have on phenology (through their influence on vertical mixing), something which could only

be indirectly inferred in this thesis.

5.3 Future Research

In my attempt to address the research objectives outlined in section 1.4.1, many new questions where raised that could shape future research activities. With regards to characterizing and understanding Antarctic SSIZ phenology, the results of Chapter 2 point to exciting future for autonomous platforms in this challenging environment. For example, under ice gliders capable of sampling at much higher frequencies (sub-daily - e.g. Swart et al. (2015); Little et al. (2018)) would reduce the uncertainties in both phenological metrics (e.g. growth initiation, peak, decline) and melt timing derived from float data. Uncertainty in melt timing could be further constrained if location data for under ice floats was made available, although this remains a challenging objective (Riser et al., 2018). Nevertheless, high resolution satellite ice concentration data could then be matched to the float location, with the timing of concentration reduction compared to the timing of freshwater release measured by the float to arrive at a more robust estimate of melt timing. Indeed, such a comparison of under ice profiles collocated with satellite data may already be possible with the instrumented seal dataset, although biogeochemical data are lacking in that case.

In Chapter 2 we also saw that fairly simple models could be used in conjunction with observations to gain further insight into under ice phenology. Although our specific research question warranted the use of a box model, slightly more complex 1-D biogeochemical models could be employed in a similar fashion. Such models could then simulate a dynamic mixed layer which responds to forcing, allowing for an investigation of the potential role played by the relative shoaling of the turbocline and mixed layer depths, which would impact under ice phenology. An active sea ice model could also be coupled, which would permit a more sophisticated representation of the ice cover than was presented in Chapter 2. For example, a simple slab mixed layer model described by Doble (2009) explicitly takes into account the frazil/pancake ice formation cycle, simulating a varying fraction of the two ice types for a short period in autumn. This could be extended to give differing light penetration based the fraction of frazil ice present, allowing for light availability even under complete ice cover.

In the case of coupled 3-D models, the results of Chapters 3 and 4 suggest that much further research is needed into the simulation of the unique Southern Ocean ice surface and it's modulation of atmosphere-ocean fluxes. In particular, processes involved in frazil and pancake formation (see section 1.2.2) should be included in fully coupled

simulations, which to my knowledge, have only been included in specialized case studies (i.e. not in ocean GCMs, see for example Doble (2009); Matsumura and Ohshima (2015)). This would potentially allow models to better capture heat fluxes in the ice covered ocean by maintaining a highly permeable fraction of frazil throughout the winter, thus deepening the mixed layer as was seen in Chapter 4 and possibly improving phenology. Indeed, investigating the response of under ice phytoplankton to the perturbations imposed in Chapter 4 would require coupling with a biogeochemical model, which may provide an interesting future research project. Whether this can be implemented with the standard viscous-plastic rheology certainly requires in depth research.

References

Abernathey, R.P., Cerovecki, I., Holland, P.R., Newsom, E., Mazloff, M., Talley, L.D., 2016. Water-mass transformation by sea ice in the upper branch of the Southern Ocean overturning. Nature Geoscience 9, 596–601. URL: http://www.nature.com/doifinder/10.1038/ngeo2749, doi:doi: 10.1038/ngeo2749.

Adachi, Y., Yukimoto, S., Deushi, M., Obata, A., Nakano, H., Tanaka, T.Y., Hosaka, M., Sakami, T., Yoshimura, H., Hirabara, M., Shindo, E., Tsujino, H., Mizuta, R., Yabu, S., Koshiro, T., Ose, T., Kitoh, A., 2013. Basic performance of a new earth system model of the Meteorological Research Institute. Papers in Meteorology and Geophysics 64, 1–19. doi:doi: 10.2467/mripapers.64.1.

Alberello, A., Onorato, M., Bennetts, L., Vichi, M., Eayrs, C., MacHutchon, K., Toffoli, A., 2019. Brief communication: Pancake ice floe size distribution during the winter expansion of the Antarctic marginal ice zone. The Cryosphere 13, 41–48. URL: https://www.the-cryosphere.net/13/41/2019/, doi:doi: 10.5194/tc-13-41-2019.

Anav, A., Friedlingstein, P., Kidston, M., Bopp, L., Ciais, P., Cox, P., Jones, C., Jung, M., Myneni, R., Zhu, Z., 2013. Evaluating the Land and Ocean Components of the Global Carbon Cycle in the CMIP5 Earth System Models. Journal of Climate 26, 6801–6843. URL: https://doi.org/10.1175/JCLI-D-12-00417.1, doi:doi: 10.1175/JCLI-D-12-00417.1.

Andreas, E.L., Tucker III, W.B., Ackley, S.F., 1984. Atmospheric boundary-layer modification, drag coefficient, and surface heat flux in the Antarctic marginal ice zone. Journal of Geophysical Research: Oceans 89, 649–661. URL: https://agupubs.onlinelibrary.wiley.com/doi/abs/10.1029/JC089iC01p00649, doi:doi: 10.1029/JC089iC01p00649.

Ardyna, M., Claustre, H., D'Ortenzio, F., van Dijken, G., Arrigo, K.R., D'Ovidio, F., Gentili, B., Sallée, J.B., 2017. Delineating environmental control of phytoplankton biomass and phenology in the Southern Ocean. Geophysical Research Letters 44, 5016–5024. doi:doi: 10.1002/2016gl072428.

Arndt, S., Hoppmann, M., Schmithüsen, H., Fraser, A.D., Nicolaus, M., 2020. Seasonal and interannual variability of landfast sea ice in Atka Bay, Weddell Sea, Antarctica. The Cryosphere 14, 2775–2793. URL: https://tc.copernicus.org/articles/14/2775/2020/, doi:doi: 10.5194/tc-14-2775-2020.

Arndt, S., Meiners, K.M., Ricker, R., Krumpen, T., Katlein, C., Nicolaus, M., 2017. Influence of snow depth and surface flooding on light transmission through

Antarctic pack ice. Journal of Geophysical Research: Oceans 122, 2108–2119. URL: https://agupubs.onlinelibrary.wiley.com/doi/abs/10.1002/2016JC012325, doi:doi: 10.1002/2016JC012325.

Arrigo, K., 2017. Sea ice as a habitat for primary producers, in: Thomas, D. (Ed.), Sea Ice. thrid ed.. John Wiley & Sons, Ltd. chapter 14, pp. 353 – 369.

Arrigo, K., Perovich, D.K., Pickart, R.S., Brown, Z.W., van Dijken, G.L., Lowry, K.E., Mills, M.M., Palmer, M.A., Balch, W.M., Bahr, F., Bates, N.R., Benitez-Nelson, C., Bowler, B., Brownlee, E., Ehn, J.K., Frey, K.E., Garley, R., Laney, S.R., Lubelczyk, L., Mathis, J., Matsuoka, A., Mitchell, B.G., Moore, G.W.K., Ortega-Retuerta, E., Pal, S., Polashenski, C.M., Reynolds, R.A., Schieber, B., Sosik, H.M., Stephens, M., Swift, J.H., 2012. Massive Phytoplankton Blooms Under Arctic Sea Ice. Science 336, 1408. URL: https://science.sciencemag.org/content/336/6087/1408, doi:doi: 10.1126/science.1215065.

Arrigo, K., Thomas, D., 2004. Large scale importance of sea ice biology in the Southern Ocean. Antarctic Science 16, 471–486. URL: http://www.journals.cambridge.org/abstract{_}S0954102004002263, doi:doi: 10.1017/S0954102004002263.

Assmy, P., Fernández-Méndez, M., Duarte, P., Meyer, A., Randelhoff, A., Mundy, C.J., Olsen, L.M., Kauko, H.M., Bailey, A., Chierici, M., Cohen, L., Doulgeris, A.P., Ehn, J.K., Fransson, A., Gerland, S., Hop, H., Hudson, S.R., Hughes, N., Itkin, P., Johnsen, G., King, J.A., Koch, B.P., Koenig, Z., Kwasniewski, S., Laney, S.R., Nicolaus, M., Pavlov, A.K., Polashenski, C.M., Provost, C., Rösel, A., Sandbu, M., Spreen, G., Smedsrud, L.H., Sundfjord, A., Taskjelle, T., Tatarek, A., Wiktor, J., Wagner, P.M., Wold, A., Steen, H., Granskog, M.A., 2017. Leads in Arctic pack ice enable early phytoplankton blooms below snow-covered sea ice. Scientific Reports 7, 40850. URL: https://doi.org/10.1038/srep40850http://10.0.4.14/srep40850https://www.nature.com/articles/srep40850{#}supplementary-information.

Behrenfeld, M.J., 2010. Abandoning Sverdrup's Critical Depth Hypothesis on phytoplankton blooms. Ecology 91, 977–989. URL: https://esajournals.onlinelibrary.wiley.com/doi/abs/10.1890/09-1207.1, doi:doi: 10.1890/09-1207.1.

Behrenfeld, M.J., Boss, E.S., 2014. Resurrecting the Ecological Underpinnings of Ocean Plankton Blooms. Annual Review of Marine Science 6, 167–194. URL: http://www.annualreviews.org/doi/10.1146/annurev-marine-052913-021325, doi:doi: 10.1146/annurev-marine-052913-021325.

Behrenfeld, M.J., Boss, E.S., 2018. Student's tutorial on bloom hypotheses in the context of phytoplankton annual cycles. Global Change Biology 24, 55–77. doi:doi: 10.1111/gcb.13858.

Behrenfeld, M.J., Hu, Y., O'Malley, R.T., Boss, E.S., Hostetler, C.A., Siegel, D.A., Sarmiento, J.L., Schulien, J., Hair, J.W., Lu, X., Rodier, S., Scarino, A.J., 2017. Annual boom–bust cycles of polar phytoplankton biomass revealed by space-based lidar. Nature Geoscience 10, 118–122. URL: https://doi.org/10.1038/ngeo2861, doi:doi: 10.1038/ngeo2861.

Bellacicco, M., Volpe, G., Colella, S., Pitarch, J., Santoleri, R., 2016. Influence of photoacclimation on the phytoplankton seasonal cycle in the Mediterranean Sea as

seen by satellite. Remote Sensing of Environment 184, 595–604. URL: http://www.sciencedirect.com/science/article/pii/S0034425716303078, doi:doi: https://doi.org/10.1016/j.rse.2016.08.004.

Bernard, B., Madec, G., Penduff, T., Molines, J.M., Treguier, A.M., Le Sommer, J., Beckmann, A., Biastoch, A., Böning, C., Dengg, J., Derval, C., Durand, E., Gulev, S., Remy, E., Talandier, C., Theetten, S., Maltrud, M., McClean, J., De Cuevas, B., 2006. Impact of partial steps and momentum advection schemes in a global ocean circulation model at eddy-permitting resolution. Ocean Dynamics 56, 543–567. URL: https://doi.org/10.1007/s10236-006-0082-1, doi:doi: 10.1007/s10236-006-0082-1.

Bing, T., Peng, L., Zhijun, L., Runling, L., 2013. Form drag on pressure ridges and drag coefficient in the northwestern Weddell Sea, Antarctica, in winter. Annals of Glaciology 54, 133–138. doi:doi: 10.3189/2013AoG62A092.

Blockley, E., Vancoppenolle, M., Hunke, E., Bitz, C., Feltham, D., Lemieux, J.F., Losch, M., Maisonnave, E., Notz, D., Rampal, P., Tietsche, S., Tremblay, B., Turner, A., Massonnet, F., Ólason, E., Roberts, A., Aksenov, Y., Fichefet, T., Garric, G., Iovino, D., Madec, G., Rousset, C., y Melia, D., Schroeder, D., 2020. The Future of Sea Ice Modeling: Where Do We Go from Here? Bulletin of the American Meteorological Society 101, E1304–E1311. URL: https://doi.org/10.1175/BAMS-D-20-0073.1, doi:doi: 10.1175/BAMS-D-20-0073.1.

Bouman, H.A., Platt, T., Doblin, M., Figueiras, F.G., Gudmundsson, K., Gudfinnsson, H.G., Huang, B., Hickman, A., Hiscock, M., Jackson, T., Lutz, V.A., Melin, F., Rey, F., Pepin, P., Segura, V., Tilstone, G.H., van Dongen-Vogels, V., Sathyendranath, S., 2018. Photosynthesis irradiance parameters of marine phytoplankton: synthesis of a global data set. Earth System Science Data 10, 251–266. URL: http://plymsea.ac.uk/id/eprint/7822/, doi:doi: https://doi.org/10.5194/essd-10-251-2018.

Boyd, P., LaRoche, J., Gall, M., Frew, R., McKay, R.M.L., 1999. Role of iron, light, and silicate in controlling algal biomass in subantarctic waters SE of New Zealand. Journal of Geophysical Research: Oceans 104, 13395–13408. URL: https://agupubs.onlinelibrary.wiley.com/doi/abs/10.1029/1999JC900009, doi:doi: 10.1029/1999JC900009.

Boyd, P.W., 2002. Review of environmental factors controlling phytoplankton processes in the Southern Ocean 1. Journal of Phycology 38, 844–861. doi:doi: 10.1046/j.1529-8817.2002.t01-1-01203.x.

Bracegirdle, T.J., Shuckburgh, E., Sallee, J.B., Wang, Z., Meijers, A.J.S., Bruneau, N., Phillips, T., Wilcox, L.J., 2013. Assessment of surface winds over the atlantic, indian, and pacific ocean sectors of the southern ocean in cmip5 models: Historical bias, forcing response, and state dependence. Journal of Geophysical Research Atmospheres 118, 547–562. doi:doi: 10.1002/jgrd.50153.

Briggs, E.M., Martz, T.R., Talley, L.D., Mazloff, M., Johnson, K.S., 2017. Physical and Biological Drivers of Biogeochemical Tracers Within the Seasonal Sea Ice Zone of the Southern Ocean From Profiling Floats. Journal of Geophysical Research: Oceans 123, 746–758. doi:doi: 10.1002/2017JC012846.

Brucker, L., Cavalieri, D.J., Markus, T., Ivanoff, A., 2014. NASA Team 2 Sea Ice Concentration Algorithm Retrieval Uncertainty. IEEE Transactions on Geoscience and Remote Sensing 52, 7336–7352. doi:doi: 10.1109/TGRS.2014.2311376.

Buchan, A., LeCleir, G.R., Gulvik, C.A., González, J.M., 2014. Master recyclers: features and functions of bacteria associated with phytoplankton blooms. Nature Reviews Microbiology 12, 686–698. URL: https://doi.org/10.1038/nrmicro3326, doi:doi: 10.1038/nrmicro3326.

Buesseler, K.O., Barber, R.T., Dickson, M.L., Hiscock, M.R., Moore, J.K., Sambrotto, R., 2003. The effect of marginal ice-edge dynamics on production and export in the Southern Ocean along 170°W. Deep-Sea Research Part II: Topical Studies in Oceanography 50, 579–603. doi:doi: 10.1016/S0967-0645(02)00585-4.

Carranza, M., Gille, S., 2014. Southern Ocean wind-driven entrainment enhances satellite chlorophyll-a through the summer. Journal of Geophysical Research: Oceans , 1022–1037doi:doi: 10.1002/2013JC009415.Received.

Carranza, M.M., Gille, S.T., Franks, P.J.S., Johnson, K.S., Pinkel, R., Girton, J.B., 2018. When Mixed Layers Are Not Mixed. Storm-Driven Mixing and Bio-optical Vertical Gradients in Mixed Layers of the Southern Ocean. Journal of Geophysical Research: Oceans 123, 7264–7289. URL: https://agupubs.onlinelibrary.wiley.com/doi/abs/10.1029/2018JC014416, doi:doi: 10.1029/2018JC014416.

Carvalho, F., Kohut, J., Oliver, M.J., Schofield, O., 2017. Defining the ecologically relevant mixed-layer depth for Antarctica's coastal seas. Geophysical Research Letters 44, 338–345. URL: https://agupubs.onlinelibrary.wiley.com/doi/abs/10.1002/2016GL071205, doi:doi: 10.1002/2016GL071205.

Cavanagh, R.D., Murphy, E.J., Bracegirdle, T.J., Turner, J., Knowland, C.A., Corney, S.P., Smith, W.O., Waluda, C.M., Johnston, N.M., Bellerby, R.G.J., Constable, A.J., Costa, D.P., Hofmann, E.E., Jackson, J.A., Staniland, I.J., Wolf-Gladrow, D., Xavier, J.C., 2017. A Synergistic Approach for Evaluating Climate Model Output for Ecological Applications. Frontiers in Marine Science 4. URL: http://journal.frontiersin.org/article/10.3389/fmars.2017.00308/full, doi:doi: 10.3389/fmars.2017.00308.

Chylek, P., J., Li, M., K., Dubey, M., W., Lesins, G., 2011. Observed and model simulated 20th century Arctic temperature variability: Canadian Earth System Model CanESM2. Atmospheric Chemistry and Physics Disscussions .

Coale, K.H., Johnson, K.S., Chavez, F.P., Buesseler, K.O., Barber, R.T., Brzezinski, M.A., Cochlan, W.P., Millero, F.J., Falkowski, P.G., Bauer, J.E., Wanninkhof, R.H., Kudela, R.M., Altabet, M.A., Hales, B.E., Takahashi, T., Landry, M.R., Bidigare, R.R., Wang, X., Chase, Z., Strutton, P.G., Friederich, G.E., Gorbunov, M.Y., Lance, V.P., Hilting, A.K., Hiscock, M.R., Demarest, M., Hiscock, W.T., Sullivan, K.F., Tanner, S.J., Gordon, R.M., Hunter, C.N., Elrod, V.A., Fitzwater, S.E., Jones, J.L., Tozzi, S., Koblizek, M., Roberts, A.E., Herndon, J., Brewster, J., Ladizinsky, N., Smith, G., Cooper, D., Timothy, D., Brown, S.L., Selph, K.E., Sheridan, C.C., Twining, B.S., Johnson, Z.I., 2004. Southern Ocean Iron Enrichment Experiment: Carbon Cycling in High- and Low-Si Waters. Science 304, 408–414. URL: https://science.sciencemag.org/content/304/5669/408, doi:doi: 10.1126/science.1089778.

Cole, H., Henson, S., Martin, A., Yool, A., 2012. Mind the gap: The impact of missing data on the calculation of phytoplankton phenology metrics. Journal of Geophysical Research: Oceans 117. URL: https://agupubs.onlinelibrary.wiley.com/doi/abs/10.1029/2012JC008249, doi:doi: 10.1029/2012JC008249.

Collins, W.J., Bellouin, N., Doutriaux-Boucher, M., Gedney, N., Halloran, P., Hinton, T., Hughes, J., Jones, C.D., Joshi, M., Liddicoat, S., Martin, G., O'Connor, F., Rae, J., Senior, C., Sitch, S., Totterdell, I., Wiltshire, A., Woodward, S., 2011. Development and evaluation of an Earth-System model – HadGEM2. Geoscientific Model Development 4, 1051–1075. URL: http://www.geosci-model-dev.net/4/1051/2011/, doi:doi: 10.5194/gmd-4-1051-2011.

Cushman-Roisin, B., Beckers, J.M., 2007. Introduction to Geophysical Fluid Dynamics: Physical and Numerical Aspects. Academic Press.

Dafner, E., Mordasova, N., Arzhanova, N., Maslennikov, V., Mikhailovsky, Y., Naletova, I., Sapozhnikov, V., Selin, P., Zubarevich, V., 2003. Major nutrients and dissolved oxygen as indicators of the frontal zones in the Atlantic sector of the Southern Ocean. Journal of Geophysical Research: Oceans 108. URL: https://agupubs.onlinelibrary.wiley.com/doi/abs/10.1029/1999JC000288, doi:doi: 10.1029/1999JC000288.

de Boyer Montégut, C., Madec, G., Fischer, A.S., Lazar, A., Iudicone, D., 2004. Mixed layer depth over the global ocean: An examination of profile data and a profile-based climatology. Journal of Geophysical Research: Oceans 109. URL: https://agupubs.onlinelibrary.wiley.com/doi/abs/10.1029/2004JC002378, doi:doi: 10.1029/2004JC002378.

Deppeler, S.L., Davidson, A.T., 2017. Southern Ocean Phytoplankton in a Changing Climate. Frontiers in Marine Science 4, 40. URL: http://journal.frontiersin.org/article/10.3389/fmars.2017.00040/full, doi:doi: 10.3389/fmars.2017.00040.

Doble, M.J., 2009. Simulating pancake and frazil ice growth in the Weddell Sea: A process model from freezing to consolidation. Journal of Geophysical Research: Oceans 114. URL: https://agupubs.onlinelibrary.wiley.com/doi/abs/10.1029/2008JC004935, doi:doi: 10.1029/2008JC004935.

Doble, M.J., Coon, M.D., Wadhams, P., 2003. Pancake ice formation in the Weddell Sea. Journal of Geophysical Research: Oceans 108. URL: https://agupubs.onlinelibrary.wiley.com/doi/abs/10.1029/2002JC001373, doi:doi: 10.1029/2002JC001373.

Dubinsky, Z., Stambler, N., 2009. Photoacclimation processes in phytoplankton: mechanisms, consequences, and applications . Aquatic Microbial Ecology 56, 163–176. URL: https://www.int-res.com/abstracts/ame/v56/n2-3/p163-176/.

Dunne, J.P., John, J.G., Shevliakova, S., Stouffer, R.J., Krasting, J.P., Malyshev, S.L., Milly, P.C.D., Sentman, L.T., Adcroft, A.J., Cooke, W., Dunne, K.A., Griffies, S.M., Hallberg, R.W., Harrison, M.J., Levy, H., Wittenberg, A.T., Phillips, P.J., Zadeh, N., 2013a. GFDL's ESM2 global coupled climate-carbon earth system models. Part I: Physical Formulation and Baseline Simulation Characteristics. Journal of Climate 26, 2247–2267. doi:doi: 10.1175/JCLI-D-12-00150.1.

Dunne, J.P., John, J.G., Shevliakova, S., Stouffer, R.J., Krasting, J.P., Malyshev, S.L., Milly, P.C.D., Sentman, L.T., Adcroft, A.J., Cooke, W., Dunne, K.A., Griffies, S.M., Hallberg, R.W., Harrison, M.J., Levy, H., Wittenberg, A.T., Phillips, P.J., Zadeh, N., 2013b. GFDL's ESM2 global coupled climate-carbon earth system models. Part II: Carbon system formulation and baseline simulation characteristics. Journal of Climate 26, 2247–2267. doi:doi: 10.1175/JCLI-D-12-00150.1.

Dutkiewicz, S., 2020. Synergy between Ocean Colour and Biogeochemical/Ecosystem Models. IOCCG Report Series 19. URL: http://dx.doi.org/10.25607/OBP-711.

Eayrs, C., Holland, D., Francis, D., Wagner, T., Kumar, R., Li, X., 2019. Understanding the Seasonal Cycle of Antarctic Sea Ice Extent in the Context of Longer-Term Variability. Reviews of Geophysics 57, 1037–1064. URL: https://agupubs.onlinelibrary.wiley.com/doi/abs/10.1029/2018RG000631, doi:doi: 10.1029/2018RG000631.

Elvidge, A.D., Renfrew, I.A., Weiss, A.I., Brooks, I.M., Lachlan-Cope, T.A., King, J.C., 2016. Observations of surface momentum exchange over the marginal ice zone and recommendations for its parametrisation. Atmospheric Chemistry and Physics 16, 1545–1563. doi:doi: 10.5194/acp-16-1545-2016.

Fauchereau, N., Tagliabue, A., Bopp, L., Monteiro, P.M.S., 2011. The response of phytoplankton biomass to transient mixing events in the Southern Ocean. Geophysical Research Letters 38, 1–6. doi:doi: 10.1029/2011GL048498.

Fischer, A.D., Moberg, E.A., Alexander, H., Brownlee, E.F., Hunter-Cevera, K.R., Pitz, K.J., Rosengard, S.Z., Sosik, H.M., 2014. Sixty years of Sverdrup a retrospective of progress in the study of phytoplankton blooms. Oceanography 27, 222–235. doi:doi: 10.5670/oceanog.2014.26.

Flather, R.A., 1994. A Storm Surge Prediction Model for the Northern Bay of Bengal with Application to the Cyclone Disaster in April 1991. Journal of Physical Oceanography 24, 172–190. URL: https://doi.org/10.1175/1520-0485(1994)024{%}3C0172:ASSPMF{%}3E2.0.CO;2, doi:doi: 10.1175/1520-0485(1994)024⟨0172:ASSPMF⟩2.0.CO;2.

Flato, G.M., 2011. Earth system models: an overview. WIREs Climate Change 2, 783–800. URL: https://onlinelibrary.wiley.com/doi/abs/10.1002/wcc.148, doi:doi: 10.1002/wcc.148.

Franks, P.J.S., 2015. Has Sverdrup's critical depth hypothesis been tested? Mixed layers vs. turbulent layers. ICES Journal of Marine Science 72, 1897–1907. doi:doi: 10.1093/icesjms/fsu175.

Fritsen, C.H., Wirthlin, E.D., Momberg, D.K., Lewis, M.J., Ackley, S.F., 2011. Bio-optical properties of Antarctic pack ice in the early austral spring. Deep Sea Research Part II: Topical Studies in Oceanography 58, 1052–1061. URL: https://www.sciencedirect.com/science/article/pii/S0967064510003139, doi:doi: 10.1016/J.DSR2.2010.10.028.

Frölicher, T.L., Sarmiento, J.L., Paynter, D.J., Dunne, J.P., Krasting, J.P., Winton, M., 2015. Dominance of the Southern Ocean in Anthropogenic Carbon and Heat Uptake in CMIP5 Models. Journal of Climate 28, 862–886. URL: https://doi.org/10.1175/JCLI-D-14-00117.1, doi:doi: 10.1175/JCLI-D-14-00117.1.

Garrison, D.L., Buck, K.R., Fryxell, G.A., 1987. ALGAL ASSEMBLAGES IN ANTARCTIC PACK ICE AND IN ICE-EDGE PLANKTON1. Journal of Phycology 23, 564–572. URL: https://onlinelibrary.wiley.com/doi/abs/10.1111/j.1529-8817.1987.tb04206.x, doi:doi: 10.1111/j.1529-8817.1987.tb04206.x.

Giles, A.B., Massom, R.A., Lytle, V.I., 2008. Fast-ice distribution in East Antarctica during 1997 and 1999 determined using RADARSAT data. Journal of Geophysical Research: Oceans 113. URL: https://agupubs.onlinelibrary.wiley.com/doi/abs/10.1029/2007JC004139, doi:doi: 10.1029/2007JC004139.

Gill, A., 1982. Atmosphere-Ocean Dynamics. International Geophysics.

Gille, S.T., McKee, D.C., Martinson, D.G., 2016. Temporal Changes in the Antarctic Circumpolar Current: Implications for the Antarctic Continental Shelves. Oceanography 29, 96–105. URL: http://www.jstor.org/stable/24862285.

Goosse, H., Fichefet, T., 1999. Importance of ice-ocean interactions for the global ocean circulation: A model study. Journal of Geophysical Research: Oceans 104, 23337–23355. URL: https://agupubs.onlinelibrary.wiley.com/doi/abs/10.1029/1999JC900215, doi:doi: 10.1029/1999JC900215.

Gordon, A.L., 1981. Seasonality of Southern Ocean sea ice. Journal of Geophysical Research: Oceans 86, 4193–4197. URL: https://agupubs.onlinelibrary.wiley.com/doi/abs/10.1029/JC086iC05p04193, doi:doi: 10.1029/JC086iC05p04193.

Gordon, A.L., Huber, B.A., 1984. Thermohaline stratification below the Southern Ocean sea ice. Journal of Geophysical Research: Oceans 89, 641–648. URL: https://agupubs.onlinelibrary.wiley.com/doi/abs/10.1029/JC089iC01p00641, doi:doi: 10.1029/JC089iC01p00641.

Gordon, A.L., Huber, B.A., 1990. Southern ocean winter mixed layer. Journal of Geophysical Research: Oceans 95, 11655–11672. URL: https://agupubs.onlinelibrary.wiley.com/doi/abs/10.1029/JC095iC07p11655, doi:doi: 10.1029/JC095iC07p11655.

Graham, R.M., de Boer, A.M., Heywood, K.J., Chapman, M.R., Stevens, D.P., 2012. Southern Ocean fronts: Controlled by wind or topography? Journal of Geophysical Research: Oceans 117. URL: https://agupubs.onlinelibrary.wiley.com/doi/abs/10.1029/2012JC007887, doi:doi: 10.1029/2012JC007887.

Gran, H.H., 1931. On the conditions for the production of plankton in the sea. Conseil Perm. Internat. pour I'Explor. de la Mer. Rapp. et Proces-Verb. 75, 37–46.

Gran, H.H., Braarud, T., 1935. A Quantitative Study of the Phytoplankton in the Bay of Fundy and the Gulf of Maine (including Observations on Hydrography, Chemistry and Turbidity). Journal of the Biological Board of Canada 1, 279–467. URL: https://doi.org/10.1139/f35-012, doi:doi: 10.1139/f35-012.

Han, B.P., Virtanen, M., Koponen, J., Straškraba, M., 2000. Effect of photoinhibition on algal photosynthesis: a dynamic model. Journal of Plankton Research 22, 865–885. URL: https://doi.org/10.1093/plankt/22.5.865, doi:doi: 10.1093/plankt/22.5.865.

Hancke, K., Lund-Hansen, L.C., Lamare, M.L., Højlund Pedersen, S., King, M.D., Andersen, P., Sorrell, B.K., 2018. Extreme Low Light Requirement for Algae Growth Underneath Sea Ice: A Case Study From Station Nord, NE Greenland. Journal of Geophysical Research: Oceans 123, 985–1000. URL: https://agupubs.onlinelibrary.wiley.com/doi/abs/10.1002/2017JC013263, doi:doi: 10.1002/2017JC013263.

Hart, T.J., 1934. On the phytoplankton of the southeast Atlantic and the Bellingshausen Sea, 1929-1931. Discovery Reports 8, 1–268.

Haumann, F.A., Gruber, N., Münnich, M., Frenger, I., Kern, S., 2016. Sea-ice transport driving Southern Ocean salinity and its recent trends. Nature 537, 89–92. URL: http://www.nature.com/doifinder/10.1038/nature19101, doi:doi: 10.1038/nature19101.

Heil, P., 2006. Atmospheric conditions and fast ice at Davis, East Antarctica: A case study. Journal of Geophysical Research: Oceans 111. URL: https://agupubs.onlinelibrary.wiley.com/doi/abs/10.1029/2005JC002904, doi:doi: 10.1029/2005JC002904.

Hendey, N.I., 1937. The plankton diatoms of the southern seas. Discovery Reports 16, 151–364.

Hill, V.J., Light, B., Steele, M., Zimmerman, R.C., 2018. Light availability and phytoplankton growth beneath arctic sea ice: Integrating observations and modeling. Journal of Geophysical Research: Oceans 123, 3651–3667. doi:doi: 10.1029/2017JC013617.

Hiraike, Y., Ikeda, M., 2009. Descending surface water at the antarctic marginal ice zone and its contribution to intermediate water: An ice-ocean model. Journal of Oceanography 65, 587–603. doi:doi: 10.1007/s10872-009-0050-8.

Hobbs, W.R., Massom, R., Stammerjohn, S., Reid, P., Williams, G., Meier, W., 2016. A review of recent changes in Southern Ocean sea ice, their drivers and forcings. Global and Planetary Change 143, 228–250. URL: http://www.sciencedirect.com/science/article/pii/S0921818116300364, doi:doi: https://doi.org/10.1016/j.gloplacha.2016.06.008.

Holland, P.R., Kwok, R., 2012. Wind-driven trends in Antarctic sea-ice drift. Nature Geoscience 5, 872–875. URL: http://www.nature.com/doifinder/10.1038/ngeo1627, doi:doi: 10.1038/ngeo1627.

Holte, J., Talley, L., 2009. A new algorithm for finding mixed layer depths with applications to argo data and subantarctic mode water formation. Journal of Atmospheric and Oceanic Technology 26, 1920–1939. doi:doi: 10.1175/2009JTECHO543.1.

Hunke, E.C., Dukowicz, J.K., 1997. An Elastic–Viscous–Plastic Model for Sea Ice Dynamics. Journal of Physical Oceanography 27, 1849–1867. URL: https://doi.org/10.1175/1520-0485(1997)027{%}3C1849:AEVPMF{%}3E2.0.CO;2, doi:doi: 10.1175/1520-0485(1997)027⟨1849:AEVPMF⟩2.0.CO;2.

Ilyina, T., Six, K.D., Segschneider, J., Maier-Reimer, E., Li, H., Núñez-Riboni, I., 2013. Global ocean biogeochemistry model HAMOCC: Model architecture and performance as component of the MPI-Earth system model in different CMIP5 experimental realizations. Journal of Advances in Modeling Earth Systems 5, 287–315. doi:doi: 10.1029/2012MS000178.

Iversen, M.H., Ploug, H., 2013. Temperature effects on carbon-specific respiration rate and sinking velocity of diatom aggregates – potential implications for deep ocean export processes. Biogeosciences 10, 4073–4085. URL: https://www.biogeosciences.net/10/4073/2013/, doi:doi: 10.5194/bg-10-4073-2013.

Jeffries, M., Schwartz, K., Morris, K., Veazey, A., Krouse, H., Gushing, S., 1995. Evidence for platelet ice accretion in Arctic sea ice development. Journal of Geophysical Research: Oceans 100, 10905–10914. doi:doi: 10.1029/95JC00804.

Jeffries, M.O., Krouse, H.R., Hurst-Cushing, B., Maksym, T., 2001. Snow-ice accretion and snow-cover depletion on Antarctic first-year sea-ice floes. Annals of Glaciology 33, 51–60. doi:doi: 10.3189/172756401781818266.

Jeffries, M.O., Morris, K., Weeks, W.F., Worby, A.P., 1997. Seasonal variations in the properties and structural composition of sea ice and snow cover in the Bellingshausen and Amundsen Seas, Antarctica. Journal of Glaciology 43, 138–151. doi:doi: 10.3189/S0022143000002902.

Jena, B., Ravichandran, M., Turner, J., 2019. Recent Reoccurrence of Large Open-Ocean Polynya on the Maud Rise Seamount. Geophysical Research Letters 46, 4320–4329. URL: https://agupubs.onlinelibrary.wiley.com/doi/abs/10.1029/2018GL081482, doi:doi: 10.1029/2018GL081482.

Ji, R., Jin, M., Varpe, Ø., 2013. Sea ice phenology and timing of primary production pulses in the Arctic Ocean. Global Change Biology 19, 734–741. URL: https://onlinelibrary.wiley.com/doi/abs/10.1111/gcb.12074, doi:doi: 10.1111/gcb.12074.

Johnson, K.S., Plant, J.N., Coletti, L.J., Jannasch, H.W., Sakamoto, C.M., Riser, S.C., Swift, D.D., Williams, N.L., Boss, E., Haëntjens, N., Talley, L.D., Sarmiento, J.L., 2017. Biogeochemical sensor performance in the SOCCOM profiling float array. Journal of Geophysical Research: Oceans 122, 6416–6436. URL: https://agupubs.onlinelibrary.wiley.com/doi/abs/10.1002/2017JC012838, doi:doi: 10.1002/2017JC012838.

Kawamura, T., Ohshima, K.I., Takizawa, T., Ushio, S., 1997. Physical, structural, and isotopic characteristics and growth processes of fast sea ice in Lützow-Holm Bay, Antarctica. Journal of Geophysical Research: Oceans 102, 3345–3355. URL: https://agupubs.onlinelibrary.wiley.com/doi/abs/10.1029/96JC03206, doi:doi: 10.1029/96JC03206.

Kimura, N., 2004. Sea Ice Motion in Response to Surface Wind and Ocean Current in the Southern Ocean. Journal of the Meteorological Society of Japan 82, 1223–1231. doi:doi: 10.2151/jmsj.2004.1223.

Kirchman, D.L., 1999. Phytoplankton death in the sea. Nature 398, 293–294. URL: https://doi.org/10.1038/18570, doi:doi: 10.1038/18570.

Kohout, A.L., Williams, M.J.M., Dean, S.M., Meylan, M.H., 2014. Storm-induced sea-ice breakup and the implications for ice extent. Nature 509, 604–607. URL: https://doi.org/10.1038/nature13262, doi:doi: 10.1038/nature13262.

Kuosa, H., Norrman, B., Kivi, K., Brandini, F., 1992. Effects of Antarctic sea ice biota on seeding as studied in aquarium experiments. Polar Biology 12, 333–339. URL: https://doi.org/10.1007/BF00243104, doi:doi: 10.1007/BF00243104.

Lancelot, C., Mathot, S., Veth, C., de Baar, H., 1993. Factors controlling phytoplankton ice-edge blooms in the marginal ice-zone of the northwestern Weddell Sea during sea ice retreat 1988: Field observations and mathematical modelling. Polar Biology 13, 377–387. doi:doi: 10.1007/BF01681979.

Lange, M.A., Ackley, S.F., Wadhams, P., Dieckmann, G.S., Eicken, H., 1989. Development of Sea Ice in the Weddell Sea. Annals of Glaciology 12, 92–96. doi:doi: 10.3189/S0260305500007023.

Lange, M.A., Eicken, H., 1991. Textural characteristics of sea ice and the major mechanisms of ice growth in the Weddell Sea. Annals of Glaciology 15, 210–215. URL: https://www.cambridge.org/core/product/identifier/S0260305500009757/type/journal{_}article, doi:doi: 10.3189/1991AoG15-1-210-215.

Lange, A., Schlosser, P., Ackley, S.F., Wadhams, P., Dieckmann, G.S., 1990. 18O Concentrations In Sea Ice Of The Weddell Sea, Antarctica. Journal of Glaciology 36, 315–323. doi:doi: 10.3189/002214390793701291.

Lannuzel, D., Vancoppenolle, M., van der Merwe, P., de Jong, J., Meiners, K.M., Grotti, M., Nishioka, J., Schoemann, V., 2016. Iron in sea ice: Review and new insights. Elem Sci Anth 4, p.000130. URL: https://www.elementascience.org/articles/10.12952/journal.elementa.000130/, doi:doi: http://doi.org/10.12952/journal.elementa.000130.

Large, W.G., Yeager, S., 2004. Diurnal to decadal global forcing for ocean and sea-ice models: the data sets and flux climatologies. University Corporation for Atmospheric Research doi:doi: 10.5065/D6KK98Q6.

Leeuwe, M.A.V., Scharek, R., Baar, H.J.W.D., Jong, J.T.M.D., Goeyens, L., 1997. Iron enrichment experiments in the Southern Ocean: physiological responses of plankton communities. Deep Sea Research Part II: Topical Studies in Oceanography 44, 189–207. URL: http://www.sciencedirect.com/science/article/pii/S0967064596000690, doi:doi: https://doi.org/10.1016/S0967-0645(96)00069-0.

Lenton, A., Tilbrook, B., Law, R.M., Bakker, D., Doney, S.C., Gruber, N., Ishii, M., Hoppema, M., Lovenduski, N.S., Matear, R.J., McNeil, B.I., Metzl, N., Mikaloff Fletcher, S.E., Monteiro, P.M.S., Rödenbeck, C., Sweeney, C., Takahashi, T., 2013. Sea-air CO2 fluxes in the Southern Ocean for the period 1990-2009. Biogeosciences 10, 4037–4054. URL: https://www.biogeosciences.net/10/4037/2013/, doi:doi: 10.5194/bg-10-4037-2013.

Leonard, G.H., Purdie, C.R., Langhorne, P.J., Haskell, T.G., Williams, M.J.M., Frew, R.D., 2006. Observations of platelet ice growth and oceanographic conditions during the winter of 2003 in McMurdo Sound, Antarctica. Journal of Geophysical Research: Oceans 111. URL: https://agupubs.onlinelibrary.wiley.com/doi/abs/10.1029/2005JC002952, doi:doi: 10.1029/2005JC002952.

Lindemann, C., St. John, M.A., 2014. A seasonal diary of phytoplankton in the North Atlantic. Frontiers in Marine Science 1, 37. URL: https://www.frontiersin.org/article/10.3389/fmars.2014.00037, doi:doi: 10.3389/fmars.2014.00037.

Little, H.J., Vichi, M., Thomalla, S.J., Swart, S., 2018. Spatial and temporal scales of chlorophyll variability using high-resolution glider data. Journal of Marine Systems 187, 1–12. URL: http://www.sciencedirect.com/science/article/pii/S0924796317304530, doi:doi: https://doi.org/10.1016/j.jmarsys.2018.06.011.

Lytle, V.I., Ackley, S.F., 1996. Heat flux through sea ice in the western Weddell Sea: Convective and conductive transfer processes. Journal of Geophysical Research:

Oceans 101, 8853–8868. URL: https://agupubs.onlinelibrary.wiley.com/doi/abs/10.1029/95JC03675, doi:doi: 10.1029/95JC03675.

Madec, G., team, N., 2016. NEMO ocean engine. Note du Pole de modelisation, Institut Pierre-Simon Laplace (IPSL), France.

Mahlstein, I., Gent, P.R., Solomon, S., 2013. Historical Antarctic mean sea ice area, sea ice trends, and winds in CMIP5 simulations. Journal of Geophysical Research Atmospheres 118, 5105–5110. doi:doi: 10.1002/jgrd.50443.

Maksym, T., 2019. Arctic and Antarctic Sea Ice Change: Contrasts, Commonalities, and Causes. Annual Review of Marine Science 11, 187–213. doi:doi: 10.1146/annurev-marine-010816-060610.

Maksym, T., Markus, T., 2008. Antarctic sea ice thickness and snow-to-ice conversion from atmospheric reanalysis and passive microwave snow depth. Journal of Geophysical Research: Oceans 113. URL: https://agupubs.onlinelibrary.wiley.com/doi/abs/10.1029/2006JC004085, doi:doi: 10.1029/2006JC004085.

Maksym, T., Stammerjohn, S.E., Ackley, S., Massom, R., 2012. Antarctic sea ice- A polar opposite? Oceanography 25, 140–151. doi:doi: 10.5670/oceanog.2012.88.

Mangoni, O., Saggiomo, M., Modigh, M., Catalano, G., Zingone, A., Saggiomo, V., 2009. The role of platelet ice microalgae in seeding phytoplankton blooms in Terra Nova Bay (Ross Sea, Antarctica): a mesocosm experiment. Polar Biology 32, 311–323. URL: https://doi.org/10.1007/s00300-008-0507-z, doi:doi: 10.1007/s00300-008-0507-z.

Markus, T., Kottmeier, C., Fahrbach, E., 2013. Ice Formation in Coastal Polynyas In the Weddell Sea and Their Impact on Oceanic Salinity. American Geophysical Union (AGU). pp. 273–292. URL: https://agupubs.onlinelibrary.wiley.com/doi/abs/10.1029/AR074p0273, doi:doi: 10.1029/AR074p0273.

Marshall, J., Speer, K., 2012. Closure of the meridional overturning circulation through Southern Ocean upwelling. Nature Geoscience 5, 171–180. doi:doi: 10.1038/ngeo1391.

Martin, J.H., Fitzwater, S.E., Gordon, R.M., 1990a. Iron deficiency limits phytoplankton growth in Antarctic waters. Global Biogeochemical Cycles 4, 5–12. URL: https://agupubs.onlinelibrary.wiley.com/doi/abs/10.1029/GB004i001p00005, doi:doi: 10.1029/GB004i001p00005.

Martin, J.H., Gordon, R.M., Fitzwater, S.E., 1990b. Iron in Antarctic waters. Nature 345, 156–158. URL: https://doi.org/10.1038/345156a0, doi:doi: 10.1038/345156a0.

Martinson, D.G., 1990a. Evolution of the southern ocean winter mixed layer and sea ice: Open ocean deepwater formation and ventilation. Journal of Geophysical Research: Oceans 95, 11641–11654. URL: https://doi.org/10.1029/JC095iC07p11641, doi:doi: 10.1029/JC095iC07p11641.

Martinson, D.G., 1990b. Southern ocean–sea-ice interaction: implications for climate and modelling. Transactions of the Royal Society of Edinburgh: Earth Sciences 81, 397–405. doi:doi: 10.1017/S0263593300020885.

Martinson, D.G., Wamser, C., 1990. Ice drift and momentum exchange in winter Antarctic pack ice. Journal of Geophysical Research: Oceans 95, 1741–1755. URL: https://agupubs.onlinelibrary.wiley.com/doi/abs/10.1029/JC095iC02p01741, doi:doi: 10.1029/JC095iC02p01741.

Massom, R.A., Eicken, H., Hass, C., Jeffries, M.O., Drinkwater, M.R., Sturm, M., Worby, A.P., Wu, X., Lytle, V.I., Ushio, S., Morris, K., Reid, P.A., Warren, S.G., Allison, I., 2001. Snow on Antarctic sea ice. Reviews of Geophysics 39, 413–445. URL: https://agupubs.onlinelibrary.wiley.com/doi/abs/10.1029/2000RG000085, doi:doi: 10.1029/2000RG000085.

Massom, R.A., Stammerjohn, S.E., 2010. Antarctic sea ice change and variability - Physical and ecological implications. Polar Science 4, 149–186. URL: http://dx.doi.org/10.1016/j.polar.2010.05.001, doi:doi: 10.1016/j.polar.2010.05.001.

Massom, R.A., Stammerjohn, S.E., Smith, R.C., Pook, M.J., Iannuzzi, R.A., Adams, N., Martinson, D.G., Vernet, M., Fraser, W.R., Quetin, L.B., Ross, R.M., Massom, Y., Krouse, H.R., 2006. Extreme Anomalous Atmospheric Circulation in the West Antarctic Peninsula Region in Austral Spring and Summer 2001/02, and Its Profound Impact on Sea Ice and Biota. Journal of Climate 19, 3544–3571. URL: https://doi.org/10.1175/JCLI3805.1, doi:doi: 10.1175/JCLI3805.1.

Matsumura, Y., Ohshima, K.I., 2015. Lagrangian modelling of frazil ice in the ocean. Annals of Glaciology 56, 373–382. URL: https://www.cambridge.org/core/product/identifier/S0260305500261570/type/journal{_}article, doi:doi: 10.3189/2015AoG69A657.

McPhee, M., 2008. Air-Ice-Ocean Interaction: Turbulent Ocean Boundary Layer Exchange Processes. Springer, New York.

McPhee, M., Morison, J., 2001. Under-ice Boundary Layer. Encyclopedia of Ocean Sciences , 3071–3078doi:doi: 10.1006/rwos.2001.0146.

Meijers, A.J.S., 2014. The Southern Ocean in the Coupled Model Intercomparison Project phase 5. Philosophical transactions of the Royal Society A 372, 20130296. URL: http://www.ncbi.nlm.nih.gov/pubmed/24891395{%}7B{%}25{%}7D5Cnhttp://www.pubmedcentral.nih.gov/articlerender.fcgi?artid=PMC4032513, doi:doi: 10.1098/rsta.2013.0296.

Meiners, K.M., Vancoppenolle, M., Thanassekos, S., Dieckmann, G.S., Thomas, D.N., Tison, J.L., Arrigo, K.R., Garrison, D.L., McMinn, A., Lannuzel, D., van der Merwe, P., Swadling, K.M., Smith Jr., W.O., Melnikov, I., Raymond, B., 2012. Chlorophyll a in Antarctic sea ice from historical ice core data. Geophysical Research Letters 39. URL: https://agupubs.onlinelibrary.wiley.com/doi/abs/10.1029/2012GL053478, doi:doi: 10.1029/2012GL053478.

Meredith, M.P., Brandon, M.A., 2017. Oceanography and sea ice in the Southern Ocean. thrid ed.. John Wiley & Sons, Ltd. chapter 8. pp. 216–238. URL: https://onlinelibrary.wiley.com/doi/abs/10.1002/9781118778371.ch8, doi:doi: 10.1002/9781118778371.ch8.

Meredith, M.P., Woodworth, P.L., Chereskin, T.K., Marshall, D.P., Allison, L.C., Bigg, G.R., Donohue, K., Heywood, K.J., Hughes, C.W., Hibbert, A., Hogg, A.M., Johnson, H.L., Jullion, L., King, B.A., Leach, H., Lenn, Y.D., Morales Maqueda,

M.A., Munday, D.R., Naveira Garabato, A.C., Provost, C., Sallée, J.B., Sprintall, J., 2011. SUSTAINED MONITORING OF THE SOUTHERN OCEAN AT DRAKE PASSAGE: PAST ACHIEVEMENTS AND FUTURE PRIORITIES. Reviews of Geophysics 49. URL: https://agupubs.onlinelibrary.wiley.com/doi/abs/10.1029/2010RG000348, doi:doi: 10.1029/2010RG000348.

Meylan, M.H., Bennetts, L.G., Kohout, A.L., 2014. In situ measurements and analysis of ocean waves in the Antarctic marginal ice zone. Geophysical Research Letters 41, 5046–5051. URL: https://agupubs.onlinelibrary.wiley.com/doi/abs/10.1002/2014GL060809, doi:doi: 10.1002/2014GL060809.

Mongwe, P., Vichi, M., Monteiro, P.M.S., 2018. Mechanisms of the Sea- Air CO2 Flux Seasonal Cycle biases in CMIP5 Earth Systems Models in the Southern Ocean. Biogeosciences doi:doi: 10.5194/bg-15-2851-2018.

Moore, C.M., Suggett, D.J., Hickman, A.E., Kim, Y.N., Tweddle, J.F., Sharples, J., Geider, R.J., Holligan, P.M., 2006. Phytoplankton photoacclimation and photoadaptation in response to environmental gradients in a shelf sea. Limnology and Oceanography 51, 936–949. URL: https://aslopubs.onlinelibrary.wiley.com/doi/abs/10.4319/lo.2006.51.2.0936, doi:doi: 10.4319/lo.2006.51.2.0936.

Nelson, D.M., Smith Jr., W.., 1991. Sverdrup revisited: Critical depths, maximum chlorophyll levels, and the control of Southern Ocean productivity by the irradiance-mixing regime. Limnology and Oceanography 36, 1650–1661. URL: https://aslopubs.onlinelibrary.wiley.com/doi/abs/10.4319/lo.1991.36.8.1650, doi:doi: 10.4319/lo.1991.36.8.1650.

Nicholson, S.A., Lévy, M., Llort, J., Swart, S., Monteiro, P.M.S., 2016. Investigation into the impact of storms on sustaining summer primary productivity in the Sub-Antarctic Ocean. Geophysical Research Letters 43, 9192–9199. URL: https://agupubs.onlinelibrary.wiley.com/doi/abs/10.1002/2016GL069973, doi:doi: 10.1002/2016GL069973.

Nihashi, S., Cavalieri, D.J., 2006. Observational evidence of a hemispheric-wide ice–ocean albedo feedback effect on Antarctic sea-ice decay. Journal of Geophysical Research: Oceans 111. URL: https://agupubs.onlinelibrary.wiley.com/doi/abs/10.1029/2005JC003447, doi:doi: 10.1029/2005JC003447.

Notz, D., 2012. Challenges in simulating sea ice in Earth System Models. WIREs Climate Change 3, 509–526. URL: https://onlinelibrary.wiley.com/doi/abs/10.1002/wcc.189, doi:doi: 10.1002/wcc.189.

Ohshima, K.I., Nihashi, S., 2005. A Simplified Ice–Ocean Coupled Model for the Antarctic Ice Melt Season. Journal of Physical Oceanography 35, 188–201. URL: https://doi.org/10.1175/JPO-2675.1, doi:doi: 10.1175/JPO-2675.1.

Orsi, A.H., Whitworth, T., Nowlin, W.D., 1995. On the meridional extent and fronts of the Antarctic Circumpolar Current. Deep Sea Research Part I: Oceanographic Research Papers 42, 641–673. URL: https://www.sciencedirect.com/science/article/pii/096706379500021W, doi:doi: 10.1016/0967-0637(95)00021-W.

Paget, M.J., Worby, A.P., Michael, K.J., 2001. Determining the floe-size distribution of East Antarctic sea ice from digital aerial photographs. Annals of Glaciology 33, 94–100. doi:doi: 10.3189/172756401781818473.

Parkinson, C.L., 2019. A 40-y record reveals gradual Antarctic sea ice increases followed by decreases at rates far exceeding the rates seen in the Arctic. Proceedings of the National Academy of Sciences 116, 14414–14423. URL: https://www.pnas.org/content/116/29/14414, doi:doi: 10.1073/pnas.1906556116.

Pellichero, V., Sallee, J.B., Schmidtko, S., Roquet, F., Charrassin, J.B., 2016. The ocean mixed layer under Southern Ocean sea-ice: Seasonal cycle and forcing. Journal of Geophysical Research: Oceans 121, 4056–4076. doi:doi: 10.1002/2015JC011572. Received.

Penrose, J.D., Conde, M., Pauly, T.J., 1994. Acoustic detection of ice crystals in Antarctic waters. Journal of Geophysical Research: Oceans 99, 12573–12580. URL: https://agupubs.onlinelibrary.wiley.com/doi/abs/10.1029/93JC03507, doi:doi: 10.1029/93JC03507.

Perovich, D.K., 2017. Sea ice and sunlight. thrid ed.. John Wiley & Sons, Ltd. chapter 4. pp. 110–137. URL: https://onlinelibrary.wiley.com/doi/abs/10.1002/9781118778371.ch4, doi:doi: 10.1002/9781118778371.ch4.

Petrich, C., Eicken, H., 2016. Overview of sea ice growth and properties. John Wiley & Sons, Ltd. chapter 1. pp. 1–41. URL: https://onlinelibrary.wiley.com/doi/abs/10.1002/9781118778371.ch1, doi:doi: 10.1002/9781118778371.ch1.

Platt, T., Sathyendranath, S., 2008. Ecological indicators for the pelagic zone of the ocean from remote sensing. Remote Sensing of Environment 112, 3426–3436. URL: http://www.sciencedirect.com/science/article/pii/S0034425708001272, doi:doi: https://doi.org/10.1016/j.rse.2007.10.016.

du Plessis, M., Swart, S., Ansorge, I.J., Mahadevan, A., Thompson, A.F., 2019. Southern Ocean Seasonal Restratification Delayed by Submesoscale Wind–Front Interactions. Journal of Physical Oceanography 49, 1035–1053. URL: https://doi.org/10.1175/JPO-D-18-0136.1, doi:doi: 10.1175/JPO-D-18-0136.1.

Prend, C.J., Gille, S.T., Talley, L.D., Mitchell, B.G., Rosso, I., Mazloff, M.R., 2019. Physical Drivers of Phytoplankton Bloom Initiation in the Southern Ocean's Scotia Sea. Journal of Geophysical Research: Oceans 124, 5811–5826. URL: https://agupubs.onlinelibrary.wiley.com/doi/abs/10.1029/2019JC015162, doi:doi: 10.1029/2019JC015162.

Purich, A., Cai, W., England, M.H., Cowan, T., 2016. Evidence for link between modelled trends in Antarctic sea ice and underestimated westerly wind changes. Nature Communications 7, 10409. URL: http://www.nature.com/doifinder/10.1038/ncomms10409, doi:doi: 10.1038/ncomms10409, arXiv:arXiv:1011.1669v3.

Racault, M.F., Le Quéré, C., Buitenhuis, E., Sathyendranath, S., Platt, T., 2012. Phytoplankton phenology in the global ocean. Ecological Indicators 14, 152–163. URL: http://dx.doi.org/10.1016/j.ecolind.2011.07.010, doi:doi: 10.1016/j.ecolind.2011.07.010.

Riaux-Gobin, C., Poulin, M., Dieckmann, G., Labrune, C., Vétion, G., 2011. Spring phytoplankton onset after the ice break-up and sea-ice signature (Adélie Land, East Antarctica). Polar Research 30, 5910. URL: https://doi.org/10.3402/polar.v30i0.5910, doi:doi: 10.3402/polar.v30i0.5910.

Rintoul, S.R., Naveira Garabato, A.C., 2013. Dynamics of the southern ocean circulation. volume 103. 2 ed., Elsevier Ltd. URL: http://dx.doi.org/10.1016/B978-0-12-391851-2.00018-0, doi:doi: 10.1016/B978-0-12-391851-2.00018-0.

Riser, S.C., Swift, D., Drucker, R., 2018. Profiling Floats in SOCCOM: Technical Capabilities for Studying the Southern Ocean. Journal of Geophysical Research: Oceans 123, 4055–4073. doi:doi: 10.1002/2017JC013419.

Roach, L.A., Dean, S.M., Renwick, J.A., 2018a. Consistent biases in Antarctic sea ice concentration simulated by climate models. The Cryosphere 12, 365–383. URL: https://tc.copernicus.org/articles/12/365/2018/, doi:doi: 10.5194/tc-12-365-2018.

Roach, L.A., Horvat, C., Dean, S.M., Bitz, C.M., 2018b. An Emergent Sea Ice Floe Size Distribution in a Global Coupled Ocean-Sea Ice Model. Journal of Geophysical Research: Oceans 123, 4322–4337. URL: https://agupubs.onlinelibrary.wiley.com/doi/abs/10.1029/2017JC013692, doi:doi: 10.1029/2017JC013692.

Rohr, T., Long, M.C., Kavanaugh, M.T., Lindsay, K., Doney, S.C., 2017. Variability in the mechanisms controlling Southern Ocean phytoplankton bloom phenology in an ocean model and satellite observations. Global Biogeochemical Cycles 31, 922–940. doi:doi: 10.1002/2016GB005615.

Romanou, A., Gregg, W.W., Romanski, J., Kelley, M., Bleck, R., Healy, R., Nazarenko, L., Russell, G., Schmidt, G.A., Sun, S., Tausnev, N., 2013. Natural air-sea flux of CO2 in simulations of the NASA-GISS climate model: Sensitivity to the physical ocean model formulation. Ocean Modelling 66, 26–44. URL: http://dx.doi.org/10.1016/j.ocemod.2013.01.008, doi:doi: 10.1016/j.ocemod.2013.01.008.

Rousset, C., Vancoppenolle, M., Madec, G., Fichefet, T., Flavoni, S., Barthélemy, A., Benshila, R., Chanut, J., Levy, C., Masson, S., Vivier, F., 2015. The Louvain-La-Neuve sea ice model LIM3.6: global and regional capabilities. Geoscientific Model Development 8, 2991–3005. URL: https://gmd.copernicus.org/articles/8/2991/2015/, doi:doi: 10.5194/gmd-8-2991-2015.

Sallée, J.B., Llort, J., Tagliabue, A., Levy, M., 2015. Characterization of distinct bloom phenology regimes in the Southern Ocean. ICES Journal of Marine Science 72, 1985 – 1998. doi:doi: 10.1038/278097a0.

Sallée, J.B., Matear, R.J., Rintoul, S.R., Lenton, A., 2012. Localized subduction of anthropogenic carbon dioxide in the Southern Hemisphere oceans. Nature Geoscience 5, 579–584. URL: https://doi.org/10.1038/ngeo1523, doi:doi: 10.1038/ngeo1523.

Sallée, J.B., Shuckburgh, E., Bruneau, N., Meijers, A.J.S., Bracegirdle, T.J., Wang, Z., 2013a. Assessment of Southern Ocean mixed-layer depths in CMIP5 models: Historical bias and forcing response. Journal of Geophysical Research: Oceans 118, 1845–1862. doi:doi: 10.1002/jgrc.20157.

Sallée, J.B., Shuckburgh, E., Bruneau, N., Meijers, A.J.S., Bracegirdle, T.J., Wang, Z., Roy, T., 2013b. Assessment of Southern Ocean water mass circulation and characteristics in CMIP5 models: Historical bias and forcing response. Journal of Geophysical Research: Oceans 118, 1830–1844. doi:doi: 10.1002/jgrc.20135.

Sarmiento, J., Gruber, N., 2006. Ocean Biogeochemical Dynamics. volume 53. Princeton UNiversity Press, Princeton. doi:doi: 10.1017/CBO9781107415324.004, arXiv:arXiv:1011.1669v3.

Schroeter, S., Hobbs, W., Bindoff, N.L., 2017. Interactions between Antarctic sea ice and large-scale atmospheric modes in CMIP5 models. The Cryosphere 11, 789–803. URL: https://www.the-cryosphere.net/11/789/2017/, doi:doi: 10.5194/tc-11-789-2017.

Schultz, C., Doney, S.C., Zhang, W.G., Regan, H., Holland, P.R., Meredith, M.P., Stammerjohn, S.E., 2020. Modeling of the Influence of Sea Ice Cycle and Langmuir Circulation on the Upper Ocean Mixed Layer Depth and Freshwater Distribution at the West Antarctic Peninsula. Journal of Geophysical Research: Oceans URL: https://www.essoar.org/doi/10.1002/essoar.10502066.1.

Séférian, R., Bopp, L., Gehlen, M., Orr, J.C., Ethé, C., Cadule, P., Aumont, O., Salas y Mélia, D., Voldoire, A., Madec, G., 2013. Skill assessment of three earth system models with common marine biogeochemistry. Climate Dynamics 40, 2549–2573. doi:doi: 10.1007/s00382-012-1362-8.

Serreze, M.C., Hurst, C.M., 2000. Representation of Mean Arctic Precipitation from NCEP–NCAR and ERA Reanalyses. Journal of Climate 13, 182–201. URL: https://doi.org/10.1175/1520-0442(2000)013{%}3C0182:ROMAPF{%}3E2.0.CO;2, doi:doi: 10.1175/1520-0442(2000)013⟨0182:ROMAPF⟩2.0.CO;2.

Smedsrud, L.H., Martin, T., 2015. Grease ice in basin-scale sea-ice ocean models. Annals of Glaciology 56, 295–306. doi:doi: 10.3189/2015AoG69A765.

Smetacek, V., Scharek, R., Gordon, L., Eicken, H., Fahrback, E., Rohardt, G., Moore, S., 1992. Early spring phytoplankton blooms in ice platelet layers of the southern Weddell Sea, Antarctica. Deep-Sea Research Part A. Oceanographic Research Papers 39, 153–168.

Smith, W.O., Comiso, J.C., 2008. Influence of sea ice on primary production in the Southern Ocean : A satellite perspective. Journal of Geophysical Research 113, 1–19. doi:doi: 10.1029/2007JC004251.

Smith, W.O., Nelson, D.M., 1985. Phytoplankton Bloom Produced by a Receding Ice Edge in the Ross Sea: Spatial Coherence with the Density Field. Science 227, 163–166. URL: http://www.sciencemag.org/cgi/doi/10.1126/science.227.4683.163, doi:doi: 10.1126/science.227.4683.163.

Smith, W.O., Nelson, D.M., 1986. Importance of Ice Edge Phytoplankton Production in the Southern Ocean. BioScience 36, 251–257. URL: http://www.jstor.org/stable/1310215.

Smith, W.O., Nelson, D.M., 1990. Phytoplankton growth and new production in the Weddell Sea marginal ice zone in the austral spring and autumn. Limnology and Oceanography 35, 809–821. URL: papers2://publication/uuid/864BB12B-9A19-4100-A7F6-F9A6E6A65220, doi:doi: 10.4319/lo.1990.35.4.0809.

Sokolov, S., 2008. Chlorophyll blooms in the Antarctic Zone south of Australia and New Zealand in reference to the Antarctic Circumpolar Current fronts and sea ice forcing. Journal of Geophysical Research 113. doi:doi: 10.1029/2007JC004329.

Sokolov, S., Rintoul, S.R., 2007. Multiple Jets of the Antarctic Circumpolar Current South of Australia*. Journal of Physical Oceanography 37, 1394–1412. URL: http://journals.ametsoc.org/doi/abs/10.1175/JPO3111.1, doi:doi: 10.1175/JPO3111.1.

Stammerjohn, S., Maksym, T., 2017. Gaining (and losing) Antarctic sea ice: variability, trends and mechanisms. John Wiley & Sons, Ltd. chapter 10. pp. 261–289. URL: https://onlinelibrary.wiley.com/doi/abs/10.1002/9781118778371.ch10, doi:doi: 10.1002/9781118778371.ch10.

Steele, M., Boyd, T., 1998. Retreat of the cold halocline layer in the Arctic Ocean. Journal of Geophysical Research: Oceans 103, 10419–10435. URL: https://agupubs.onlinelibrary.wiley.com/doi/abs/10.1029/98JC00580, doi:doi: 10.1029/98JC00580.

Steele, M., Morison, J.H., Untersteiner, N., 1989. The partition of air-ice-ocean momentum exchange as a function of ice concentration, floe size, and draft. Journal of Geophysical Research: Oceans 94, 12739–12750. URL: https://agupubs.onlinelibrary.wiley.com/doi/abs/10.1029/JC094iC09p12739, doi:doi: 10.1029/JC094iC09p12739.

Stopa, J.E., Sutherland, P., Ardhuin, F., 2018. Strong and highly variable push of ocean waves on Southern Ocean sea ice. Proceedings of the National Academy of Sciences 115, 5861–5865. URL: https://www.pnas.org/content/115/23/5861, doi:doi: 10.1073/pnas.1802011115.

Stroeve, J.C., Jenouvrier, S., Campbell, G.G., Barbraud, C., Delord, K., 2016. Mapping and assessing variability in the Antarctic marginal ice zone, pack ice and coastal polynyas in two sea ice algorithms with implications on breeding success of snow petrels. Cryosphere 10, 1823–1843. doi:doi: 10.5194/tc-10-1823-2016.

Strzepek, R.F., Boyd, P.W., Sunda, W.G., 2019. Photosynthetic adaptation to low iron, light, and temperature in Southern Ocean phytoplankton. Proceedings of the National Academy of Sciences 116, 4388–4393. URL: https://www.pnas.org/content/116/10/4388, doi:doi: 10.1073/pnas.1810886116.

Sullivan, C.W., McClain, C.R., Comiso, J.C., Smith Jr., W.O., 1988. Phytoplankton standing crops within an Antarctic ice edge assessed by satellite remote sensing. Journal of Geophysical Research: Oceans 93, 12487–12498. URL: https://agupubs.onlinelibrary.wiley.com/doi/abs/10.1029/JC093iC10p12487, doi:doi: 10.1029/JC093iC10p12487.

Sutherland, G., Reverdin, G., Marié, L., Ward, B., 2014. Mixed and mixing layer depths in the ocean surface boundary. Geophysical Research Lettershysical re 41, 1–8. doi:doi: 10.1002/2014GL061939.A.

Sutherland, P., Dumont, D., 2018. Marginal Ice Zone Thickness and Extent due to Wave Radiation Stress. Journal of Physical Oceanography 48, 1885–1901. URL: https://doi.org/10.1175/JPO-D-17-0167.1, doi:doi: 10.1175/JPO-D-17-0167.1.

Sverdrup, H.U., 1953. On Conditions for the Vernal Blooming of Phytoplankton. ICES Journal of Marine Science 18, 287–295. URL: https://doi.org/10.1093/icesjms/18.3.287, doi:doi: 10.1093/icesjms/18.3.287.

Swart, S., Gille, S.T., Delille, B., Josey, S., Mazloff, M., Newman, L., Thompson, A.F., Thomson, J., Ward, B., du Plessis, M.D., Kent, E.C., Girton, J., Gregor, L., Heil, P., Hyder, P., Pezzi, L.P., de Souza, R.B., Tamsitt, V., Weller, R.A., Zappa, C.J., 2019. Constraining Southern Ocean Air-Sea-Ice Fluxes Through Enhanced Observations. Frontiers in Marine Science 6, 421. URL: https://www.frontiersin.org/article/10.3389/fmars.2019.00421, doi:doi: 10.3389/fmars.2019.00421.

Swart, S., Thomalla, S.J., Monteiro, P.M., 2015. The seasonal cycle of mixed layer dynamics and phytoplankton biomass in the Sub-Antarctic Zone: A high-resolution glider experiment. Journal of Marine Systems 147, 103–115. URL: http://dx.doi.org/10.1016/j.jmarsys.2014.06.002, doi:doi: 10.1016/j.jmarsys.2014.06.002.

Tagliabue, A., Aumont, O., DeAth, R., Dunne, J.P., Dutkiewicz, S., Galbraith, E., Misumi, K., Moore, K., Ridgwell, A., Sherman, E., Stock, C., Vichi, M., Volker, C., Yool, A., 2014a. How well do global ocean biogeochemistry models simulate dissolved iron distributions? Global Biogeochemical Cycles 30, 149 – 174. doi:doi: 10.1002/2015GB005289.

Tagliabue, A., Sallée, J.B., Bowie, A.R., Lévy, M., Swart, S., Boyd, P.W., 2014b. Surface-water iron supplies in the Southern Ocean sustained by deep winter mixing. Nature Geoscience 7, 314–320. URL: http://www.nature.com/doifinder/10.1038/ngeo2101, doi:doi: 10.1038/ngeo2101.

Tamura, T., Ohshima, K.I., Nihashi, S., 2008. Mapping of sea ice production for Antarctic coastal polynyas. Geophysical Research Letters 35. URL: https://agupubs.onlinelibrary.wiley.com/doi/abs/10.1029/2007GL032903, doi:doi: 10.1029/2007GL032903.

Taylor, M.H., Losch, M., Bracher, A., 2013. On the drivers of phytoplankton blooms in the Antarctic marginal ice zone: A modeling approach. Journal of Geophysical Research: Oceans 118, 63–75. doi:doi: 10.1029/2012JC008418.

Tedesco, L., Vichi, M., 2014. Sea Ice Biogeochemistry: A Guide for Modellers. PLOS ONE 9, 1–14. URL: https://doi.org/10.1371/journal.pone.0089217, doi:doi: 10.1371/journal.pone.0089217.

Tedesco, L., Vichi, M., Haapala, J., Stipa, T., 2010. A dynamic Biologically Active Layer for numerical studies of the sea ice ecosystem. Ocean Modelling 35, 89–104. URL: http://www.sciencedirect.com/science/article/pii/S1463500310001010, doi:doi: https://doi.org/10.1016/j.ocemod.2010.06.008.

Tedesco, L., Vichi, M., Scoccimarro, E., 2019. Sea-ice algal phenology in a warmer Arctic. Science Advances 5, eaav4830. URL: http://advances.sciencemag.org/content/5/5/eaav4830.abstract, doi:doi: 10.1126/sciadv.aav4830.

Tedesco, L., Vichi, M., Thomas, D.N., 2012. Process studies on the ecological coupling between sea ice algae and phytoplankton. Ecological Modelling 226, 120–138. URL: https://www.sciencedirect.com/science/article/pii/S0304380011005400, doi:doi: 10.1016/J.ECOLMODEL.2011.11.011.

Thomalla, S.J., Fauchereau, N., Swart, S., Monteiro, P.M.S., 2011. Regional scale characteristics of the seasonal cycle of chlorophyll in the Southern Ocean. Biogeosciences 8, 2849–2866. doi:doi: 10.5194/bg-8-2849-2011.

Thomalla, S.J., Ogunkoya, A.G., Vichi, M., Swart, S., 2017. Using Optical Sensors on Gliders to Estimate Phytoplankton Carbon Concentrations and Chlorophyll-to-Carbon Ratios in the Southern Ocean. Frontiers in Marine Science 4, 34. URL: https://www.frontiersin.org/article/10.3389/fmars.2017.00034, doi:doi: 10.3389/fmars.2017.00034.

Tsamados, M., Feltham, D.L., Schroeder, D., Flocco, D., Farrell, S.L., Kurtz, N., Laxon, S.W., Bacon, S., 2014. Impact of Variable Atmospheric and Oceanic Form Drag on Simulations of Arctic Sea Ice. Journal of Physical Oceanography 44, 1329–1353. URL: https://doi.org/10.1175/JPO-D-13-0215.1, doi:doi: 10.1175/JPO-D-13-0215.1.

Turner, J., Bracegirdle, T.J., Phillips, T., Marshall, G.J., Scott Hosking, J., 2013. An initial assessment of antarctic sea ice extent in the CMIP5 models. Journal of Climate 26, 1473–1484. doi:doi: 10.1175/JCLI-D-12-00068.1.

Uchida, T., Balwada, D., Abernathey, R., Prend, C.J., Boss, E., Gille, S.T., 2019. Southern Ocean Phytoplankton Blooms Observed by Biogeochemical Floats. Journal of Geophysical Research: Oceans 124, 7328–7343. URL: https://agupubs.onlinelibrary.wiley.com/doi/abs/10.1029/2019JC015355, doi:doi: 10.1029/2019JC015355.

Uotila, J., Vihma, T., Launiainen, J., 2000. Response of the Weddell Sea pack ice to wind forcing. Journal of Geophysical Research: Oceans 105, 1135–1151. URL: https://agupubs.onlinelibrary.wiley.com/doi/abs/10.1029/1999JC900265, doi:doi: 10.1029/1999JC900265.

Van Leeuwe, M.A., Tedesco, L., Arrigo, K.R., Assmy, P., Campbell, K., Meiners, K.M., Rintala, J.M., Selz, V., Thomas, D.N., Stefels, J., Others, 2018. Microalgal community structure and primary production in Arctic and Antarctic sea ice: A synthesis. Elementa: Science of the Anthropocene .

Vancoppenolle, M., Bouillon, S., Fichefet, T., Goosse, H., Lecomte, O., Angel, M., Maqueda, M., Madec, G., 2012. The Louvain-la-Neuve sea Ice Model. Note du Pôle de modélisation de l'Institut Pierre-Simon Laplace .

Vancoppenolle, M., Fichefet, T., Goosse, H., Bouillon, S., Madec, G., Maqueda, M.A.M., 2009. Simulating the mass balance and salinity of Arctic and Antarctic sea ice. 1. Model description and validation. Ocean Modelling 27, 33–53. URL: https://www.sciencedirect.com/science/article/pii/S1463500308001613, doi:doi: 10.1016/J.OCEMOD.2008.10.005.

Vancoppenolle, M., Meiners, K.M., Michel, C., Bopp, L., Brabant, F., Carnat, G., Delille, B., Lannuzel, D., Madec, G., Moreau, S., Tison, J.L., van der Merwe, P., 2013. Role of sea ice in global biogeochemical cycles: Emerging views and challenges. Quaternary Science Reviews doi:doi: 10.1016/j.quascirev.2013.04.011.

Veth, C., Lancelot, C., Ober, S., 1992. On processes determining the vertical stability of surface waters in the marginal ice zone of the north-western Weddell Sea and their relationship with phytoplankton bloom development. Polar Biology 12, 237–243. doi:doi: 10.1007/BF00238265.

Vichi, M., Eayrs, C., Alberello, A., Bekker, A., Bennetts, L., Holland, D., de Jong, E., Joubert, W., MacHutchon, K., Messori, G., Mojica, J.F., Onorato, M., Saunders, C.,

Skatulla, S., Toffoli, A., 2019. Effects of an Explosive Polar Cyclone Crossing the Antarctic Marginal Ice Zone. Geophysical Research Letters 46, 5948–5958. doi:doi: 10.1029/2019GL082457.

Vichi, M., Lovato, T., Lazzari, P., Cossarini, G., Gutierrez Mlot E., Mattia G., Masina S., McKiver W. J., Pinardi N., Solidoro C., Tedesco L., Z.M., 2015. The Biogeochemical Flux Model (BFM): Equation Description and User Manual. Bfm versio ed., Bologna, Italy. URL: http://bfm-community.eu.

Vichi, M., Masina, S., 2009. Skill assessment of the PELAGOS global ocean biogeochemistry model over the period 1980–2000. Biogeosciences 6, 2333–2353. URL: https://bg.copernicus.org/articles/6/2333/2009/, doi:doi: 10.5194/bg-6-2333-2009.

Vichi, M., Masina, S., Navarra, A., 2007. A generalized model of pelagic biogeochemistry for the global ocean ecosystem. Part II: Numerical simulations. Journal of Marine Systems 64, 110–134. doi:doi: 10.1016/j.jmarsys.2006.03.014.

Voldoire, A., Sanchez-Gomez, E., Salas y Mélia, D., Decharme, B., Cassou, C., Sénési, S., Valcke, S., Beau, I., Alias, A., Chevallier, M., Déqué, M., Deshayes, J., Douville, H., Fernandez, E., Madec, G., Maisonnave, E., Moine, M.P., Planton, S., Saint-Martin, D., Szopa, S., Tyteca, S., Alkama, R., Belamari, S., Braun, A., Coquart, L., Chauvin, F., 2013. The CNRM-CM5.1 global climate model: Description and basic evaluation. Climate Dynamics 40, 2091–2121. doi:doi: 10.1007/s00382-011-1259-y.

Wang, S., Bailey, D., Lindsay, K., Moore, J.K., Holland, M., 2014. Impact of sea ice on the marine iron cycle and phytoplankton productivity. Biogeosciences 11, 4713–4731. doi:doi: 10.5194/bg-11-4713-2014, arXiv:arXiv:1011.1669v3.

Watson, A.J., Meredith, M.P., Marshall, J., 2014. The Southern Ocean, carbon and climate. Philosophical Transactions of the Royal Society A: Mathematical, Physical and Engineering Sciences 372, 20130057. URL: https://royalsocietypublishing.org/doi/abs/10.1098/rsta.2013.0057, doi:doi: 10.1098/rsta.2013.0057.

Worby, A.P., Geiger, C.A., Paget, M.J., Van Woert, M.L., Ackley, S.F., DeLiberty, T.L., 2008. Thickness distribution of Antarctic sea ice. Journal of Geophysical Research: Oceans 113. URL: https://agupubs.onlinelibrary.wiley.com/doi/abs/10.1029/2007JC004254, doi:doi: 10.1029/2007JC004254.

Wu, L., Rutgersson, A., Sahlée, E., 2015. Upper-ocean mixing due to surface gravity waves. Journal of Geophysical Research: Oceans 120, 8210–8228. URL: https://agupubs.onlinelibrary.wiley.com/doi/abs/10.1002/2015JC011329, doi:doi: 10.1002/2015JC011329.

Ye, Y., Shokr, M., Heygster, G., Spreen, G., 2016. Improving Multiyear Sea Ice Concentration Estimates with Sea Ice Drift. Remote Sensing 8, 397.